

**UCLA**

**UCLA Electronic Theses and Dissertations**

**Title**

Leveraging bioinspired resources for synthesis of sustainable polymeric systems

**Permalink**

<https://escholarship.org/uc/item/0t8433gh>

**Author**

Pumford, Elizabeth

**Publication Date**

2024

Peer reviewed|Thesis/dissertation

UNIVERSITY OF CALIFORNIA

Los Angeles

Leveraging bioinspired resources for synthesis of sustainable  
polymeric systems

A dissertation submitted in partial satisfaction of the  
requirements for the degree Doctor of Philosophy in  
Bioengineering

by

Elizabeth Anne Pumford

2024

© Copyright by  
Elizabeth Anne Pumford  
2024

## ABSTRACT OF THE DISSERTATION

Leveraging bioinspired resources for synthesis of sustainable  
polymeric systems

by

Elizabeth Anne Pumford

Doctor of Philosophy in Bioengineering

University of California, Los Angeles, 2024

Professor Andrea M. Kasko, Chair

This dissertation represents a broad exploration of polymer chemistry, anchored in the principles of the Circular Economy and sustainability. The work presented herein places a strong emphasis on utilizing monomers and polymers sourced from nature. We endeavor to enhance the utility of lignin-derived polymers for commercial applications by improving solubility and thermal properties, while also delving into the synthesis of aromatic-aliphatic polyesters from renewable resources. Lignin-derived poly(ether-amide)s are targeted initially, with the aim of overcoming their solubility limitations through thiol-ene reactions. By introducing small thiol-tagged molecules, the repeating double bonds are reduced, leading to increased chain flexibility and in turn, improved solubility and glass transition temperatures. We then explored the copolymerization of lignin-derived components with lactones for the synthesis of aromatic-aliphatic polyesters. Lactones, such as lactide and glycolide, are natural building blocks pervasive across nature. They

were used in ring-opening polymerizations to produce aliphatic alcohol linkers. The lactone linkers underwent condensation polymerizations with hydroxycinnamate dimers, creating sustainable, high molecular weight polyesters with desirable thermal properties. These approaches not only enhance the viability of polymers from biomass but also align with the ethos of sustainability by repurposing natural materials.

We then pivot to focus on the development of hydrogel wound dressings, as a biomimetic extracellular matrix. Bioinspired polymers were used to initiate redox hydrogel crosslinking, leading to hydrogels with improved biocompatibility compared to the gold standard approach (APS and TEMED). Finally, this was expanded to the development of *in situ* forming hydrogel wound dressings that sequester and release antibiotics, analgesics, and hemostatic agents. These hydrogels exhibited rapid formation, controlled release of therapeutic agents, and biocompatibility, addressing the acute need for hemostasis and infection prevention in traumatic blast wounds. *In vivo* studies demonstrated the safety and efficacy of these hydrogel wound dressings in reducing bacterial burden and promoting wound healing. Overall, this work presents a holistic approach to polymer science, drawing inspiration from nature and rooted in sustainability. By harnessing the potential of natural monomers and polymers, we seek to advance the field while addressing pressing challenges in materials science and healthcare.

The dissertation of Elizabeth Anne Pumford is approved.

Timothy J. Deming

Ximin He

Paul S. Weiss

Andrea M. Kasko, Committee Chair

University of California, Los Angeles

2024

*To Mom and Dad*

## TABLE OF CONTENTS

CHAPTER 1: Introduction and Background .....	1
1.1 Introduction.....	1
1.2 Bio-based Resources .....	3
1.3 Bioinspired Materials.....	10
1.4 Perspective .....	12
1.5 Dissertation Summary.....	13
1.6 References.....	14
CHAPTER 2: Thiol-ene modification of biomass-derived poly(ether-amide)s .....	22
2.1 Introduction.....	22
2.2 Results and Discussion .....	26
2.3 Conclusions.....	39
2.4 Experimental.....	39
2.5 Appendix A.....	47
2.6 References.....	52
CHAPTER 3: Bio-based ring-opening and condensation polymerizations.....	56
3.1 Introduction.....	56
3.2 Results and Discussion .....	62
3.3 Conclusions.....	75



3.4	Experimental .....	77
3.5	Appendix B .....	83
3.6	References .....	87
CHAPTER 4: Nontoxic hydrogels initiated by bioinspired polymers.....		93
4.1	Introduction.....	93
4.2	Results and Discussion .....	96
4.3	Conclusions.....	105
4.4	Experimental .....	106
4.5	Appendix C .....	110
4.6	References .....	119
CHAPTER 5: Tunable drug eluting hydrogel wound dressings for prolonged field care.....		122
5.1	Introduction.....	122
5.2	Results and Discussion .....	126
5.3	Conclusions.....	139
5.4	Experimental .....	140
5.5	Appendix D.....	146
5.6	References.....	154
CHAPTER 6: Conclusions and Broader Impact.....		158
6.1	Conclusions and Summary .....	158
6.2	Future Development.....	160

6.3	Broader Impact.....	160
6.4	References.....	162

## LIST OF FIGURES

### CHAPTER 1

1.1	Global annual plastic production and carbon emissions in million tonnes.....	2
1.2	Lignocellulosic biomass is primarily composed of cellulose, hemicellulose, and lignin..	4
1.3	Lignin is polymerized from (a) monolignols and (b) hydroxycinnamates .....	5
1.4	Previously synthesized and characterized lignin-based poly(ester-amide)s and poly(ether-amide)s.....	8
1.5	Lactones are synthesized via intramolecular esterification of fatty acids.....	8
1.6	Hydrogel crosslinking using redox initiators APS and TEMED.....	10
1.7	Structures of (A) linear polyethyleneimine and (B) spermine.....	11

### CHAPTER 2

2.1	Lignin monomers include (a) monolignols and (b) hydroxycinnamates.....	23
2.2	Thiol-tagged molecules tested in this work include 2-mercaptoethanol, pentaerythritol tetrakis(3-mercaptopropionate (S4P) and methyl 3-mercaptopropionate .....	26
2.3	Interfacial polymerization of hydroxycinnamate dimers (1) with diamines to synthesize poly(ether-amide)s (2).....	30
2.4	IR fingerprint region of poly(ether-amide)s (A) before modification and (B) after thiol-ene functionalization .....	32
2.5	Stacked GPC traces of poly(ether-amide)s before and after thiol-ene modification .....	35

2.6	Stacked DSC traces of thiol-modified poly(ether-amide)s .....	37
2.7	Thermogravimetric analysis (TGA) traces of thiol-modified (A) <i>p</i> -coumaryl, (B) ferulyl, and (C) sinapyl poly(ether-amide)s .....	38
S2.1	<sup>1</sup> H NMR of butyrate-protected <i>p</i> -coumaric acid, in CDCl <sub>3</sub> .....	47
S2.2	<sup>1</sup> H NMR of butyrate-protected ferulic acid, in CDCl <sub>3</sub> .....	48
S2.3	<sup>1</sup> H NMR of butyrate-protected sinapinic acid, in CDCl <sub>3</sub> .....	48
S2.4	<sup>1</sup> H NMR of thiol-ene reaction of butyrate-protected <i>p</i> -coumaric acid with methyl 3-mercaptopropionate, in CDCl <sub>3</sub> .....	49
S2.5	<sup>1</sup> H NMR of thiol-ene reaction of butyrate-protected ferulic acid with methyl 3-mercaptopropionate, in CDCl <sub>3</sub> .....	50
S2.6	<sup>1</sup> H NMR of thiol-ene reaction of ferulyl tert-butyl ether dimer, in CDCl <sub>3</sub> .....	51

### CHAPTER 3

3.1	Plastic production has been steadily increasing, and is primarily used in packaging, building and construction, and transportation industries.....	57
3.2	Chemical structures of lactones investigated in this research.....	59
3.3	Naming convention of condensation polymers .....	69
3.4	IR fingerprint region of condensation polymers incorporating (A) ferulic dimers with ROP linkers, (B) sinapic dimers with ROP linkers, and (C) hydroxycinnamates without linkers .....	70
3.5	Stacked DSC traces of (A) ferulic and (B) sinapic condensation polymers .....	74

3.6	Thermogravimetric analysis (TGA) of model (A) ferulic and (B) sinapic condensation polymers .....	75
S3.1	MALDI-TOF spectra of 1:1 <i>p</i> -coumaric acid:L-lactide in HFIP ( <i>top</i> ) and THF ( <i>bottom</i> ) .....	83
S3.2	MALDI-TOF spectra of 1:1 <i>p</i> -coumaric acid:glycolide in HFIP ( <i>top</i> ) and THF ( <i>bottom</i> ) .....	84
S3.3	MALDI-TOF spectra of 1:10 <i>p</i> -coumaric acid:glycolide in HFIP ( <i>top</i> ) and THF ( <i>bottom</i> ) .....	84
S3.4	MALDI-TOF spectra of 1:10 ferulic acid:glycolide in HFIP ( <i>top</i> ) and THF ( <i>bottom</i> )...	85
S3.5	Example <sup>1</sup> H NMR of diol linker synthesized via Sn(Oct) <sub>2</sub> and ethylene glycol-initiated ring-opening polymerization of DL-lactide (here, a 1:25 ethylene glycol:DL-lactide ratio), in CDCl <sub>3</sub> .....	85
S3.6	<sup>1</sup> H NMR of enzyme-catalyzed diol linker synthesized via 1:10 ethylene glycol:ε-caprolactone ring-opening polymerization, in CDCl <sub>3</sub> .....	86

## CHAPTER 4

4.1	Hydrogel mass swelling ratio increases and elastic modulus decreases as a function of amine ratio .....	101
4.2	Direct-contact cell viability via resazurin metabolic assay.....	104
4.3	Direct-contact cell viability via live/dead staining .....	104
S4.1	<sup>1</sup> H NMR of poly(ethylene glycol)-diacrylate (PEGDA) 3350, in CDCl <sub>3</sub> .....	110

S4.2	<sup>1</sup> H NMR of Glycofect™, in D <sub>2</sub> O.....	111
S4.3	Photographs of hydrogels (A) during gelation in the casting device and (B) after gelation and sample disc preparation using a 3 mm and 6 mm biopsy punch .....	111
S4.4	Rheological curve of TEMED 1 NR <sub>x</sub> hydrogel.....	112
S4.5	Rheological curves of glucosamine (A) 1 NR <sub>x</sub> , (B) 2 NR <sub>x</sub> , (C) 10 NR <sub>x</sub> , and (D) 20 NR <sub>x</sub> hydrogels .....	112
S4.6	Rheological curves of glycine (A) 1 NR <sub>x</sub> , (B) 2 NR <sub>x</sub> , and (C) 10 NR <sub>x</sub> hydrogels .....	113
S4.7	Rheological curves of PEI (A) 0.5 NR <sub>x</sub> , (B) 0.667 NR <sub>x</sub> , (C) 1 NR <sub>x</sub> , (D) 1.44 NR <sub>x</sub> , (E) 2 NR <sub>x</sub> , (F) 10 NR <sub>x</sub> , and (G) 20 NR <sub>x</sub> , hydrogels .....	114
S4.8	Rheological curves of chitosan (A) 1 NR <sub>x</sub> , (B) 2 NR <sub>x</sub> , and (C) 10 NR <sub>x</sub> hydrogels .....	115
S4.9	Rheological curves of Glycofect™ (A) 0.5 NR <sub>x</sub> , (B) 1 NR <sub>x</sub> , (C) 2 NR <sub>x</sub> , and (D) 10 NR <sub>x</sub> hydrogels .....	116
S4.10	Rheological curves of polylysine (A) 1 NR <sub>x</sub> and (B) 2 NR <sub>x</sub> hydrogels .....	116

## CHAPTER 5

5.1	Graphical depiction of the hydrogel wound dressing used in far-forward combat setting .....	124
5.2	Elastic moduli and mass swelling ratios of hydrogels fabricated with varied molecular weights of PEGDA .....	127
5.3	Mass swelling ratios of PEGDA 2000 hydrogels with varied concentration of polyacrylic acid .....	128

5.4	Mechanical properties of PEGDA 3350 hydrogels incorporating varied amounts of sodium polyacrylate .....	129
5.5	<i>In vitro</i> therapeutic release characterization workflow.....	131
5.6	Therapeutic release curves of (a) vancomycin, (b) tobramycin, (c) lidocaine, and (d) tranexamic acid from PEGDA 3350 hydrogels.....	132
5.7	Vancomycin release from (A) PEGDA 3350 and (B) PEGDA 4600 hydrogels with and without acrylic acid .....	133
5.8	Therapeutic release curves of (A) vancomycin and (B) lidocaine from PEGDA 3350 hydrogels with and without sodium polyacrylate.....	134
5.9	Broth microdilution assay for PEGDA 3350 hydrogels (A) loaded with either tobramycin or vancomycin and (B) loaded with both tobramycin and vancomycin.....	135
5.10	Longitudinal bioluminescence, reflecting bacterial burden, of murine open fracture model treated with hydrogel wound dressing.....	137
5.11	Hydrogel wound dressing eradicated a robust <i>S. aureus</i> infection in Merino sheep wound model.....	138
S5.1	<sup>1</sup> H NMR of PEGDA 2000, in CDCl <sub>3</sub> .....	146
S5.2	<sup>1</sup> H NMR of PEGDA 3350, in CDCl <sub>3</sub> .....	147
S5.3	<sup>1</sup> H NMR of PEGDA 4600, in CDCl <sub>3</sub> .....	148
S5.4	<sup>1</sup> H NMR of PEGDA 3350 at 0 days ( <i>blue</i> ), 1 day ( <i>red</i> ), 1 week ( <i>green</i> ), and 3 months ( <i>purple</i> ), in CDCl <sub>3</sub> .....	149

S5.5	Calibration curves relating concentration to absorbance of (A) vancomycin at 281 nm, (B) tobramycin with 0.2% Fe(III)Cl at 370 nm, (C) lidocaine at 283 nm, and (D) tranexamic acid with 0.2% Fe(III)Cl at 370 nm.....	150
S5.6	Calibration curves for tobramycin at high concentrations, with copper sulfate detection at either 330 nm ( <i>grey</i> ) or 540 nm ( <i>blue</i> ) .....	150
S5.7	Lidocaine release from PEGDA 2000 with and without acrylic acid .....	151
S5.8	Additional calibration curves of vancomycin and tobramycin in PBS.....	151
S5.9	Plate maps for broth microdilution assay using tobramycin and vancomycin released from hydrogel .....	152
S5.10	Murine open fracture model .....	153
S5.11	Ovine complex musculoskeletal wound with injuries to the anterior tibia, muscle, fascia, and periosteum .....	153



## LIST OF TABLES

### CHAPTER 1

- 1.1 Lignin and monolignol distribution of soft wood, hard wood, and grasses..... 5

### CHAPTER 2

- 2.1 Solubility of poly(ether-amide)s before and after thiol-ene functionalization ..... 33
- 2.2 Molecular weight characterization of poly(ether-amide)s by gel permeation chromatography before and after thiol-ene functionalization ..... 34
- 2.3 Thermal characterization of poly(ether-amide)s by TGA and DSC before and after thiol-ene functionalization ..... 37
- S2.1 Yields of thiol-ene reactions performed directly on poly(ether-amide)s..... 51

### CHAPTER 3

- 3.1 Iterations of ethylene glycol ring-opening polymerizations performed and the experimentally determined degree of polymerization (via  $^1\text{H NMR}$ ) ..... 65
- 3.2 Hydroxycinnamate-based condensation polymers ..... 69
- 3.3 Molecular weight of hydroxycinnamate-based condensation polymers via RI GPC ..... 73
- S3.1 Yields of tin-catalyzed ROPs of hydroxycinnamate monomers with lactones ..... 85

### CHAPTER 4

4.1	Alternative initiator amine ratios ( $NR_x$ ) and amount required per hydrogel for all candidates tested via rheology.....	97
4.2	Rheological data of hydrogels fabricated using amine-based initiators at various amine ratios ( $NR_x$ ).....	100
4.2	Hydrogel mesh size and crosslink density, calculated via Flory-Rehner equation.....	103

## CHAPTER 5

5.1	Experimental and derived mechanical properties of hydrogels.....	128
5.2	MIC of antibiotics released from hydrogels against <i>S. Aureus</i> and <i>E. Coli</i> .....	136
5.3	Final reagent concentrations in pre-gel solution.....	141

## LIST OF SCHEMES

### CHAPTER 2

- 2.1 Approaches to functionalizing the  $\alpha,\beta$ -unsaturated linkage of lignin-based compounds with a thiol-tagged molecule via (A) thia-Michael addition or (B) thiol-ene addition ... 25
- 2.2 Synthesis of protected hydroxycinnamate monomers (*p*-coumaric acid:  $R_1 = R_2 = -H$ ; ferulic acid:  $R_1 = -OCH_3, R_2 = -H$ ; sinapinic acid:  $R_1 = R_2 = -OCH_3$ )..... 27
- 2.3 Optimizing thiol-ene reactions on protected hydroxycinnamate monomers (*p*-coumaric acid:  $R_1 = R_2 = -H$ ; ferulic acid:  $R_1 = -OCH_3, R_2 = -H$ ; sinapinic acid:  $R_1 = R_2 = -OCH_3$ ) ..... 27
- 2.4 Benzoyl peroxide homolysis into free radicals ..... 27
- 2.5 Synthesis of hydroxycinnamate diacids with ether linkages ..... 29
- 2.6 Direct thiol-ene reaction of biomass-derived poly(ether-amide)s with methyl 3-mercaptopropionate ..... 30

### CHAPTER 3

- 3.1  $Sn(Oct)_2$ -facilitated pathway for ring-opening polymerizations (ROPs)..... 60
- 3.2 Novozym 435 enzymatically catalyzes ROPs and polycondensation in several ionic liquids ..... 61
- 3.3 ROP of lactide or glycolide off of the phenol of hydroxycinnamates ..... 63
- 3.4 Diol linkers, synthesized through ROPs of lactones with ethylene glycol (1), undergo condensation polymerizations with hydroxycinnamate dimers (2)..... 64

3.5	Lipase B-catalyzed ROP of $\epsilon$ -caprolactone in ionic liquids .....	66
3.6	Lipase B-catalyzed ROP of 1:10 ethylene glycol: $\epsilon$ -caprolactone in ionic liquids .....	67
3.7	Toluene azeotrope-mediated condensation polymerizations of (A) modified sinapinic acid and (B) <i>p</i> -coumaric acid .....	68

## CHAPTER 4

4.1	Charge-transfer complex and radical formation from a) APS and TEMED and b) APS and PEI or Glycofect .....	94
4.2	Synthesis of polyethylen glycol diacrylate (PEGDA) .....	96
4.3	Synthesis of dimethyl meso-galactarate and Glycofect <sup>TM</sup> .....	96

My deepest gratitude to Professor Andrea M. Kasko—I truly wouldn't be here were it not for you and the chance you were willing to take on me. You have been an incredible advisor, always providing opportunities for growth, and helped me become into a better scientist, mentor, and marketer. Beyond that, I'm also grateful to know you as a person; it has been an honor to be a part of your lab. Thank you to my committee members, Professors Deming, Weiss, and He, for granting me your time and expertise, and for helping shape the course of this project. Finally, thank you to the Bernthal and Wenke teams for all that you've done for the DOD collaboration over the years.

*To my ma*—Thank you for EVERYTHING. You have been my #1 cheerleader, editor, travel buddy, art partner, and zoo co-member. You made this a genuinely happy Ph.D. experience, and you'll never know just how grateful I am for having you along for this process.

*To my dad*—I wouldn't be here without you; thank you for raising us to be limitless. I learned so much from you and I wish you were here.

*To my sister*—Who knows if I'd even be getting a Ph.D. if I didn't have you to compete against? Thank you for always pushing me to be better and always reminding me that there is not a thing in this world that we can't do.

*To my little girl*—You're my world.

*To Dr. Hlady*—You shaped the course of my research career. Even as an undergrad, you gave me the creative freedom in my research that helped prepare me to excel as a Ph.D. student.

*To Dr. Hall*—My experiences at Cambridge were some of the most amazing of my life. I remain so proud of the lepto project; thank you for taking a chance on me.

*To Maddie and Lexie*—Thank you for always being proud of me, I love you.

*To Shadi*—There aren't words. I'm forever grateful that the Kasko lab brought you into my life. I learned so much from you and your approach to research, and really admire how you work.

Beyond that, you're one of my favorite people in the world and I miss you every day.

*To Brooke*—Dream team fr; you are the yin to my yang. I absolutely loved working with you, both with lab responsibilities and collabs, I could always count on you in every regard. You taught me so much of what I know, and you kept me grounded throughout my Ph.D.

*To Amaka*—I was so excited when you joined the lab, and it has been incredible seeing your growth over the years. You're an amazing person and I'm grateful to call you a friend.

*To Kirstie, James, & Kelly*—You made lab such a happy experience, and the grind was so much more fun with company. I'm grateful Kasko lab brought you into my life, you all truly feel more like family than co-workers.

*To Kaylee & Morgan*—I never could have hoped for a friendship this beautiful. You two were probably the most involved throughout this experience, seeing as we have our constant flow of Powerpuff consciousness. I don't know what I would have done without you both.

*To Cassy*—Thank you for 27 years of friendship.

*To Jonny, Joey, Devin, & Bryan*—Thank you for bringing me into your world, it has truly been a dream.

*To the cousins (incl. Sophie)*—Even if we weren't family, I would pick you as friends every time. I can never thank you enough for being there when life got tough, and equally being there when things were easy. You are the most fun people to be around and I love you all so much.

*To the Aunts & Uncles*—Thank you for your unwavering support and for being the ultimate hype men (and women); I am so lucky to have you in my life.

## VITA

- 2019 B.S. and M.S., Biomedical Engineering  
University of Utah
- 2024 Ph.D., Bioengineering (*expected*)  
University of California, Los Angeles

## PUBLICATIONS

**Pumford, E.A.**\*, Jackson Hoffman\*, B.A., Kasko, A.M. (2024) Nontoxic initiator alternatives to TEMED for redox hydrogel polymerization. *ACS Applied BioMaterials*, 7(4), 2264-71.  
\*These authors contributed equally

Jackson, B.A., **Pumford, E.A.**, Enueme, A., Fetah, K., Kasko, A.M. (2023) Engineered macromolecular toll-like receptor agents and assemblies. *Trends in Biotechnology*, 41(9), 1139-54.

**Pumford, E.A.**, Rahman, S.M. Hlady, V. (2021) Effect of upstream priming on transient downstream platelet-substrate interactions. *Colloids and Surfaces B: Biointerfaces*, 206, 111925.

**Pumford, E.A.**, Lu, J., Spaczai, I., Prasetyo, M.E., Zheng, E.M., Zhang, H., Kamei, D.T. (2020) Developments in integrating nucleic acid isothermal amplification and detection systems for point-of-care diagnostics. *Biosensors and Bioelectronics*, 170, 112674.

Henderson, C., **Pumford, E.**, Seevarthnam, D., Hall, E., Daly, R. (2019) Gene to Diagnostic: Self immobilizing protein for silica microparticle biosensor, modelled with sarcosine oxidase. *Biomaterials*, 193, 58-70.

**Pumford, E.**, Santschi, L., Imondi, R. (2012) *Sebastes serranoides* voucher VH-24 cytochrome oxidase subunit 1 (COI) gene, partial cds; mitochondrial. GenBank Accession Number: JQ694030.

## IN PREPARATION

**Pumford, E.A.**\*, Hamad, C.\* , Enueme, A., Mamouei, Z., Wainwright, J., Cook, C., Wenke, J., Bernthal, N., Kasko, A.M. (2024) Advanced drug eluting hydrogel wound dressing for prolonged field care: Innovations in drug delivery and trauma management. \*These authors contributed equally

**Pumford, E.A.**, Kasko, A.M. (2024) Thiol-ene modification of biomass-derived poly(ether-amide)s for improved solubility.

Enueme, A., Jackson Hoffman, B.A., **Pumford, E.A.** (2024) Bioengineered interventions for complications of sickle cell disease.

## PRESENTATIONS

**Pumford, E.**, Kasko, A., Upton, B. (2022). Biomass-derived polymers incorporating hydroxycinnamates. ACS Western Regional Meeting 2022. October 19-22, 2022, Las Vegas, NV.

**Pumford, E.\***, Jackson, B.\*, Kasko, A. (2023). PEGDA hydrogels utilizing polycationic initiators. ACS Fall 2023. August 13-17, 2023, San Francisco, CA. \*These authors contributed equally

**Pumford, E.**, Upton, B., Kasko, A. (2023). Sustainable biomass-derived polymers for commercial applications. UCLA Bioengineering Research Day. February 10, 2023, Los Angeles, CA.

**Pumford, E.**, Upton, B., Kasko, A. (2022). Sustainable biomass-derived polymers for commercial applications. ACS Western Regional Meeting 2022. October 19-22, 2022, Las Vegas, NV.

**Pumford, E.**, Cook, K., Kasko, A. (2021). Synthesis and drug release kinetics of robust poly(ethylene glycol) hydrogels for field dressings. UCLA Bioengineering Research Day. February 5, 2021, Los Angeles, CA.

**Pumford, E.**, Zudova, S.Z., Hlady, V. (2018). Combined effects of transient upstream priming and hematocrit on downstream platelet rolling. Utah Biomedical Engineering Conference. December 7, 2018, Salt Lake City, UT.

**Pumford, E.**, Zudova, S.Z., Hlady, V. (2018). Combined effects of transient upstream priming and hematocrit on downstream platelet rolling. BMES 2018 Annual Meeting. October 17-20, 2018, Atlanta, GA.

**Pumford, E.** (2018). Platelet rolling following upstream activation. Undergraduate Bioengineering Symposium. April 20, 2018, Salt Lake City, UT. First place poster out of all graduating bioengineers.

**Pumford, E.**, Hlady, V. (2017) Platelet rolling and adhesion following upstream activation. Undergraduate Research Symposium. April 4, 2017, Salt Lake City, UT.



## CHAPTER 1: Introduction and background

### 1.1 Introduction

**Impact of Petroleum-Derived Plastics.** Plastic production and consumption has been exponentially increasing over the past century (**Figure 1.1**) [1], [2], [3]. While mass production of plastics did not begin until World War II, production has rapidly increased to 367 million tons per year in 2020 [1]. In fact, more than half of the plastic that has ever been produced has been made since the year 2000. The plastics industry is now the third largest manufacturing sector in the US. Monomers used are generally derived from hydrocarbon gas liquids, 86% of which come from natural gas processing, and the remainder of which come from crude oil refineries [4]. Plastics on the market are rarely biodegradable, and can only be eliminated by destructive thermal treatment. This leads to accumulation of plastic waste, contaminating water systems and terrestrial habitats with an estimated 4.8-12.7 million tons of plastic each year [4], [5], [6].

There is also growing concern over the long-term effects of microplastics—1 to 5,000  $\mu\text{m}$  particles, that are either intentionally manufactured (e.g., microbeads in skincare products) or are degradation products—on human health and terrestrial and aquatic ecosystems [7]. While our knowledge of the health effects of microplastics exposure and ingestion remains limited, microplastics generally release toxins and there is evidence supporting that oxidative stress and inflammatory response leads to cytotoxicity. Additionally, the immune system's inability to remove the particles may lead to chronic inflammation [8]. Microplastics are particularly harmful to our aquatic environments. Organic chemical contaminants are typically hydrophobic and are found on the surfaces of bodies of water. As microplastics enter aquatic environments, these contaminants adsorb to the surface of the particles and are then ingested in large quantities by fish

as well as frogs [9]. In terrestrial environments, microplastics affect soil quality (both directly and through their impact on soil microorganisms), which impairs the growth of many plants; they also result in food-chain contamination, biomagnifying with each level/transfer [10].

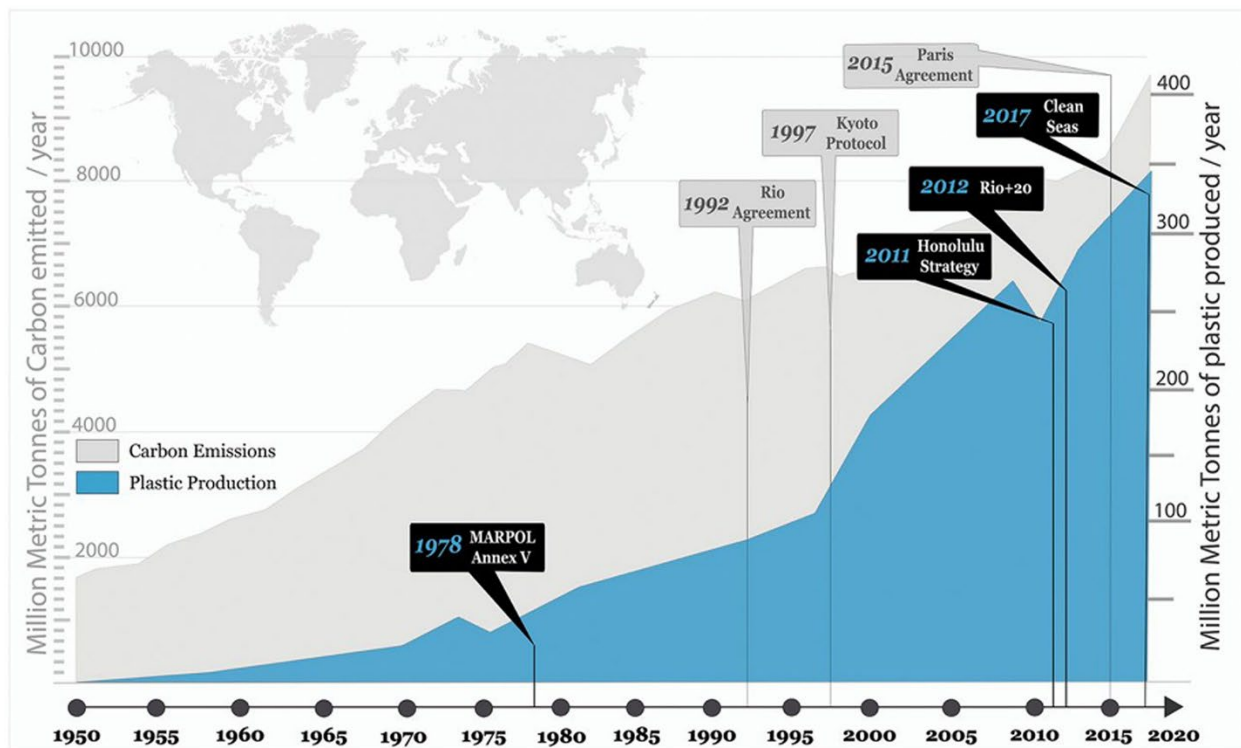


**Figure 1.1.** Global annual plastic production and carbon emissions in million tonnes [3]

Environmental concerns related to the isolation of fossil fuels and the generation of petrochemicals, as well as the impact of accumulating non-degradable plastic waste, is driving increased interest in alternative feedstocks from sustainable, bio-based sources. Bioplastics, synthesized using renewable sources, eliminate this dependence on fossil fuels and can be engineered to rapidly biodegrade, helping reduce waste accumulation. However, bioplastics currently comprise only 1% of commodity plastics, with a worldwide production of approximately 2.15 million tons per year, which pales in comparison to current petroleum-derived plastic production [11]. In addition to cost barriers, bioplastics often exhibit weak thermomechanical

properties, as there has been limited research exploring incorporating aromatic bio-polymers to improve strength [12]. Further, it is important to consider the feedstock source to ensure that it does not place an additional environmental burden, such as requiring fertile soil or water, as other approaches to bio-plastics often do [13]. Overcoming these limitations and employing bio-based feedstocks for polymer synthesis will help scale production of bioplastics to rival that of petroleum-derived plastics, with significant immediate and long-lasting environmental benefits.

## **1.2 Bio-based Resources**

The unifying theme throughout this body of work is an emphasis on bio-based resources, which are renewable materials found in nature, as an alternative to petroleum-derived materials. As sustainability is coming to the forefront, there is growing interest in circular economy, opposed to our current “take-make-dispose” approach. The circular economy is regenerative by design, as it aims to reduce both input and waste, emission, and energy consumption [14], [15]. Ideally, when products are no longer usable, they will be broken down into their starting materials and either used to create something new (i.e., monomers are re-polymerized and re-processed) or if biodegradable, returned to the earth via composting.

The principles of circular economy are a driving factor for the diverse projects discussed herein. In addition to transitioning to bio-sourced starting materials, the energy consumption, impact of chemical solvents, bio-based alternatives for traditional catalysis, and long-term fate of these materials all influenced the direction of this research [16], [17], [18], [19]. This can be probed through life cycle analysis which examines a product at five phases: raw material extraction, manufacturing and processing, transportation, usage, and waste disposal [20].

**Lignin.** One compelling feedstock candidate, with the potential to overcome these barriers to bioplastics, is lignocellulosic biomass. Biomass is the sole truly sustainable source of organic carbon, requiring only atmospheric CO<sub>2</sub>, water, and sunlight for synthesis [21], [22], [23]. Lignocellulosic biomass is composed of cellulose (25-55%), hemicellulose (20-35%), and lignin (10-25%) (**Figure 1.2**). Industrial biomass is pre-treated by physical, chemical, or biological means to isolate cellulose and hemicellulose [24]. Unlike the other components, lignin is regularly discarded as a byproduct—generally incinerated to produce energy—emitting toxic pollutants. While approximately 70 million tons of lignin are isolated annually from the pulp and paper industry, less than 2% is used as a high-value product [25], [26]. The reason behind this is likely twofold: (1) the pre-treatment applied to raw biomass to isolate cellulose significantly reduces the yield of lignin, and (2) the breakdown products of lignin are disparate, impeding the isolation of homogenous building blocks [27], [28], [29], [30]. However, lignin has the potential to serve as a rich renewable resource.

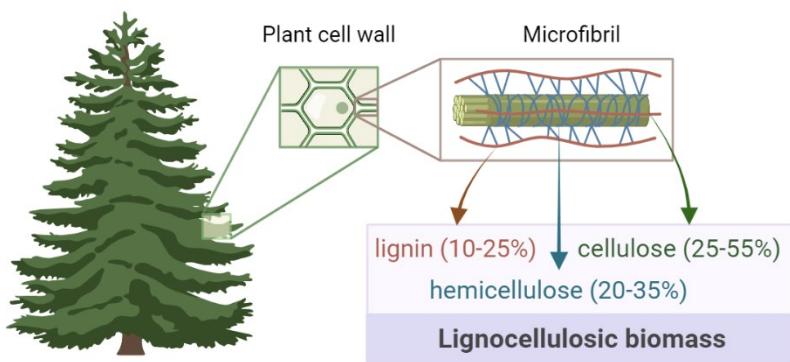


**Figure 1.2.** Lignocellulosic biomass is primarily composed of cellulose, hemicellulose, and lignin.

Lignin is an amorphous, aromatic biopolymer that makes up 30% of carbon in the biosphere. As such, lignin is the most abundant and renewable aromatic carbon source [23], [31]. In woody plants, lignin provides mechanical support and enables water transport, as its aromaticity gives rise to hydrophobicity and rigidity [32], [33]. Lignin polymers are synthesized from monolignols (**Figure 1.3**), including p-coumaryl alcohol, coniferyl alcohol, and sinapyl alcohol, by combinatorial radical oxidative coupling in the cell wall of plants. Each monolignol structure

includes two key aromatic substituents- an  $\alpha$ - $\beta$  double bond *para* to a phenol. Monolignols are not restricted to just these three cinnamyl alcohols, and often incorporate other phenol-based groups, lending to the diverse structures and properties of lignin [32].

Different plant types yield different lignocellulosic biomass distributions. In general, the highest amount of lignin can be found in soft woods (25-31 wt%), followed by hard woods (16-24 wt%), and grasses (wheat, corn, rice straw; 16-21 wt%) [34], [36]. Additionally, the relative

content of monolignols depends on the biomass source (**Table 1.1**). While soft woods have the highest overall lignin content, they are almost entirely made up of ferulic groups. Hard woods have the second highest lignin content, with a nearly even distribution of ferulic and sinapinic monolignols. Finally, grasses have the lowest lignin yield, but their monolignol content is more diverse, incorporating all three classes of monolignols (p-coumaryl alcohol, coniferyl alcohol, and sinapyl alcohol).

There are many research groups investigating lignin valorization and isolation of hydroxycinnamates and monolignols [36], [37]. The vast majority of technical lignins (Kraft, soda, bisulfite) are produced by the pulp industry [34]. Lignin extraction began in the mid-1800s with

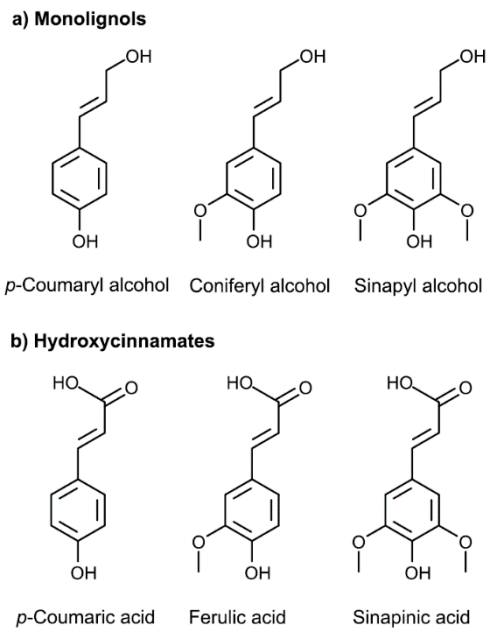


**Figure 1.3.** Lignin is polymerized from (a) monolignols and (b) hydroxycinnamates.

**Table 1.1.** Lignin and monolignol distribution of soft wood, hard wood, and grasses [34], [35].

	Lignin (wt %)	Percentage of total (%)		
		<i>p</i> -Coumaryl alcohol	Coniferyl alcohol	Sinapyl alcohol
Soft wood/Conifers	25-31	<5	>95	0
Hard wood	16-24	0-8	25-50	46-75
Grasses	16-21	5-33	33-80	20-54

soda pulping, cleaving  $\beta$ -O-4 ether linkages under alkaline conditions, resulting in technical lignin. Around 1890, Kraft pulping came into widespread use. This method entailed heating raw biomass with sodium hydroxide and sodium hydrosulfide, introducing a sulfur onto the phenolic side chain [38]. In 1930, the pulping industry transitioned to sulfite pulping to produce lignosulfate [39]. Sulfite pulping was similar to the Kraft lignin approach, heating wood lignin in a solution of sulfite. The key difference was that the lignosulfonate salt became water soluble, as the sulfonic groups incorporated with the aliphatic side chain. A major advance took place in 1968 with the development of organosolv lignin, in which lignin is selectively extracted into a common organic solvent and purified via precipitation [40].

The next phase of valorization is the depolymerization of technical lignin via pyrolysis, solvolysis, and oxidative/reductive reactions. Pyrolysis involved heating the biomass (350-800C) to obtain bio-gas, bio-oil, and solid residue (bio-char). However, this approach is difficult to control and results in heterogeneous products. Lignin solvolysis is generally acid- or base-catalyzed to depolymerize lignins into their monomeric components. Catalytic oxidative and reductive depolymerization uses transition metal catalysts or metal oxides to facilitate the cleavage of  $\beta$ -O-4 bonds, which resulted in a moderate yield of lignin monomers. Current approaches are focusing on reductive catalytic fractionation, involving extraction, depolymerization (via catalytic hydrogenolysis), and stabilization of the intermediates. There is evidence to support ethanol as the solvent for reductive catalytic fractionation, as it aids both depolymerization and stabilization through alkylation [41]. Due to the number of research groups optimizing lignin depolymerization and their anticipated success, the present work will use isolated hydroxycinnamates and monolignols for polymer synthesis.

**Lignin-Derived Polymers.** The products of lignin depolymerization have been used to

synthesize a number of thermosetting polymers, primarily polyurethanes and phenolic resins [42]. There is also growing interest in synthesizing thermoplastics including polyanhydrides and polyesters from lignin-derived monomers, using their hydroxyl-rich structures to incorporate hydrolyzable bonds into the polymer chain [43], [44].

Our group has previously reported the synthesis and characterization of a series of hydroxycinnamate-based poly(ester-amide)s and poly(ether-amide)s as bio-based, biodegradable analogues of commodity aramids (**Fig. 1.4**) [45], [46]. These aromatic-aliphatic-aliphatic poly(ester-amide)s and poly(ether-amide)s featured a range of polymer properties, including  $T_g$ , molecular weight, and degradability. As a whole, they were insoluble in common organic solvents, had moderate thermal stability, and were generally amorphous. This work demonstrates that lignin-derived polymers can be synthesized with tunable properties, by exchanging the comonomer type (i.e., aromatic or aliphatic) and length. While these poly(ester amide)s and poly(ether amide)s incorporating hydroxycinnamates are an advance in the field, their synthetic approach utilized traditional organic solvents and generated significant waste. Furthermore, the intractability of these polymers limited their processing. Because all of the polymers incorporated repeating aromatic regions and an unsaturated bond, solubility limitations present a major barrier to polymer processing.

To advance this project towards high performance materials with a low carbon footprint, the present research utilizes Dr. Upton's work as a platform to improve upon and expand our library of lignin-derived polymers. In addition to functionalizing the lignin-derived poly(ether-amide)s (which eliminate degradation via hydrolysis) to improve solubility in organic solvents, this work also aims to synthesize polymers and copolymers incorporating (modified) hydroxycinnamate monomers derived from lignin via enzymatic condensation reactions, and to

evaluate the properties of the generated polymers and copolymers as plant-derived alternatives to commodity and high performance polymeric materials.

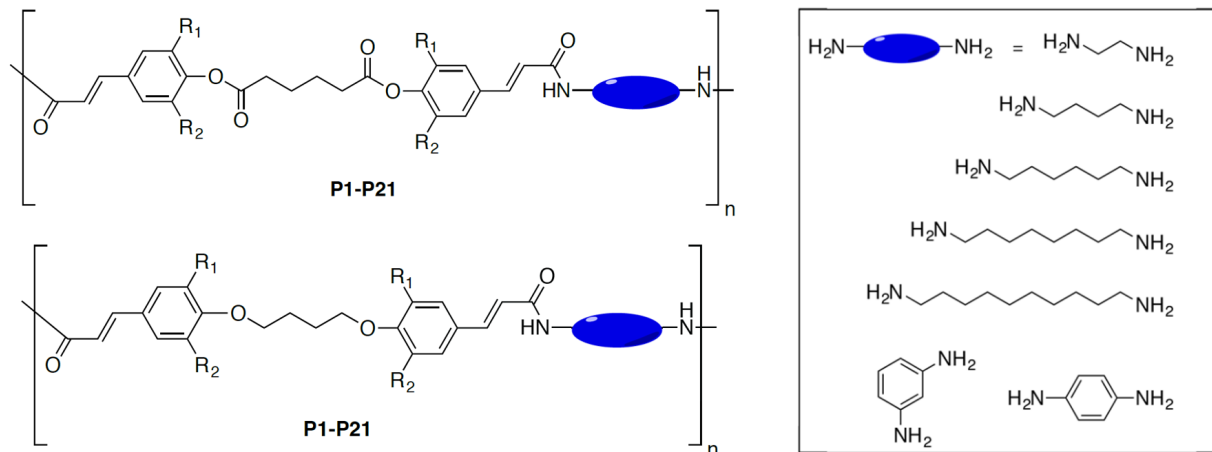


**Figure 1.4.** Previously synthesized and characterized lignin-based poly(ester-amide)s and poly(ether-amide)s [45], [46].

**Lactones.** In expanding the library of lignin-derived polymers, additional bio-based monomers were explored. One monomer class of particular interest are lactones—cyclic carboxylic esters, created by intramolecular esterification of fatty acids (**Figure 1.5**). They are unique starting materials to synthesize polyesters via ring-opening polymerizations (ROPs), driven by the ring strain.

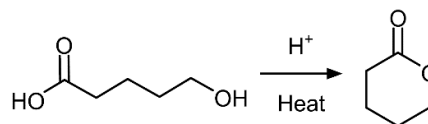


**Figure 1.5.** Lactones are synthesized via intramolecular esterification of fatty acids.

This work focuses on three lactones: lactide, glycolide, and ε-caprolactone. Lactide and glycolide are formed through dehydration reactions of bio-based lactic acid and glycolic acid, respectively, making them renewable bio-based monomers. There have been recent advances in making the synthesis of lactide and glycolide more “green” [47], [48], [49], [50]. Additionally, ε-caprolactone is derived from caproic acid, which is a fatty acid found in a wide range of animal



fats and oils. These lactones (lactide, glycolide, and  $\epsilon$ -caprolactone) exhibit the characteristic ring strain that makes them well-suited for ROPs.

Incorporating lactones into lignin-derived polymers will be explored as an approach to addressing solubility limitations. Ring-opening polymerizations of lactide and glycolide will be used to synthesize symmetrical polyesters, co-catalyzed by the alcohol groups of ethylene glycol (also progressing towards sustainable synthesis from biomass [51]), that can undergo condensation polymerization with hydroxycinnamate dimers. We expect that incorporating longer chains with polar bonds will improve solubility of hydroxycinnamate-based polymers. Additionally, because esters are hydrolytically degradable, this introduces the potential of fabricating biodegradable, and even compostable, polymers that break down into entirely plant-based starting materials.

**Enzymes.** The ring-opening polymerizations of several lactones can be efficiently catalyzed by the enzyme Lipase B [52]. While the present work primarily used a tin catalyst, we wanted to establish a proof-of-concept that the ROP linkers for condensation polymerization could be catalyzed by Lipase B as well. We used immobilized Lipase B from *Candida antarctica* (Novozym 435), a yeast that was originally identified in Antarctic Lake Vanda [53].

Using enzymes to catalyze ROPs presents several distinct advantages. First, they are from inexpensive and renewable resources, and are nontoxic and biodegradable. Additionally, enzymes are the most efficient catalysts in nature, effective even under mild reaction conditions. This plays into their selectivity and specificity, which can eliminate the need for several protection/deprotection steps. Finally, they are recyclable; after a reaction, Lipase B can be isolated, washed, dried, and used in subsequent reactions with minimal reduction in activity.

### 1.3 Bioinspired materials

In addition to bio-based resources, this work also employs bioinspired materials, which are inspired by or based on biological materials. In nature, biological systems have evolved over billions of years to produce adaptable, multiscale hierarchical structures (including biomass) [54]. They are often simple systems that are able to efficiently perform their intended mechanical or functional roles. For instance, despite being made of brittle minerals, shell nacre has a high tensile strength, fracture toughness, and Young's modulus. The hierarchical structure of gecko feet allows them to climb walls, the topography of lotus leaves enables self-cleaning, and starfish and sea cucumbers are able to rapidly and reversibly increase the stiffness of their dermis as a defense mechanism [55], [56]. When bioengineering new polymers and higher-order materials, it can be beneficial to take inspiration from nature. This has enabled unique research advances such as stimuli-responsive materials, superwettability, functional nanospheres (harnessing the self-assembling capabilities of DNA), and bioactive scaffolds for bone and tissue regeneration [57], [58].

**Hydrogels.** A hierarchical structure often found in nature are hydrogels, with the most well-known being collagen and gelatin. Hydrogels have become a widely explored bioengineering platform, as they are biocompatible, tunable, have a high water content, and can be engineered to respond to stimuli. Due to their similar mechanical properties and ability to sequester and release bioactive compounds, hydrogels can serve as a platform to engineer extracellular matrix analogues [59], [60]. These

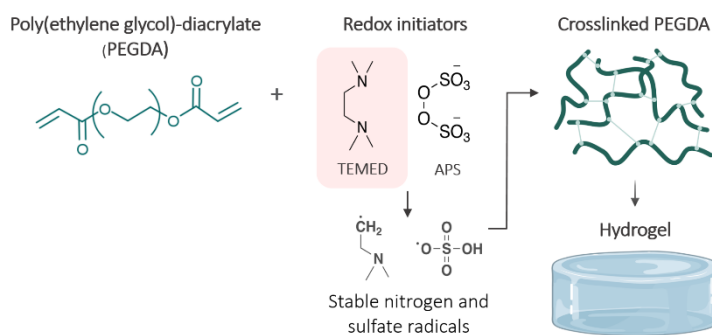


**Figure 1.6.** Hydrogel crosslinking using redox initiators TEMED and APS

properties also make them ideal for wound dressing applications.

In Chapter 4, we will discuss the development of a non-toxic hydrogel crosslinking system. Acrylate-based hydrogels are often fabricated using redox polymerization crosslinking—primarily using ammonium persulfate (APS) and tetramethylethylenediamine (TEMED) (**Figure 1.6**). The bidentate structure of TEMED allows it to form a charge-transfer complex with APS, producing stable sulfate and nitrogen radicals that crosslink the acrylate groups of adjacent polymer chains. The problem with the APS/TEMED system is that TEMED is cytotoxic and has the potential to impede wound healing. We theorized that by replacing TEMED with a bioinspired, amine-containing compound, we could similarly form a charge-transfer complex with APS and generate radicals to achieve hydrogel crosslinking while improving cytotoxicity. As such, we explored the following amine-containing monomers and polymers: glucosamine, glycine, polyethyleneimine (PEI), chitosan, Glycofect™, and polylysine. Chitosan comes from the shells of crustaceans, and glycine and lysine are amino acids found in the body, while glucosamine is an amino sugar that is used in the biosynthesis of glycosaminoglycans and glycoproteins. PEI and Glycofect™ can be more loosely considered bioinspired. Due to the positive charge density resulting from the repeating amino groups, PEI is widely used in biomedical applications (e.g. non-viral gene delivery). While it is not inherently bioinspired, its structure bears a number of similarities to spermine, which is involved in cellular metabolism (**Figure 1.7**). Researchers are increasingly exploring bio-derived versions of polymers with structures similar to PEI to enhance their biocompatibility and reduce environmental impact.

Similarly, while Glycofect™ is a synthetic polymer, it is a poly(glycoamidoamine), which draws inspiration from natural carbohydrates.

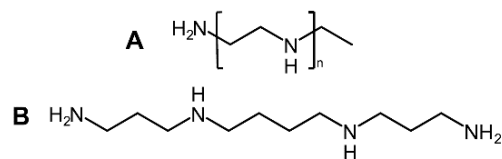


**Figure 1.7.** Structures of (A) linear polyethyleneimine and (B) spermine.

## 1.4 Perspective

While there has been growing interest in renewable alternatives to commodity plastics, growth in the field has lagged behind. Sustainable bio-based polymeric materials require a holistic approach, considering the impact of the feedstock (including cultivation and transportation), the synthetic process and required chemicals, as well as the effect of breakdown products.

The proposed work seeks to shift the paradigm of current commodity polymer development. While most ongoing research developing bioplastics focuses on finding alternative sources for traditional monomers (styrene, lactic acid, etc.), our work aims to utilize products of lignin valorization to synthesize new materials. The significance of this approach is three-fold: (1) it would reduce lignin incineration and subsequent environmental damage, (2) it utilizes a waste product of an existing industry and therefore places no additional environmental burden to cultivate this feedstock, and (3) it harnesses the unique properties of these monomers to develop polymers with diverse and desirable properties. Advances in lignin valorization and polymer synthesis offer pathways to develop high-performance, biodegradable polymers with reduced environmental impact. Further, exploring bio-based monomers like lactones expands the scope of sustainable polymer synthesis, paving the way for novel materials with improved properties. These bio-based compounds inspired additional work, using them in the fabrication of non-toxic bioinspired hydrogels, designed to mimic the properties of native extracellular matrices. By harnessing the potential of lignin and other bio-based resources, coupled with advancements in polymer science and engineering, we can drive innovation towards sustainable materials with tangible environmental benefits.

## 1.5 Dissertation Summary

This work is unified by the principles of Circular Economy for the development of bio-derived, sustainable polymers that break down into eco-friendly materials. This begins in Chapter 2 with the modification of biomass-derived poly(ether-amide)s with small thiol-tagged molecules to improve their processability. Thiol-ene functionalization could be performed directly on the polymers, and led to improved solubility and more desirable thermal properties. Chapter 3 explores bio-based ring-opening polymerizations, followed by condensation reactions with hydroxycinnate dimers. These reactions aim to minimize the required amount of organic solvent, as they are driven by the removal of water, and result in degradable polymers that break down into nature-derived starting materials. In Chapter 4, bio-based and non-toxic amine-based monomers and polymers are explored as alternatives to the traditional toxic approach to crosslinking poly(ethylene glycol) diacrylate hydrogels using redox system APS/TEMED. We identified two alternatives—polyethyleneimine and Glycofect—that work with APS to crosslink hydrogels. In addition to comparable mechanical properties, these hydrogels exhibited superior biocompatibility compared to the TEMED “gold standard”. Finally, Chapter 5 discusses a collaborative project with the David Geffen School of Medicine and the Department of Defense, developing a field-polymerizing hydrogel for blast wounds. The hydrogel forms in situ, molding to the contours of the wound bed to provide controlled release of both a gram-positive and gram-negative antibiotic, an analgesic, and hemostatic agent.

## 1.6 References

- [1] R. Geyer, “Production, use, and fate of synthetic polymers,” in *Plastic Waste and Recycling*, Elsevier Inc., 2020, pp. 13–32.
- [2] C. Arkin, D. Azoulay, A. Caterbow, *et al.*, *Plastic Atlas*, 2nd ed. Heinrich Böll Foundation, Berlin, Germany, and Break Free From Plastic, 2019.
- [3] S. B. Borrelle, C. M. Rochman, M. Liboiron, *et al.*, “Why we need an international agreement on marine plastic pollution,” *PNAS*, vol. 114, no. 38, pp. 9994–9997, 2017.
- [4] R. Geyer, J. R. Jambeck, and K. L. Law, “Production, use, and fate of all plastics ever made,” *Sci. Adv.*, vol. 3, no. 7, p. e1700782, 2017.
- [5] J. Gasperi, R. Dris, V. Rocher, *et al.*, “Microplastics in the continental area: An emerging challenge,” *Norman Bull.*, no. 4, pp. 18–19, 2015.
- [6] J. R. Jambeck, R. Geyer, C. Wilcox, *et al.*, “Plastic waste inputs from land into the ocean,” *Science*, vol. 347, no. 6223, pp. 768–771, 2015.
- [7] R. C. Hale, M. E. Seeley, M. J. La Guardia, *et al.*, “A global perspective on microplastics,” *JGR Ocean.*, vol. 125, no. 1, p. e2018JC014719, 2020.
- [8] J. C. Prata, J. P. da Costa, I. Lopes, *et al.*, “Environmental exposure to microplastics: An overview on possible human health effects,” *Sci. Total Environ.*, vol. 702, p. 134455, 2020.
- [9] A. C. Vivekanand, S. Mohapatra, and V. K. Tyagi, “Microplastics in aquatic environment: Challenges and perspectives,” *Chemosphere*, vol. 282, p. 131151, 2021.

- [10] P. D. Dissanayake, S. Kim, B. Sarkar, *et al.*, “Effects of microplastics on the terrestrial environment: A critical review,” *Environ. Res.*, vol. 209, p. 112734, 2022.
- [11] J. W. R. Chong, K. S. Khoo, G. Y. Yew, *et al.*, “Advances in production of bioplastics by microalgae using food waste hydrolysate and wastewater: A review,” *Bioresour. Technol.*, vol. 342, p. 125947, 2021.
- [12] E. Bioplastics, “Bioplastics market data,” Plastics Europe.
- [13] S. Ghosh, R. Gnaim, S. Greiserman, *et al.*, “Macroalgal biomass subcritical hydrolysates for the production of polyhydroxyalkanoate (PHA) by *Haloferax mediterranei*,” *Bioresour. Technol.*, vol. 271, pp. 166–173, 2019.
- [14] N. Suchek, C. I. Fernandes, S. Kraus, *et al.*, “Innovation and the circular economy: A systematic literature review,” *Bus. Strateg. Environ.*, vol. 30, no. 8, pp. 3686–3702, 2021.
- [15] M. Geissdoerfer, P. Savaget, N. M. P. Bocken, *et al.*, “The circular economy - A new sustainability paradigm?,” *J. Clean. Prod.*, vol. 143, pp. 757–768, 2017.
- [16] C. Capello, U. Fischer, and K. Hungerbühler, “What is a green solvent? A comprehensive framework for the environmental assessment of solvents,” *Green Chem.*, vol. 9, no. 9, pp. 927–93, 2007.
- [17] A. Turner and M. Filella, “Hazardous metal additives in plastics and their environmental impacts,” *Environ. Int.*, vol. 156, p. 106622, 2021.
- [18] J. Engel, A. Cordellier, L. Huang, *et al.*, “Enzymatic ring-opening polymerization of lactones: Traditional approaches and alternative strategies,” *ChemCatChem*, vol. 11, no. 20, pp. 4983–4997, 2019.

- [19] S. Agarwal, “Biodegradable polymers: Present opportunities and challenges in providing a microplastic-free environment,” *Macromol. Chem. Phys.*, vol. 221, no. 6, p. 2000017, 2020.
- [20] R. Heijungs, G. Huppes, and J. B. Guinée, “Life cycle assessment and sustainability analysis of products, materials and technologies. Toward a scientific framework for sustainability life cycle analysis,” *Polym. Degrad. Stab.*, vol. 95, no. 3, pp. 422–428, 2010.
- [21] F. H. Isikgor and C. R. Becer, “Lignocellulosic biomass: A sustainable platform for the production of bio-based chemicals and polymers,” *Polym. Chem.*, vol. 6, no. 25, pp. 4497–4559, 2015.
- [22] A. J. Ragauskas, C. K. Williams, B. H. Davison, *et al.*, “The path forward for biofuels and biomaterials,” *Science*, vol. 311, no. 5760, pp. 484–489, 2006.
- [23] C. H. Zhou, X. Xia, C. X. Lin, *et al.*, “Catalytic conversion of lignocellulosic biomass to fine chemicals and fuels,” *Chem. Soc. Rev.*, vol. 40, no. 11, pp. 5588–5617, 2011.
- [24] J. Baruah, B. K. Nath, R. Sharma, *et al.*, “Recent trends in the pretreatment of lignocellulosic biomass for value-added products,” *Front. Energy Res.*, vol. 6, p. 141, 2018.
- [25] S. Kumar, A. K. Mohanty, L. Erickson, *et al.*, “Lignin and its applications with polymers,” *J. Biobased Mater. Bioenergy*, vol. 3, no. 1, pp. 1–24.
- [26] J. H. Lora and W. G. Glasser, “Recent industrial applications of lignin: A sustainable alternative to nonrenewable materials,” *J. Polym. Environ.*, vol. 10, no. 1–2, pp. 39–48,



2002.

- [27] J. S. Luterbacher, D. M. Alonso, and J. A. Dumesic, “Targeted chemical upgrading of lignocellulosic biomass to platform molecules,” *Green Chem.*, vol. 16, no. 12, pp. 4816–4838, 2014.
- [28] W. Schutyser, T. Renders, S. Van den Bosch, *et al.*, “Chemicals from lignin: An interplay of lignocellulose fractionation, depolymerisation, and upgrading,” *Chem. Soc. Rev.*, vol. 47, pp. 852–908, 2018.
- [29] A. J. Ragauskas, G. T. Beckham, M. J. Bidy, *et al.*, “Lignin valorization: Improving lignin processing in the biorefinery,” *Science*, vol. 344, no. 6185, p. 1246843, 2014.
- [30] H. Chung and N. R. Washburn, “Chemistry of lignin-based materials,” *Green Mater.*, vol. 1, no. 3, pp. 137–160, 2013.
- [31] J. Ralph, K. Lundquist, G. Brunow, *et al.*, “Lignins: Natural polymers from oxidative coupling of 4-hydroxyphenyl- propanoids,” *Phytochem. Rev.*, vol. 3, pp. 29–60, 2004.
- [32] J. C. Del Río, J. Rencoret, A. Gutiérrez, *et al.*, “Lignin monomers from beyond the canonical monolignol biosynthetic pathway: Another brick in the wall,” *ACS Sustain. Chem. Eng.*, vol. 8, no. 13, pp. 4997–5012, 2020.
- [33] E. Ten and W. Vermerris, “Recent developments in polymers derived from industrial lignin,” *J. Appl. Polym. Sci.*, vol. 132, no. 24, p. 42069, 2015.
- [34] X. Liu, F. P. Bouxin, J. Fan, *et al.*, “Recent advances in the catalytic depolymerization of lignin towards phenolic chemicals: A review,” *ChemSusChem*, vol. 13, no. 17, pp. 4296–4317, 2020.

- [35] M. V. Galkin and J. S. M. Samec, “Lignin valorization through catalytic lignocellulose fractionation: A fundamental platform for the future biorefinery,” *ChemSusChem*, vol. 9, no. 13, pp. 1544–1558, 2016.
- [36] S. Zhou, Y. Xue, A. Sharma, *et al.*, “Lignin valorization through thermochemical conversion: Comparison of hardwood, softwood and herbaceous lignin,” *ACS Sustain. Chem. Eng.*, vol. 4, no. 12, pp. 6608–6617, 2016.
- [37] D. M. Neiva, J. Rencore, G. Marques, *et al.*, “Lignin from tree barks: Chemical structure and valorization,” *ChemSusChem*, vol. 13, no. 17, pp. 4537–4547, 2020.
- [38] F. S. Chakar and A. J. Ragauskas, “Review of current and future softwood kraft lignin process chemistry,” *Ind. Crops Prod.*, vol. 20, no. 2, pp. 131–141, 2004.
- [39] A. Tejado, C. Peña, J. Labidi, *et al.*, “Physico-chemical characterization of lignins from different sources for use in phenol–formaldehyde resin synthesis,” *Bioresour. Technol.*, vol. 98, no. 8, pp. 1655–1663, 2007.
- [40] N. Brosse, M. H. Hussin, and A. A. Rahim, “Organosolv processes,” *Biorefineries*, pp. 153–176, 2017.
- [41] X. Huang, C. Atay, T. I. Korányi, *et al.*, “Role of Cu–Mg–Al mixed oxide catalysts in lignin depolymerization in supercritical ethanol,” *ACS Catal.*, vol. 5, no. 12, pp. 7359–7370, 2015.
- [42] E. Feghali, K. M. Torr, D. J. van de Pas, *et al.*, “Thermosetting polymers from lignin model compounds and depolymerized lignins,” in *Lignin Chemistry*, Springer, 2018, pp. 69–93.

- [43] B. M. Upton and A. M. Kasko, "Strategies for the conversion of lignin to high-value polymeric materials: Review and perspective," *Chem. Rev.*, vol. 116, no. 4, pp. 2275–2306, 2016.
- [44] A. Llevot, E. Grau, S. Carlotti, *et al.*, "From lignin-derived aromatic compounds to novel biobased polymers," *Macromol. Rapid Commun.*, vol. 37, no. 1, pp. 9–28, 2015.
- [45] B. M. Upton and A. M. Kasko, "Biodegradable aromatic–aliphatic poly(ester–amides) from monolignol-based ester dimers," *ACS Sustain. Chem. Eng.*, vol. 6, pp. 3659–3668, 2018.
- [46] B. M. Upton and A. M. Kasko, "Biomass-derived poly(ether–amide)s incorporating hydroxycinnamates," *Biomacromolecules*, vol. 20, no. 2, pp. 758–766, 2019.
- [47] W. Huang, Y. Qi, N. Cheng, *et al.*, "Green synthesis of enantiomerically pure L-lactide and D-lactide using biogenic creatinine catalyst," *Polym. Degrad. Stab.*, vol. 101, pp. 18–23, 2014.
- [48] B. L. Cunha, J. O. Bahú, L. F. Xavier, *et al.*, "Lactide: Production routes, properties, and applications," *Bioengineering*, vol. 9, no. 4, p. 164, 2022.
- [49] V. Botvin, S. Karaseva, D. Salikova, *et al.*, "Syntheses and chemical transformations of glycolide and lactide as monomers for biodegradable polymers," *Polym. Degrad. Stab.*, vol. 183, p. 109427, 2021.
- [50] X. Zhou, M. Zha, J. Cao, *et al.*, "Glycolic acid production from ethylene glycol via sustainable biomass energy: Integrated conceptual process design and comparative techno-economic–society–environment analysis," *ACS Sustain. Chem. Eng.*, vol. 9, no.

- 32, pp. 10948–10962, 2021.
- [51] M. K. Wong, S. S. M. Lock, Y. H. Chan, *et al.*, “Towards sustainable production of bio-based ethylene glycol: Progress, perspective and challenges in catalytic conversion and purification,” *Chem. Eng. J.*, vol. 468, p. 143699, 2023.
- [52] C. Bonduelle, B. Martin-Vaca, and D. Bourissou, “Lipase-catalyzed ring-opening polymerization of the O-carboxylic anhydride derived from lactic acid,” *Biomacromolecules*, vol. 10, no. 11, pp. 3069–3073, 2009.
- [53] C. Ortiz, M. L. Ferreira, O. Barbosa, *et al.*, “Novozym 435: the ‘perfect’ lipase immobilized biocatalyst?,” *Catal. Sci. Technol.*, vol. 9, no. 10, pp. 2380–2420, 2019.
- [54] F. J. Martin-Martinez, K. Jin, D. L. Barreiro, *et al.*, “The rise of hierarchical nanostructured materials from renewable sources: Learning from nature,” *ACS Nano*, vol. 12, no. 8, pp. 7425–7433, 2018.
- [55] Y. Wang, S. E. Naleway, and B. Wang, “Biological and bioinspired materials: Structure leading to functional and mechanical performance,” *Bioact. Mater.*, vol. 5, no. 4, pp. 745–757, 2020.
- [56] J. R. Capadona, K. Shanmuganathan, D. J. Tyler, *et al.*, “Stimuli-responsive polymer nanocomposites inspired by the sea cucumber dermis,” *Science*, vol. 319, no. 5868, pp. 1370–1374, 2008.
- [57] M. S. Ganewatta, Z. Wang, and C. Tang, “Chemical syntheses of bioinspired and biomimetic polymers toward biobased materials,” *Nat. Rev. Chem.*, vol. 5, no. 11, pp. 753–772, 2021.

- [58] R. R. Naik and S. Singamaneni, “Introduction: Bioinspired and biomimetic materials,” *Chem. Rev.*, vol. 117, no. 20, pp. 12581–12583, 2017.
- [59] U. Blache and M. Ehrbar, “Inspired by nature: Hydrogels as versatile tools for vascular engineering,” *Adv. Wound Care*, vol. 7, no. 7, pp. 232–246, 2018.
- [60] E. Prince and E. Kumacheva, “Design and applications of man-made biomimetic fibrillar hydrogels,” *Nat. Rev. Mater.*, vol. 4, pp. 99–115, 2019.

## CHAPTER 2: Thiol-ene modification of biomass-derived poly(ether-amide)s

### 2.1 Introduction

Plastic production and consumption has been exponentially increasing over the past century [1], [2]. The environmental impact due to the plastics industry is undeniable; 99% of commodity plastics are derived from petroleum-based sources, few are biodegradable, and this non-degradable waste accumulates and pollutes the environment [2], [3]. There is growing interest in reducing exploitation of fossil fuel resources and turning towards more environmentally friendly alternatives. Bioplastics introduce the possibility of eliminating this dependence on petroleum. They are sourced from renewable feedstocks, and can be engineered to rapidly biodegrade, helping reduce the accumulation of waste [4]. One potential feedstock for bio-based plastics is lignocellulosic biomass, which is the most abundant and renewable carbon source. Lignin, often considered a waste product of lignocellulosic biomass, is also the only natural source of aromatic building blocks.

This aromaticity has the potential to provide the high rigidity and thermal strength that bioplastics are often lacking. Therefore, this work aims to engineer a library of lignin-based polymers with tunable properties and utilize these to develop novel polymer composites for commercial applications. We propose to functionalize monolignols and hydroxycinnamates prior to polymerization, enabling a range of properties to be engineered. The polymers will undergo pre- or post-polymerization modifications to improve workability. After characterization, they will be used to synthesize novel bio-based composites. The outcome of this work will be a series of new, high-performance materials that offer a targeted alternative to petroleum-derived commercial plastics [1].

Biomass-derived polymers present a promising alternative. Biomass is the sole truly sustainable source of organic carbon, requiring only atmospheric CO<sub>2</sub>, water, and sunlight for synthesis [5], [6], [7]. Lignocellulosic biomass is composed of cellulose (25-55%), hemicellulose (20-35%), and lignin (10-25%). Industrial biomass is pre-treated by physical, chemical, or biological means to isolate cellulose and hemicellulose [8]. Unlike the other components, lignin is regularly discarded as a byproduct—generally incinerated to produce energy—emitting toxic pollutants. While approximately 70 million tons of lignin are isolated annually from the pulp and paper industry, less than 2% is used as a high-value product [9], [10]. The reason behind this is likely twofold: (1) the pre-treatment applied to raw biomass to isolate cellulose significantly reduces the yield of lignin, and (2) the breakdown products of lignin are disparate, impeding the isolation of homogenous building blocks [11], [12], [13], [14]. However, lignin has the potential to serve as a rich renewable resource.

Lignin is an amorphous, aromatic biopolymer that makes up 30% of carbon in the biosphere. As such, lignin is the most abundant and renewable aromatic carbon source [7], [15]. In woody plants, lignin provides mechanical support and enables water transport, as its aromaticity gives rise to hydrophobicity and rigidity [16], [17]. Lignin polymers are synthesized from monolignols (**Figure 2.1**), including *p*-coumaryl alcohol, coniferyl alcohol, and sinapyl alcohol, by combinatorial radical oxidative coupling in the cell wall

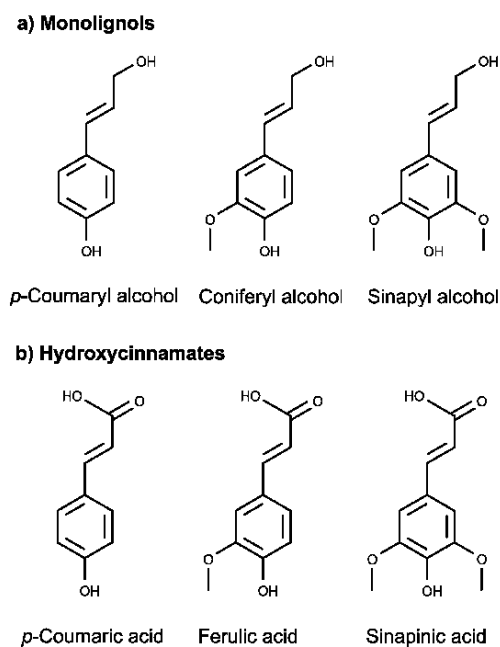


**Figure 2.1.** Lignin monomers include (a) monolignols and (b) hydroxycinnamates.

of plants. Each monolignol structure includes two key aromatic substituents- an  $\alpha$ - $\beta$  double bond

*para* to a phenol. Monolignols are not restricted to just these three cinnamyl alcohols, and often incorporate other phenol-based groups, lending to the diverse structures and properties of lignin [16].

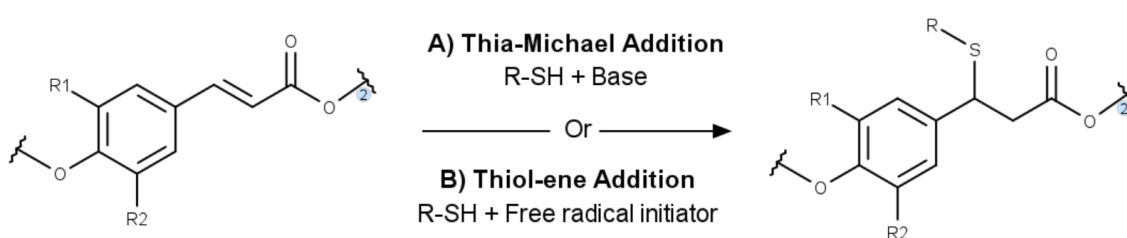
Lignin-derived poly(ether-amide)s were previously synthesized in our laboratory as a means to eliminate hydrolytic degradation, improve solubility in common organic solvents, and improve thermal properties [18]. However, these poly(ether-amide)s still exhibited significant solubility limitations. They exhibited a solubility of 23.7-81.5% in DMF with 10 mM LiBr, depending on the hydroxycinnamate and linker they incorporated. This is expected, as the aromatic regions and alkenes of the hydroxycinnamate dimers are highly non-polar and contribute to the brittleness of the polymers.

To improve the solubility of the poly(ether-amide)s, we aimed to functionalize the  $\alpha,\beta$ -unsaturated linkage, characteristic of hydroxycinnamates, using small thiol-tagged molecules. Eliminating this double bond is expected to improve polymer flexibility, and therefore solubility as well as thermal properties. Additionally, because thiols contribute to polarity, they will also make a small contribution to improving solubility.

To this end, a graft-from and a graft-to approach was explored (**Scheme 2.1**). For grafting from the unsaturated bond, a thia-Michael addition reaction was used. Thia-Michael reactions are the most commonly employed approach to synthesizing organosulfur compounds, due to its efficiency, reaction speed, and selectivity [19]. It is a form of conjugate addition, in which nucleophilic sulfur-based compounds, which serve as Michael donors, attack the  $\beta$ -carbon of alkenes, the Michael acceptors, in the presence of a catalyst. In the graft-to approach, a radical thiol-ene addition reaction was used. These additions can be initiated by light, heat, or radical initiators. In this work, AIBN with thermal initiation was chosen instead of photoinitiation,



because cinnamates are strongly UV absorbing and lead to the attenuation of light. Upon mild heating, AIBN decomposes to create a radical. The radical abstracts a hydrogen from the thiol to generate a thiyl radical. This undergoes anti-Markovnikov addition with the unsaturated bond, forming an intermediate radical. The intermediate abstracts a hydrogen from another thiol to generate a new thiyl radical, and the cycle repeats until all double bonds are consumed or the thiol is quenched. Comprehensive work by Fache et al. showed the synthesis of vanillin-based monomers, functionalized with amines, alcohols, and acids using UV-initiated thiol-ene reactions, lending to the feasibility of this approach for hydroxycinnamate-incorporating compounds [20]. While the majority of thiol-ene reactions reported in literature were used to modify terminal alkenes, there are a number of resources supporting the feasibility of this approach to modify 1,2-disubstituted alkenes [21], [22], [23], [24]. These reactions were first attempted and optimized on protected hydroxycinnamate monomers. After optimization, thiol functionalization was performed directly on the poly(ether-amide)s. We hypothesized that even moderate conversion would result in improvements in solubility and thermal properties, helping make these unique polymers more compatible with commercially scalable polymer processing.



**Scheme 2.1.** Approaches to functionalizing the  $\alpha,\beta$ -unsaturated linkage of lignin-based compounds with a thiol-tagged molecule via (A) thia-Michael addition or (B) thiol-ene addition.

## 2.2 Results and Discussion

**Thiol-tagged Molecules for Addition Reactions.** Reactions grafting thiol-tagged molecules to or from the unsaturated linkage of the hydroxycinnamate-based compounds underwent an iterative process to identify the best reaction conditions, including which thiol-tagged molecule was best. Those tested were 2-mercaptoethanol, pentaerythritol tetrakis(3-mercaptopropionate) (S4P), and methyl 3-mercaptopropionate (**Figure 2.2**).

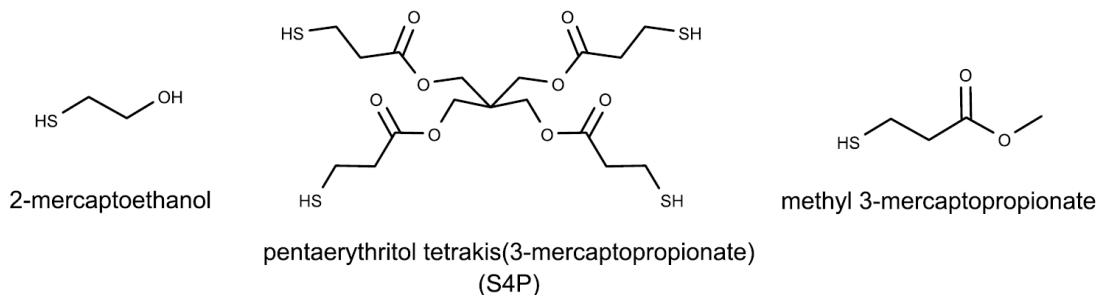
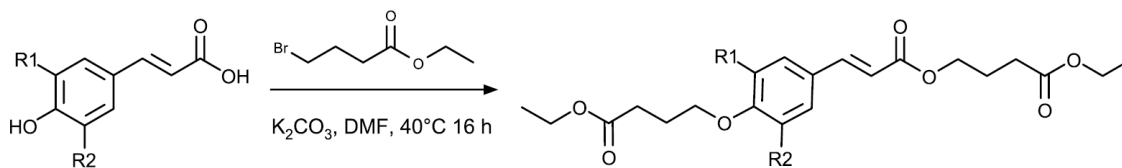


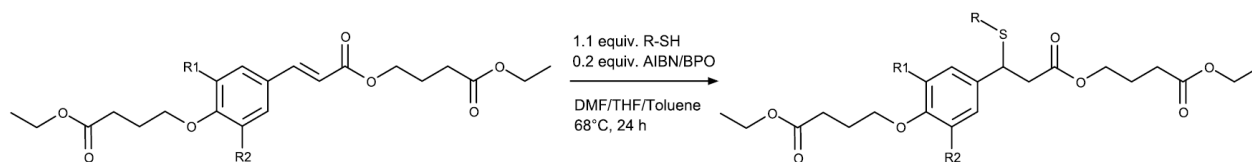
**Figure 2.2.** Thiol-tagged molecules tested in this work include 2-mercaptoethanol, pentaerythritol tetrakis(3-mercaptopropionate) (S4P), and methyl 3-mercaptopropionate.

**Thia-Michael Reaction of Monomers.** Hydroxycinnamate monomers were alkylated using ethyl 4-bromobutyrate to be used for initial reaction optimization (**Scheme 2.2, Figures S2.1-2.3**). This eliminated potential interference from the phenol and carboxylic acid groups. The protected hydroxycinnamates were then used in preliminary thiol addition reactions. Triethylamine-catalyzed thia-Michael addition of methyl 3-mercaptopropionate to protected *p*-coumaric acid did not proceed. Using  $^1\text{H}$  NMR to characterize the product, none of the peaks exhibited any shift or change in splitting pattern. The same reaction was attempted using S4P as the thiol, yet the reaction again did not proceed. We then transitioned to thiol-ene functionalization.



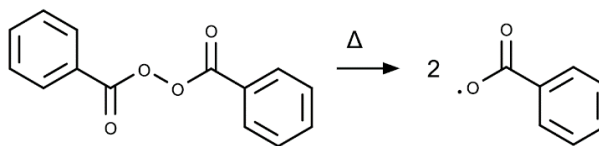
**Scheme 2.2.** Synthesis of protected hydroxycinnamate monomers (*p*-coumaric acid:  $R_1 = R_2 = -H$ ; ferulic acid:  $R_1 = -OCH_3$ ,  $R_2 = -H$ ; sinapinic acid:  $R_1 = R_2 = -OCH_3$ ).

**Thiol-ene Reaction of Monomers.** Thiol-ene reaction conditions were optimized using the protected hydroxycinnamate monomers, adjusting the thiol-tagged molecule used, the radical initiator, and the reaction solvent (**Scheme 2.3**). AIBN-initiated thiol-ene reactions of alkylated coumaric, ferulic, and sinapinic acid using 2-mercaptoethanol in THF did not proceed as confirmed via TLC and  $^1H$  NMR, and had conversions of 0%. The same reactions of protected ferulic acid and sinapinic acid were repeated in toluene, with no improvement in conversion (*yield*: 60.3% and 61.9%, respectively). It was theorized that the hydroxyl group was quenching the radicals.



**Scheme 2.3.** Optimizing thiol-ene reactions on protected hydroxycinnamate monomers (*p*-coumaric acid:  $R_1 = R_2 = -H$ ; ferulic acid:  $R_1 = -OCH_3$ ,  $R_2 = -H$ ; sinapinic acid:  $R_1 = R_2 = -OCH_3$ ).

To overcome this, we transitioned to S4P, which has four terminal thiol groups. These molecules were successfully grafted to alkylated *p*-coumaric acid with a conversion of 35.6% and a yield of 65.1%. The thiol-ene reaction was also tested using benzoyl peroxide as a radical initiator. Benzoyl peroxide features a relatively weak O-O bond that readily undergoes homolysis when subjected to heat, forming free radicals (**Scheme 2.4**). The same thiol-ene

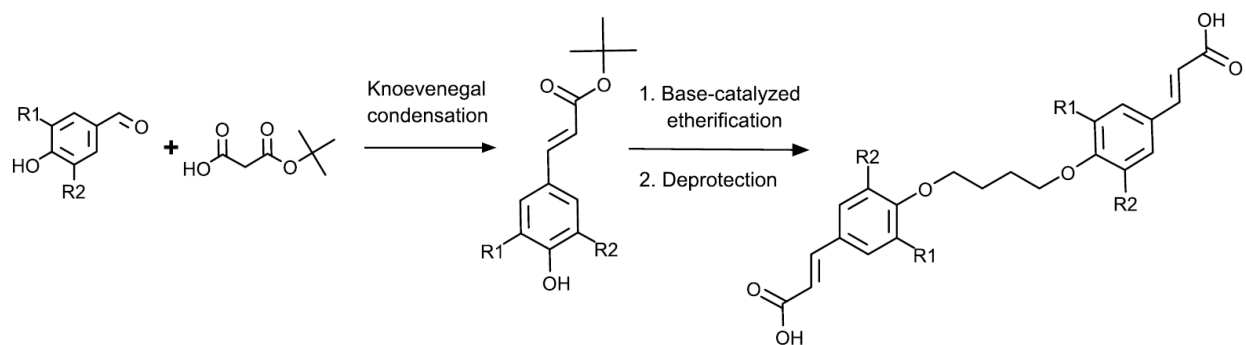


**Scheme 2.4** Benzoyl peroxide homolysis into free radicals.

addition of S4P to the alkylated *p*-coumaric acid was attempted using benzoyl peroxide instead of AIBN, with a conversion of ~35% and yield of 92.7%.

However, the tetrafunctionality of S4P introduces the risk of disulfide formation and crosslinking. For this reason, we transitioned to using methyl 3-mercaptopropionate, which has one terminal thiol group, with the other side an unreactive methyl ester group. Using methyl 3-mercaptopropionate as the thiol, the thiol-ene reaction of protected *p*-coumaric and ferulic acids resulted in improved conversions of 51.7% and 42.2%, respectively, with yields of 76% and 81%. For subsequent thiol-ene addition reactions, AIBN initiation was used to graft methyl 3-mercaptopropionate from the double bonds.

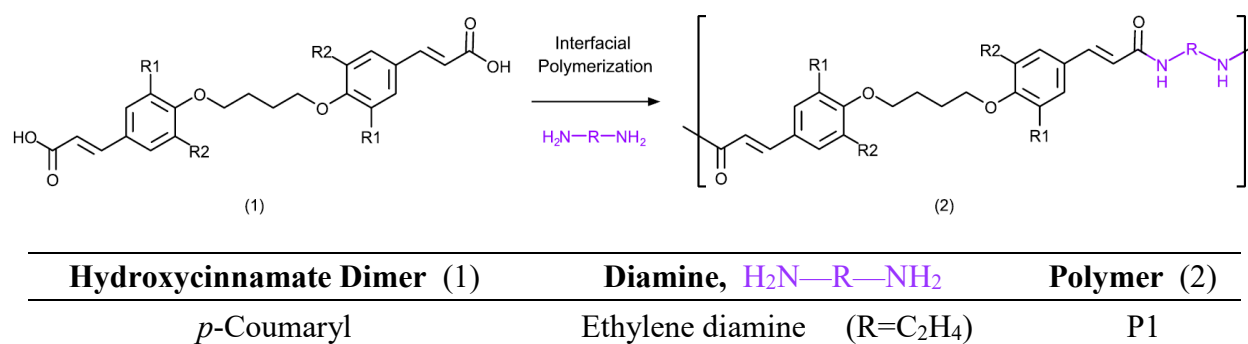
**Thiol-ene Reaction of Dimers.** The thiol-ene reaction was then performed on hydroxycinnamate-based dimers before attempting directly on the poly(ether-amide)s. This was done on the *tert*-butyl protected dimers, with one an ester dimer and the other an ether dimer, to prevent potential reaction interference due to the carboxylic acids present after dimer deprotection. In brief, *tert*-butyl protected *p*-coumaroyl, feruloyl, and sinapoyl esters were synthesized via a Doebner-modified Knoevenagel condensation with *tert*-butyl malonate and their respective precursor aldehydes. *Tert*-butyl ether dimers were then synthesized by dimerizing each of the *tert*-butyl hydroxycinnamates using 1,4-dibromobutane. For ester dimers, adipoyl chloride was used instead of 1,4-dibromobutane. The *tert*-butyl group was removed with trifluoroacetic acid to yield hydroxycinnamate diacid dimers (**Scheme 2.5**). The dimers were either used directly to optimize thiol-functionalization reactions or in interfacial polymerizations with diamine linkers to synthesize poly(ether-amide)s, described in **Figure 2.3**.



**Scheme 2.5.** Synthesis of hydroxycinnamate diacids with ether linkages.

Methyl 3-mercaptopropionate was grafted from the ferulyl *tert*-butyl ether dimer and *p*-coumaryl *tert*-butyl ester dimers, with yields of 42.6% and 65.4%, respectively. The feasibility of this reaction on larger compounds incorporating hydroxycinnamate was confirmed via  $^1\text{H}$  NMR analysis (**Figures S2.6**). The ferulyl dimer had a thiol-ene conversion of 50.5% and the *p*-coumaryl dimer had a conversion of 32.0%. As reaction efficiency was approximately the same for both monomers and dimers, the reaction was then attempted directly on hydroxycinnamate-based poly(ether-amide)s.

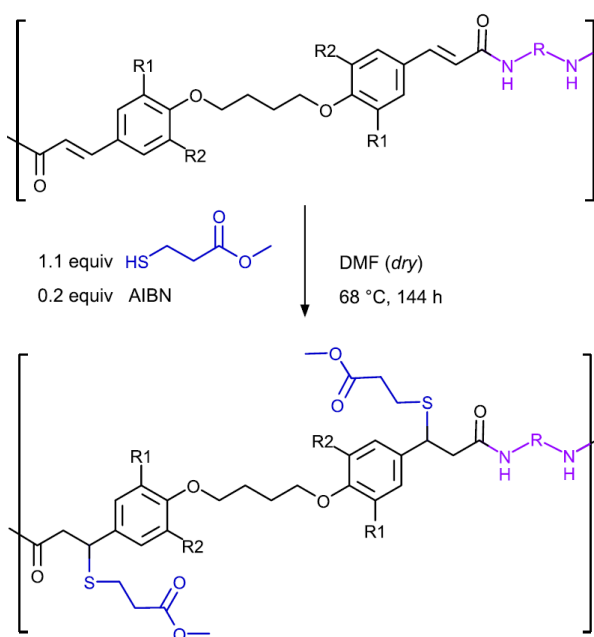
**Thiol-ene Reaction of Polymers.** Lignin-based poly(ether-amide)s were synthesized as previously described [18], [25]. The hydroxycinnamate dimers were converted *in situ* into acid chlorides and underwent interfacial polymerizations with diamine linkers to synthesize poly(ether-amide)s (**Figure 2.3**). For thiol-modification, this work focused on 2-carbon and 8-carbon aliphatic diamine linkers.



(R <sub>1</sub> = R <sub>2</sub> = -H)	1,8-Diaminooctane (R=C <sub>8</sub> H <sub>16</sub> )	P4
Ferulyl	Ethylene diamine	P8
(R <sub>1</sub> = -H, R <sub>2</sub> = -OCH <sub>3</sub> )	1,8-Diaminooctane	P11
Sinapyl	Ethylene diamine	P15
(R <sub>1</sub> = R <sub>2</sub> = -OCH <sub>3</sub> )	1,8-Diaminooctane	P18

**Figure 2.3.** Interfacial polymerization of hydroxycinnamate dimers (1) with diamines to synthesize poly(ether-amide)s (2).

The poly(ether-amide)s used in direct thiol-ene reactions were synthesized by B. Upton, using the exact same products that she extensively characterized to eliminate potential differences in degree of polymerization between iterations (**Scheme 2.6**) [18]. At the start of the reaction, the polymers exhibited very limited solubility in DMF. With stirring and heat and as the reaction progressed, polymers became increasingly soluble. Additional AIBN was added at 24 h and 72 h, as it has a half-life of



**Scheme 2.6.** Direct thiol-ene reaction of biomass-derived poly(ether-amide)s with methyl 3-mercaptopropionate.

AIBN is approximately 10 h at this temperature, rendering the initial amount insufficient for a 5-day reaction. The thiol-ene reaction solutions were concentrated under heat and reduced pressure and precipitated into cold ether, with yields ranging from 39% to 68% (**Table S2.1**). To determine whether the unrecovered polymer was remaining in the ether filtrate, the ether fraction of P1 and P18 following the thiol-ene reaction and work-up was retained and dried under vacuum. After the thiol-ene reaction of P1, 60.5% of the product as obtained as the dried precipitate. The dried ether filtrate had a yield of 14.6%. Similarly, the P18 thiol-ene reaction had a yield of 52.0% for the

precipitate, while the dried ether fraction recovered an additional 7.9% of the poly(ether-amide). There is still a significant portion of the polymer that remains unaccounted for.

**<sup>1</sup>H and FTIR Spectroscopy.** Due to the limited solubility of the poly(ether-amide)s in common NMR solvents, thiol-ene reaction conversion efficiency could not be quantified via <sup>1</sup>H NMR. Therefore, FTIR spectroscopy was used to evaluate thiol functionalization.

FTIR spectra of both the starting and thiol-modified poly(ether-amide)s show peaks characteristic of amides, with a C=O stretch at 1660-1650 cm<sup>-1</sup> and an N-H bend ~1560-1540 cm<sup>-1</sup>. The unmodified polymers show large C=C bending at 980-968 cm<sup>-1</sup> and a C=C stretch peak at 1600 cm<sup>-1</sup>, indicative of the hydroxycinnamates' characteristic 1,2-disubstituted alkene (**Figure 2.4A**). The thiol-modified poly(ether-amide)s exhibit decreased amplitude of the peaks associated with alkene groups, indicating that some of these bonds had been functionalized; consistent with <sup>1</sup>H NMR data, full conversion had not been achieved (**Figure 2.4B**). After the thiol-ene reaction, the polymers also display a weak thioether C-S stretch at ~635 cm<sup>-1</sup>, though signal background noise at this low of a wavenumber makes this stretch difficult to discern [26], [27]. Through the retention of peaks associated with C=O and N-H bonds, it appears that the polymers are not cleaving during the thiol-ene reaction. Additionally, the decrease in the amplitude of C=C peaks after thiol functionalization, as well as the subtle appearance of peaks indicative of thioether bonds confirm that the thiol-ene reaction can be performed directly on these biomass-derived poly(ether-amide)s.

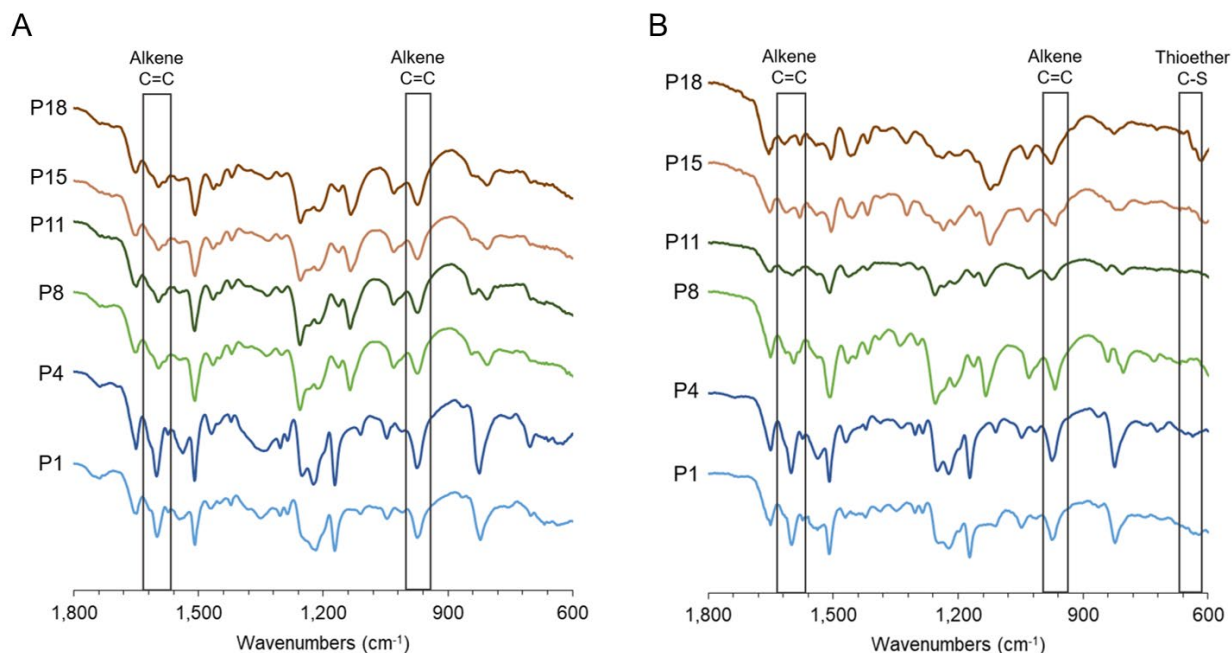


**Figure 2.4.** IR fingerprint region of poly(ether-amide)s (A) before modification and (B) after thiol-ene functionalization.

**Solubility Characterization.** To evaluate solubility, each polymer sample was placed in DMF with 10 mM LiBr for 24 h at room temperature. The mass of undissolved sample (after decanting the solvent and vacuum drying) was used to calculate wt% of soluble polymer. This performed with the initial poly(ether-amide)s as well as those that had undergone thiol-ene addition reactions using methyl 3-mercaptopropionate to compare changes in solubility (**Table 2.1**). For the unmodified poly(ether-amide)s, solubility was lowest, below 25%, for those incorporating *p*-coumaric groups. Poly(ether-amide)s with ferulic and sinapic groups had more moderate solubility, between 43-80 wt%. This difference is likely due to the lack of methoxy substitution of the *p*-coumaric-based polymers limiting their solubility in DMF [18]. In general, increasing substitution on the aromatic ring improved polymer solubility.

For the *p*-coumaric and sinapic-based poly(ether-amide)s, thiol modification with methyl 3-mercaptopropionate substantially improved solubility. Solubility of the *p*-coumaric polymers



(P1 and P4) increased to 79 and 28 wt%, respectively, while the sinapic polymers (P15 and P18) demonstrated the most drastically improved solubility of 99 and 94 wt%, respectively. Ferulic-based polymers (P8 and P11) surprisingly experienced a slight decrease (~10 wt%) in solubility after thiol-ene functionalization. We expect that this is because the symmetry of *p*-coumaryl and sinapyl dimers results in polymers with greater crystallinity, and thus, lower solubility. As such, they experience a more stated increase in solubility following thiol-ene functionalization compared to the ferulyl polymers.

**Table 2.1.** Solubility of poly(ether-amide)s before and after thiol-ene functionalization.

Dimer	Diamine	Name	wt% Soluble*	
			Unmodified	Thiol-ene
<i>P</i> -coumaryl	Ethylene diamine	P1	21.3	78.6
	1,8-diaminooctane	P4	22.7	27.8
Ferulyl	Ethylene diamine	P8	80.2	67.8
	1,8-diaminooctane	P11	45.9	38.4
Sinapyl	Ethylene diamine	P15	59.3	98.6
	1,8-diaminooctane	P18	43.5	94.2

\*10 mg sample in DMF with 10 mM LiBr for 24 h; decanted liquid & dried residual solid to determine insoluble wt%

**Molecular Weight Characterization.** Gel permeation chromatography (GPC) was used to determine  $M_n$ ,  $M_w$ , and  $\bar{D}$  for the six thiol-modified poly(ether-amide)s and compared to those of the unmodified polymers (**Table 2.2, Figure 2.5**). For polymers of this size, grafting a small molecule (methyl 3-mercaptopropionate, MW=120.2 g/mol), with a presumed reaction conversion of ~30%, should have a negligible impact on polymer molecular weight. Instead, it is expected to be more reflective of changes in poly(ether-amide) solubility, as the GPC is able to detect a greater range of molecular weights.

Molecular weight increased for all but two of the polymers after the thiol-ene reaction, with the exceptions being ferulyl and sinapyl dimers with ethylene diamine linkers. As the thiol-ene reaction improves rotational freedom of the polymeric backbone and in turn improves solubility, higher molecular weight components of the polymers are able to be detected via GPC. This appears to be supported by the ferulic-based poly(ether-amide)s, which experienced minimal change or even a decrease in molecular weight, as they also exhibited decreased solubility following the thiol-ene reaction.

**Table 2.2.** Molecular weight characterization of poly(ether-amide)s by gel permeation chromatography before and after thiol-ene functionalization.

Polymer	Dimer	Diamine	Unmodified			Thiol-ene		
			$M_n^a$	$M_w^a$	$\mathcal{D}^b$	$M_n^a$	$M_w^a$	$\mathcal{D}^b$
P1	<i>p</i> -coumaryl	ethylene diamine	3,700	5,060	1.37	7,170	9,010	1.26
P4		1,8-diaminooctane	6,410	9,130	1.42	7,730	9,830	1.27
P8	ferulyl	ethylene diamine	12,780	24,830	1.94	12,560	15,850	1.26
P11		1,8-diaminooctane	13,870	21,900	1.58	16,030	21,000	1.31
P15	sinapyl	ethylene diamine	26,640	47,560	1.79	18,620	22,990	1.23
P18		1,8-diaminooctane	12,160	26,300	2.16	16,950	27,270	1.61

<sup>a</sup>Determined by GPC, 1 mL/min, DMF with 10 mM LiBr; <sup>b</sup> $\mathcal{D}=M_w/M_n$

It is important to note, however, that GPC separates molecular components based on their hydrodynamic volume, retaining different sizes for a different duration, and that chain conformation is dependent on solvent quality. It is likely that after thiol modification of the poly(ether-amide)s, the DMF with 10 mM LiBr is a poor solvent, leading to preferential polymer-polymer interactions and thus polymer contraction. The reduced hydrodynamic volume would lead to molecular weights obtained from GPC that are skewed lower than they are in reality. While absolute molecular weight, determined using static light scattering, initially seems like a promising

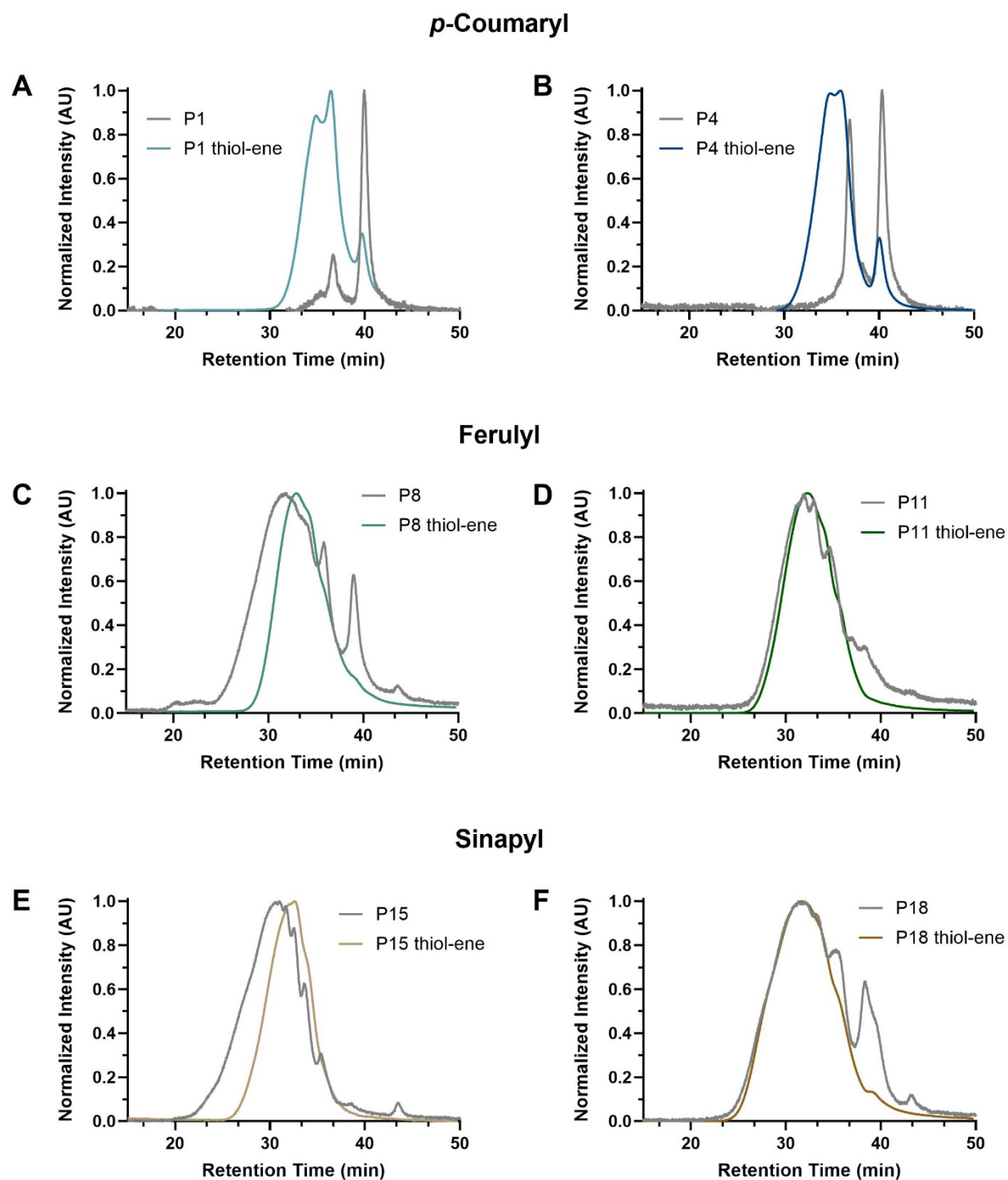


**Figure 2.5.** Stacked GPC traces of poly(ether-amide)s before and after thiol-ene modification. Thiol functionalized *p*-coumaryl polymers (A) P1 and (B) P11, ferulyl polymers (C) P8 and (D) P11, and sinapyl polymers (E) P15 and (F) P18 are shown with their respective unmodified polymer trace in grey.

alternative characterization approach, the unknown concentration and range of molecular weights of these polymers renders it ineffective for this application. A required parameter for light scattering is the refractive index increment ( $dn/dc$ ). The refractive index increment indicates the rate of change of refractive index with respect to sample concentration at a particular wavelength, temperature, and solvent. However, polymers in the sample are chemically distinct, and likely have varying degrees of modification. Because the refractive index increment depends on the degree of modification, this would lead to an inaccurate  $dn/dc$  and thus inaccurate molecular weight.

One key takeaway from these data, however, is that dispersity improved for all polymers after thiol modification, with decreases ranging from 0.11 to 0.68. All dispersity values after the thiol-ene reaction fell between 1.23-1.61, which is a notable improvement over the unmodified poly(ether-amide) dispersities of 1.37-2.16. The peaks became much more uniform, which is reflective of a more narrow distribution of molecular weights, likely offering a more accurate reflection of the unmodified poly(ether-amide) molecular weight, that had been impeded by solubility limitations.

**Thermal Characterization.** The thermal behavior of poly(ether-amide)s after thiol-ene functionalization was studied using differential scanning calorimetry (DSC) and thermogravimetric analysis (TGA) and compared to that of the unmodified polymers, characterized by Brianna Upton [18]. Due to rotational restrictions of aromatic polymers, glass transition temperatures ( $T_g$ ) are generally higher than aliphatic polymers. Additionally, backbone flexibility is limited due to the unsaturated double bond of hydroxycinnamates. Through the thiol-ene reaction, the pi bond of the alkenes are broken as they are reduced to alkanes through radical addition of the thiol-tagged molecules. This is expected to improve the rotational freedom of the backbone and decrease the polymers'  $T_g$ .

The stacked DSC traces of the thiol-modified polymers are shown in **Figure 2.6**. The traces in blue are *p*-coumaryl polymers, those in green are ferulyl, and brown traces are sinapyl polymers. All polymers exhibited a decrease in  $T_g$ , to approximately 60-85°C (**Table 2.3**). As this work aims to

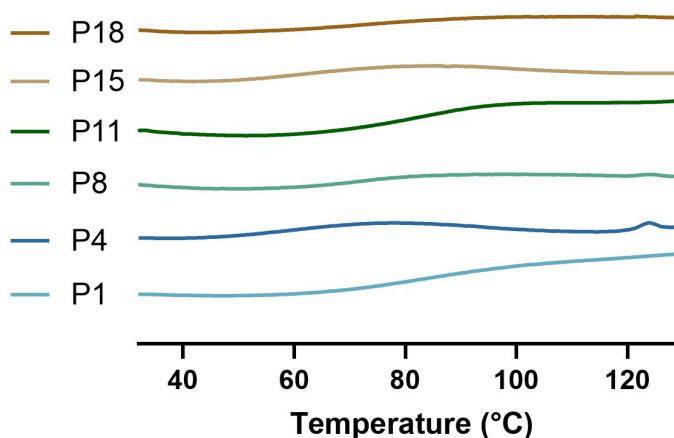


**Figure 2.6.** Stacked DSC traces of thiol-modified poly(ether-amide)s.

improve the tractability of lignin-based poly(ether-amide)s, this is a consequential outcome. The improved  $T_g$  indicates that polymers become glassy and chain flexibility increases at a lower temperature. It has important implications for both solubility as well as downstream polymer processing, enabling more mild thermal and chemical conditions.

**Table 2.3.** Thermal characterization of poly(ether-amide)s by TGA and DSC before and after thiol-ene functionalization [18].

Polymer	Unmodified				Thiol-ene			
	$T_g$ (°C)	$T_{d5}$ (°C)	$T_{d10}$ (°C)	$T_{d25}$ (°C)	$T_g$ (°C)	$T_{d5}$ (°C)	$T_{d10}$ (°C)	$T_{d25}$ (°C)
P1	91	244	290	336	74	108	159	337
P4	81	254	292	328	59	315	368	419
P8	103	144	277	345	74	150	244	353
P11	110	194	265	311	84	167	294	357
P15	107	227	271	318	66	154	240	334
P18	85	122	155	328	75	132	226	352

The poly(ether-amide)s that underwent thiol-ene reactions were also characterized using TGA to determine decomposition temperatures at 5%, 10%, and 25% mass loss ( $T_{d5}$ ,  $T_{d10}$ ,  $T_{d25}$ ; **Table 2.3**). The initial mass loss ( $T_{d5}$ ) varied greatly between polymers (108-315°C), with some

exhibiting increases and decreases relative to the unmodified polymers. Despite extensively drying all samples prior to analysis, this variability can likely be attributed to residual water. This is further supported by the higher temperatures at 10% mass loss ( $T_{d10}$ ). These decomposition temperatures are expected to increase following more extensive removal of water. Interestingly, the decomposition temperature at 25% mass loss increased for all poly(ether-amide)s after thiol functionalization, with all  $T_{d25}$  above 330°C. Additionally, for the three hydroxycinnamates,  $T_{d25}$  was higher for the eight-carbon linker than the two-carbon linker. This trend is easily observed in the TGA traces of the thiol-modified poly(ether-amide)s (**Figure 2.7**), separated by hydroxycinnamate—where (A) are the *p*-coumaric polymer, (B) are the ferulic polymers, and (C) are the sinapinic polymers. The thiol-modified polymers exhibit moderate thermal stability with potential for downstream melt processing. Commercial thermosets are generally heated to approximately 180°C during processing, or 80-150°C for fused filament fabrication 3D printing [28]. Given the low  $T_g$ s and moderate thermal stability of the poly(ether-amide)s following thiolene functionalization, they are well-suited to additive manufacturing processing approaches.

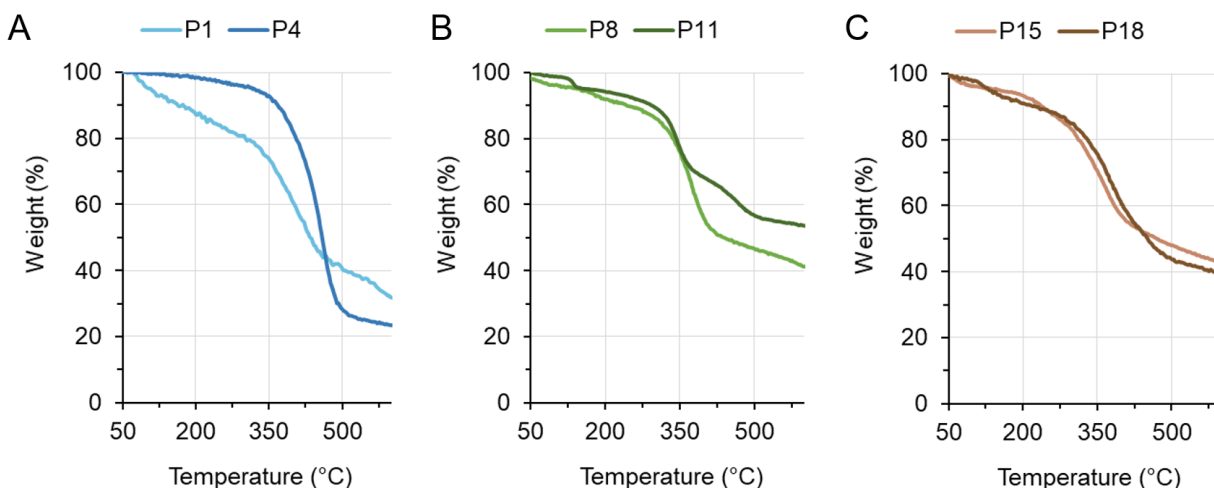


**Figure 2.7.** Thermogravimetric analysis (TGA) traces of thiol-modified (A) *p*-coumaryl, (B) ferulyl, and (C) sinapyl poly(ether-amide)s.

## 2.3 Conclusions

Lignin-derived polymers typically suffer from poor solubility, due to the high degree of aromaticity and the characteristic  $\alpha,\beta$ -unsaturated bonds, limiting their utility for commercial applications. This work aimed to reduce the repeating double bond of hydroxycinnamate-based poly(ether-amide)s through the addition of small thiol-tagged molecules to improve chain flexibility. Thiol-ene reactions were optimized to be performed directly on the poly(ether-amide)s. The thiol-ene addition reaction improved solubility of most of the polymers in DMF. This was also reflected in molecular weight improvements, particularly in the polydispersity index. The poly(ether-amide)s that experienced increased solubility after the thiol-ene reaction also exhibited an increase in molecular weight. It is likely that this molecular weight change is more reflective of improved solubility after reducing the double bond than actual changes in the molecular weight due to the added thiol-tagged molecule. Additionally, the poly(ether-amide)s showed much more uniform molecular weight distributions after thiol functionalization as a greater amount (and range of molecular weights) of the polymer dissolved in the GPC solvent. Finally, the thiol-modified poly(ether-amide)s exhibited improved thermal properties. All polymers had an increased thermal degradation at 25% mass loss, and a decreased glass transition temperature. These thermal properties, combined with the improved solubility, are expected to overcome the barriers to polymer processing for these hydroxycinnamate-based poly(ether-amide)s.

## 2.4 Experimental

**Materials.** 4-Hydroxybenzaldehyde (98%, Alfa Aesar), vanillin (98%, Alfa Aesar), 3,5-dimethoxy-4-hydroxybenzaldehyde (98%, ACROS Organics), trans *p*-coumaric acid (98+%, TCI America), trans-ferulic acid (98+%, TCI America), 3,5-dimethoxy-4-hydroxycinnamic acid

(98+%, TCI America), ethyl acetate (Certified ACS, Fisher Chemical), magnesium sulfate ( $\text{MgSO}_4$ , Certified, Fisher Chemical), lithium bromide (LiBr, 99+%, Alfa Aesar), dimethylformamide (DMF, HPLC Grade, Sigma Aldrich), and were used as received. 2-Mercaptoethanol (99%, ACROS Organics), pentaerythritol tetrakis(3-mercaptopropionate) (97%, Sigma Aldrich), and methyl 3-mercaptopropionate (98%, Fisher) were treated with immobilized TCEP gel (Thermo Scientific) prior to use. Pyridine (Certified ACS, Fisher Chemical) was distilled over KOH prior to use. Dichloromethane (DCM, Certified ACS, Fisher Chemical) and toluene (Certified ACS, Fisher Chemical) were distilled from  $\text{CaH}_2$  prior to use. Hydroxycinnamate-based dimers were prepared as previously described, modified from a method reported by the Uhrich group [18], [29], [30], [31]. Biomass-derived poly(ether-amide)s were synthesized by Brianna Upton as previously reported [18]. NMR solvents  $d_6$ -DMSO and  $\text{CDCl}_3$  were obtained from Acros Organics;  $d_6$ -DMSO was dried over activated sieves and  $\text{MgSO}_4$ , while  $\text{CDCl}_3$  was used as received.

**$^1\text{H}$  and FTIR Spectroscopy.**  $^1\text{H}$  NMR spectra were recorded on Bruker AV-300 or Bruker AV-400 spectrometers at room temperature in either  $\text{CDCl}_3$  or  $d_6$ -DMSO. Chemical shifts are reported with respect to the internal solvent, 7.26 ppm ( $\text{CDCl}_3$ ) or 2.50 ppm ( $d_6$ -DMSO). Infrared absorption spectra were collected using a ThermoScientific Nicolet™ iS 5 FTIR spectrometer. All samples were dried overnight prior to characterization.

**Molecular Weight Characterization.** Molecular weight ( $M_n$  and  $M_w$ ) and dispersity ( $\mathcal{D} = M_w/M_n$ ) were determined using gel permeation chromatography (GPC). Samples were dissolved at room temperature in DMF containing 10 mM LiBr at a concentration of 6 mg/mL. All samples were passed through a 0.20  $\mu\text{m}$  PTFE filter (Millex®-LG) directly before injection. GPC for all polymers was performed on a Jasco system equipped with a refractive index detector (RI-2031



Plus), UV detector (UV-2075 Plus), a Waters Styragel guard column, and four Waters HR Styragel 5  $\mu\text{m}$  columns (100-5 K, 500-30 K, 50-100 K, 5-600 K). The system was run using DMF with 10 mM LiBr at a flow rate of 1.0 mL/min. Calibration was performed with near-monodisperse polystyrene standards (Jordi Laboratories,  $M_n = 1,250 - 549,000$  g/mol). Chromatograms were recorded and analyzed using ChromNAV chromatography software.

**Solubility Characterization.** After drying at 40  $^{\circ}\text{C}$  under high vacuum, polymer samples (10 mg) were transferred to a vial and 1.0 mL of DMF with 10 mM LiBr was added to each. The samples were kept at room temperature for 24 h. The solvent was carefully decanted and the residual solid was dried at 40  $^{\circ}\text{C}$  under high vacuum. The mass of the residual solid was recorded to determine the mass of polymer that was insoluble, and calculate the wt% of polymer that solubilized.

**Thermal Characterization.** All samples were dried at 40  $^{\circ}\text{C}$  under high vacuum prior to thermal characterization. Differential scanning calorimetry (DSC) was conducted on a PerkinElmer DSC 8000. Polymer samples (5-10 mg) were placed in an aluminum crucible, and sealed with pierced aluminum cover. Samples were heated to 200  $^{\circ}\text{C}$  and cooled to 0  $^{\circ}\text{C}$  at a rate of 10  $^{\circ}\text{C}/\text{min}$  for a total of 3 heating and 2 cooling cycles. DSC data was recorded and analyzed using PerkinElmer Pyris<sup>TM</sup> Software to identify glass transition temperature ( $T_g$ ) and melting temperature ( $T_m$ ), measured from the second heating cycle. Thermogravimetric analysis (TGA) was performed using a PerkinElmer TGA 8000. The TGA instrument was operated under a nitrogen atmosphere, using platinum crucibles. Samples (6 mg) were heated from 40 to 600  $^{\circ}\text{C}$  at a rate of 10  $^{\circ}\text{C}/\text{min}$ . Pyris<sup>TM</sup> Software was used to analyze the data. Decomposition temperatures  $T_{d5}$ ,  $T_{d10}$ , and  $T_{d25}$  were measured at 5, 10, and 25% mass loss.

**Synthesis of protected hydroxycinnamate monomers.** *P*-coumaric acid, ferulic acid, or sinapinic acid (0.01 mol, 1 equiv) was weighed and added to a 2-necked round bottom flask along with 30 mL of HPLC-grade DMF under Ar. Potassium carbonate (0.03 mol, 3 equiv) was added and the solution was stirred for 10 min at room temperature. A solution of ethyl 4-bromobutyrate (0.03 mol, 3 equiv) in 20 mL DMF was then added dropwise over 30 min via an addition funnel. The solution was stirred at 40°C overnight. The product was precipitated in ice water, collected via filtration, and dried overnight in vacuo. After drying, the product was subjected to the same reaction, with a reduced amount of potassium carbonate (0.005 mol, 0.5 equiv) and ethyl 4-bromobutyrate (0.005 mol, 0.5 equiv). The product was again precipitated into ice water, collected via filtration, and dried overnight in vacuo, yielding a white powder.

*Protected p-coumaric acid.* Yield: 3.6 g, 92.8%. <sup>1</sup>H NMR (400 MHz, CDCl<sub>3</sub>): δH 7.63 (d, 1H), 7.46 (d, 2H), 6.88 (d, 2H), 6.29 (d, 1H), 4.23 (t, 2H), 4.14 (q, 4H), 4.04 (t, 2H), 2.48 (dt, 4H), 2.08 (dq, 4H), 1.26 (t, 6H).

*Protected ferulic acid.* Yield: 0.42 g, 50.2%. <sup>1</sup>H NMR (400 MHz, CDCl<sub>3</sub>): δH 7.59 (d, 1H), 7.04 (m, 2H), 6.85 (d, 1H), 6.27 (d, 1H), 4.21 (t, 2H), 4.13 (m, 6H), 3.86 (s, 3H), 2.50 (t, 2H), 2.42 (t, 2H), 2.14 (q, 2H), 2.01 (q, 2H), 1.21 (t, 6H).

*Protected sinapinic acid.* Yield: 0.29 g, 56.7%. <sup>1</sup>H NMR (400 MHz, CDCl<sub>3</sub>): δH 7.56 (d, 1H), 6.71 (s, 2H), 6.30 (d, 1H), 4.22 (t, 2H), 4.12 (q, 4H), 4.01 (t, 2H), 3.83 (s, 6H), 2.57 (t, 2H), 2.42 (t, 2H), 2.01 (q, 4H), 1.23 (t, 6H).

**Thia-Michael Reaction of Monomers.** Protected *p*-coumaric acid, the least hindered of the hydroxycinnamates, was used in model thia-Michael reactions. The alkylated *p*-coumaric acid (0.150 mmol, 0.0589 g) was first reacted with 2-mercaptoethanol (1.1 equiv, 0.165 mmol, 11.6

$\mu\text{L}$ ) or pentaerythritol tetrakis(3-mercaptopropionate) (1.1 equiv., 0.165 mmol, 63  $\mu\text{L}$ ) as the thiol-tagged molecule, with trimethylamine (0.2 equiv, 0.03 mmol, 4.2  $\mu\text{L}$ ) as the base, in 2.5 mL DMSO. The solution was degassed via freeze-pump-thaw, and reacted at room temperature overnight. The product was isolated by precipitating into ice water and collected via filtration. After drying under vacuum, the product was evaluated via  $^1\text{H}$  NMR. The reaction with 2-mercaptoethanol had a yield of 47.9% and S4P had a yield of only 15.0%, which was likely due in part to its 0% conversion and the miscibility of DMSO with water, with no evident grafting of the thiol-tagged molecule. The thia-Michael reaction was also tested using methyl 3-mercaptopropionate as the thiol. Protected *p*-coumaric acid (0.150 mmol, 0.0589 g) was combined with triethylamine (0.2 equiv, 0.03 mmol, 4.2  $\mu\text{L}$ ) and methyl 3-mercaptopropionate (1.1 equiv, 0.165 mmol, 18.3  $\mu\text{L}$ ) in 2.5 mL DMF. The solution was stirred at room temperature overnight and worked up the same as the previous reaction. The attempt in DMF had an improved yield of 47.9%, but the conversion remained 0%.

*Thia-Michael of protected p-coumaric acid, both with pentaerythritol tetrakis(3-mercaptopropionate) and with methyl 3-mercaptopropionate.*  $^1\text{H}$  NMR (400 MHz,  $\text{CDCl}_3$ ):  $\delta\text{H}$  7.63 (d, 1H), 7.46 (d, 2H), 6.88 (d, 2H), 6.29 (d, 1H), 4.23 (t, 2H), 4.14 (q, 4H), 4.04 (t, 2H), 2.48 (dt, 4H), 2.08 (dq, 4H), 1.26 (t, 6H).

**Thiol-ene Reaction of Monomers.** Three thiol-tagged molecules were explored: 2-mercaptoethanol, pentaerythritol tetrakis(3-mercaptopropionate), and methyl 3-mercaptopropionate. The following procedure was used during optimization, with any deviations noted in the text. In general, the protected hydroxycinnamates (1 equiv.), 1.1 equiv. of the thiol-tagged molecule, and 0.2 equiv. AIBN were combined in a Schlenk flask in 2.5-5 mL DMF. The solution was degassed via freeze-pump-thaw, and heated to 68°C for 24 h. The product was

isolated by precipitating into an excess of ice water and collected via filtration. After drying, the products were evaluated via  $^1\text{H}$  NMR.

The reaction was first performed using 2-mercaptoethanol on the alkylated *p*-coumaric, sinapic, and ferulic acids on a 0.15 mmol scale in DMF, and worked up as previously described. These had yields of 99.1%, 97.8%, and 96.0%, respectively. These reactions were also attempted in THF and toluene on a 0.1 mmol scale (sinapic yields: 97.8% and 61.9%, respectively; ferulic yields: 96.0% and 60.3%, respectively). After the overnight reaction, the solutions were concentrated under reduced pressure and re-suspended in DCM. They were washed extensively with DI H<sub>2</sub>O and brine, and the organic layer was dried over sodium sulfate and concentrated via rotovap. However, 0% conversion was obtained in all cases.

The thiol-tagged molecule was changed to S4P, with four terminal thiol groups. The thiol-ene addition of S4P to the alkylated *p*-coumaric acid was performed on a 0.15 mmol scale in DMF. The reaction successfully proceeded, with a yield of 65.1% and a conversion of 35.6%. For our goal of improving solubility, more than 25% conversion was considered sufficient for this reaction.

The same thiol-ene addition of S4P to the alkylated *p*-coumaric acid was attempted using benzoyl peroxide instead of AIBN. The protected *p*-coumaric acid (0.15 mmol, 0.0589 g) was combined with S4P (1.1 equiv, 0.165 mmol, 63.0  $\mu\text{L}$ ) and benzoyl peroxide (0.2 equiv, 0.03 mmol, 0.0097 g) in 2.5 mL toluene. The reaction was degassed via freeze-pump-thaw, and heated to 75°C overnight. The product was precipitated into ice water, but appeared as waxy spots instead of a precipitate for this reaction. The product was instead extracted into ethyl acetate and dried prior to  $^1\text{H}$  NMR analysis. The benzoyl peroxide-initiated reaction had a yield of 92.7% and a conversion of 31-39%.

To mitigate the risk of disulfide formation and crosslinking, thiol-ene addition of methyl 3-mercaptopropionate was then tested. Protected *p*-coumaric acid and ferulic acid (1 equiv, 0.15 mmol) were combined with methyl 3-mercaptopropionate (1.1 equiv, 0.165 mmol, 18.3  $\mu$ L) and AIBN (0.2 equiv, 0.03 mmol) in 2.5 mL DMF. The solution was degassed via freeze-pump-thaw, and heated to 68°C for 24 h. After cooling to RT, 5 mL DI H<sub>2</sub>O was added to the reaction solution, extracted with ethyl acetate, washed with DI H<sub>2</sub>O, dried over MgSO<sub>4</sub> and dried under reduced pressure. The products were evaluated via <sup>1</sup>H NMR. The thiol-ene reaction using methyl 3-mercaptopropionate and protected *p*-coumaric acid had a conversion of 55.9% and a yield of 76.1%, while the reaction of protected ferulic acid had a conversion of 48.0% and a yield of 80.7%. This is considered the optimized thiol-ene protocol, with equivalence adjusted based on the number of  $\alpha,\beta$ -unsaturated bonds in the starting material.

*Thiol-ene of protected p-coumaric acid with methyl 3-mercaptopropionate.* <sup>1</sup>H NMR (400 MHz, CDCl<sub>3</sub>):  $\delta$ H 7.63 (d, 1H), 7.46 (d, 2H), 6.88 (d, 2H), 6.29 (d, 1H), 4.23 (t, 2H), 4.14 (q, 4H), 4.04 (t, 2H), 2.48 (dt, 4H), 2.08 (dq, 4H), 1.26 (t, 6H).

*Thiol-ene of protected ferulic acid with methyl 3-mercaptopropionate.* <sup>1</sup>H NMR (400 MHz, CDCl<sub>3</sub>):  $\delta$ H 7.03 (t, 2H), 6.84 (d, 1H), 4.24-4.01 (m, 8H), 3.85 (s, 3H), 3.67 (s, 3H), 3.03 (t, 2H), 2.94 (t, 2H), 2.75 (t, 2H), 2.48 (dt, 4H), 2.16 (t, 4H), 2.08 (t, 4H), 1.26 (t, 6H)

**Thiol-ene Reaction of Dimers.** Before attempting directly on poly(ether-amide)s, the thiol-ene reaction was attempted on ferulyl *tert*-butyl ether dimer and *p*-coumaryl *tert*-butyl ester dimers. The dimers (1 equiv., 0.144 mmol) were combined with methyl 3-mercaptopropionate (1.1 equiv., 0.158 mmol) and AIBN (0.2 equiv., 0.029 mmol) in 2.5 mL DMF. The solution was degassed via freeze-pump-thaw, and heated to 68°C for 24 h. After cooling to RT, 5 mL DI H<sub>2</sub>O was added to the reaction solution, extracted with ethyl acetate, washed with DI H<sub>2</sub>O, dried over

MgSO<sub>4</sub> and dried under reduced pressure. The isolated ferulic and *p*-coumaric products were evaluated via <sup>1</sup>H NMR.

*Thiol-ene of p-coumaryl t-butyl ester dimer.* Yield: 0.014 g, 65.4%. *Thiol-ene of ferulyl t-butyl ether dimer.* Yield: 0.021 g, 42.6%. <sup>1</sup>H NMR (400 MHz, CDCl<sub>3</sub>): δH 8.04 (d, 2H), 7.15 (d, 2H), 6.22 (s, 2H), 4.13 (d, 4H), 3.91 (s, 6H), 3.71 (s, 6H), 2.92 (m, 12H), 2.75 (t, 6H), 1.51 (s, 18H).

**Thiol-ene Reaction of Polymers.** A concentrated stock solution of AIBN in DMF was prepared. As with the dimers, each poly(ether-amide) (1 equiv., ~0.100 g) was combined with methyl 3-mercaptopropionate (1.1 equiv.) and AIBN (0.2 equiv.) in 2.5 mL DMF. The solutions were degassed via freeze-pump-thaw, and heated to 68°C for 5 days. After 24 h, additional methyl 3-mercaptopropionate (1.1 equiv.) and AIBN (0.2 equiv.) were added to the reaction through the rubber septa. After 72 h, additional AIBN (0.2 equiv.) was added. The samples were dried at 40°C under vacuum to remove a large amount of the DMF, and the products were precipitated into cold ether. After stirring for at least 3 h, the product was collected via filtration and dried under reduced pressure.

## 2.5 Appendix A

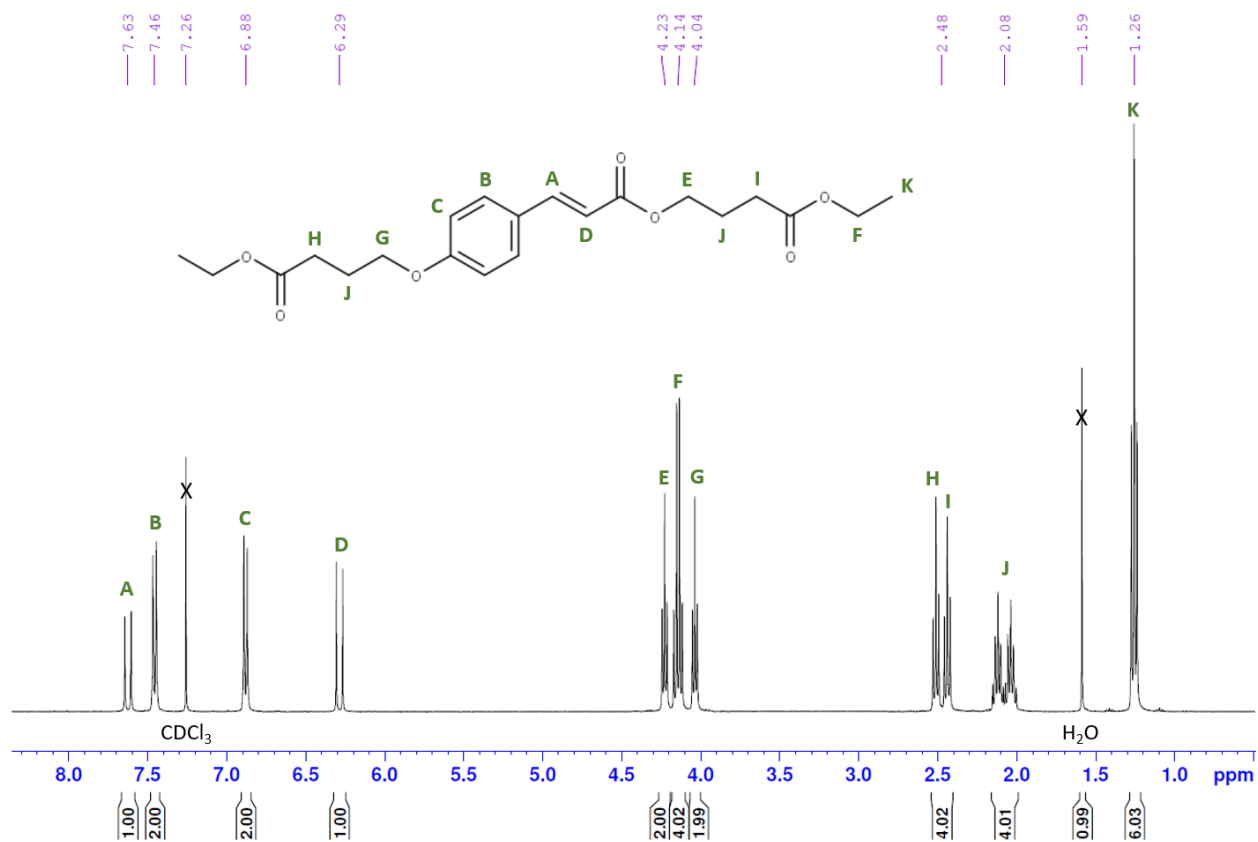


**Figure S2.1.** <sup>1</sup>H NMR of butyrate-protected *p*-coumaric acid, in CDCl<sub>3</sub>.

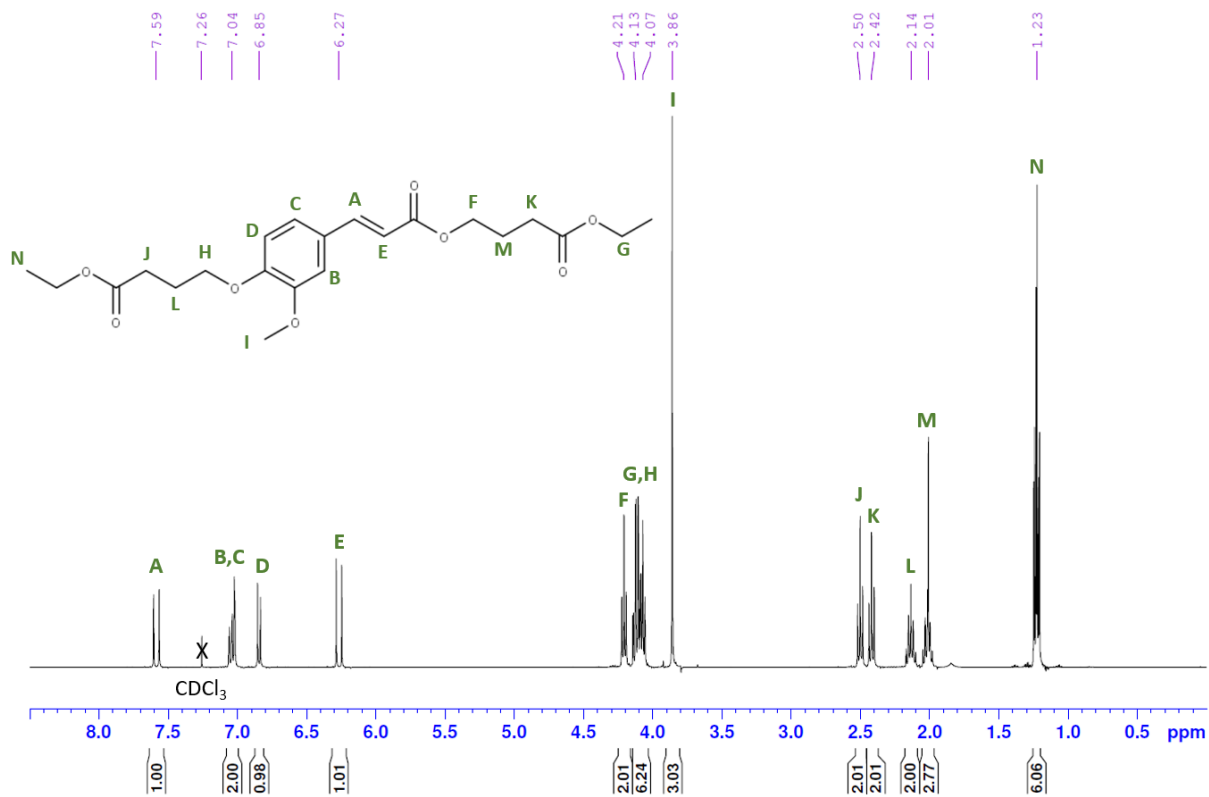


Figure S2.2.  $^1\text{H}$  NMR of butyrate-protected ferulic acid, in  $\text{CDCl}_3$ .

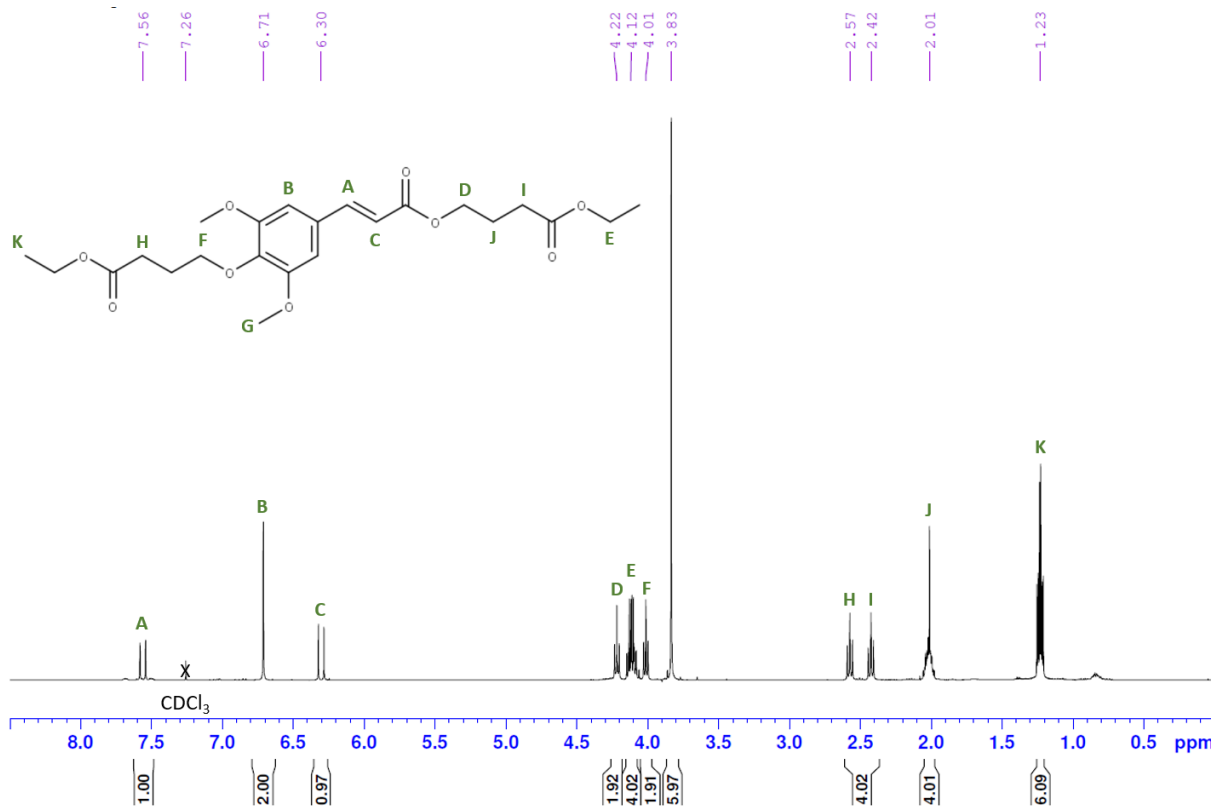
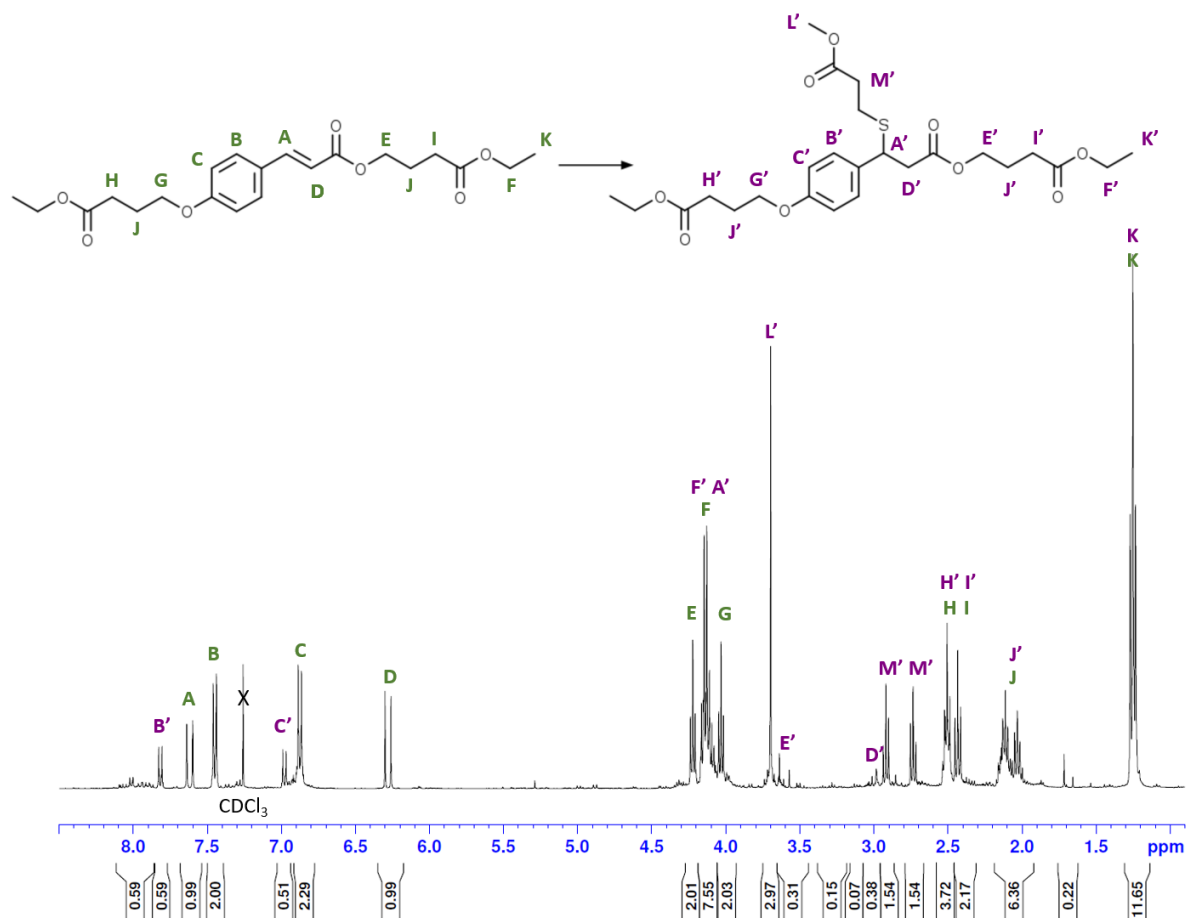
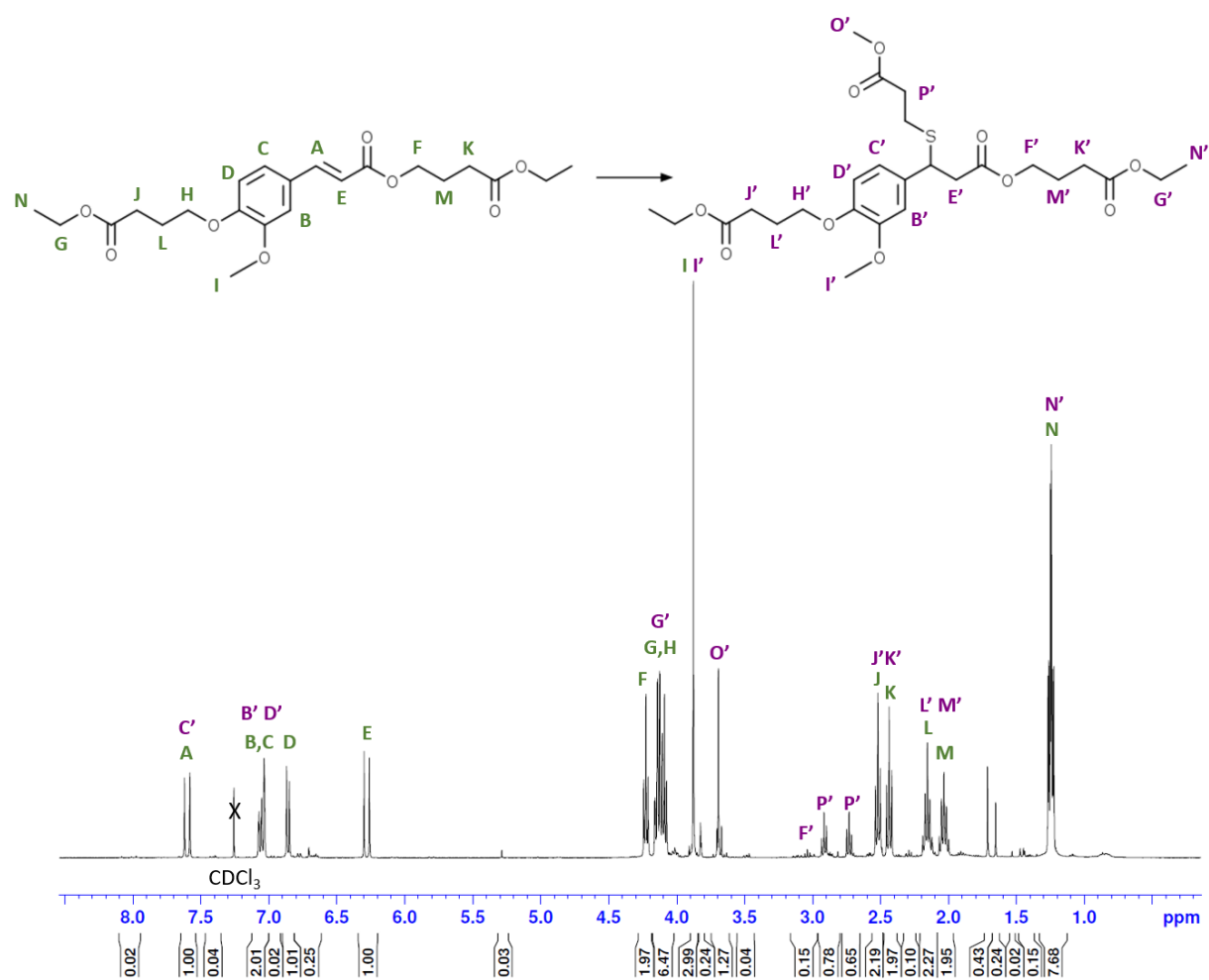


Figure S2.3  $^1\text{H}$  NMR of butyrate-protected sinapinic acid, in  $\text{CDCl}_3$ .





**Figure S2.4.**  $^1\text{H}$  NMR of thiol-ene reaction of butyrate-protected *p*-coumaric acid with methyl 3-mercaptopropionate, in  $\text{CDCl}_3$ .



**Figure S2.5.**  $^1\text{H}$  NMR of thiol-ene reaction of butyrate-protected ferulic acid with methyl 3-mercaptopropionate, in  $\text{CDCl}_3$ .

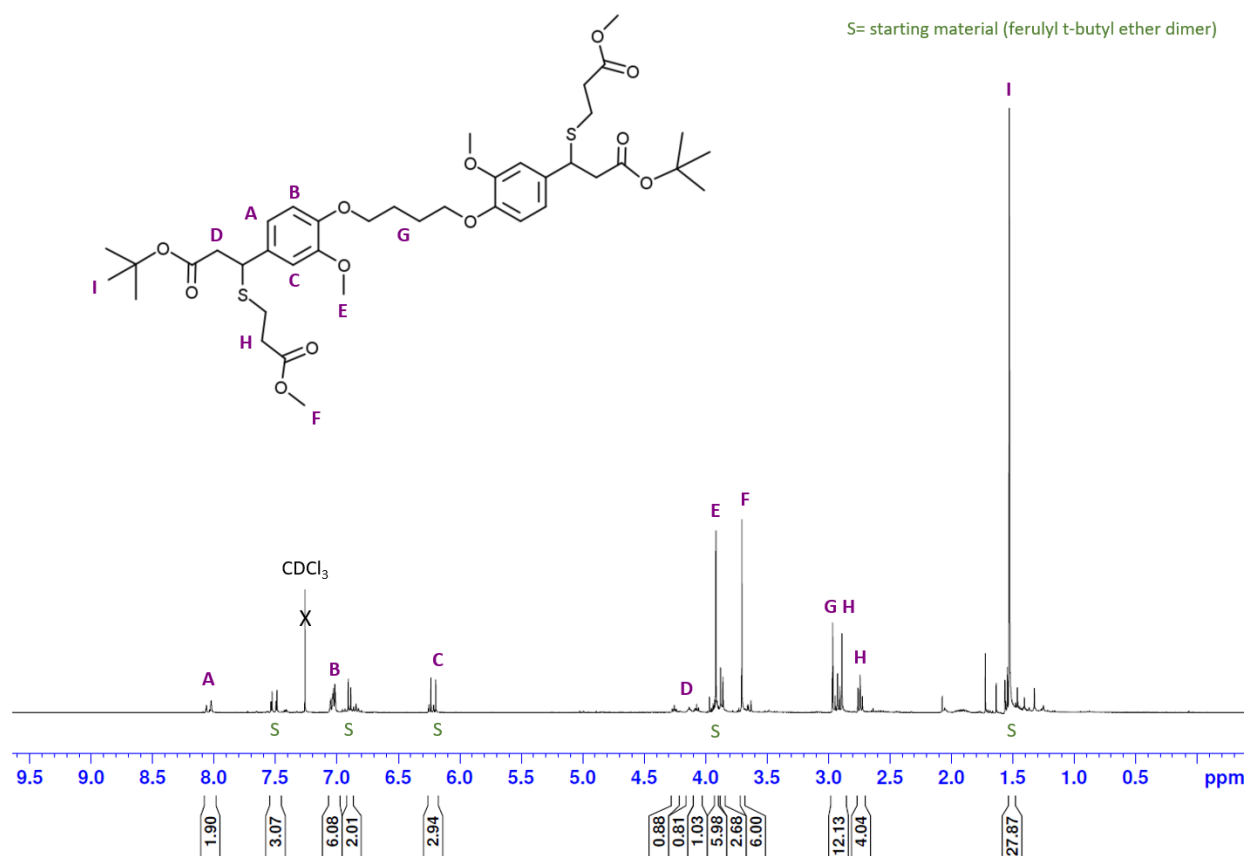


**Figure S2.6.** <sup>1</sup>H NMR of thiol-ene reaction of ferulyl tert-butyl ether dimer, in CDCl<sub>3</sub>.

**Table S2.1.** Yields of thiol-ene reactions performed directly on poly(ether-amide)s.

Polymer	Hydroxycinnamate	Diamine	Amount (mg)	Precipitate Yield (%)	Ether Filtrate Yield (%)
P1	<i>p</i> -Coumaryl	Ethylene diamine	65.8	60.5	14.6
P4		1,8-diaminooctane	97.5	67.9	—
P8	Ferulyl	Ethylene diamine	75.2	51.7	—
P11		1,8-diaminooctane	83.7	55.8	—
P15	Sinapyl	Ethylene diamine	56.3	38.6	—
P18		1,8-diaminooctane	62.1	52.0	7.9

## 2.6 References

- [1] R. Geyer, “Production, use, and fate of synthetic polymers,” in *Plastic Waste and Recycling*, Elsevier Inc., 2020, pp. 13–32.
- [2] C. Arkin, D. Azoulay, A. Caterbow, *et al.*, *Plastic Atlas*, 2nd ed. Heinrich Böll Foundation, Berlin, Germany, and Break Free From Plastic, 2019.
- [3] J. Gasperi, R. Dris, V. Rocher, *et al.*, “Microplastics in the continental area: An emerging challenge,” *Norman Bull.*, no. 4, pp. 18–19, 2015.
- [4] S. Spierling, E. Knüpfper, H. Behnsen, *et al.*, “Bio-based plastics - A review of environmental, social and economic impact assessments,” *J. Clean. Prod.*, vol. 185, pp. 476–491, 2018.
- [5] F. H. Isikgor and C. R. Becer, “Lignocellulosic biomass: A sustainable platform for the production of bio-based chemicals and polymers,” *Polym. Chem.*, vol. 6, no. 25, pp. 4497–4559, 2015.
- [6] A. J. Ragauskas, C. K. Williams, B. H. Davison, *et al.*, “The path forward for biofuels and biomaterials,” *Science (80-. )*, vol. 311, no. 5760, pp. 484–489, 2006.
- [7] C. H. Zhou, X. Xia, C. X. Lin, *et al.*, “Catalytic conversion of lignocellulosic biomass to fine chemicals and fuels,” *Chem. Soc. Rev.*, vol. 40, no. 11, pp. 5588–5617, 2011.
- [8] J. Baruah, B. K. Nath, R. Sharma, *et al.*, “Recent trends in the pretreatment of lignocellulosic biomass for value-added products,” *Front. Energy Res.*, vol. 6, p. 141, 2018.

- [9] S. Kumar, A. K. Mohanty, L. Erickson, *et al.*, “Lignin and its applications with polymers,” *J. Biobased Mater. Bioenergy*, vol. 3, no. 1, pp. 1–24.
- [10] J. H. Lora and W. G. Glasser, “Recent industrial applications of lignin: A sustainable alternative to nonrenewable materials,” *J. Polym. Environ.*, vol. 10, no. 1–2, pp. 39–48, 2002.
- [11] J. S. Luterbacher, D. M. Alonso, and J. A. Dumesic, “Targeted chemical upgrading of lignocellulosic biomass to platform molecules,” *Green Chem.*, vol. 16, no. 12, pp. 4816–4838, 2014.
- [12] W. Schutyser, T. Renders, S. Van den Bosch, *et al.*, “Chemicals from lignin: An interplay of lignocellulose fractionation, depolymerisation, and upgrading,” *Chem. Soc. Rev.*, vol. 47, pp. 852–908, 2018.
- [13] A. J. Ragauskas, G. T. Beckham, M. J. Bidy, *et al.*, “Lignin valorization: Improving lignin processing in the biorefinery,” *Science (80-. )*, vol. 344, no. 6185, p. 1246843, 2014.
- [14] H. Chung and N. R. Washburn, “Chemistry of lignin-based materials,” *Green Mater.*, vol. 1, no. 3, pp. 137–160, 2013.
- [15] J. Ralph, K. Lundquist, G. Brunow, *et al.*, “Lignins: Natural polymers from oxidative coupling of 4-hydroxyphenyl- propanoids,” *Phytochem. Rev.*, vol. 3, pp. 29–60, 2004.
- [16] J. C. Del Río, J. Rencoret, A. Gutiérrez, *et al.*, “Lignin monomers from beyond the canonical monolignol biosynthetic pathway: Another brick in the wall,” *ACS Sustain. Chem. Eng.*, vol. 8, no. 13, pp. 4997–5012, 2020.

- [17] E. Ten and W. Vermerris, “Recent developments in polymers derived from industrial lignin,” *J. Appl. Polym. Sci.*, vol. 132, no. 24, p. 42069, 2015.
- [18] B. M. Upton and A. M. Kasko, “Biomass-derived poly(ether-amide)s incorporating hydroxycinnamates,” *Biomacromolecules*, vol. 20, no. 2, pp. 758–766, 2019.
- [19] P. Wadhwa, A. Kharbanda, and A. Sharma, “Thia-Michael addition: An emerging strategy in organic synthesis,” *Asian J. Org. Chem.*, vol. 7, no. 4, pp. 634–661, 2018.
- [20] M. Fache, E. Darroman, V. Besse, *et al.*, “Vanillin, a promising biobased building-block for monomer synthesis,” *Green Chem.*, vol. 16, no. 4, pp. 1987–1998, 2014.
- [21] S. Nagashima, T. Shimasaki, N. Teramoto, *et al.*, “Trehalose-incorporated polymer network by thiol-ene photopolymerization,” *Polym. J.*, vol. 46, no. 10, pp. 728–735, 2014.
- [22] M. Shibata, K. Sugane, and Y. Yanagisawa, “Biobased polymer networks by the thiol-ene photopolymerization of allylated p-coumaric and caffeic acids,” *Polym. J.*, vol. 51, no. 5, pp. 461–470, 2019.
- [23] G. B. Bantchev, J. A. Kenar, G. Biresaw, *et al.*, “Free radical addition of butanethiol to vegetable oil double bonds,” *J. Agric. Food Chem.*, vol. 57, no. 4, pp. 1282–1290, 2009.
- [24] M. Claudino, M. Johansson, and M. Jonsson, “Thiol-ene coupling of 1,2-disubstituted alkene monomers: The kinetic effect of cis/trans-isomer structures,” *Eur. Polym. J.*, vol. 46, no. 12, pp. 2321–2332, 2010.
- [25] B. M. Upton, “Biomass-derived polymers and copolymers incorporating monolignols and their derivatives,” University of California, Los Angeles, 2016.
- [26] D. C. P. Singh, S. R. Hashim, and R. G. Singhal, “Synthesis and antimicrobial activity of

- some new thioether derivatives of quinoxaline,” *E-Journal Chem.*, vol. 8, no. 2, pp. 635–642, 2011.
- [27] S. J. Mary and S. Indira, “Phytochemical and FT-IR spectral analysis of *Rhododendron arboreum* sm. ssp. *nilagiricum* (Zenker) Tagg,” *Biosci. Discov*, vol. 8, no. 1, pp. 9–13, 2017.
- [28] B. Wang, Z. Zhang, Z. Pei, *et al.*, “Current progress on the 3D printing of thermosets,” *Adv. Compos. Hybrid Mater.*, vol. 3, pp. 462–472, 2020.
- [29] B. M. Upton and A. M. Kasko, “Biodegradable aromatic–aliphatic poly(ester–amides) from monolignol-based ester dimers,” *ACS Sustain. Chem. Eng.*, vol. 6, pp. 3659–3668, 2018.
- [30] M. A. Ouimet, N. D. Stebbins, and K. E. Uhrich, “Biodegradable coumaric acid-based poly(anhydride-ester) synthesis and subsequent controlled release,” *Macromol. Rapid Commun.*, vol. 34, no. 15, pp. 1231–1236, 2013.
- [31] M. A. Ouimet, J. Griffin, A. L. Carbone-Howell, *et al.*, “Biodegradable ferulic acid-containing poly (anhydride-ester): degradation products with controlled release and sustained antioxidant activity,” *Biomacromolecules*, vol. 14, no. 3, pp. 854–861, 2013.

## CHAPTER 3: Bio-based ring-opening and condensation polymerizations

### 3.1 Introduction

The plastics industry is the third largest manufacturing industry in the United States, with North America accounting for approximately 20% of global plastic production [1]. These polymeric materials appear in many different market sectors (i.e. packaging, building and construction, transportation, electronics, furniture, and industrial machinery) (**Figure 3.1**) [2]. Most troubling is that 31% of plastic produced in 2019 went towards packaging. While packaging is only required for short durations, the plastic manufactured for this purpose will have permanent environmental ramifications.

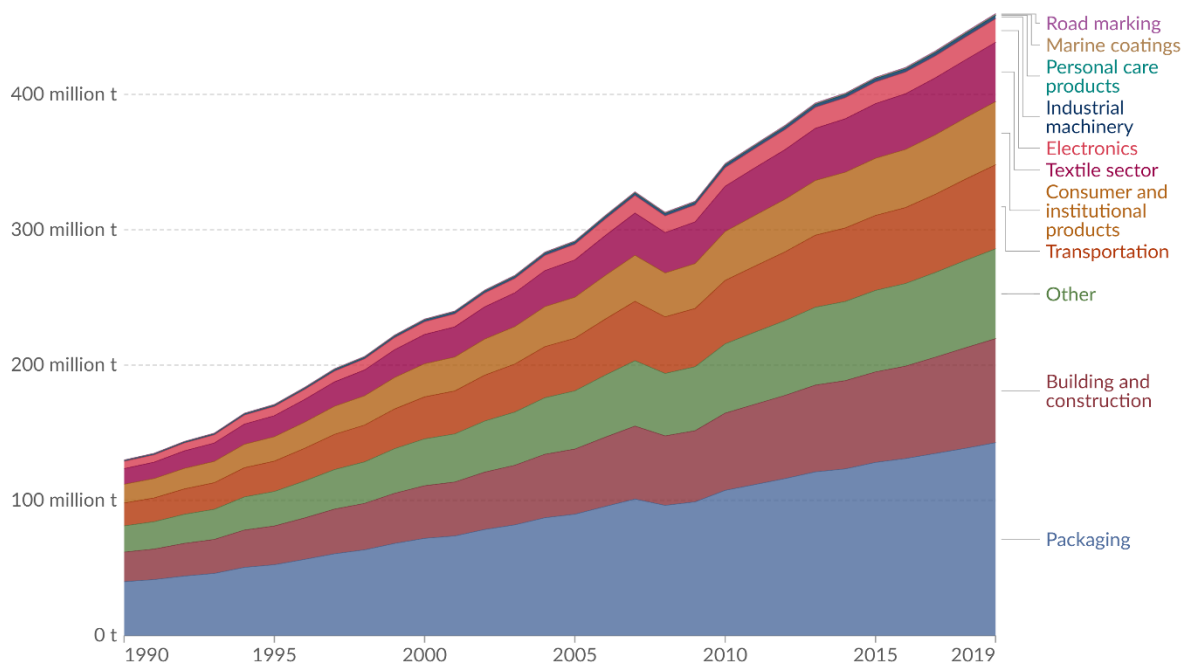
In addition to pollution caused by plastic waste and the manufacturing process itself, the starting chemicals used to fabricate plastics are commonly sourced from petroleum. In the United States, these chemicals are derived from hydrocarbon gas liquids, 91% of which comes from natural gas processing and 9% of which comes from crude oil refineries [3]. Plastic manufacturing currently accounts for 4-8% of total oil consumption, with half going towards the material feedstock and half being used to fuel the production process [4]. Due to increased fossil fuel demand, its sensitivity to political disruption, and significant environmental impact, demand for alternative plastic feedstocks is increasing.

Bioplastics are plastics derived from renewable biomass resources. Plastics based on starch and cellulose are used in a number of packaging application. Examples available on the market include BioBag, Cosmedia HP Starch, Eastman Trēva™, and Novamont's Mater-Bi. While commercial products produced from bio-based polymers are available, they generally exhibit weak thermo-mechanical properties in comparison to other commodity materials. Some bio-based



## Global primary plastic production by industrial sector, 1990 to 2019

Plastic production is measured in tonnes per year.



Data source: OECD (2022)

[OurWorldInData.org/plastic-pollution](https://OurWorldInData.org/plastic-pollution) | CC BY

**Figure 3.1.** Plastic production has been steadily increasing, and is primarily used in packaging, building and construction, and transportation industries (CC by 4.0 DEED) [46].

feedstocks have been identified and utilized to replace materials that were previously made from petroleum-derived feedstocks (i.e. poly(lactic acid) clamshell food containers). However, analogues of specialty or high-performance polymers have yet to be developed. Specifically, few bio-based equivalents to commodity aromatic polymers have been produced, in stark contrast to the vast number of bio-based aliphatic polymeric materials available [5], [6], [7], [8], [9]. The difficulty in the production of these bio-based materials results from a lack of sources for biologically-derived aromatic monomers. There are only a few examples of well-defined, scalable aromatic-aliphatic polymers from plant-based sources [10], [11], [12], [13].

Lignin is one of the most important structural polymers in nature, and is the only naturally occurring aromatic polymer. It is an inexpensive and widely available resource, as lignin is

generally considered a waste product of the pulp and paper industry, with cellulose and hemicellulose considered the desirable components of lignocellulosic biomass. Further, it has desirable mechanical and antioxidant properties, along with biodegradability and excellent thermal stability. While lignins have been incorporated into polymer composites (as the filler), little research has been done to utilize lignin as a source for new polymers [14], [15], [16], [17]. The unique characteristics of lignin building blocks (monolignols and hydroxycinnamates), as well as their functional groups that enable straightforward modification, introduce vast potential for polymer synthesis. While the aromaticity of hydroxycinnamates lends itself to high strength and thermal resistance, it can make lignin-derived polymers brittle and intractable. Incorporating aliphatic and hydrolytically degradable regions into hydroxycinnamate-based polymers is expected to improve thermomechanical properties, solubility, and degradability.

In the endeavor to develop aromatic-aliphatic polymers from renewable resources, bio-based co-monomers must be considered from the circular economy perspective [18]. The ideal feedstock should minimize the environmental burden, such as requiring fertile soil or water, should not compete with food sources, and should minimize the required processing and transportation energy. One compelling class of feedstock candidates to copolymerize with lignin are lactones—cyclic esters of organic acids.

Lactones found in nature are primarily  $\gamma$ - and  $\delta$ -lactones, formed through intramolecular esterification of hydroxy fatty acids. They are natural building blocks pervasive across the biosphere—contributing to the aroma of fruits and cheese, present in oak wood to flavor barrel-aged beers, and in the biosynthesis of hormones, antibiotics, and even anti-cancer drugs [19], [20], [21], [22], [23]. For this work, we were particularly interested in lactide, glycolide, and  $\epsilon$ -

caprolactone (**Figure 3.2**). Lactide and glycolide are derived from lactic acid and glycolic acid, respectively, making them renewable bio-based monomers. E-caprolactone is derived from caproic

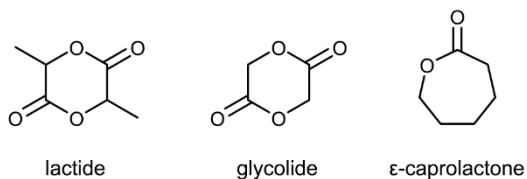


**Figure 3.2.** Chemical structures of lactones investigated in this research.

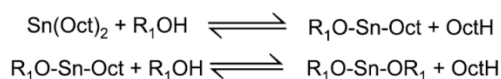
acid, which is a fatty acid found in a wide range of animal fats and oils. A recently developed biorefinery process isolates caproic acid from mixed organic waste—similarly to lignin, this would turn a “waste product” into a high-value monomer source [24]. The ring strain of these lactones (lactide, glycolide, and ε-caprolactone) makes them well-suited for ring-opening polymerizations (ROPs).

ROPs are chain-growth polymerizations, driven by relief of the ring strain as the cyclic esters are opened. The reactive polymer chain end attacks the cyclic monomers to propagate the chain. Tin 2-ethylhexanoate ( $\text{Sn}(\text{Oct})_2$ ) is commonly used to catalyze ROPs of cyclic esters; due to its low toxicity, it is often used for biomedical applications, and it has been approved by the FDA as a food additive [25]. It is also a preferred approach to synthesizing biodegradable aliphatic polyesters.

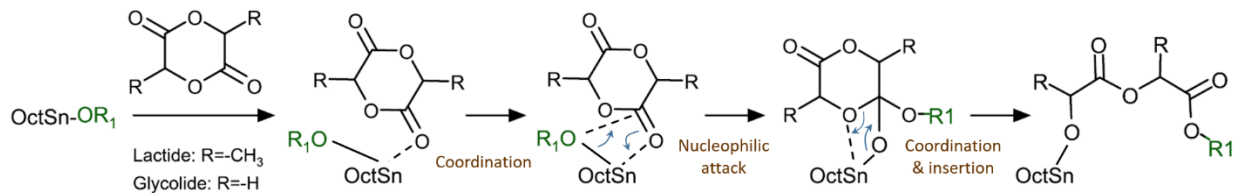
$\text{Sn}(\text{Oct})_2$ , along with an alcohol, form an initiating complex to facilitate living/controlled polymerization via a coordination-insertion mechanism. The tin catalyst and initiating alcohol form an  $\text{OctSn-OR}_1$  complex. In the dominant pathway, the coordination occurs between  $\text{OctSn-OR}_1$  and the carbonyl of the lactone to facilitate the ring-opening process (**Scheme 3.1**) [26].

Previous work by Hans Kricheldorf used salicylic acid as a co-catalyst with  $\text{Sn}(\text{Oct})_2$  for the ring-opening polymerization of L-lactide [27]. In addition to being sourced from nature, salicylic acid has a similar structure to hydroxycinnamates and is also a hydroxybenzoic acid. Instead of the traditional approach, with an aliphatic alcohol serving as the co-initiator, the

### Pre-coordination



### Coordination-Insertion Primary Pathway



**Scheme 3.1.** Sn(Oct)<sub>2</sub>-facilitated pathway for ring-opening polymerizations (ROPs) [26].

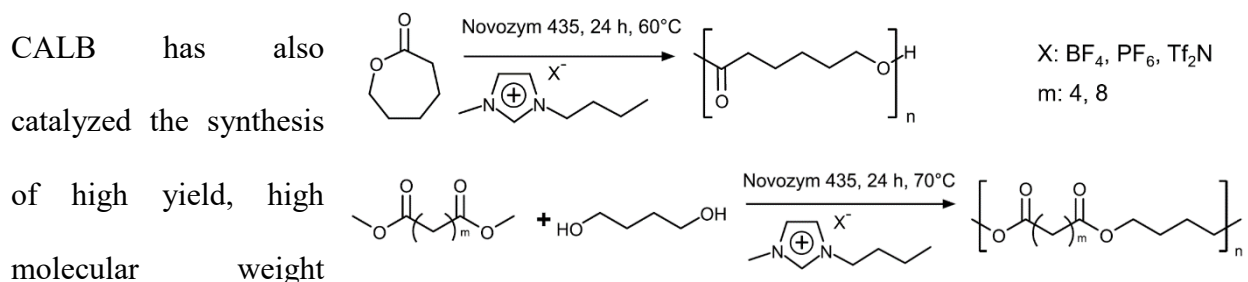
phenolic group of salicylic acid formed the initiating complex with Sn(Oct)<sub>2</sub> [28]. At temperatures below 130°C and moderate conversion, this ROP can behave like a living polymerization, with a narrow molecular weight distribution.

Assuming the phenol of the hydroxycinnimates would similarly act as a co-initiator with Sn(Oct)<sub>2</sub>, lactones could be polymerized directly from this end via ring-opening. In this chapter, several approaches to this reaction are explored. First, poly(lactic acid) or poly(glycolic acid) were polymerized off of the phenol of a single hydroxycinnamate. The repeating ester bonds in the polymer chain are expected to be hydrolysable, enabling the polymer to be broken down into eco-friendly fragments (i.e., hydroxycinnamate and lactic acid/glycolic acid). Then, to increase the relative incorporation of the lignin-derived components, we split the reaction into two separate steps. In the first step, the lactide or glycolide underwent ROP with ethylene glycol, forming symmetrical aliphatic alcohol linkers. These linkers were then used in condensation polymerizations with our previously synthesized hydroxycinnamate diacids. Through this, we successfully synthesized hydrolysable, biomass-derived aromatic-aliphatic poly(ester-ether)s.

Finally, to advance this project towards high performance materials with a low carbon footprint, we performed preliminary experiments synthesizing condensation polymers

incorporating hydroxycinnamate dimers derived from lignin with polyesters obtained via enzymatic ROP. Although known for decades, enzymatic synthesis of polyesters has experienced renewed and increased interest in recent years as an environmentally-friendly alternative to traditional organic synthesis [29]. In nature, enzymes catalyze the breakdown of natural polymers (i.e., lignocellulose) and can catalyze polymer synthesis, providing a greener alternative to chemical catalysts [30], [31]. They offer a number of distinct advantages over traditional approaches: (1) enzymes are the most efficient catalysts in nature, allowing for mild reaction conditions, (2) they are selective and specific, avoiding many protection/deprotection steps and functional group activation, and (3) they are derived from inexpensive and renewable resources, are biodegradable, and essentially non-toxic [32], [33].

These enzyme-catalyzed ROPs were performed using Novozym 435, a commercially available immobilized lipase B from *Candida antarctica* (CALB). Use of CALB permits mild reaction conditions that enable controlled structure with high selectivity. Importantly, CALB-catalyzed ROPs have been successfully performed in ionic liquids (**Scheme 3.2**) [30], [34]. Ionic liquids are low melting point ionic salts that provide a green alternative to traditional solvents, as they are reusable, non-volatile, and thermally stable [35], [36], [37], [38]. Ionic liquids also provide lipase stabilization, accelerating transesterification and facilitating lipase recycling [39]. CALB-catalyzed ROPs of L-lactide and glycolide have been performed successfully several ILs [40]. As



**Scheme 3.2.** Novozym 435 enzymatically catalyzes ROPs and polycondensation in several ionic liquids (cite :Enzymatic polyester synthesis in ionic liquids)

we believe we can transition our synthetic strategy to this greener approach [41]. There is literature precedent for enzyme-mediated condensation reactions of lignin precursors in ILs ([C<sub>2</sub>OHmim][PF<sub>6</sub>] and [C<sub>5</sub>O<sub>2</sub>mim][PF<sub>6</sub>]) [42]. Feruloyl esterase was used to catalyze the esterification of glycerol, a byproduct of biodiesel formation, with sinapic acid, with conversion of ~76%. By combining these strategies, we expected that we can perform CALB-catalyzed ROPs of lactones initiated by alcohols and diols in ionic liquids. The symmetrical enzyme-catalyzed polyesters were then subjected to the same condensation polymerization reactions with hydroxycinnamate dimers as the tin-catalyzed polyesters.

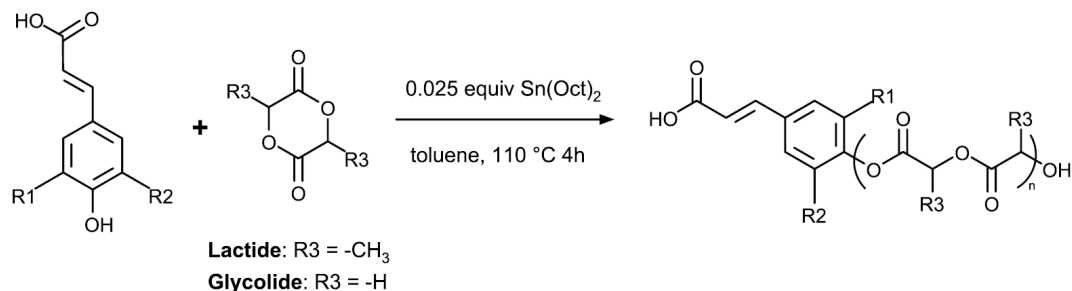
Through this, a library of bio-based polyesters, incorporating hydroxycinnamates and bioderived lactones, was synthesized and characterized to provide insight into their unique properties. In particular, the thermal properties were thoroughly evaluated in hopes of identifying potential candidates for 3D printing. The ideal candidates would have a  $T_g$  between 55°C and 85°C and, if applicable, a  $T_m$  between 150°C and 250°C. This will pave the way for the next phase of translational research, fabricating the 3D printing filament and testing its degradation and compostability.

## 3.2 Results and Discussion

### *Optimizing Ring-Opening Polymerizations*

**Hydroxycinnamate monomer lactide and glycolide ROPs (Sn(Oct)<sub>2</sub>).** A series of hydroxycinnamates with lactones (L-lactide or glycolide) ring opened off of the phenolic groups were obtained with high yields ( $\geq 90\%$ ) (**Scheme 3.3, Table S3.1**). Ratios indicate the molar ratio of hydroxycinnamate to lactone. Sn(Oct)<sub>2</sub>-catalyzed ROPs were used to synthesize *p*-coumaric

polylactic acid (1:1 and 1:10), *p*-coumaric polyglycolic acid (1:1 and 1:10), ferulic polylactic acid (1:1), and ferulic polyglycolic acid (1:1 and 1:10).

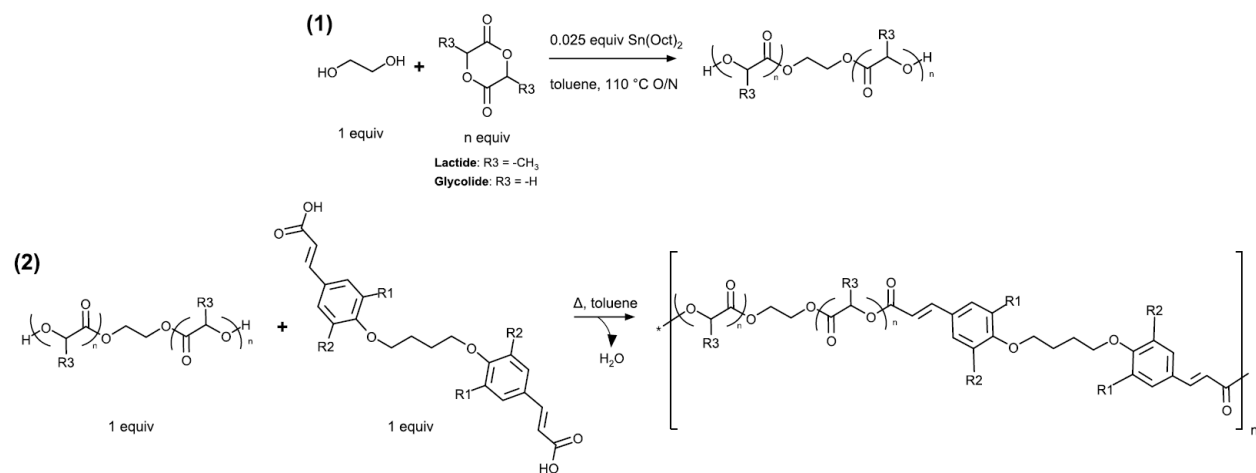


**Scheme 3.3.** ROP of lactide or glycolide off of the phenol of hydroxycinnamates.

After the 4 h reaction [27], the L-lactide reactions appeared to contain crystalline solids, opposed to a viscous amorphous polymer. The L-lactide ROPs did not proceed, and were revealed by TLC to remain a mixture of starting materials. ROPs using glycolide exhibited very low solubility; the crude products appeared as a pale yellow, plastic-like solid on the bottom of the reaction flask.

Common <sup>1</sup>H NMR solvents were only able to solubilize starting material entrapped within the solid, preventing degree of polymerization from being determined using <sup>1</sup>H NMR. Similarly, the glycolide-based ROPs were insoluble in solvents compatible with our available GPC columns. As a final approach to characterizing polymer size, we attempted MALDI-TOF analysis on a few model compounds. We tested: 1:1 *p*-coumaric acid:L-lactide, 1:1 *p*-coumaric acid:glycolide, 1:10 *p*-coumaric acid:glycolide, and 1:10 ferulic acid:glycolide. This analysis was attempted using the sandwich method in both THF and HFIP, in an attempt to improve solubility and homogeneity of the sample on the target plate. Based on MALDI-TOF results, these reactions either did not polymerize or have a low ionization efficiency, rendering them unable to be detected using this approach (**Figures S3.1-S3.4**).

**Diol linkers via ethylene glycol ROPs of lactide and glycolide (Sn(Oct)<sub>2</sub>).** Due to the indeterminable polymerization efficacy and significant solubility limitations, the approach to hydroxycinnamate-based ROPs was modified. First, we transitioned from L-lactide to DL-lactide, which is a racemic mixture of D- and L-lactide isomers. The presence of the D-lactide isomer introduces structural asymmetry, creating a more open and flexible structure, thereby improving solubility in various organic solvents. Secondly, in polymerizing the lactones off of hydroxycinnamate monomers, the relative amount of hydroxycinnamates in the polymer is limited. To overcome this limitation and to increase the range of achievable molecular weights, the synthetic pathway was adapted into a two-step process. In the first step, the lactone undergoes ROP with ethylene glycol—which acts as the co-initiator with Sn(Oct)<sub>2</sub>, resulting in a symmetrical diol (**Scheme 3.4 (1)**). This diol is then subjected to condensation polymerization with the hydroxycinnamate dimers (**Scheme 2.5** from Chapter 2) to yield polyesters (**Scheme 3.4 (2)**).



**Scheme 3.4.** Diol linkers, synthesized through ROPs of lactones with ethylene glycol (1), undergo condensation polymerizations with hydroxycinnamate dimers (2).

Synthesizing the ethylene glycol ROPs was an iterative process, as it was difficult to experimentally achieve the theoretical number of polymeric repeating units, n. Using the correct



stoichiometric amounts of ethylene glycol and lactone and using mass instead of volume, the degree of polymerization was unpredictable. Because ethylene glycol is highly hygroscopic, it was expected that this was due to water in the reagent either a) initiating more ROPs than intended, leading to shorter chain lengths, or b) contributing to the mass of the ethylene glycol added to reactions, leading to a lower true amount of ethylene glycol than intended. This problem was addressed by freeze-drying the ethylene glycol and using the degree of polymerization of previous reactions to adjust the mass of ethylene glycol added. For instance, after a 1:50 ethylene glycol:DL-lactide ROP resulted in an  $n$  of 27, 0.54 times the ethylene glycol was used in the next 1:50 ethylene glycol:DL-lactide ROP, leading to an  $n$  of 48. The water wash step proved highly effective at removing residual  $\text{Sn}(\text{Oct})_2$ , as evidenced by the absence of an  $^1\text{H}$  NMR peak at 0.88 ppm (**Figure S5**). Additionally, the final experiments transitioned to melt polymerizations, enabling a solvent-free and thus more environmentally-friendly approach to these reactions.

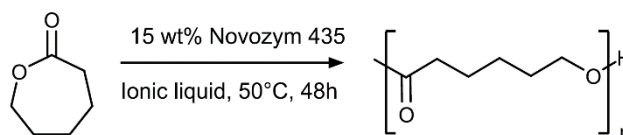
**Table 3.1** outlines the diol linkers synthesized throughout this work, specifying whether the reactions were conducted in refluxing toluene or as melt polymerizations. Glycolide and L-lactide ROPs were discontinued early on due to solubility limitations of the products. DL-lactide ROPs, both at this step and once the diols are used in condensation polymerizations, led to improved product solubility.

**Table 3.1.** Iterations of ethylene glycol ring-opening polymerizations performed and the experimentally determined degree of polymerization (via  $^1\text{H}$  NMR).

Alcohol	Lactone	Ratio (EG:lactone)	Yield (g)	Theoretical $n$	Experimental $n$	Approach
Ethylene glycol (EG)	glycolide	1:25	0.067	25	0	Toluene
		1:10	0.32	10	8	Toluene
	L-lactide		1.0	10	6	Toluene
			0.057	25	0	Toluene
		1:25	0.067	25	9	Toluene
			1.1	25	14	Toluene

		0.43	25	30	Toluene
	1:10	0.83	10	5	Toluene
		0.73	10	10	Melt
	1:25	0.53	25	15	Toluene
DL-		1.1	50	10	Toluene
lactide	1:50	0.95	50	89	Toluene
		0.99	50	27	Melt
		1.0	50	48	Melt
	1:100	2.0	100	102	Melt

**Solvent-free Enzyme-catalyzed ROPs.** These ROPs were also attempted using enzyme catalysis instead of heavy metal catalysis. A commercially available immobilized *Candida antarctica* Lipase B, Novozym 435, was used to catalyze the ROP of  $\epsilon$ -caprolactone (**Scheme 3.5**). Novozym 435 can be washed and reused in subsequent reactions, and it also enabled reactions to be performed in ionic liquids opposed to organic chemical solvents. In these preliminary experiments, reactions were attempted in the following ionic liquids: 1-butyl-3-methylimidazolium hexafluorophosphate ([BMIM][PF<sub>6</sub>]), 1-butyl-3-methylimidazolium tetrafluoroborate ([BMIM][BF<sub>4</sub>]), and 1-(2-hydroxyethyl)-3-methylimidazolium tetrafluoroborate ([C<sub>2</sub>OHMIM][BF<sub>4</sub>]) [30], [34], [43].

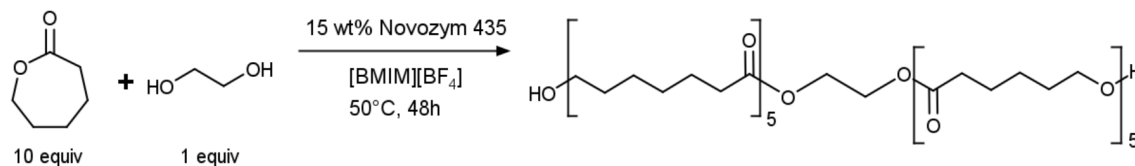


**Scheme 3.5.** Lipase B-catalyzed ROP of  $\epsilon$ -caprolactone in ionic liquids.

The first reactions were performed in [BMIM][PF<sub>6</sub>] with a crude yield of 97%, and a conversion of 94%. Further, 71% of the ionic liquid was recovered, though it appeared to retain a large fraction of the polymer. The same reaction in [BMIM][BF<sub>4</sub>] had a crude yield of 59%, a conversion of 95%, and 28% of the ionic liquid was recovered. The recovered [BMIM][BF<sub>4</sub>] was pure and free of both starting material and polycaprolactone. Finally, the ROP of  $\epsilon$ -caprolactone in [C<sub>2</sub>OHMIM][BF<sub>4</sub>] had a crude yield of 89% and a conversion of 94%, and 35% of the ionic

liquid was recovered. The recovered  $[\text{C}_2\text{OHMIM}][\text{BF}_4]$  contained a small amount of polymer that had not been fully extracted by toluene.

Because of the high monomer conversion and ease of product extraction from the ionic liquid—enabling effective recycling and reuse— $[\text{BMIM}][\text{BF}_4]$  was selected to synthesize a symmetrical ethylene glycol linker with polycaprolactone polymerized off of both ends (**Scheme 3.6**) [43]. This would be used in subsequent condensation polymerizations, similarly to the lactone-based linkers. A 1:10 ethylene glycol: $\epsilon$ -caprolactone ROP was successfully synthesized, with an  $n$  of 10 on both ends and a conversion of 97%. Yield of the linker was low, only 20%, which can be attributed to extensive extraction steps from the  $[\text{BMIM}][\text{BF}_4]$  as well as the methanol recrystallization.



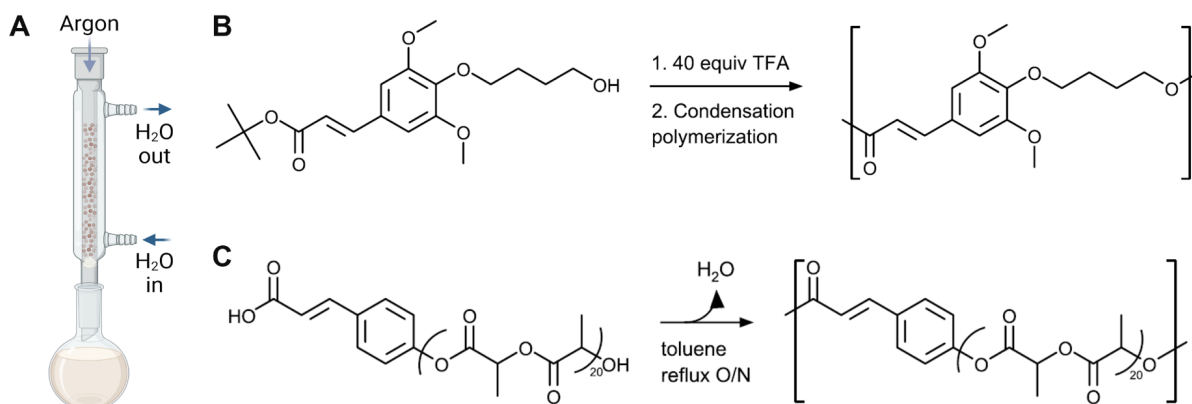
**Scheme 3.6.** Lipase B-catalyzed ROP of 1:10 ethylene glycol: $\epsilon$ -caprolactone in ionic liquids.

### *Optimizing Condensation Polymerizations*

**Condensation Polymerizations of Modified Hydroxycinnamate Monomers.** The majority of condensation polymerizations were performed in toluene, creating an azeotrope with water released during the polymerization. These polymerization set-ups incorporated a condenser filled with activated molecular sieves above the refluxing reaction to drive off water and push reaction equilibrium forward (**Scheme 3.7A**).

The first condensation polymerization was of sinapinic acid with a butanol chain extending from the phenol (**Scheme 3.7B**). After deprotecting the monomer using trifluoroacetic acid, it was

refluxed in toluene, with water removal aided by molecular sieves in the condenser. This reaction had a yield of 41.7% (0.3896 g), with product loss attributed to an unsuccessful ether precipitation. A condensation polymerization was also attempted using *p*-coumaric acid with L-lactide polymerized directly off of the phenol (**Scheme 3.7C**). This reaction also used the toluene azeotrope approach to water removal, with a yield of 89.2% (0.4786 g).



**Scheme 3.7.** Toluene azeotrope-mediated condensation polymerizations (A) of modified sinapinic acid (B) and *p*-coumaric acid (C).

However, these condensation polymerizations limited the relative amount of lignin-derived components in the final polymer. As such, we transitioned to condensation polymerizations of the hydroxycinnamate dimers with the lactones that had undergone ROP with ethylene glycol.

### Condensation Polymerizations of Hydroxycinnamate Dimers and ROP Products.

Using the same set-up as **Scheme 3.7A**, condensation polymers of the hydroxycinnamate dimers and ethylene glycol ROP products were synthesized. In Chapter 2 (**Scheme 2.5**), a series of hydroxycinnamate acid dimers were synthesized. The ferulyl and sinapyl dimers, the more substituted hydroxycinnamates, were used with the ROP diol linkers (**Scheme 3.4** and **3.6**) to

produce a series of polyesters, driving reaction equilibrium through the removal of water. The naming convention of these polymers is described in **Figure 3.3**, with yields outlined in **Table 3.2**.

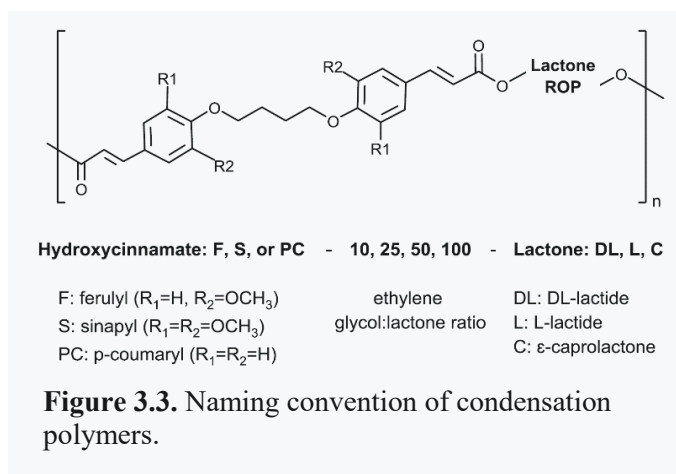


**Table 3.2.** Hydroxycinnamate-based condensation polymers.

Polymer	Hydroxycinnamate	ROP	Yield	
F-25-L	Ferulyl ether dimer	1:25 ethylene glycol:L-lactide	0.058 g	94.8%
F-25-DL		1:25 ethylene glycol:DL-lactide	0.069 g	82.1%
F-50-DL		1:50 ethylene glycol:DL-lactide	0.12 g	81.0%
F-50-DL <sup>a</sup>		1:50 ethylene glycol:DL-lactide	0.033 g	37.4%
S-25-L	Sinapyl ether dimer	1:25 ethylene glycol:L-lactide	0.11 g	96.5%
S-50-DL		1:50 ethylene glycol:DL-lactide	0.13 g	83.1%
S-100-DL <sup>b</sup>		1:100 ethylene glycol:DL-lactide	0.057 g	68.7%
S-10-C	Sinapyl ester dimer	1:10 ethylene glycol:ε-caprolactone	0.026 g	99.6%
S	Mono-functional sinapyl ether	X	0.39 g	41.7%
PC-L	<i>p</i> -coumaric acid L-lactide ROP	X	0.48 g	89.2%

<sup>a</sup>Synthesized using acid chloride-facilitated polymerization, <sup>b</sup>Synthesized with molecular sieves added directly to toluene opposed to in condenser above refluxing reaction.

Two of the condensation polymers were synthesized with modified approaches: F-50-DL<sup>a</sup> and S-100-DL<sup>b</sup>. F-50-DL<sup>a</sup> was synthesized using an acid chloride-facilitated polymerization, in which the carboxylic acid groups of the ferulyl dimer were first converted to acid chlorides. The diacyl chlorides readily undergo nucleophilic acyl substitution reactions with the diol ROP linkers

to form polyesters. However, the yield of F-50-DL<sup>a</sup> was low because it did not precipitate into ether as well as anticipated, and product was lost as the work-up was transitioned to DCM and washing. S-100-DL<sup>b</sup> was synthesized using a similar toluene/water removal approach to condensation polymerization, but instead of a drying tube, activated molecular sieves were added directly to the reaction flask. This polymerization had a nearly quantitative yield, though there is a possibility that particulate from the molecular sieves had been transferred along with the product.

**<sup>1</sup>H and FTIR Spectroscopy.** FTIR spectroscopy was used to confirm successful polymerization (**Figure 3.4**). Polymerization would be indicated by a reduction in intensity of the peaks corresponding to carboxylic acids and alcohols, relative to the starting materials, as these groups should polymerize into ester bonds.

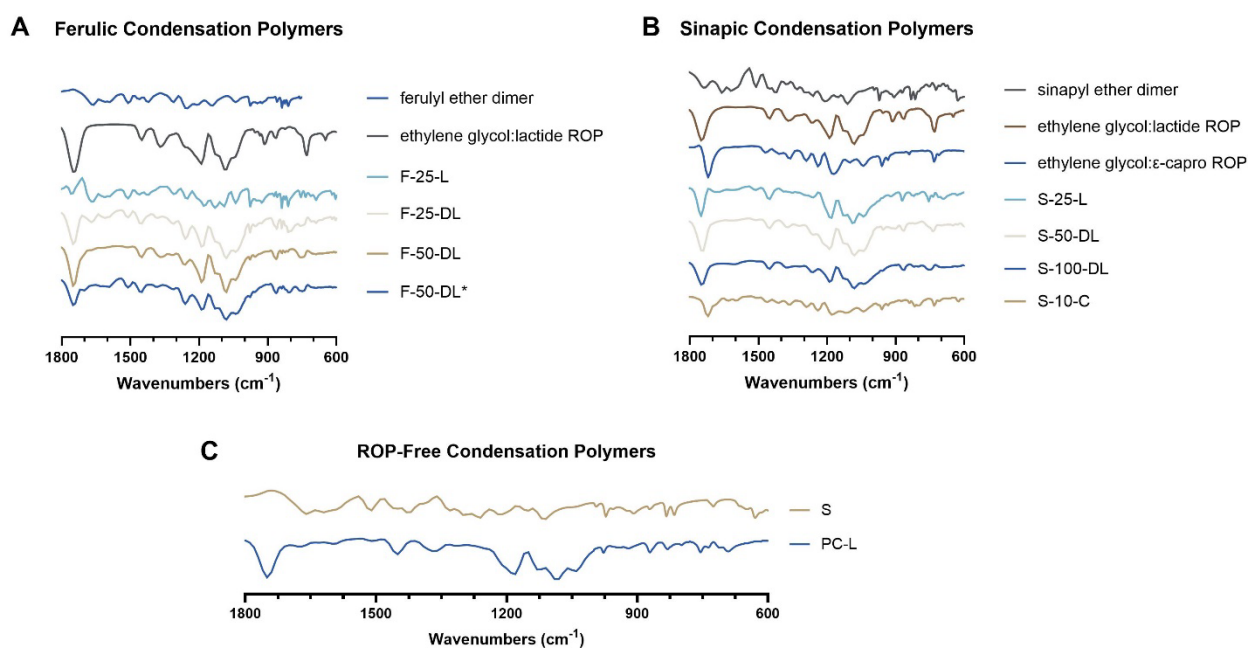


**Figure 3.4.** IR fingerprint region of condensation polymers incorporating (A) ferulic dimers with ring-opening polymerization (ROP) linkers, (B) sinapic dimers with ROP linkers, and (C) hydroxycinnamates without linkers.

The ethylene glycol:DL-lactide ROP products (1:10 in **Fig. 3.4A** and 1:50 in **Fig. 3.4B**), 1:10 ethylene glycol:ε-caprolactone ROP (**Fig. 3.4B**) and ferulyl and sinapyl ether dimers were run as controls. As expected, the traces of both of the ethylene glycol:DL-lactide ROPs, regardless of the degree of polymerization, looked very similar and showed large peaks at 1745  $\text{cm}^{-1}$  and 1190  $\text{cm}^{-1}$ , indicating the presence of ester groups. Additionally, they both exhibited C-O stretches at 1090  $\text{cm}^{-1}$  and O-H bends at 1370  $\text{cm}^{-1}$ , confirming the presence of the diol end groups. The ethylene glycol:ε-caprolactone ROP similarly showed C-O stretching at 1170  $\text{cm}^{-1}$  and O-H bending at 1360  $\text{cm}^{-1}$ , as well as the carbonyl stretch C=O of esters at 1740  $\text{cm}^{-1}$ , providing further evidence that the polyester diol linkers had been successfully synthesized. In addition to the expected aromatic peaks (840-810  $\text{cm}^{-1}$ ), both ferulyl and sinapyl ether dimers exhibited peaks in the fingerprint region indicative of their terminal carboxylic acids: a C=O stretch from 1740-1670  $\text{cm}^{-1}$ , a C-O stretch at 1210-1260  $\text{cm}^{-1}$ , and O-H bends at 1420  $\text{cm}^{-1}$  and 930-910  $\text{cm}^{-1}$ . For the condensation polymers, we expect to observe a decreased intensity in these carboxylic acid peaks and in the alcohol peaks of the ROP linkers, as well as an increase in intensity of ester peaks in the polyesters.

For both the ferulic (**Fig. 3.4A**) and sinapinic condensation polymers (**Fig. 3.4B**), they all display the aromatic peaks confirming that the hydroxycinnamate dimer is incorporated. We see a notable disappearance of the O-H bend at 1360  $\text{cm}^{-1}$  associated with the diol ROP, and the presence of large ester peaks (C=O stretch  $\sim 1750 \text{ cm}^{-1}$  and C-O stretching at 1190 and 1086  $\text{cm}^{-1}$ ). This confirms the successful polymerization of F-25-L, F-25-DL, F-50-DL, and F-50-DL\* and S-25-L, S-50-DL, S-100-DL, and S-10-C.

Finally, for the ROP-free condensation polymers, polymerization would also be indicated by the presence of minimal alcohol and carboxylic acid peaks along with pronounced peaks

indicative of ester bonds (**Figure 3.4C**). The trace of mono-functional sinapyl ether polymer (S) did not display the characteristic C=O peaks, and appeared to still possess a C-O stretch at 1110  $\text{cm}^{-1}$  that would present near the alcohol. Based on this, it appears that S did not successfully polymerize. On the other hand, the condensation polymer of *p*-coumaric acid with L-lactide polymerized off the hydroxycinnamate phenol (PC-L) exhibited a large ester peaks at 1180 and 1750  $\text{cm}^{-1}$ , offering confidence that this reaction had been successful. From the FTIR data, it appears that all condensation polymerizations, with the exception of mono-functional sinapyl ether, successfully proceeded.

**Molecular Weight Characterization.** Gel permeation chromatography (GPC) was used to determine  $M_n$ ,  $M_w$ , and  $\bar{D}$  for the condensation polymers (**Table 3.3**). In general, the condensation polymers incorporating poly(lactic acid) linkers had molecular weights ranging from 13,380 – 40,990 g/mol and all exhibited remarkably good polydispersities, between 1.03-1.25. Molecular weights were higher for polymers incorporating DL-lactide based ROPs, compared to L-lactide based ROPs, which can be attributed to the improved solubility of the former. As anticipated, molecular weight increased as a function of increasing ROP linker length. For example, the  $M_n$  of sinapyl condensation polymers increased from 13,380 to 16,190 to 40,990 as the ROP linker increased from 1:25 to 1:50 to 1:100 ethylene glycol:DL-lactide.

The two modified approaches, either using acid chloride-facilitated condensation polymerization (F-50-DL<sup>a</sup>) or by refluxing with molecular sieves added directly to the flask (S-100-DL<sup>b</sup>), resulted in the highest molecular weights, while retaining a low dispersity. These alternative approaches provide a good starting platform for future research employing a similar approach to aromatic-aliphatic condensation polymerizations.



**Table 3.3.** Molecular weight of hydroxycinnamate-based condensation polymers via RI GPC.

Polymer	Hydroxycinnamate	ROP	M <sub>n</sub>	M <sub>w</sub>	Đ
F-25-L		1:25 EG:L-lactide	13,920	17,420	1.25
F-25-DL	Ferulyl ether dimer	1:25 EG:DL-lactide	20,770	22,110	1.06
F-50-DL		1:50 EG:DL-lactide	24,200	29,350	1.21
F-50-DL <sup>a</sup>		1:50 EG:DL-lactide	37,910	41,260	1.09
S-25-L	Sinapyl ether dimer	1:25 EG:L-lactide	13,380	18,180	1.22
S-50-DL		1:50 EG:DL-lactide	16,190	17,310	1.07
S-100-DL <sup>b</sup>	Sinapyl ester dimer	1:100 EG:DL-lactide	40,990	44,110	1.08
S-10-C		1:10 EG:ε-caprolactone	18,590	20,110	1.08
S	Mono-functional sinapyl ether	X	3,680	3,800	1.03
C-L	<i>p</i> -coumaric acid L-lactide ROP	X	11,860	14,020	1.18

EG-ethylene glycol. <sup>a</sup>Synthesized using acid chloride-facilitated polymerization, <sup>b</sup>Synthesized with molecular sieves added directly to toluene opposed to in condenser above refluxing reaction.

Overall, the molecular weights for these condensation polymers were approximately double what could be obtained when synthesizing poly(ether-amide)s using an interfacial polymerization synthetic approach, even after the thiol-ene reaction improved their solubility. This increased molecular weight is expected to improve processability and resistance to thermal degradation.

**Thermal Characterization.** The thermal behavior of the condensation polymers was studied using differential scanning calorimetry (DSC) to gain insight into their thermal transitions, in particular glass transition temperature,  $T_g$  and, if applicable, melting temperature,  $T_m$ . Glass transition temperatures are observed as subtle shifts in the baseline.

All of the polyesters synthesized demonstrated remarkably low  $T_g$  (**Figure 3.5**). Ferulic condensation polymers exhibited  $T_g$  in the range of 27.3-33.2°C. Only one of the ferulic polymers

exhibited a melting temperature—F-25-L, with a 1:25 ethylene glycol:L-lactide linker, had a  $T_m$  of 51.1°C. Polymers incorporating L-lactide ROPs are more likely to exhibit a  $T_m$  and a higher  $T_g$  due to their higher crystallinity, which restricts the movement of polymer chains. Sinapic polyesters had very similar  $T_g$ , ranging from 22.4 to 38.2°C, the highest of which incorporated the L-lactide ROP. Two of the sinapic polymers displayed a melting temperature: S-25-L and S-10-C. Interestingly, of B. Upton’s poly(ether-amide)s, the only ones to exhibit a  $T_m$  were those that incorporated sinapic dimers, and they ranged from 63.6 to 141.9°C. S-25-L had a  $T_m$  of 126.7, while S-10-C, incorporating the polycaprolactone linker, exhibited a  $T_m$  of 51.2°C. While aromatic polymers tend to have high glass transition temperatures, these results seem to indicate that incorporating flexible aliphatic linkers can drastically reduce it.

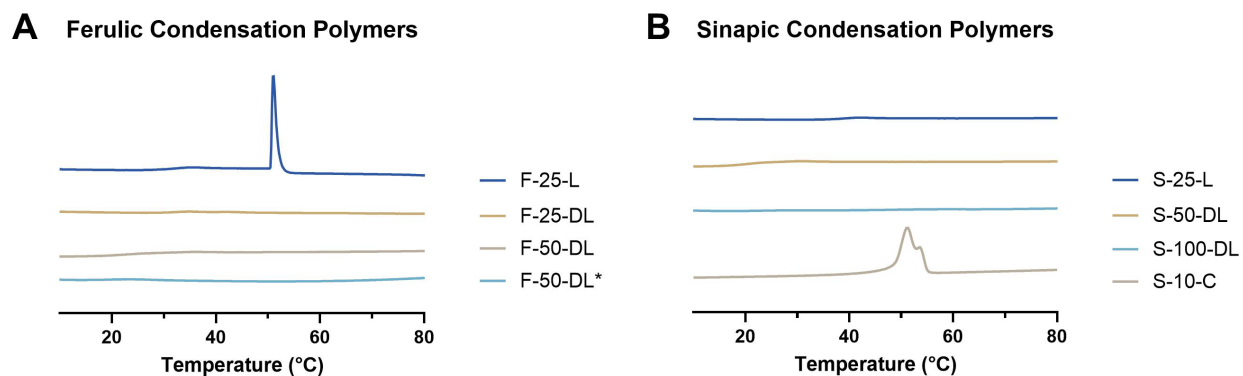


**Figure 3.5.** Stacked DSC traces of (A) ferulic and (B) sinapic condensation polymers.

Thermogravimetric analysis (TGA) was performed on two model polymers- ferulyl ether-lactic acid (F-50-DL<sup>a</sup>) and sinapyl ester-lactic acid (S-100-DL<sup>b</sup>). TGA provides insight into the thermal stability of polymers, and degradation can be visualized as the polymer mass decreases as the sample temperature is ramped (**Fig. 3.6**). The ferulyl ether-lactic acid polymer had  $T_{d5}$  of 167.3°C,  $T_{d10}$  of 217.9°C,  $T_{d25}$  of 312.2°C, and fully degraded at 544.8°C. The sinapyl ester-lactic acid polymer exhibited similar trends, with  $T_{d5}$  of 156.1°C,  $T_{d10}$  of 222.0°C,  $T_{d25}$  of 304.2°C,

though it never fully degraded, even at 800°C. These values all fall within the ranges reported by B. Upton for her series of lignin-derived poly(ether-amide)s, though they generally are lower than the degradation temperatures that she determined for the series of poly(ester-amide)s [44], [45].

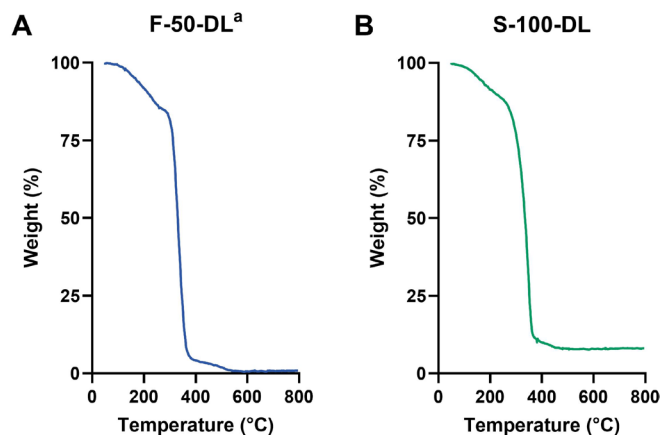


**Figure 3.6.** Thermogravimetric analysis (TGA) of model (A) ferulic and (B) sinapic condensation polymers.

### 3.3 Conclusions

The plastic industry's reliance on petroleum derived feedstocks raises significant environmental concerns. There is increasing interest in developing sustainable alternatives, but the current landscape of bio-based polymers is primarily composed of low-performance materials, underscoring the need for advancements in the field. Addressing the challenge of developing more environmentally friendly alternatives requires innovative approaches to polymer synthesis, emphasizing renewable resources and green chemistry principles. In this work, we take a holistic approach to the synthesis of sustainable aromatic-aliphatic polyesters, by repurposing our previously synthesized hydroxycinnamate dimers in condensation polymerizations with bio-based ring-opened polymers.

Lactones served as our co-monomers sourced from nature. Lactones are cyclic esters, pervasive across the biosphere, that are well-suited for ring-opening polymerizations. It is an optimal approach for fabricating biodegradable polyesters that break down into eco-friendly degradation products. A series of symmetrical diol linkers was synthesized by using ethylene

glycol as the co-catalyst in tin-catalyzed lactone ring-opening polymerizations. We also performed proof-of-concept reactions to demonstrate that these symmetrical linkers can be catalyzed using the enzyme Lipase B (eliminating the heavy metal catalyst) in ionic liquids. This approach would eliminate the bulk of required petroleum derived organic solvents, improve reaction efficiency, and reduce required materials because both the enzyme and ionic liquids can be reused in subsequent reactions.

The ring-opened linkers all feature terminal alcohol groups that enabled condensation polymerizations with the carboxylic acid end groups of the hydroxycinnamate dimers. The catalyst-free condensation polymerizations were driven by the removal of water, with most polymers yielding >80%. Through this, we developed a library of aromatic-aliphatic polyesters, characterized by their unique thermal and mechanical properties. These polymers exhibited moderate molecular weights, with low dispersity, and low glass transition temperatures.

Based on their thermomechanical properties, these polyesters have great potential as a material for additive manufacturing. In line with the Circular Economy, the local feedstocks for the majority of the synthesis are fully renewable, with reusable enzymes sourced from nature. These polymers are expected to hydrolyze over time, with fully biocompatible degradation products. The next phase of this work will be characterizing the hydrolysis of this series of polyesters and conducting thorough compostability testing, while transitioning to thermal processing to verify compatibility with extrusion. These findings underscore the potential of our bio-based condensation polymers as sustainable alternatives to traditional plastics. By leveraging renewable resources and green chemistry, there is room to develop polymers with a reduced carbon footprint, contributing to a more sustainable future for plastics.

### 3.4 Experimental

**Materials.** Trans *p*-coumaric acid (98+%, TCI America), trans-ferulic acid (98+%, TCI America), magnesium sulfate (MgSO<sub>4</sub>, Certified, Fisher Chemical), immobilized *C. antarctica* Lipase B (Novozym<sup>®</sup> 435, Strem Chemicals), and tin(II) 2-ethylhexanoate (Sn(Oct)<sub>2</sub>, 95%, Thermo Scientific) were used as received. Ethylene glycol (certified, Fisher Chemical) was freeze-dried on the Shlenk line prior to use. L-lactide (98+%, Thermo Scientific), DL-lactide (99%, Thermo Scientific), glycolide (98+%, TCI America), and ε-caprolactone (99%, Thermo Scientific) were recrystallized from ethanol and dried under reduced pressure. Ionic liquids—1-Butyl-3-methylimidazolium hexafluorophosphate ([BMIM][PF<sub>6</sub>], 98+%, TCI America), 1-Butyl-3-methylimidazolium tetrafluoroborate ([BMIM][BF<sub>4</sub>], 98+%, Thermo Scientific), and 1-(2-Hydroxyethyl)-3-methylimidazolium tetrafluoroborate ([C<sub>2</sub>OHMIM][BF<sub>4</sub>], 98+%, TCI America)—were dried under reduced pressure prior to use. 3Å molecular sieves (Thermo Scientific) were activated under heat and reduced pressure prior to use. Toluene (Certified ACS, Fisher Chemical) was distilled from CaH<sub>2</sub> prior to use. NMR solvents d<sub>6</sub>-DMSO and CDCl<sub>3</sub> were obtained from Acros Organics and used as received.

**<sup>1</sup>H and FTIR Spectroscopy.** <sup>1</sup>H NMR spectra were recorded on Bruker AV-300 or Bruker AV-400 spectrometers at room temperature in either CDCl<sub>3</sub> or d<sub>6</sub>-DMSO. Chemical shifts are reported with respect to the internal solvent, 7.26 ppm (CDCl<sub>3</sub>) or 2.50 ppm (d<sub>6</sub>-DMSO). Infrared absorption spectra were collected using a ThermoScientific Nicolet<sup>™</sup> iS 5 FTIR spectrometer. All samples were dried overnight prior to characterization.

**Molecular Weight Characterization.** Molecular weight (M<sub>n</sub> and M<sub>w</sub>) and dispersity (Đ = M<sub>w</sub>/M<sub>n</sub>) were determined using gel permeation chromatography (GPC). Samples were dissolved at room temperature in DMF containing 10 mM LiBr at a concentration of 6 mg/mL. All samples

were passed through a 0.20  $\mu\text{m}$  PTFE filter (Millex<sup>®</sup>-LG) directly before injection. GPC for all polymers was performed on a Jasco system equipped with a refractive index detector (RI-2031 Plus), UV detector (UV-2075 Plus), a Waters Styragel guard column, and four Waters HR Styragel 5  $\mu\text{m}$  columns (100-5 K, 500-30 K, 50-100 K, 5-600 K). The system was run using DMF with 10 mM LiBr at a flow rate of 1.0 mL/min. Calibration was performed with near-monodisperse polystyrene standards (Jordi Laboratories,  $M_n = 1,250 - 549,000$  g/mol). Chromatograms were recorded and analyzed using ChromNAV chromatography software.

For polymers insoluble in common GPC solvents, matrix-assisted laser desorption/ionization time-of flight (MALDI-TOF) mass spectrometry was attempted to evaluate molecular weight. The MALDI-TOF (UltraFlex, Bruker Daltronics) instrument was equipped with an  $\text{N}_2$  laser (337 nm wavelength) in the reflectron mode, collected in the mass range of 200-20,000  $m/z$ . Each sample was dissolved in either THF or HFIP at 10  $\mu\text{M}$ , and a dithranol matrix solution (10 mg/mL) containing a NaTFA ionization agent (0.4 mg/mL) was prepared. The polymer samples were spotted on a steel target plate, sandwiched between a base and top layer of the matrix solution, with a sample:matrix:salt ratio of 5:25:1. Each layer was spotted with a micropipette tip and allowed to slowly evaporate before applying the next layer.

**Thermal Characterization.** All samples were dried at 40  $^\circ\text{C}$  under high vacuum prior to thermal characterization. Differential scanning calorimetry (DSC) was conducted on a PerkinElmer DSC 8000. Polymer samples (5-10 mg) were placed in an aluminum crucible, and sealed with pierced aluminum cover. Samples were heated to 400  $^\circ\text{C}$  and cooled to -60  $^\circ\text{C}$  at a rate of 10  $^\circ\text{C}/\text{min}$  for a total of 3 heating and 2 cooling cycles. DSC data was recorded and analyzed using PerkinElmer Pyris<sup>TM</sup> Software to identify glass transition temperature ( $T_g$ ) and melting temperature ( $T_m$ ), measured from the second heating cycle. Thermogravimetric analysis (TGA)

was performed using a PerkinElmer TGA 8000. The TGA instrument was operated under a nitrogen atmosphere, using platinum crucibles. Samples (6 mg) were heated from 40 to 600 °C at a rate of 10°C/min. Pyris™ Software was used to analyze the data. Decomposition temperatures  $T_{d5}$ ,  $T_{d10}$ , and  $T_{d25}$  were measured at 5, 10, and 25% mass loss.

**Hydroxycinnamate monomer lactide and glycolide ROPs ( $\text{Sn}(\text{Oct})_2$ ).** The length of the poly(lactic acid) or poly(glycolid acid) chain was varied by adjusting the ratio of hydroxycinnamate to lactone (i.e. 1:1 or 1:10).  $\text{Sn}(\text{Oct})_2$  was diluted in toluene to prepare a 0.5 M stock solution. In general, the hydroxycinnamate (1 equiv., 0.5 mmol) was combined with the lactone (1 or 10 equiv, 0.5 or 5 mmol) and 25  $\mu\text{L}$  of the 0.5 M  $\text{Sn}(\text{Oct})_2$  stock solution (0.025 equiv.,  $1.25 \times 10^{-5}$  mmol) in 10 mL toluene in a 50 mL round bottom flask. The reaction was refluxed under Ar at 110°C for 4h, after which it was transferred to a vial and dried under reduced pressure.

**Diol linkers via ethylene glycol ROPs of lactide and glycolide ( $\text{Sn}(\text{Oct})_2$ ).**  $\text{Sn}(\text{Oct})_2$  was diluted in toluene to prepare a 0.5 M stock solution. Freeze-dried ethylene glycol (1 equiv., 0.139 mmol) was combined with the lactone (varied equiv.) and 25  $\mu\text{L}$  of the 0.5 M  $\text{Sn}(\text{Oct})_2$  stock solution (0.025 equiv.,  $1.25 \times 10^{-5}$  mmol) in 2.5 mL toluene in a 5 mL round bottom flask. The reaction was refluxed overnight under Ar. After rotovaping to concentrate the product, it was dissolved in DCM and washed extensively with DI  $\text{H}_2\text{O}$  to remove the tin catalyst and dried under reduced pressure. In later reactions, this was transitioned to a melt polymerization. All reagents remained the same other than the inclusion of toluene. The reaction was heated to 150°C overnight, and after cooling to RT, the product was dissolved in DCM, washed with DI  $\text{H}_2\text{O}$ , and dried under reduced pressure. A sample  $^1\text{H}$  NMR of 1:25 ethylene glycol:DL-lactide ROP is shown in **Figure S3.5**.

*Ethylene glycol and lactide ROPs (1:n).* <sup>1</sup>H NMR (300 MHz, CDCl<sub>3</sub>): δH 5.12 (q, 2×*n* H), 4.32 (m, 4H), 1.52 (d, 6×*n* H).

**Solvent-free Enzyme-catalyzed ROPs.** The first set of reactions aimed to synthesize Novozym 435-catalyzed ε-caprolactone ROPs in ionic liquids to establish feasibility of this protocol. The following ionic liquids were tested with these reactions: [BMIM][PF<sub>6</sub>], [BMIM][BF<sub>4</sub>], and [C<sub>2</sub>OHMIM][BF<sub>4</sub>]. After drying overnight under reduced pressure, the ionic liquid (2 equiv.) was added to a 5 mL round bottom flask. The monomer/ε-caprolactone (1 equiv., 1 mmol) and 15 wt% Novozym 435 were then added. The reaction was heated to 50°C under Ar for 48 h. A minimal volume of toluene was used to transfer the solution to an M fritted filter to isolate the Novozym 435 beads. The filtrate was transferred and toluene extractions were repeated to fully extract the starting material and product from the ionic liquid. The toluene layer was dried under reduced pressure. The Novozym 435 beads were washed 3× with toluene, 3× with hexanes, and dried under reduced pressure for reuse.

*Polycaprolactone in [BMIM][PF<sub>6</sub>].* Yield: 0.11 g, 96.7%; conversion: 94%.

*Polycaprolactone in [BMIM][BF<sub>4</sub>].* Yield: 0.067 g, 58.9%; conversion: 95%.

*Polycaprolactone in [C<sub>2</sub>OHMIM][BF<sub>4</sub>].* Yield: 0.10 g, 88.9%; conversion: 94%.

A similar procedure was used to synthesize a 1:10 ethylene glycol:ε-caprolactone ROP linker. Freeze-dried ethylene glycol (1 equiv., 0.1 mmol) was weighed directly into a 5 mL round bottom flask. [BMIM][BF<sub>4</sub>] (200 μL) was pipetted into the flask, and ε-caprolactone (20 equiv., 2 mmol) and Novozym 435 (15 wt%, 0.0171 g) were added. The reaction was heated to 50°C under Ar for 48 h. Recovery of the enzyme beads and ionic liquid were performed as above, substituting



hexanes for toluene. After isolating the product in hexanes, solvent was removed and the product was recrystallized from methanol (**Fig. S6**).

*Ethylene glycol and  $\epsilon$ -caprolactone CALB ROP (1:10)*. Yield: 0.024 g, 19.9%.  $^1\text{H NMR}$  (300 MHz,  $\text{CDCl}_3$ ):  $\delta$ H 4.06 (t, 20H), 3.65 (t, 4H), 2.31 (t, 20H), 1.65 (m, 40H), 1.40 (m, 20H).

### ***Optimizing Condensation Polymerizations***

#### **Condensation Polymerizations of Modified Hydroxycinnamate Monomers.**

*Sinapinic acid with butanol chain*. The first condensation polymerization was of *tert*-butyl-protected sinapinic acid with a butanol chain extending from the phenol. The starting material was stirred with 40 equiv. of trifluoroacetic acid overnight to deprotect the monomer (*Yield*: 84.1%). The modified sinapinic acid (1 equiv., 3.75 mmol) was dissolved in 10 mL of distilled toluene. A condenser filled with activated 3Å molecular sieves was attached and the reaction was refluxed under argon overnight. The reaction was transferred to a scintillation vial and dried under reduced pressure. Yield: 0.39 g, 41.7%.

*p-Coumaric acid with polylactic acid chain*. The condensation polymerization of *p*-coumaric acid with a polylactic acid chain extending from the phenol followed a similar approach. The monomer (1 equiv., 0.743 mmol) was dissolved in 4 mL of distilled toluene. A condenser filled with activated 3Å molecular sieves was attached and the reaction was refluxed under argon overnight. The reaction was transferred to a scintillation vial and dried under reduced pressure. Yield: 0.48 g, 89.2%.

### Condensation Polymerizations of Hydroxycinnamate Dimers and ROP Products.

Unless otherwise specified, condensation polymerizations were performed by combining the ROP diol (1 equiv., 0.03 mmol) with the hydroxycinnamate dimer (1 equiv., 0.03 mmol) in 2 mL toluene. A condenser filled with activated 3Å molecular sieves was attached and the reaction was refluxed under argon overnight. The reaction was transferred to a scintillation vial and dried under reduced pressure.

The polymerization of sinapyl ester dimer and 1:100 ethylene glycol:DL-lactide ROP (S-100-DL<sup>b</sup>) was modified by eliminating the condenser and adding activated 3Å molecular sieves directly into the reaction flask instead. The hydroxycinnamate dimer and the diol were added at equal equivalents (0.0055 mmol) in 2.5 mL dry toluene and heated to 90°C under argon for 6 h.

Additionally, after synthesizing a condensation polymer of ferulyl ether dimer and 1:50 ethylene glycol:DL-lactide ROP using the previously described approach, it was also synthesized using an acid chloride-facilitated polymerization (F-50-DL<sup>a</sup>). After optimization, the ferulyl ether dimer (1 equiv., 0.012 mmol), excess thionyl chloride (20 equiv., 0.23 mmol), and a catalytic amount of DMF were refluxed for 6 h and freeze-dried on the Schlenk line. The crude product was re-suspended in 3 mL dry DCM and added dropwise to a solution of 1:50 ethylene glycol:DL lactide ROP (1 equiv., 0.012 mmol, 0.0863 g) and triethylamine (2.4 equiv., 0.028 mmol, 3.85 µL) in an ice bath. The reaction stirred under Ar overnight, warming from 0°C to room temperature. After approximately 16 h, the reaction was concentrated under reduced pressure, precipitated into ether, and dried under vacuum. Yields are listed in **Table 3.2**.

### 3.5 Appendix B

**Table S3.1.** Yields of tin-catalyzed ROPs of hydroxycinnamate monomers with lactones.

Hydroxycinnamate	Lactone	H:L Ratio	Yield
<i>p</i> -Coumaric acid	L-lactide	1:1	94.8%, 0.13 g
		1:10	93.5%, 0.61 g
	Glycolide	1:1	94.7%, 0.11 g
		1:10	93.1%, 0.66 g
Ferulic acid	L-lactide	1:1	89.6%, 0.14 g
	Glycolide	1:1	99.1%, 0.68 g
		1:10	99.0%, 0.15 g

#### MALDI-TOF Spectra

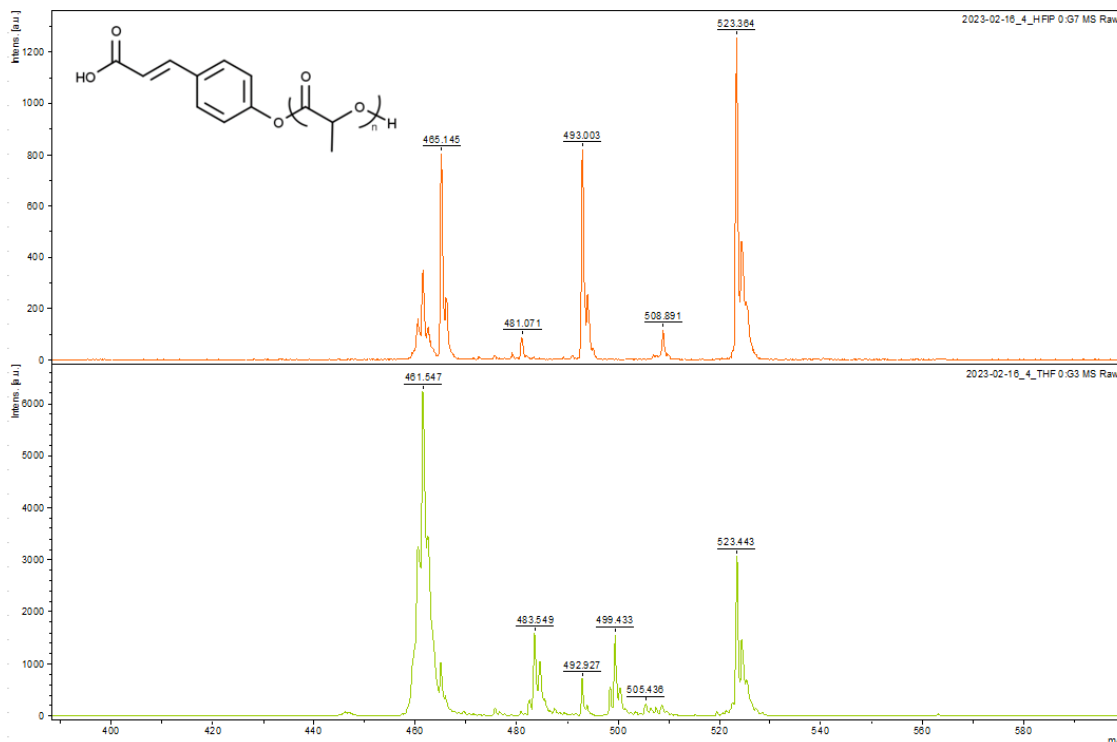


**Figure S3.1.** MALDI-TOF spectra of 1:1 *p*-coumaric acid:L-lactide in HFIP (*top*) and THF (*bottom*).

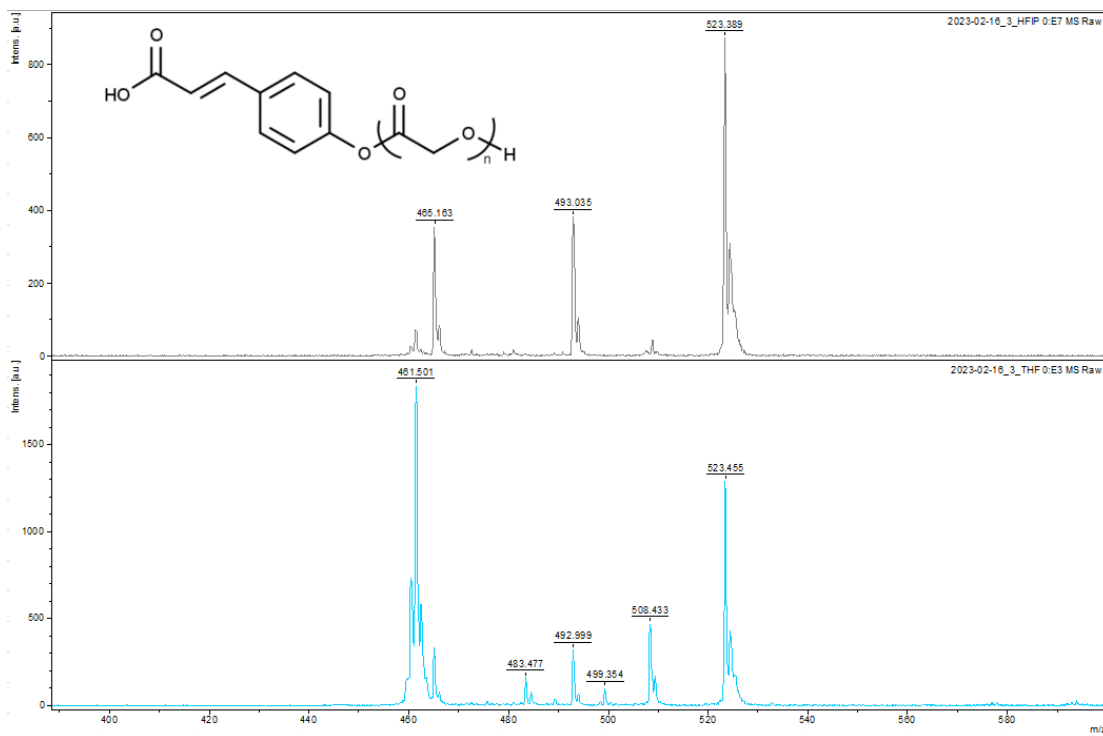


**Figure S3.2.** MALDI-TOF spectra of 1:1 *p*-coumaric acid:glycolide in HFIP (*top*) and THF (*bottom*).

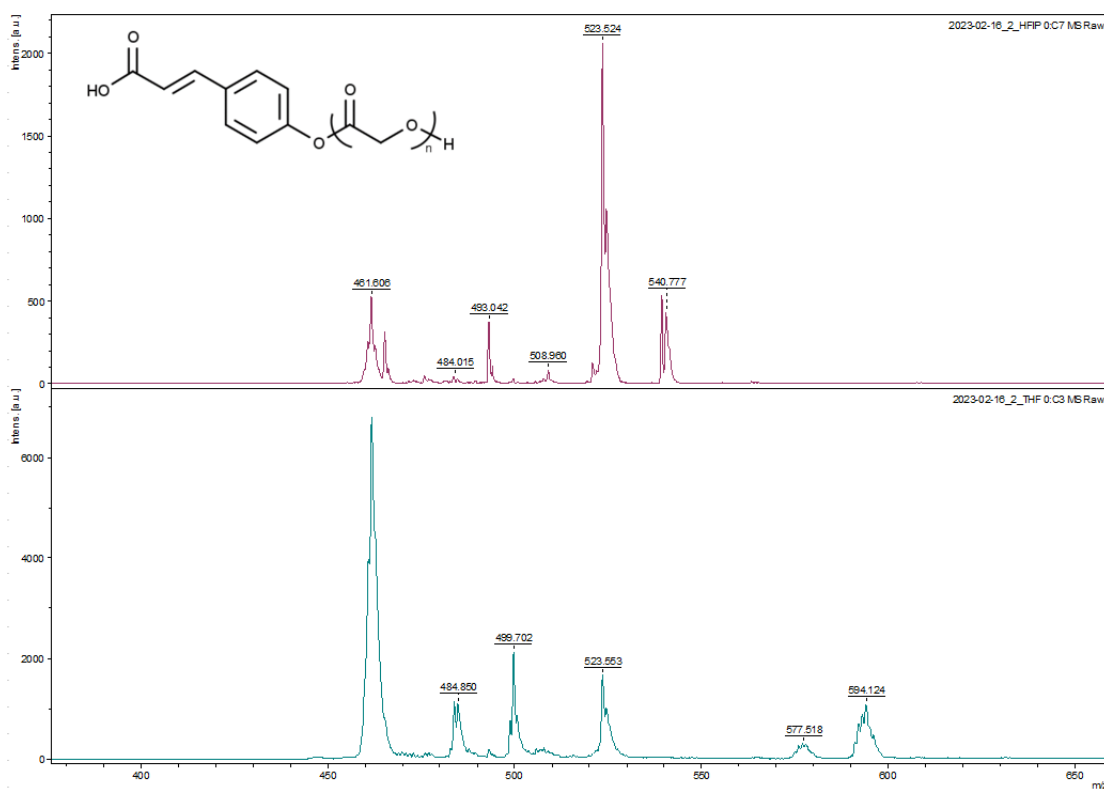


**Figure S3.3.** MALDI-TOF spectra of 1:10 *p*-coumaric acid:glycolide in HFIP (*top*) and THF (*bottom*).

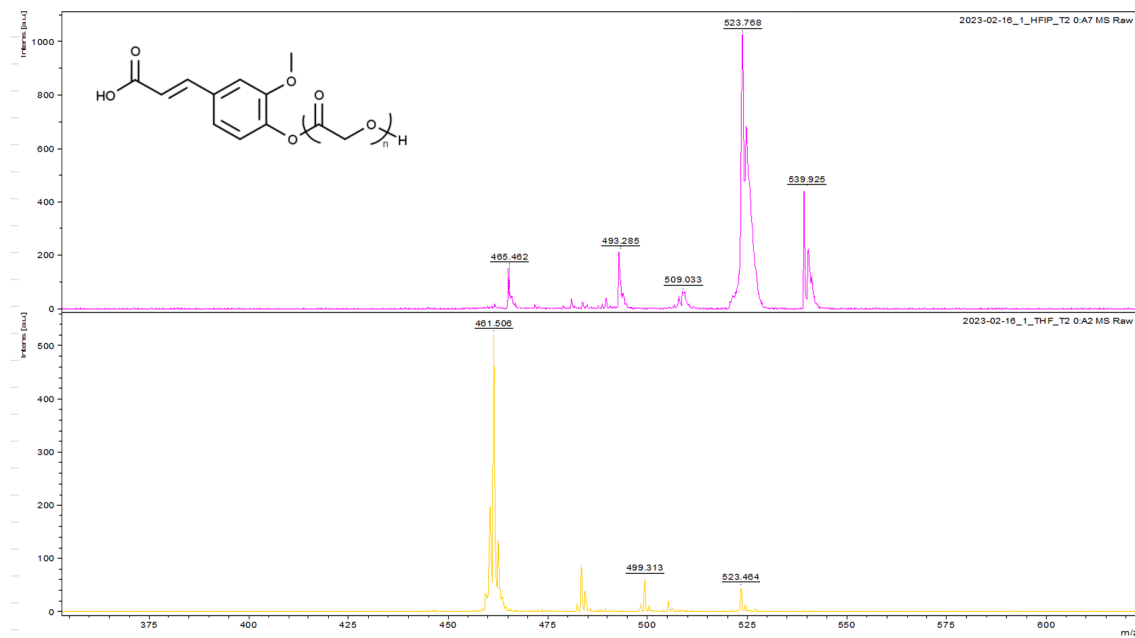


**Figure S3.4.** MALDI-TOF spectra of 1:10 ferulic acid:glycolide in HFIP (*top*) and THF (*bottom*).

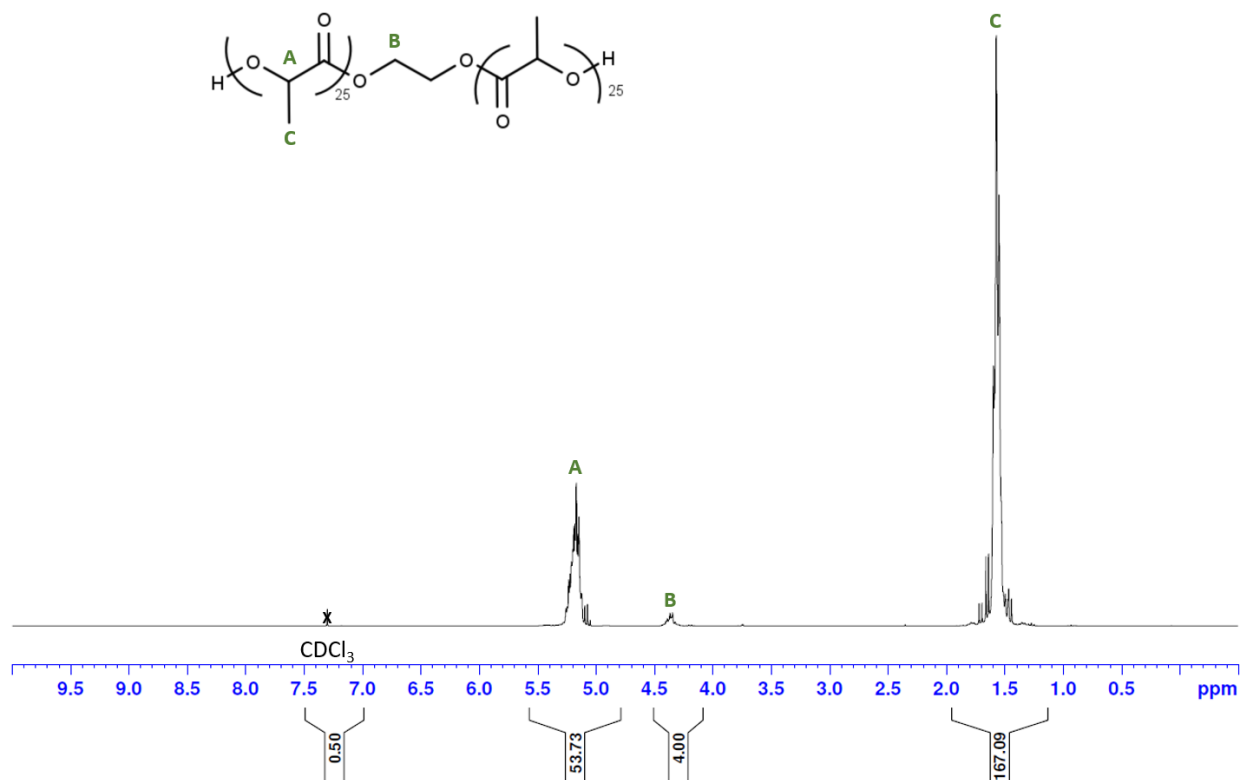


**Figure S3.5.** Example <sup>1</sup>H NMR of diol linker synthesized via Sn(Oct)<sub>2</sub> and ethylene glycol-initiated ring-opening polymerization of DL-lactide (here, a 1:25 ethylene glycol:DL-lactide ratio), in CDCl<sub>3</sub>.

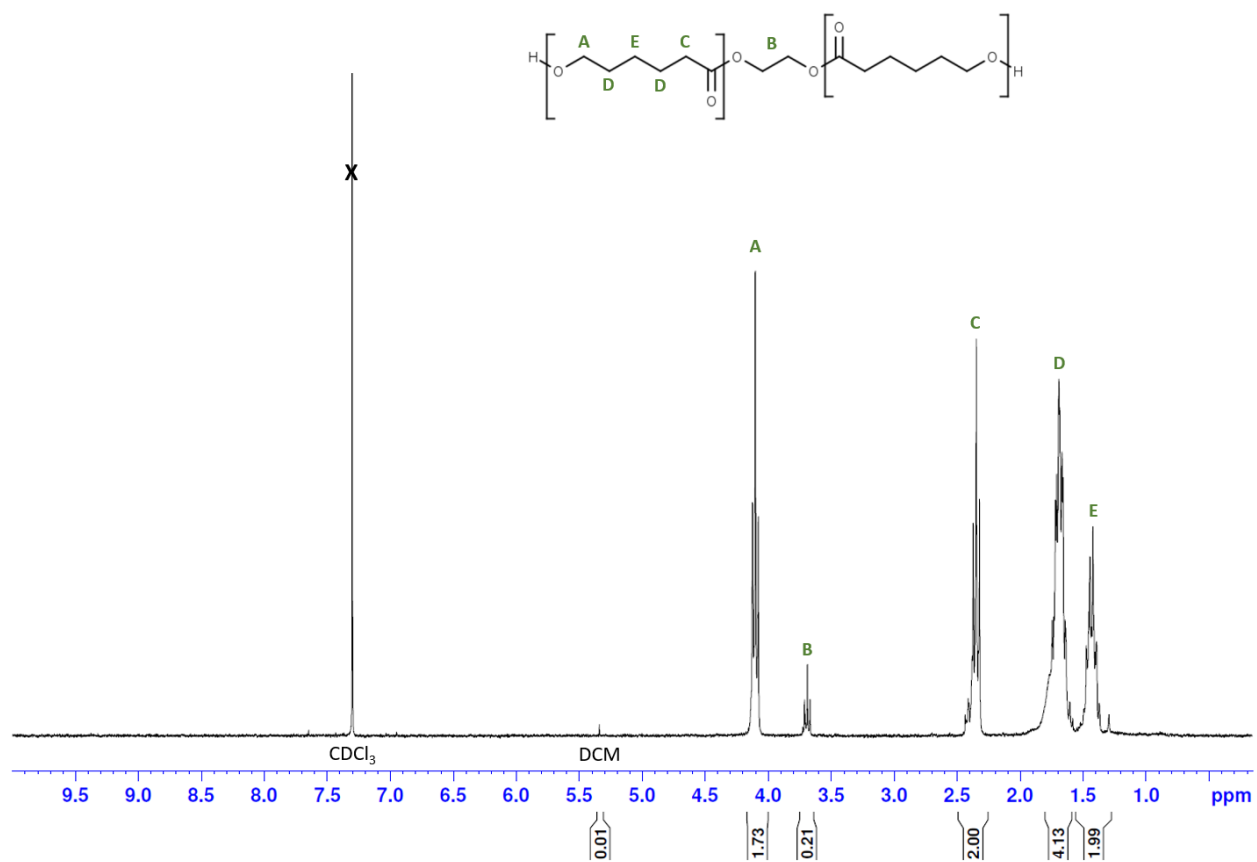


**Figure S3.6.**  $^1\text{H}$  NMR of enzyme-catalyzed diol linker synthesized via 1:10 ethylene glycol: $\epsilon$ -caprolactone ring-opening polymerization, in  $\text{CDCl}_3$ .

### 3.6 References

- [1] Plastics Europe, “Plastics - the Facts 2020,” 2020.
- [2] H. Ritchie, V. Samborska, and M. Roser, “Global plastics production [dataset],” in *Plastic Pollution*, Data adapted from Geyer et al., “Production, use, and fate of all plastics ever made”; OECD, “Global Plastics Outlook - Plastics use by application,” 2023.
- [3] U.S. Energy Information Administration, “Petroleum Supply Annual, August 2023,” 2023.
- [4] W. E. Forum, “The new plastics economy: Rethinking the future of plastics,” 2016.
- [5] L. Mialon, A. G. Pemba, and S. A. Miller, “Biorenewable polyethylene terephthalate mimics derived from lignin and acetic acid,” *Green Chem.*, vol. 12, no. 10, pp. 1704–1706, 2010.
- [6] L. Mialon, R. Vanderhenst, A. G. Pemba, *et al.*, “Polyalkylenehydroxybenzoates (PAHBs): Biorenewable aromatic/aliphatic polyesters from lignin,” *Macromol. Rapid Commun.*, vol. 32, no. 17, pp. 1386–1392, 2011.
- [7] A. Díaz, R. Katsarava, and J. Puiggali, “Synthesis, properties and applications of biodegradable polymers derived from diols and dicarboxylic acids: From polyesters to poly(ester amide)s,” *Int. J. Mol. Sci.*, vol. 15, no. 5, pp. 7064–7123, 2014.
- [8] A. Gandini, T. M. Lacerda, A. J. F. Carvalho, *et al.*, “Progress of polymers from renewable resources: Furans, vegetable oils, and polysaccharides,” *Chem. Rev.*, vol. 116, no. 3, pp. 1637–1669, 2016.

- [9] M. A. Hillmyer and W. B. Tolman, "Aliphatic polyester block polymers: Renewable, degradable, and sustainable," *Acc. Chem. Res.*, vol. 47, no. 8, pp. 2390–2396, 2014.
- [10] S. S. Kuhire, C. V. Avadhani, and P. P. Wadgaonkar, "New poly(ether urethane)s based on lignin derived aromatic chemicals via A-B monomer approach: Synthesis and characterization," *Eur. Polym. J.*, vol. 71, pp. 547–557, 2015.
- [11] A. Llevot, E. Grau, S. Carlotti, *et al.*, "Renewable (semi)aromatic polyesters from symmetrical vanillin-based dimers," *Polym. Chem.*, vol. 6, no. 33, pp. 6058–6066, 2015.
- [12] F. Pion, P.-H. Ducrot, and F. Allais, "Renewable alternating aliphatic–aromatic copolyesters derived from biobased ferulic acid, diols, and diacids: Sustainable polymers with tunable thermal properties," *Macromol. Chem. Phys.*, vol. 215, no. 5, pp. 431–439, 2014.
- [13] M. Z. Oulame, F. Pion, S. Allauddin, *et al.*, "Renewable alternating aliphatic-aromatic poly(ester-urethane)s prepared from ferulic acid and bio-based diols," *Eur. Polym. J.*, vol. 63, pp. 186–193, 2015.
- [14] M. R. Ridho, E. A. Agustiany, M. R. Dn, *et al.*, "Lignin as green filler in polymer composites: Development methods, characteristics, and potential applications," *Adv. Wood Compos.*, pp. 1–33, 2022.
- [15] C. Zhang, H. Wu, and M. R. Kessler, "High bio-content polyurethane composites with urethane modified lignin as filler," *Polymer (Guildf)*, vol. 69, pp. 52–57, 2015.
- [16] N. A. Mohamad Aini, N. Othman, M. H. Hussin, *et al.*, "Lignin as alternative reinforcing filler in the rubber industry: A review," *Front. Mater.*, vol. 6, p. 329, 2020.



- [17] O. Gordobil, R. Delucis, I. Egüés, *et al.*, “Kraft lignin as filler in PLA to improve ductility and thermal properties,” *Ind. Crops Prod.*, vol. 72, pp. 46–53, 2015.
- [18] J.-G. Rosenboom, R. Langer, and G. Traverso, “Bioplastics for a circular economy,” *Springer Nat.*, vol. 7, no. 2, pp. 117–137, 2022.
- [19] M. Alewijn, B. A. Smit, E. L. Sliwinski, *et al.*, “The formation mechanism of lactones in Gouda cheese,” *Int. Dairy J.*, vol. 17, no. 1, pp. 59–66, 2007.
- [20] S. K. Sartori, M. A. N. Diaz, and G. Diaz-Muñoz, “Lactones: Classification, synthesis, biological activities, and industrial applications,” *Tetrahedron*, vol. 84, p. 132001, 2021.
- [21] M. Chadwick, H. Trewin, F. Gawthrop, *et al.*, “Sesquiterpenoids lactones: Benefits to plants and people,” *Int. J. Mol. Sci.*, vol. 14, no. 6, pp. 12780–12805, 2013.
- [22] M. A. M. El Hadi, F.-J. Zhang, F.-F. Wu, *et al.*, “Advances in fruit aroma volatile research,” *Molecules*, vol. 18, no. 7, pp. 8200–8229, 2013.
- [23] B. M. Schneider, “Flavor compounds found in barrel aged beers,” in *Chemistry of Alcoholic Beverages*, American Chemical Society, 2023, pp. 159–172.
- [24] W.-S. Chen, D. P. B. T. B. Strik, C. J. N. Buisman, *et al.*, “Production of caproic acid from mixed organic waste: An environmental life cycle perspective,” *Environ. Sci. Technol.*, vol. 51, no. 12, pp. 7159–7168, 2017.
- [25] FDA, “Subchapter B - Food for human consumption; Part 175 -- Indirect food additives: Adhesives and components of coatings,” in *Code of Federal Regulations Title 21*, 2023, p. 21CFR175.300.
- [26] W. Rao, C. Cai, J. Tang, *et al.*, “Coordination insertion mechanism of ring-opening

- polymerization of lactide catalyzed by stannous octoate,” *Chinese J. Chem.*, vol. 39, no. 7, pp. 1965–1974, 2021.
- [27] H. R. Kricheldorf and S. M. Weidner, “About the influence of salicylic acid on tin(II)octanoate-catalyzed ring-opening polymerization of l-lactide,” *Eur. Polym. J.*, vol. 119, pp. 37–44, 2019.
- [28] M. Sobczak, “Ring-opening polymerization of cyclic esters in the presence of choline/SnOct<sub>2</sub> catalytic system,” *Polym. Bull.*, vol. 68, pp. 2219–2228, 2012.
- [29] V. Hevilla, A. Sonseca, C. Echeverría, *et al.*, “Enzymatic synthesis of polyesters and their bioapplications: Recent advances and perspectives,” *Macromol. Biosci.*, vol. 21, no. 10, p. 2100156, 2021.
- [30] R. Marcilla, M. De Geus, D. Mecerreyes, *et al.*, “Enzymatic polyester synthesis in ionic liquids,” *Eur. Polym. J.*, vol. 42, no. 6, pp. 1215–1221, 2006.
- [31] C. I. Gkountela and S. N. Vouyiouka, “Enzymatic polymerization as a green approach to synthesizing bio-based polyesters,” *Macromol*, vol. 2, no. 1, pp. 30–57, 2022.
- [32] C. Ortiz, M. L. Ferreira, O. Barbosa, *et al.*, “Novozym 435: the ‘perfect’ lipase immobilized biocatalyst?,” *Catal. Sci. Technol.*, vol. 9, no. 10, pp. 2380–2420, 2019.
- [33] R. A. Sheldon and D. Brady, “Green chemistry, biocatalysis, and the chemical industry of the future,” *ChemSusChem*, vol. 15, no. 9, p. e202102628, 2022.
- [34] H. Uyama and S. Takamoto, Tetsufumi Kobayashi, “Enzymatic synthesis of polyesters in ionic liquids,” *Polym. J.*, vol. 34, no. 2, pp. 94–96, 2002.
- [35] Z. He and P. Alexandridis, “Nanoparticles in ionic liquids: Interactions and organization,”

- Phys. Chem. Chem. Phys.*, vol. 17, no. 28, pp. 18238–18261, 2015.
- [36] P. A. Thomas and B. B. Marvey, “Room temperature ionic liquids as green solvent alternatives in the metathesis of oleochemical feedstocks,” *Molecules*, vol. 21, no. 2, p. 184, 2016.
- [37] X. Liu, F. P. Bouxin, J. Fan, *et al.*, “Recent advances in the catalytic depolymerization of lignin towards phenolic chemicals: A review,” *ChemSusChem*, vol. 13, no. 17, pp. 4296–4317, 2020.
- [38] J. Gorke, F. Srienc, and R. Kazlauskas, “Toward advanced ionic liquids: Polar, enzyme-friendly solvents for biocatalysis,” *Biotechnol. Bioprocess Eng.*, vol. 15, pp. 40–53, 2010.
- [39] T. Itoh, “Enzymatic reactions using ionic liquids for green sustainable chemical process; Stabilization and activation of lipases,” *Chem. Rec.*, vol. 23, no. 8, p. e202200275, 2023.
- [40] Y. Yang, Y. Yu, Y. Zhang, *et al.*, “Lipase/esterase-catalyzed ring-opening polymerization: A green polyester synthesis technique,” *Process Biochem.*, vol. 46, no. 10, pp. 1900–1908, 2011.
- [41] Z. Jiang, “Lipase-catalyzed synthesis of poly (amine-co-esters) via copolymerization of diester with amino-substituted diol,” *Biomacromolecules*, vol. 11, no. 4, pp. 1089–1093, 2010.
- [42] C. Vafiadi, E. Topakas, V. R. Nahmias, *et al.*, “Feruloyl esterase-catalysed synthesis of glycerol sinapate using ionic liquids mixtures,” *J. Biotechnol.*, vol. 139, no. 1, pp. 124–129, 2009.
- [43] J. Engel, A. Cordellier, L. Huang, *et al.*, “Enzymatic ring-opening polymerization of

- lactones: Traditional approaches and alternative strategies,” *ChemCatChem*, vol. 11, no. 20, pp. 4983–4997, 2019.
- [44] B. M. Upton and A. M. Kasko, “Biodegradable aromatic–aliphatic poly(ester–amides) from monolignol-based ester dimers,” *ACS Sustain. Chem. Eng.*, vol. 6, pp. 3659–3668, 2018.
- [45] B. M. Upton and A. M. Kasko, “Biomass-derived poly(ether–amide)s incorporating hydroxycinnamates,” *Biomacromolecules*, vol. 20, no. 2, pp. 758–766, 2019.
- [46] H. Ritchie, V. Samborska, and M. Roser, “Data Page: Global plastics production,” in *Plastic Pollution*, 2023.

## CHAPTER 4: Nontoxic hydrogels initiated by bioinspired polymers

Adapted with permission from:

Pumford, E.A.\* , Jackson Hoffman\* , B.A., Kasko, A.M. (2024) Nontoxic initiator alternatives to TEMED for redox hydrogel polymerization. *ACS Applied BioMaterials*, 7(4), 2264-71.

\*These authors contributed equally; Copyright 2024 American Chemical Society.

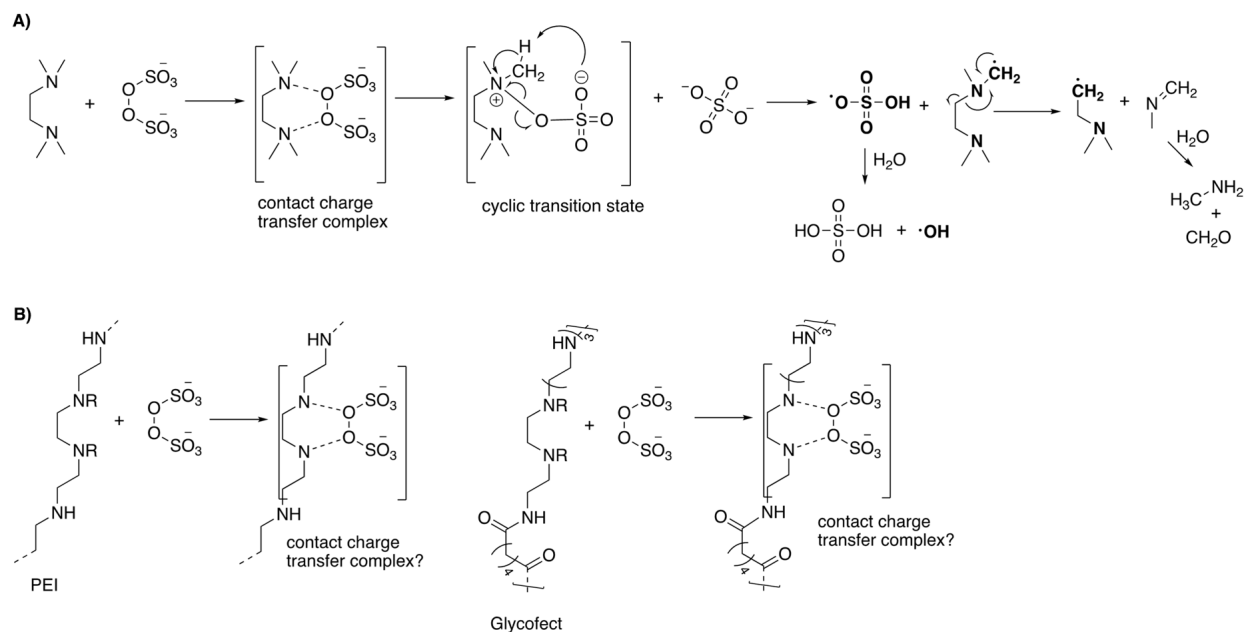
### 4.1 Introduction

Hydrogels are 3D crosslinked polymer networks, with a unique ability to swell in water while retaining their shape. Drawing inspiration from the extracellular matrix, hydrogels can mimic its structure and function, offering a biomimetic platform for various biomedical applications [1]. Due to their tunable mechanical properties, potential for controlled release of loaded compounds, and ability to maintain a moist environment, they are well-suited for wound dressing applications [2], [3]. Hydrogel crosslinking can be photo-initiated or chemically induced. For *in situ* hydrogel wound dressing fabrication, particularly in remote or low-resource environments, photo-initiated crosslinking is impractical. As such, chemically initiated redox initiation is the preferred approach for *in situ* hydrogel crosslinking.

However, a significant and often overlooked problem emerges with many of these chemically crosslinked hydrogel wound dressings: their toxicity. A common redox initiation system uses ammonium persulfate (APS) and tetramethylethylenediamine (TEMED), which affords rapid gelation to a wide range of polymer systems [4], [5], [6], [7]. Unfortunately, TEMED is cytotoxic, and cells exposed to TEMED demonstrated significantly reduced viability [4], [8]. The cytotoxicity of this common hydrogel crosslinking system introduces an inherent limitation

for wound dressing applications, as the hydrogel would be in direct contact with cells in an inflammatory state. The present work aims to overcome this limitation by replacing TEMED with a more biocompatible initiator, to be used with APS.

TEMED reacts with APS to initiate radical formation through a redox process. This occurs due to TEMED's bidentate nitrogen structure, which forms a charge-transfer complex with APS, creating stable sulfate and nitrogen-based radicals [9], [10]. According to this mechanism, amine-containing monomers and polymers can potentially form a charge-transfer complex and cyclic transition state if their nitrogen spacing resembles that of TEMED. For instance, poly(ethylene imine) (PEI) and Glycofect™ contain nitrogen repeat groups, separated by an ethylene unit, suggesting that they may be able to generate the stable radicals necessary to crosslink the diacrylate chains and form a hydrogel (**Scheme 4.1**).



**Scheme 4.1.** Charge-transfer complex and radical formation from a) APS and TEMED and b) APS and PEI or Glycofect [11].

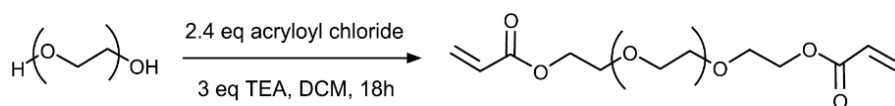
Knowing this proposed mechanism of initiation, we looked to nature to draw inspiration for amine-containing compounds that may react with APS to initiate hydrogel crosslinking, while providing improved biocompatibility. We screened a range of amine-based alternatives: chitosan, glucosamine, glycine, polylysine, PEI, and Glycofect™. All compounds other than PEI and Glycofect™ are sourced from nature, while the latter can be considered bioinspired. PEI is loosely based on spermiine, which plays a key role in metabolic functions, while Glycofect™ is a poly(glycoamidoamine), which draws inspiration from natural carbohydrates. These candidates were used with APS and poly(ethylene glycol)-diacrylate (PEGDA) and screened via rheological testing to determine the gel point and storage and loss moduli of the resultant hydrogels. Those that had reasonable gelation and comparable mechanical properties to the TEMED controls were selected to move forward with further testing. Mechanical properties were thoroughly characterized using mass swelling ratios and dynamic mechanical analysis, through which the degree of polymerization was estimated. Cytotoxicity was then quantified using metabolic assays and live/dead staining of 3T3 fibroblasts both in direct contact with hydrogels and exposed to hydrogel supernatant.

This work holds significant implications for advancing hydrogel design principles and expanding the repertoire of bio-based initiators for hydrogels for biomedical applications. Through rigorous testing, viable non-toxic alternatives to TEMED for hydrogel crosslinking were identified. Hydrogels using these alternative initiation systems were compatible with APS, exhibited comparable (and tunable) mechanical properties, and displayed significantly improved cytocompatibility compared to the TEMED “gold standard”. This has great potential for enhanced biocompatibility and functionality in hydrogel-based biomaterials, particularly for wound dressing applications.

*Note:* After rheological characterization (and with the exception of supernatant studies, which were performed solely by her), all parts of this work were performed in direct collaboration with Dr. Brooke Ann Jackson Hoffman.

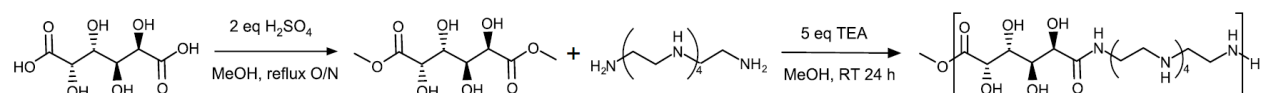
## 4.2 Results and Discussion

**Polymer synthesis.** Polyethylene glycol diacrylate (PEGDA) is used in this work as the crosslinkable polymer for hydrogel fabrication. PEGDA 3350 was synthesized with high purity and yield, and evaluated via  $^1\text{H}$  NMR to confirm an acrylation of at least 75% on each batch (**Scheme 4.2, Figure S4.1**).



**Scheme 4.2.** Synthesis of polyethylene glycol diacrylate (PEGDA).

Glycofect<sup>TM</sup> was synthesized according to previous work by the Reineke group, with a modified work-up (precipitating into ether instead of dialyzing) (**Scheme 4.3, Figure S4.2**). Through this change, yield was increased from 35% to 69%.



**Scheme 4.3.** Synthesis of dimethyl meso-galactarate and Glycofect<sup>TM</sup>.

**Initiator/reagent characterization.** The initiator system candidates we screened were prepared based on a control TEMED gel (41 mM, 1 NR<sub>x</sub>). This control concentration was determined by averaging previously reported TEMED concentrations in literature [12], [13], [14], [15], [16], [17], [18]. The concentration of APS was kept constant at 25 mM in all conditions. Since each TEMED molecule contains two amine groups, the TEMED 1 NR<sub>x</sub> control gel,



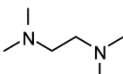
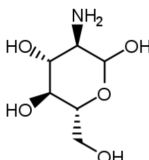
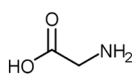
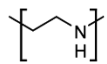
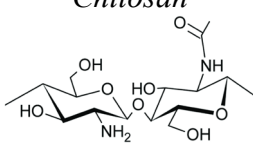
containing 41 mM TEMED, effectively contains twice the amount of amine groups (82 mM). Other TEMED controls were fabricated with respect to this number, with TEMED 0.5 NR<sub>x</sub> displaying half the amount of amines (41 mM), and TEMED 2 NR<sub>x</sub> displaying twice the amount of amines (164 mM).

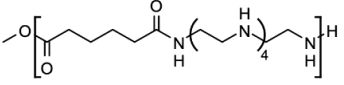
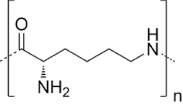
This principle extends to polymers, which may contain significantly higher numbers of amine groups per molecule, depending on the number of repeat units per polymer. Using the amine concentration of 82 mM in the TEMED 1 NR<sub>x</sub> hydrogel, we calculated the amount of amine-based polymer required to match the number of amine groups present in the TEMED 1 NR<sub>x</sub> control. Similarly, the amount of each amine-based compound was calculated for 0.5, 1, 2, and 10 NR<sub>x</sub>. **Table 4.1** displays the structure of each alternative initiator candidate, amount of amines for each amine ratio, and the mass or volume required for a 1 mL hydrogel.

**Hydrogel fabrication.** Control hydrogels were fabricated using 10 wt% PEGDA, 41 mM TEMED, and 25 mM APS. The pre-gel solution was transferred to the casting set-up, and after gelation, which was approximately 2.5 min, hydrogel sample discs were obtained using a sterile biopsy punch. Unless otherwise specified, hydrogel sample discs had a height of 2 mm and diameter of 6 mm. The hydrogel casting and sample discs are shown in **Figure S4.3**.

For experimental non-toxic hydrogels, TEMED was replaced with amine-containing monomers or polymers. The amine-containing compounds screened in this work include: glucosamine, glycine, PEI, chitosan, Glycofect<sup>TM</sup>, and polylysine. Each alternative amine-based initiator was dissolved in DI H<sub>2</sub>O overnight at the concentrations described in **Table 4.1**. PEGDA 3350 (10 wt%), the amine-based initiator, and 25 mM APS were rapidly mixed and cast and punched as described.

**Table 4.1.** Alternative initiator amine ratios (NR<sub>x</sub>) and amount required per hydrogel for all candidates tested via rheology.

Amine-Based Initiator	Amine Ratio (NR <sub>x</sub> )	mmol Amines	Amount per 1 mL Hydrogel
<p><i>TEMED</i></p> 	0.5	41	3.1 μL
	1	82	6.2 μL
	2	164	12.4 μL
	10	820	61.8 μL
<p><i>Glucosamine</i></p> 	1	82	0.0177 g
	2	164	0.0354 g
	10	820	0.1768 g
	20	1640	0.3536 g
<p><i>Glycine</i></p> 	1	82	0.0062 g
	2	164	0.0123 g
	10	820	0.0616 g
<p><i>PEI</i></p> 	0.5	41	0.0018 g
	0.667	54.667	0.0024 g
	1	82	0.0036 g
	2	164	0.0073 g
	10	820	0.0363 g
<p><i>Chitosan</i></p> 	20	1640	0.0726 g
	1	82	0.0149 g
	2	164	0.0299 g
	10	820	0.1494 g
<p><i>Glycofect</i></p>	0.5	41	0.0027 g
	1	82	0.0053 g

	2	164	0.0107 g
	10	820	0.0534 g
<i>Polylysine</i>	1	82	0.0050 g
	2	164	0.0101 g

**Rheological characterization to identify initiator candidates.** Hydrogel pre-gel solutions were pipetted directly onto the measuring plate of the rheometer. A time sweep oscillatory test was used to determine storage ( $G'$ ) and loss moduli ( $G''$ ). Complete rheological curves are shown in **Figures S4.4-S4.10**. ‘Gel point’ was identified by the crossover point of  $G'$  and  $G''$ , and elastic modulus was calculating using  $G'$  [19]. The gel point and the amplitude of  $G'$  were used to determine the best initiator candidates to move forward with testing (**Table 4.2**).

For all gels, as the  $NR_x$  increased, gel point occurred sooner. In addition to defining gelation time,  $G'$  and  $G''$  provide insight into hydrogels’ viscoelastic behavior. After the sol-gel transition, the storage modulus plateaus to a maximum value, reflective of the hydrogel’s ability to elastically store energy. Importantly, this is related to hydrogel stiffness and the strength of the crosslinked network [20]. We found that increasing  $NR_x$  of the initiators affected the maximum storage modulus. Glycofect™ 0.5-2  $NR_x$  had storage moduli of 7.73-8.39 kPa, which was most comparable to that of the TEMED 1  $NR_x$  hydrogels, at 9.77 kPa. While PEI 0.5  $NR_x$  hydrogels exhibited a slightly lower  $G'$  of 4.16 kPa, it remained on the same order of magnitude as the TEMED controls.

To balance desirable gelation times with mechanical properties, initiators that resulted in gel points of <12 min and maximum storage moduli of >300 Pa were selected as candidates for further testing. Pre-gel solutions using APS with glucosamine, glycine, PEI 1  $NR_x$  and PEI 2  $NR_x$ ,

**Table 4.2.** Rheological data of hydrogels fabricated using amine-based initiators at various amine ratios (NR<sub>x</sub>).

<b>Amine-Based Initiator</b>	<b>NR<sub>x</sub></b>	<b>Gel Point (min)</b>	<b>Maximum Storage Modulus (Pa)</b>	<b>Maximum Loss Modulus (Pa)</b>
<i>TEMED</i>	1	0.82	$9.77 \times 10^3$	14.1
<i>Glucosamine</i>	1	–	1.10	0.76
	2	–	0.88	0.60
	10	–	2.09	0.34
	20	12.0	$1.54 \times 10^2$	56.6
<i>Glycine</i>	1	–	0.32	0.56
	2	–	$3.00 \times 10^{-5}$	0.60
	10	–	0.34	0.47
<i>PEI</i>	0.5	4.59	$4.16 \times 10^3$	6.60
	0.667	4.98	$4.49 \times 10^2$	1.32
	1	–	0.58	0.23
	2	–	0.86	0.49
	10*	2.06	$1.50 \times 10^3$	41.9
	20*	0.09	$2.26 \times 10^3$	40.0
<i>Chitosan</i>	1	–	1.72	1.92
	2	–	1.42	0.48
	10	–	0.21	0.43
<i>Glycofect</i>	0.5	10.7	$8.39 \times 10^3$	8.32
	1	7.18	$8.20 \times 10^3$	10.9
	2	5.59	$7.73 \times 10^3$	11.6
	10	3.79	$3.02 \times 10^2$	4.30
<i>Polylysine</i>	1	–	0.59	0.25
	2	–	0.30	0.48

\*PEI 10 NR<sub>x</sub> and 20 NR<sub>x</sub> were not selected as potential candidates to further investigate, because 10 min and 4 min, respectively, after the storage modulus peaked, it then decreased to again cross over with the loss modulus.

chitosan, and polylysine did not meet these criteria. The initiator candidates selected for future testing were: PEI at 0.5 and 0.667 NR<sub>x</sub>, Glycofect™ at 0.5, 1, and 2, and 10 NR<sub>x</sub>, with TEMED at 0.5, 1, 2, and 10 NR<sub>x</sub> for comparison. The shortest gel times were obtained following initiation with PEI 0.5 and 0.667 NR<sub>x</sub> and Glycofect™ 2 and 10 NR<sub>x</sub>, and Glycofect™ 0.5 to 2 NR<sub>x</sub>-initiated gels resulted in gels with storage moduli most similar to the TEMED controls.

**Mechanical properties of hydrogels.** The effect of the amine ratio for each initiator on elastic modulus of the resultant hydrogels is shown in **Figure 4.1**. In general, an increase in the amine ratio correlates with a decrease in elastic modulus. This indicates that gels become softer and less stiff as the amine ratio increases.

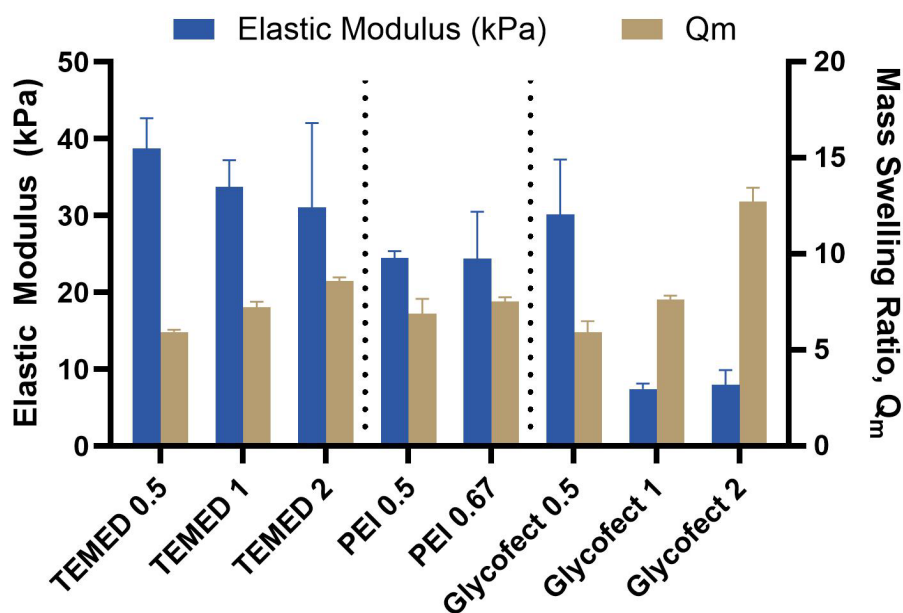


**Figure 4.1.** Hydrogel mass swelling ratio increases and elastic modulus decreases as a function of amine ratio.

There are no significant differences between TEMED trials, with the elastic modulus of TEMED 1 NR<sub>x</sub> control hydrogels at  $33.7 \pm 3.49$  kPa. However, the modulus linearly decreases from  $38.8 \pm 3.88$  kPa to  $30.5 \pm 9.02$  kPa as the NR<sub>x</sub> increases from 0.5 to 2. Glycofect™ 0.5 NR<sub>x</sub>

exhibited a modulus comparable to the TEMED 1 NR<sub>x</sub> control ( $30.3 \pm 7.12$  kPa). Glycofect™ 1 NR<sub>x</sub> and 2 NR<sub>x</sub> had significantly lower elastic moduli than the control, at  $7.42 \pm 0.74$  kPa and  $7.97 \pm 1.94$  kPa, respectively. Similarly, the elastic modulus of PEI 0.5 NR<sub>x</sub> hydrogels was significantly lower than the control, measuring at  $24.5 \pm 0.92$  kPa. The modulus of the PEI 0.667 NR<sub>x</sub> hydrogels were very similar ( $24.4 \pm 6.12$  kPa), but the large standard deviation rendered these differences insignificant.

As anticipated, the mass swelling ratios of the hydrogels exhibit inverse trends compared to their elastic modulus (**Fig. 4.1**). For each initiator, mass swelling ratio increases as the amine ratio increases. This indicates that a looser hydrogel mesh is forming, allowing for greater water infiltration and swelling of the gel.

In the TEMED hydrogel trials, as the NR<sub>x</sub> increases from 0.5 to 2, the mass swelling ratio significantly increases—from  $5.95 \pm 0.11$  to  $8.60 \pm 0.20$ . Similarly for Glycofect™, the mass swelling ratio significantly increases from  $5.92 \pm 0.31$  to  $12.7 \pm 0.14$  as the NR<sub>x</sub> increases. Due to the similar amine ratios of PEI 0.5 and 0.667 NR<sub>x</sub>, the mass swelling ratio experiences only a slight increase, from  $7.02 \pm 0.66$  to  $7.35 \pm 0.30$ , as the amine ratio increases.

The mass swelling ratios were used to calculate the volumetric swelling ratios (*Equation 2*). By applying Flory-Rehner theory, the mesh size and crosslink density for each initiator group were determined (*Appendix C—Calculating volumetric swelling ratio, degree of crosslinking, and mesh size, Table 4.3*). Across all initiators tested, mesh size increases proportionally with amine ratio, while crosslink density exhibits the inverse trend, indicating fewer crosslinks along each polymer chain. Taken together, these findings suggest that mesh size, and consequently exudate uptake or therapeutic agent release, can be adjusted by varying the amine ratio of initiator incorporated into the hydrogel.

**Table 4.3.** Hydrogel mesh size and crosslink density, calculated via Flory-Rehner equation.

Initiator	Amine Ratio (NR <sub>x</sub> )	Volumetric Swelling Ratio	Mesh Size (Å)	Crosslink Density (mol/cm <sup>3</sup> )
<i>TEMED</i>	0.5	7.0 ± 0.13	42 ± 0.54	10 ± 0.13 x10 <sup>-4</sup>
	1	8.5 ± 0.38	48 ± 1.2	9.2 ± 0.20 x10 <sup>-4</sup>
	2	10 ± 0.24	53 ± 0.62	8.6 ± 0.07 x10 <sup>-4</sup>
<i>PEI</i>	0.5	8.1 ± 0.95	47 ± 3.2	9.5 ± 0.56 x10 <sup>-4</sup>
	0.67	8.9 ± 0.27	50 ± 0.82	9.1 ± 0.12 x10 <sup>-4</sup>
<i>Glycofect</i>	0.5	7.0 ± 0.71	42 ± 3.0	11 ± 0.74 x10 <sup>-4</sup>
	1	9.1 ± 0.23	50 ± 0.71	9.0 ± 0.10 x10 <sup>-4</sup>
	2	15 ± 0.89	64 ± 1.6	7.8 ± 0.080 x10 <sup>-4</sup>

**2D Toxicity Studies.** Biocompatibility (via cell viability) of the hydrogels was determined using a fluorescence-based resazurin metabolic assay and live/dead staining. Dr. Brooke Jackson Hoffman conducted preliminary toxicity studies by exposing 3T3 fibroblasts to varied dilutions of hydrogel supernatant, with all PEI and Glycofect<sup>TM</sup> concentrations outperforming the TEMED “gold standard”.

Alongside Dr. BJ-H, direct-contact viability testing was then performed. Hydrogels were placed directly on top of a confluent layer of adhered 3T3s for 2.5 h, after which the hydrogels and media were replaced with a 10% resazurin solution or live/dead staining solution and imaged to assess cell viability. The metabolic assay results showed very low levels of viability following exposure to all TEMED hydrogels (<10%) (**Figure 4.2**). Viability significantly improved for PEI and Glycofect<sup>TM</sup> hydrogel-exposed cells relative to the TEMED 1 NR<sub>x</sub> control. The highest cell viability was achieved following exposure to the Glycofect<sup>TM</sup> 2 NR<sub>x</sub> hydrogels, at 78.8 ± 12.8%.

This was consistent with Dr. Jackson Hoffman's previous supernatant findings, with all PEI and Glycofect™ conditions significantly outperforming the TEMED 1 NR<sub>x</sub> controls.

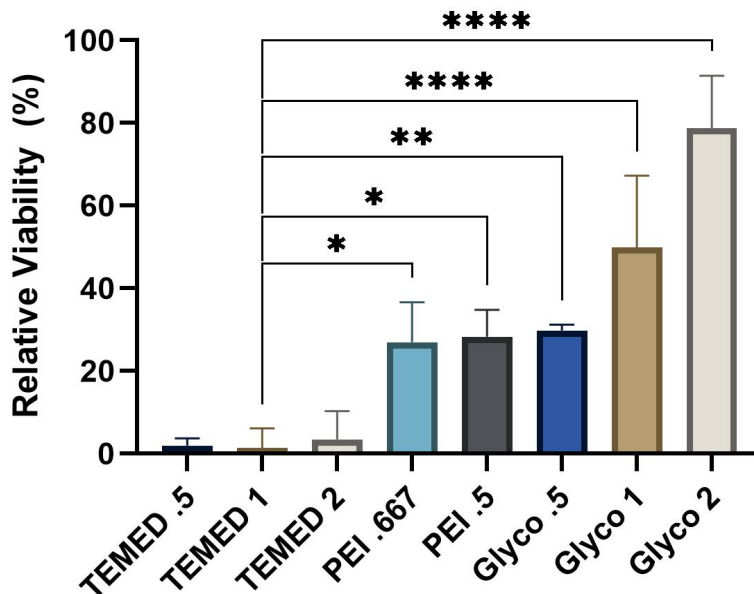


**Figure 4.2.** Direct-contact cell viability via resazurin metabolic assay. Viability is presented relative to non-hydrogel-exposed cells. \* $p < .05$ , \*\* $p < .01$ , \*\*\* $p < .001$ , \*\*\*\* $p < .001$  relative to TEMED 1 NR<sub>x</sub>.

Live/dead staining aligned with these results (Fig. 4.3). The live versus dead cells were quantified to provide an additional measure of viability. However, these data are best used as a qualitative representation, as removal of the hydrogels from the adherent 3T3s dislodged cells, skewing the results. Among the TEMED groups, viability was low, ranging from 3-8%. Both PEI

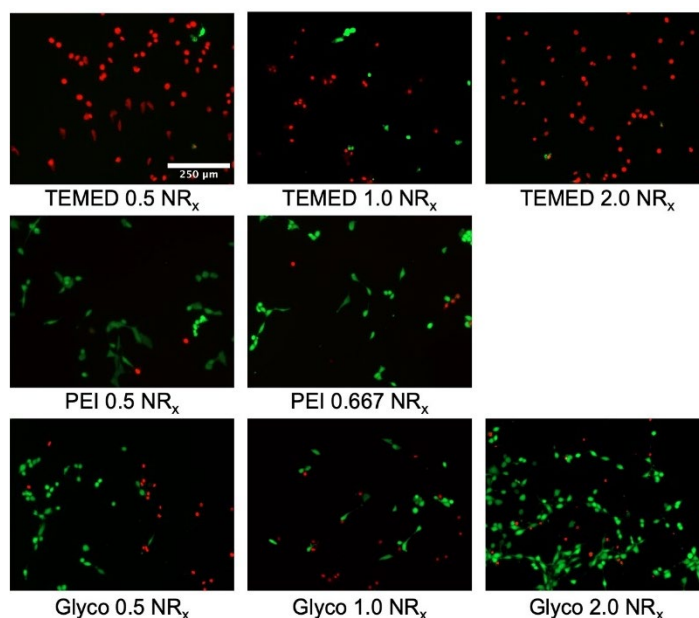


**Figure 4.3.** Direct contact cell viability via live/dead staining.



displayed a moderate viability of approximately 18%, and Glycofect<sup>TM</sup>-initiated hydrogel contact resulted in the greatest viability, ranging from 69-80%. What is particularly interesting is that in both assays, cell viability increases as a function of Glycofect<sup>TM</sup> concentration. Even at twice the relative molarity of the control (Glyco 2 NR<sub>x</sub>), we see the highest metabolic activity and number of live cells.

### 4.3 Conclusions

In this work, we successfully synthesized PEGDA and Glycofect<sup>TM</sup> with high purity and yield. The modified approach used to purify Glycofect<sup>TM</sup> was found to significantly increase the yield from 35% to 69%, providing a more efficient process and reducing required starting materials.

The investigation into alternative amine-based redox initiators, compatible with APS, effectively screened candidates using rheological analysis. Gel point and storage moduli were used as preliminary criteria to identify which systems resulted in hydrogels with comparable performance to the TEMED controls. Rheometry revealed two promising candidates- PEI and Glycofect<sup>TM</sup>. PEI (0.5 and 0.667 NR<sub>x</sub>) and Glycofect<sup>TM</sup> (0.5, 1, and 2 NR<sub>x</sub>) underwent further mechanical testing to evaluate the elastic moduli and mass swelling ratios. As the amine ratio of the initiators increased, the elastic modulus of hydrogels decreased while mass swelling ratio increased, indicating softer gels. We expect that these values can be tuned in the future by adjusting the concentration of APS added into the pre-gel solution.

The biocompatibility of the PEI- and Glycofect<sup>TM</sup>-initiated hydrogels was then evaluated using two cell viability studies—supernatant studies (described in detail in the dissertation of Dr. B. Jackson-Hoffman) and direct-contact studies. The cytocompatibility of the experimental groups

outperformed the TEMED controls, with consistently improved cell viability. This supports the potential of PEI and Glycofect™ as drop-in replacements for TEMED for improved biocompatibility in applications such as wound dressings.

Overall, this study draws inspiration from natural amine-containing monomers and polymers to contribute to the advancement of hydrogel fabrication and expands the range of available initiators for biomedical applications. It also introduces the potential to tailor hydrogel properties to meet the requirements of different applications.

#### 4.4 Experimental

**Synthesis of poly(ethylene glycol)-diacrylate 3350.** Poly(ethylene glycol)-diacrylate (PEGDA) was synthesized as previously described, with minor modifications [4]. In brief, poly(ethylene glycol) 3350 (INTEGRA–Kent, WA, USA) was dissolved in distilled DCM and placed in an ice bath. Triethylamine (3 equiv., distilled, 99+%, Alfa Aesar) was added under argon. Acryloyl chloride (2.4 equiv., distilled, 96%, Alfa Aesar) in DCM was added dropwise, and the reaction warmed from 5°C to room temperature overnight while stirring. The solution was washed with 2M K<sub>2</sub>CO<sub>3</sub>, the organic layer dried over MgSO<sub>4</sub> and concentrated by rotary evaporation. The product was precipitated into chilled ether and collected via filtration. The precipitate was dried overnight under reduced pressure to yield a white powder (6.92 g, 80.1%). <sup>1</sup>H NMR (CDCl<sub>3</sub>, ppm): δ=6.50 (d, 2H), 6.20 (m, 2H), 5.82 (d, 2H), 4.25 (t, 4H), 3.70-3.55 (m, 320H) (**Figure S1.1**).

**Synthesis of Glycofect™.** Dimethyl meso-galactarate was first synthesized by refluxing mucic acid (3.00 g, 14.3 mmol, CHEM-IMPEX, 99.8%) with concentrated sulfuric acid (1.50 mL, 28.0 mmol, Fisher Chemical) in 30 mL methanol overnight (**Scheme 4.2**) [21]. The reaction was cooled to room temperature and the product was collected via filtration. After washing with

methanol, the product was recrystallized from 160:1 methanol:triethylamine and dried (3.11 g, 91.5%).

Pentaethylene hexamine hexahydrochloride (1.53 mL, 3.43 mmol, ACROS Organics), dimethyl meso-galactarate (0.80 g, 3.36 mmol), and triethylamine (2.87 mL, 20.6 mmol) were combined in 22.4 mL methanol. The reaction was stirred under argon at room temperature for 48 h. The product was precipitated into ether and dried to obtain a pale beige powder (0.95 g, 69.0%). (**Figure S4.2**).  $^1\text{H NMR}$  ( $\text{D}_2\text{O}$ , ppm):  $\delta$  4.44 (s, 2H), 4.04 (s, 2H), 3.42 (br, 4H), 2.73 (br, 20H).

**Control hydrogel: 10 wt% PEGDA 3350, APS & TEMED.** Control hydrogels were fabricated using 1M APS (Biotechnology grade, VWR) and 1M TEMED (99+%, Thermo Scientific) in distilled water. In a scintillation vial, 41 mM TEMED was added to a 10 wt% PEGDA 3350 solution. APS (25 mM) was rapidly added and mixed, and the solution was transferred to a glass microscope slide with 2 mm vertical spacers. An additional slide was placed on top to ensure a uniform thickness. After gelation, a sterile 6 mm biopsy punch was used to punch out hydrogel disks (2 mm height, 6 mm diameter) (**Figure S4.3**).

**Non-toxic hydrogels: 10 wt% PEGDA 3350, APS & alternative amine-based initiators.** The appropriate amount of each alternative amine-based initiator (**Table 4.1**) was added to half the volume of DI water overnight to ensure complete dissolution. PEI (branched, 10-25 kDa, Aldrich Chemical) was used as received. A concentrated PEGDA 3350 stock solution was added to the initiator and adjusted to 10 wt% with DI water. APS was added at a final concentration of 25 mM, regardless of the concentration of the amine-based initiator. The pre-gel solution was rapidly mixed and pipetted onto the microscope slide assembly. After gelation, 6 mm sample discs were created using a sterile biopsy punch.

**Rheological characterization to identify initiator candidates.** Rheological properties were characterized using an Anton-Paar Modular Compact Rheometer 302. Storage and loss moduli of 250  $\mu\text{L}$  samples were determined using plate-plate geometry (25 mm diameter, 0.5 mm gap size) with a time sweep oscillatory test under constant strain amplitude of 1%, at constant oscillatory frequency (10 rad/s). The crossover point of the storage ( $G'$ ) and loss modulus ( $G''$ ) was considered the 'gel point'.

**Dynamic Mechanical Analysis (DMA).** The standard gel discs (2 mm height, 6 mm diameter) were prepared in triplicate for each initiator group, and swollen in DI  $\text{H}_2\text{O}$  at  $4^\circ\text{C}$  to equilibrium. The elastic modulus and stress and strain at fracture were characterized by uniaxial compression, using TA Instruments Q-800 DMA. The initial preload force was 0.001 N and the initial strain was 0.5%. Strain was ramped at  $10\% \text{ min}^{-1}$  to -130% strain, and the runs were manually stopped upon hydrogel fracture. Elastic modulus was calculated using the linear region of the stress-strain curve, and the fracture point was assumed to be the maximum stress prior to a sharp decline in stress.

**Mass Swelling Ratio.** An additional set of the standard gel discs were prepared in triplicate for each initiator group. The discs were flash frozen in  $\text{LN}_2$ , lyophilized, and weighed to determine the dry mass. The discs were then transferred to 1 mL Dulbecco's phosphate-buffered saline (DPBS) in a 48 well plate, and swollen at  $4^\circ\text{C}$  to equilibrium. Each hydrogel disc was gently dabbed on a Kimwipe to remove excess water prior to recording the swollen mass.

Mass swelling ratio,  $Q_m$ , was determined using the following equation:

$$Q_m = \frac{m_{\text{swollen}} - m_{\text{dry}}}{m_{\text{dry}}} \quad \text{Equation 1}$$

Equilibrium volumetric swelling,  $Q_v$ , was calculated as follows, where  $\rho_p$  is the density of PEGDA 3350 and  $\rho_s$  is the density of the solvent (water):

$$Q_v = 1 + \left( \frac{\rho_p}{\rho_s} \right) \times (q_m - 1) \quad \text{Equation 2}$$

The equilibrium volumetric swelling was then used with the Flory-Rehner equation to estimate the crosslink density and mesh size of each experimental group (Appendix C).

**Direct-contact cell viability.** To best emulate a wound dressing in contact with cells, a direct-contact viability assay, in accordance with ISO 10993-5:2009, was used (CITE). NIH/3T3 cells were seeded in a 48-well plate at  $5 \times 10^3$  per well and incubated at 37°C overnight. The following hydrogel groups were prepared aseptically: TEMED 0.5, 1, and 2 NR<sub>x</sub>; PEI 0.5 and 0.667; and Glycofect™ 0.5, 1, and 2 NR<sub>x</sub>. Using a biopsy punch, sample discs were created with a height of 2 mm and a diameter of 6 mm. After the overnight cell culture incubation, media was carefully aspirated from the wells. The hydrogels were placed on the adhered cells in triplicate, with triplicate blanks containing hydrogels alone with no cells. Fresh media (200 µL) was carefully added to each well and the plate was incubated at 37°C for 2.5 h [22]. Following incubation, the hydrogels and media were removed and replaced with either 10% resazurin in media or live/dead stain (Biotium, 2 µM calcein AM and 4 µM EthD-III in sterile PBS) and transferred to the 37°C incubator for 30 min. The live/dead plates were imaged with Alexa Fluor 488 ( $\lambda_{Em}=517$ ) and mCherry ( $\lambda_{Em}=610$ ) channels. The resazurin plates were removed and fluorescence was measured using a BioTek synergy h1 microplate reader ( $\lambda_{Ex}=570$ ,  $\lambda_{Em}=585$ , gain: 80) and collected with BioTek Gen 5 2.07 data analysis software. The readings were normalized with respect to the blanks of the resazurin solution in wells that had initially contained hydrogels with no cells. Groups were compared to the TEMED 1 NR<sub>x</sub> control using Dunnett's multiple comparison test.

## 4.5 Appendix C

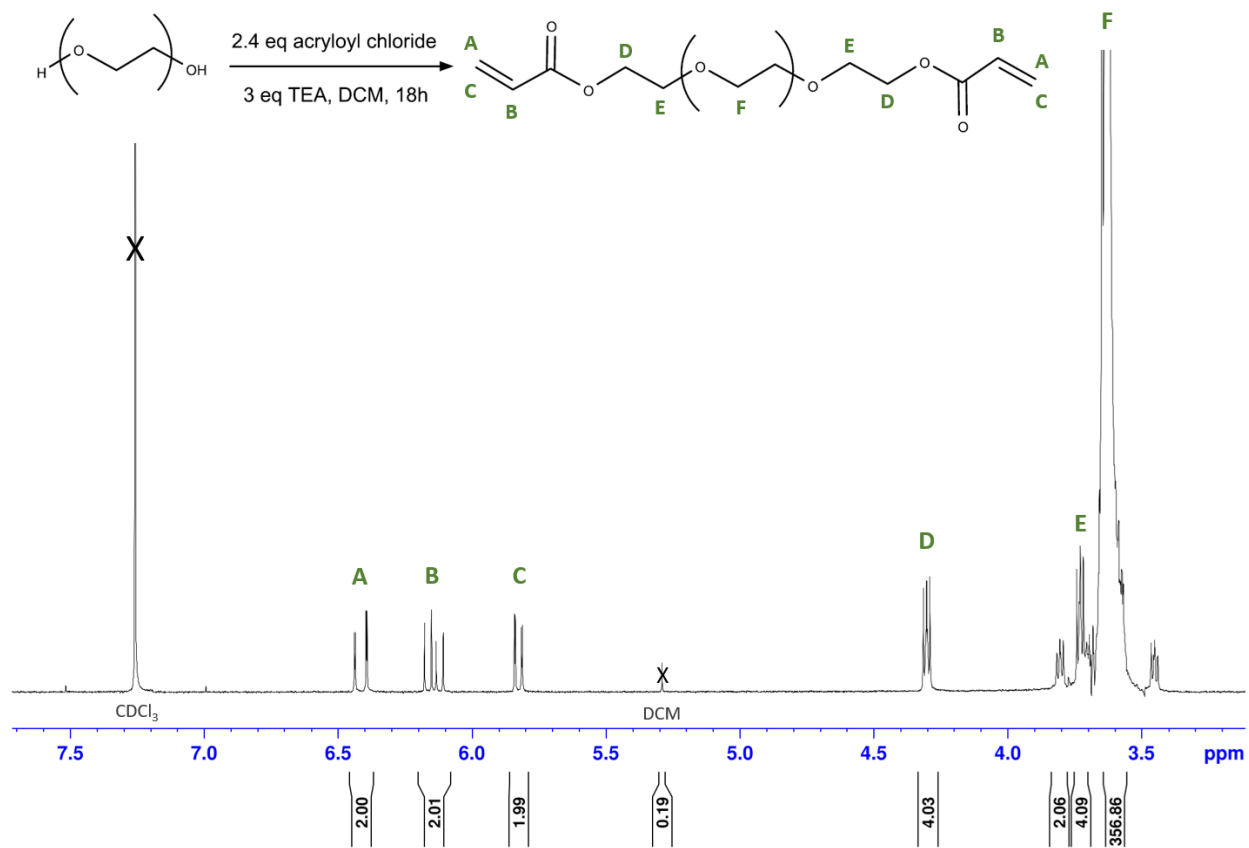


**Figure S4.1.**  $^1\text{H}$  NMR of poly(ethylene glycol)-diacrylate (PEGDA) 3350, in  $\text{CDCl}_3$ .

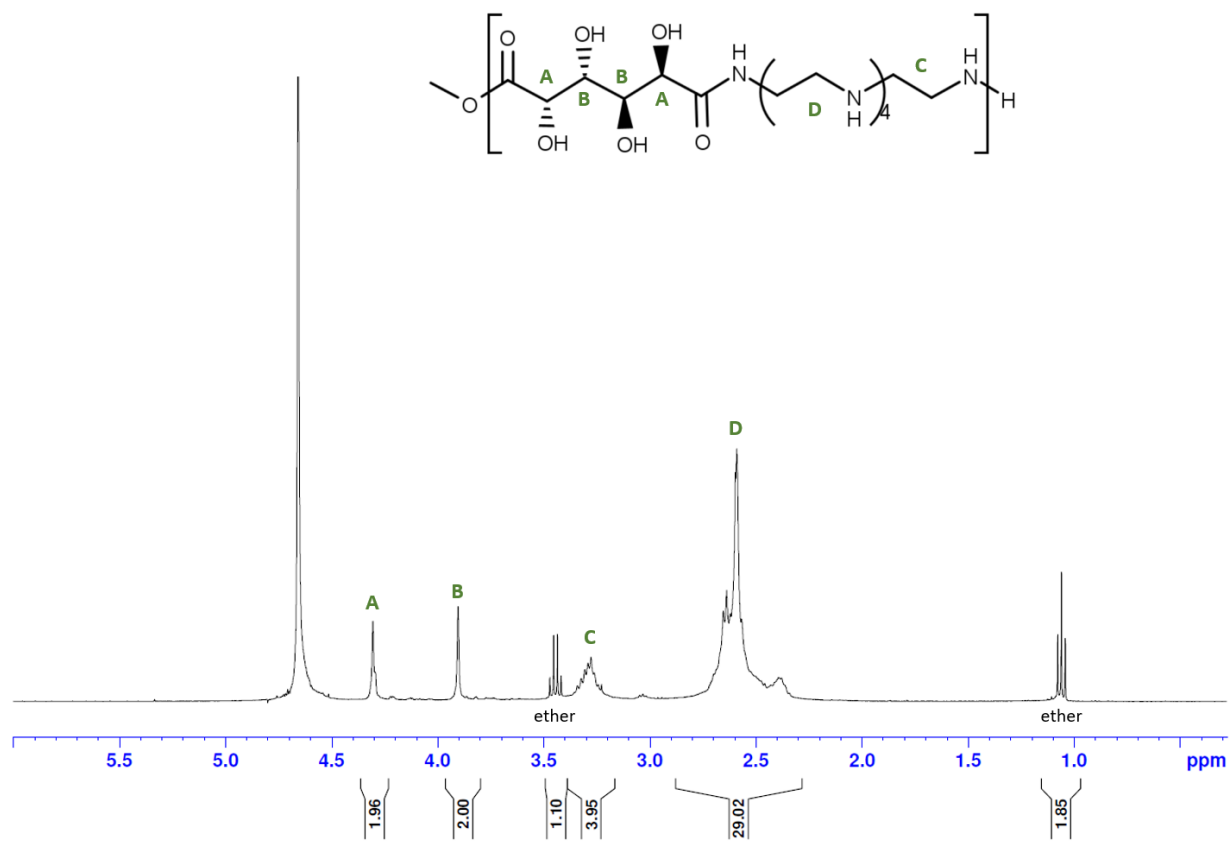


**Figure S4.2.**  $^1\text{H}$  NMR of Glycofect<sup>TM</sup>, in  $\text{D}_2\text{O}$ .

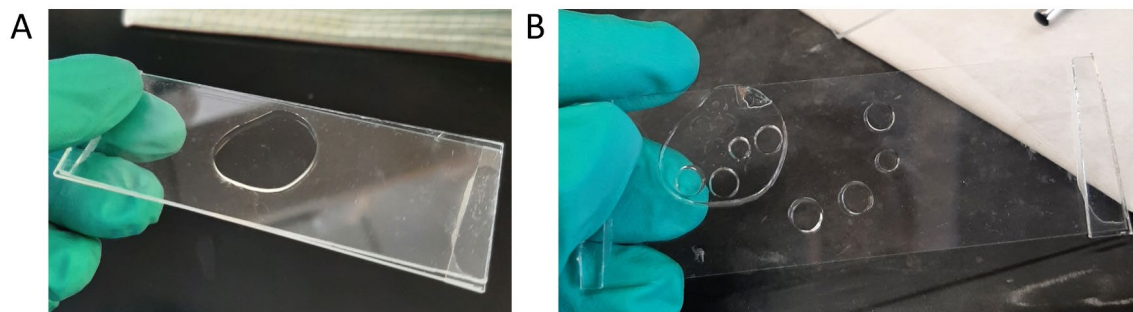


**Figure S4.3.** Photographs of hydrogels (A) during gelation in the casting device and (B) after gelation and sample disc preparation using a 3 mm and 6 mm biopsy punch.

Rheological curves of pre-gel solutions.

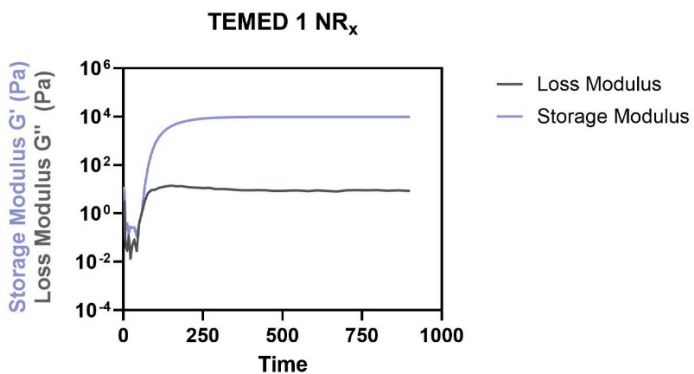


Figure S4.4. Rheological curve of TEMED 1 NR<sub>x</sub> hydrogel.

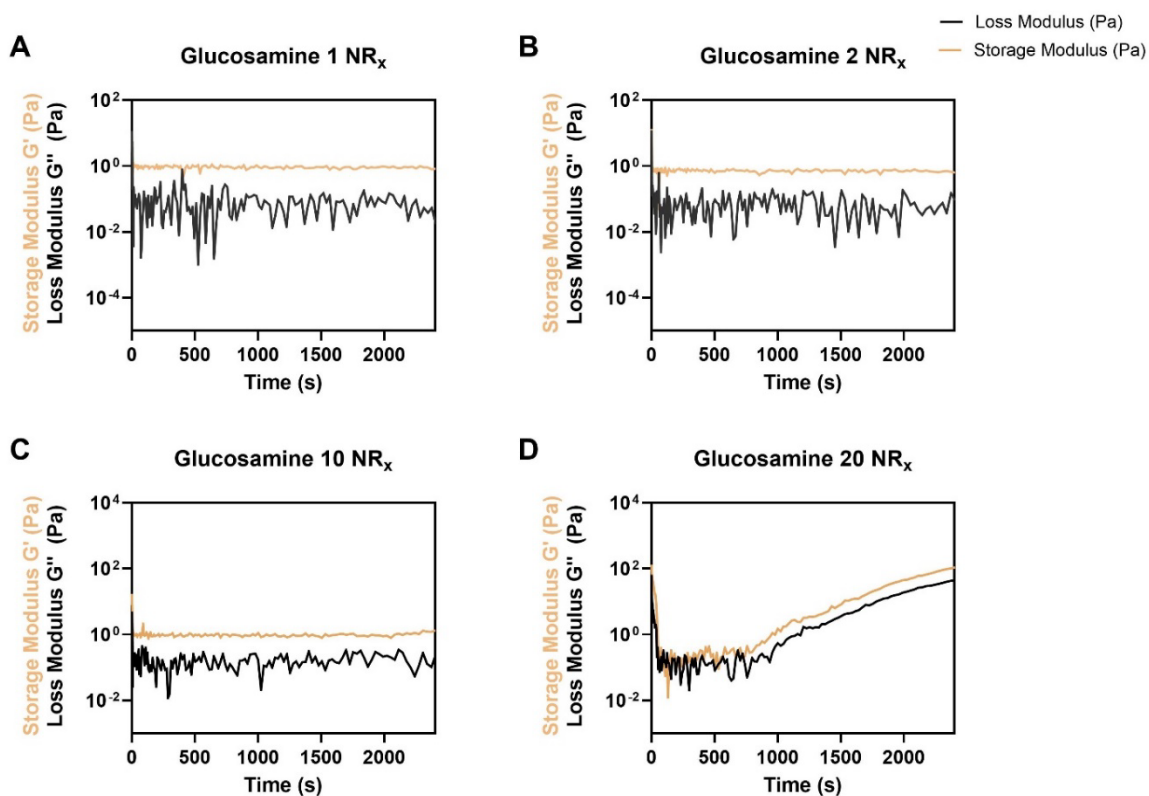
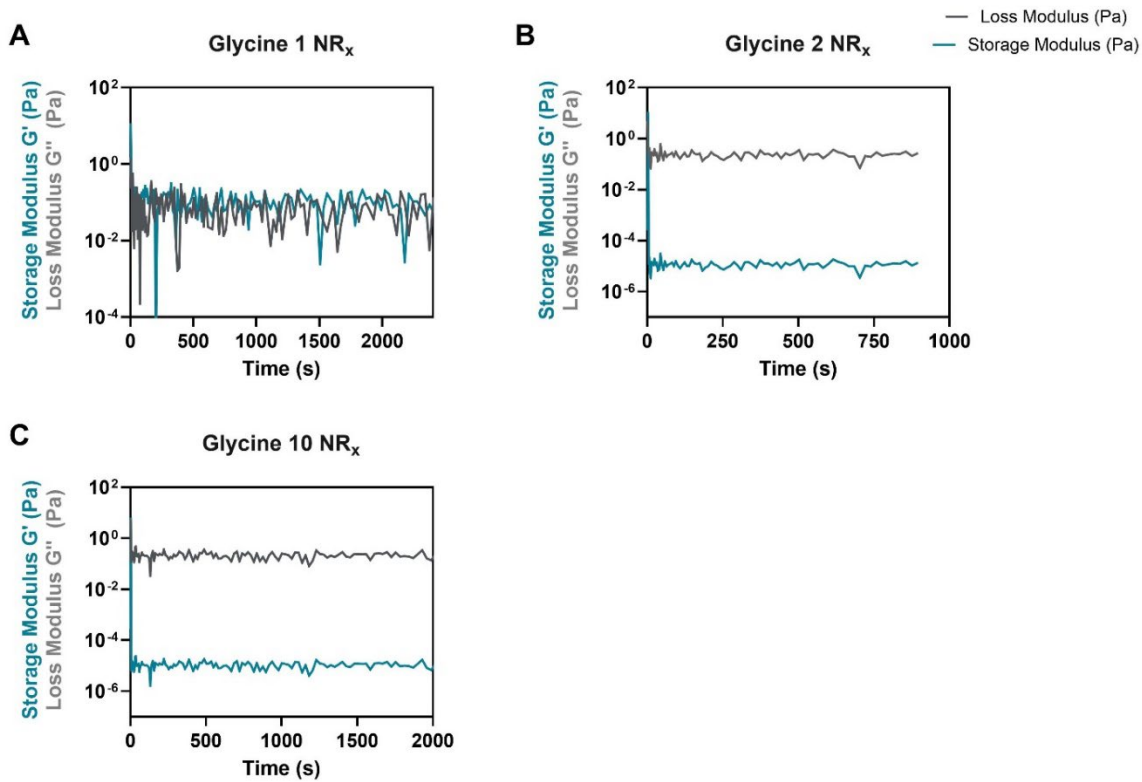
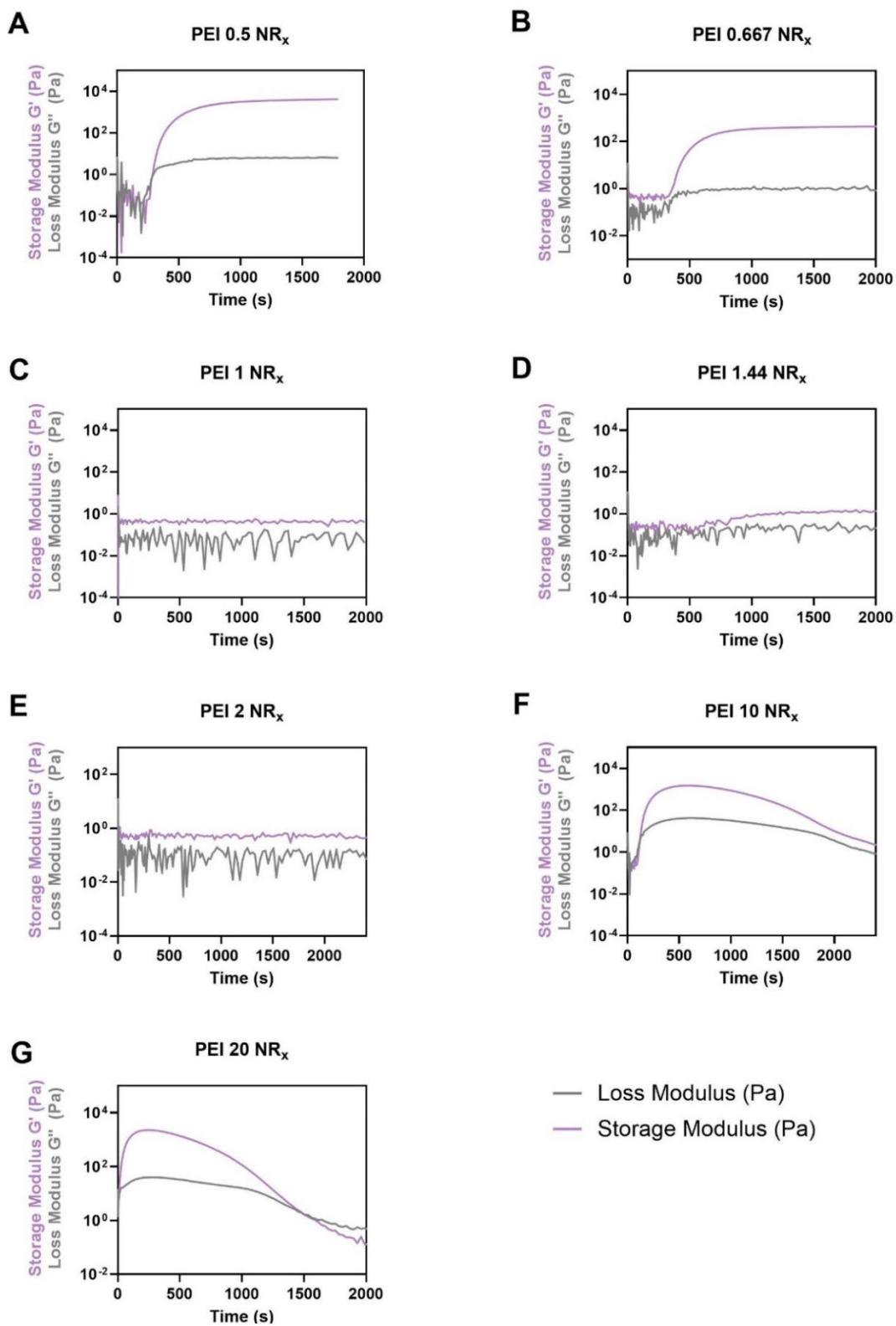


Figure S4.5. Rheological curves of glucosamine (A) 1 NR<sub>x</sub>, (B) 2 NR<sub>x</sub>, (C) 10 NR<sub>x</sub>, and (D) 20 NR<sub>x</sub> hydrogels.





**Figure S4.6.** Rheological curves of glycine (A) 1 NR<sub>x</sub>, (B) 2 NR<sub>x</sub>, and (C) 10 NR<sub>x</sub>, hydrogels.



**Figure S4.7.** Rheological curves of PEI (A) 0.5 NR<sub>x</sub>, (B) 0.667 NR<sub>x</sub>, (C) 1 NR<sub>x</sub>, (D) 1.44 NR<sub>x</sub>, (E) 2 NR<sub>x</sub>, (F) 10 NR<sub>x</sub>, and (G) 20 NR<sub>x</sub> hydrogels.

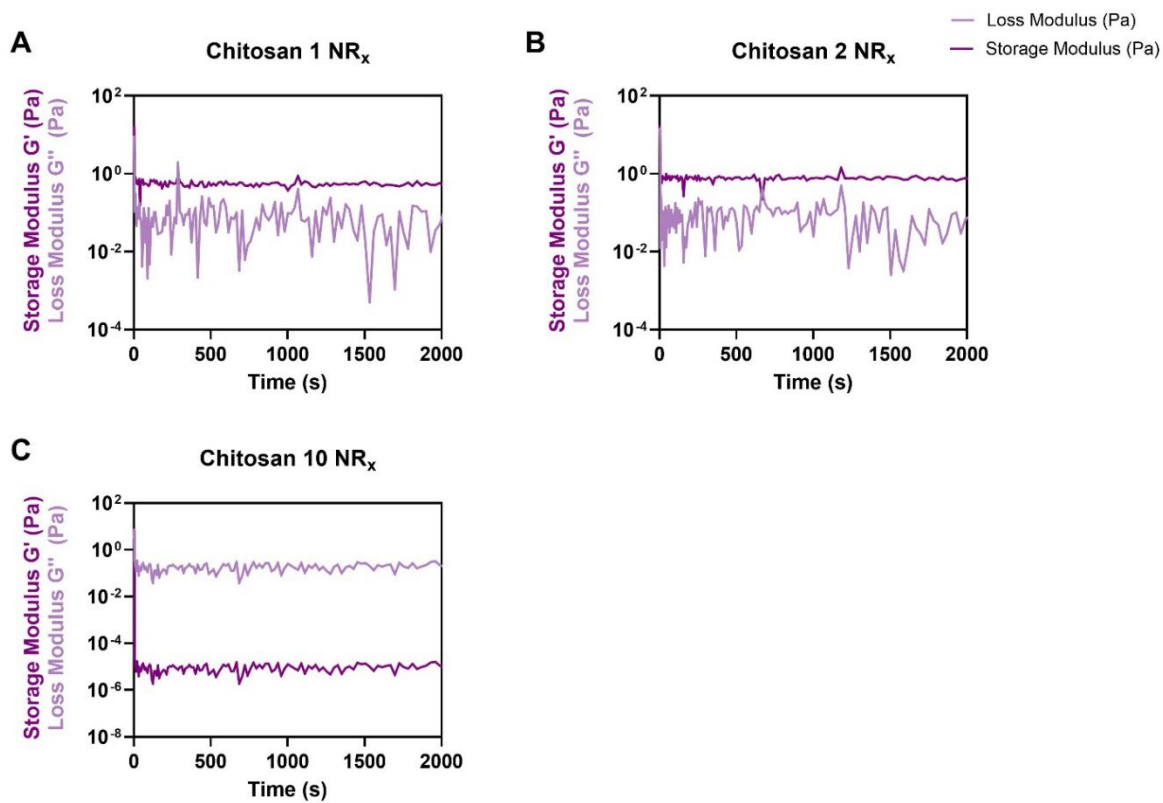


**Figure S4.8.** Rheological curves of chitosan (A) 1 NR<sub>x</sub>, (B) 2 NR<sub>x</sub>, and (C) 10 NR<sub>x</sub> hydrogels.

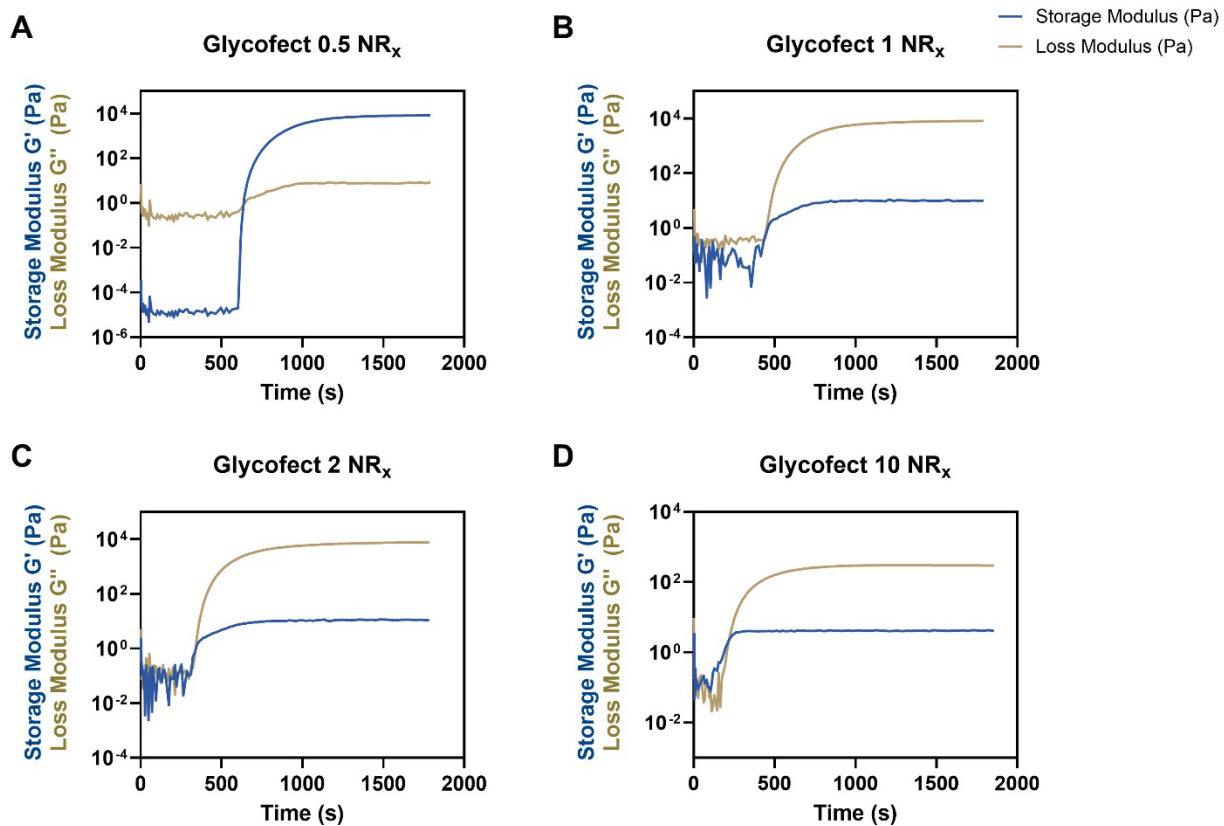


**Figure S4.9.** Rheological curves of Glycofect<sup>TM</sup> (A) 0.5 NR<sub>x</sub>, (B) 1 NR<sub>x</sub>, (C) 2 NR<sub>x</sub>, and (D) 10 NR<sub>x</sub> hydrogels.

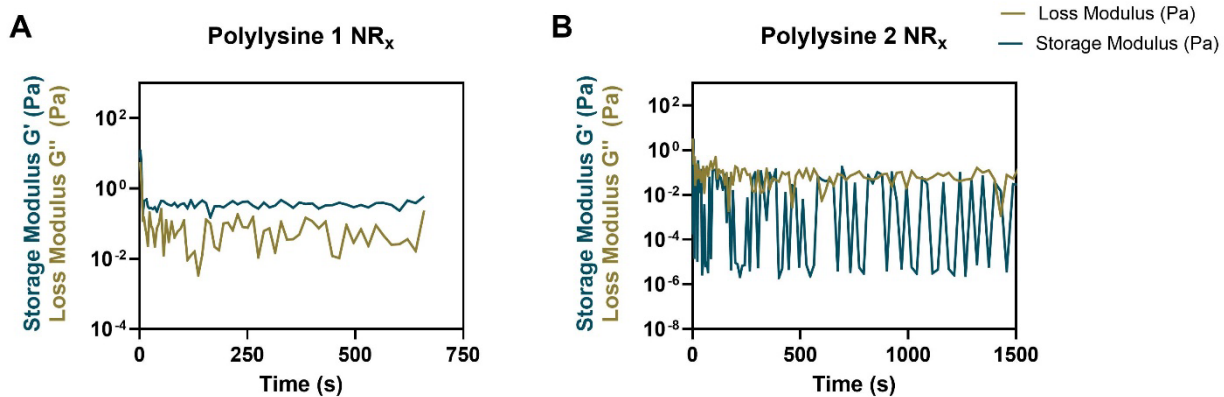


**Figure S4.10.** Rheological curves of polylysine (A) 1 NR<sub>x</sub> and (B) 2 NR<sub>x</sub> hydrogels.

*Calculating volumetric swelling ratio, degree of crosslinking, and mesh size.* To characterize hydrogel structure, the volumetric swelling ratio ( $Q_v$ ), polymer volume fraction ( $v_{2,s}$ ), and specific volume of polymer ( $v$ ) were calculated. This allowed for the molecular weight between crosslinks ( $M_c$ ) to be calculated. Using the respective values for  $M_c$ , the mesh size ( $\xi$ ) for each initiator group was determined.

Mass swelling ratio ( $q_m$ ) for each hydrogel group was experimentally determined and used to calculate volumetric swelling ratio ( $Q_v$ , Equation 2). In Equation 2,  $\rho_p$  is the density of PEGDA 3350 (1.20 g/mL), and  $\rho_p$ , the density of water, is set to 1.00 g/mL. While the specific volume of the polymer,  $v$ , is  $\rho_p/\rho_s$ , the volume fraction in the hydrogel swollen to equilibrium ( $v_{2,s}$ ) is:

$$v_{2,s} = \frac{1}{Q_v} \quad \text{Equation S1}$$

This, along with the number-average molecular weight ( $M_n$ ) of the PEGDA, the molar volume of DI H<sub>2</sub>O ( $V_1$ , 18.07 g/mol), and the Flory Huggins polymer-solvent interaction parameter ( $X_1$ , 0.426) is used to determine molecular weight of the polymer chains between two neighboring crosslinks,  $M_c$ :

$$M_c = \frac{1}{\left(\frac{2}{M_n}\right) - \left(\frac{v/V_1 \times (\log(1-v_{2,s}) + v_{2,s} + X_1 \times v_{2,s}^2)}{v_{2,s}^{1/3} - v_{2,s}/2}\right)} \quad \text{Equation S2}$$

The number of links in the chain,  $N$ , can be calculated knowing that the molecular weight of repeating units in the polymer chain ( $M_r$ ) is 44.05 g/mol.

$$N = \frac{2 \times M_c}{M_r} \quad \text{Equation S3}$$

The root mean square end-to-end distance of polymer chains between 2 neighboring crosslinks is then calculated, approximating the length of the bond along the polymer backbone,  $l$ , as 1.54 Å, and the polymer specific characteristic ratio,  $C_n$ , as 4 [23].

$$(r_0^2)^{1/2} = l \times (C_n \times N)^{1/2} \quad \text{Equation S4}$$

Combining the information from *Equations S1* and *S4*, we are able to calculate mesh size

( $\xi$ ):

$$\xi = v_{2,s}^{-1/3} \times (r_0^2)^{1/2} \quad \text{Equation S5}$$

## 4.6 References

- [1] J. Smith, A. Johnson, and M. Garcia, “Biomimetic hydrogels: Inspired by the extracellular matrix for biomedical applications,” *J. Biomed. Mater. Res. Part A*, vol. 101, no. 8, pp. 2201–2215, 2023.
- [2] Y. Liang, J. He, and B. Guo, “Functional hydrogels as wound dressing to enhance wound healing,” *ACS Nano*, vol. 15, no. 8, pp. 12687–12722, 2021.
- [3] E. A. Kamoun, E.-R. S. Kenawy, and X. Chen, “A review on polymeric hydrogel membranes for wound dressing applications: PVA-based hydrogel dressings,” *J. Adv. Res.*, vol. 8, no. 3, pp. 217–233, 2017.
- [4] E. K apyl a, S. M. Delgado, and A. M. Kasko, “Shape-changing photodegradable hydrogels for dynamic 3D cell culture,” *ACS Appl. Mater. Interfaces*, vol. 8, no. 28, pp. 17885–17893, 2016.
- [5] D. Han, Y. Li, X. Liu, *et al.*, “Rapid bacteria trapping and killing of metal-organic frameworks strengthened photo-responsive hydrogel for rapid tissue repair of bacterial infected wounds,” *Chem. Eng. J.*, vol. 396, p. 125194, 2020.
- [6] I. A. Duceac, L. Verestiuc, C. D. V. M. Dimitriu, *et al.*, “Design and preparation of new multifunctional hydrogels based on chitosan/acrylic polymers for drug delivery and wound dressing applications,” *Polymers (Basel)*, vol. 12, no. 7, p. 1473, 2020.
- [7] X. Zhao, D. Pei, Y. Yang, *et al.*, “Green tea derivative driven smart hydrogels with desired functions for chronic diabetic wound treatment,” *Adv. Funct. Mater.*, vol. 31, no. 18, p. 2009442, 2021.

- [8] E. S. Desai, M. Y. Tang, A. E. Ross, *et al.*, “Critical factors affecting cell encapsulation in superporous hydrogels,” *Biomed. Mater.*, vol. 7, no. 2, p. 024108, 2012.
- [9] X. De Feng, X. Q. Guo, and K. Y. Qiu, “Study of the initiation mechanism of the vinyl polymerization with the system persulfate/N,N,N’,N’-tetramethylethylenediamine,” *Macromol. Chem. Phys.*, vol. 189, no. 1, pp. 77–83, 1988.
- [10] B. Strachota, L. Matějka, A. Zhigunov, *et al.*, “Poly(N-isopropylacrylamide)-clay based hydrogels controlled by the initiating conditions: evolution of structure and gel formation,” *Soft Matter*, vol. 11, no. 48, pp. 9291–9306, 2015.
- [11] E. A. Pumford, B. A. Jackson Hoffman, and A. M. Kasko, “Nontoxic initiator alternatives to TEMED for redox hydrogel polymerization,” *ACS Appl. Biomater.*, vol. 7, no. 4, pp. 2264–2271, 2024.
- [12] V. Keskar, N. W. Marion, J. J. Mao, *et al.*, “In vitro evaluation of macroporous hydrogels to facilitate stem cell infiltration, growth, and mineralization,” *Tissue Eng. Part A*, vol. 15, no. 7, pp. 1695–1707, 2009.
- [13] R. Komeri and J. Muthu, “Injectable, cytocompatible, elastic, free radical scavenging and electroconductive hydrogel for cardiac cell encapsulation,” *Colloids Surfaces B Biointerfaces*, vol. 157, pp. 381–390, 2017.
- [14] R. Komeri and J. Muthu, “In situ crosslinkable elastomeric hydrogel for long-term cell encapsulation for cardiac applications,” *J. Biomed. Mater. Res. Part A*, vol. 104, no. 12, pp. 2936–2944, 2016.
- [15] Q. Ge, Z. Chen, J. Cheng, *et al.*, “3D printing of highly stretchable hydrogel with diverse



- UV curable polymers,” *Sci. Adv.*, vol. 7, no. 2, p. eaba4261, 2021.
- [16] D. Gyawali, P. Nair, H. K. Kim, *et al.*, “Citrate-based biodegradable injectable hydrogel composites for orthopedic applications,” *Biomater. Sci.*, vol. 1, no. 1, pp. 52–64, 2013.
- [17] P. Jiang, Z. Mao, and C. Gao, “Combinational effect of matrix elasticity and alendronate density on differentiation of rat mesenchymal stem cells,” *Acta Biomater.*, vol. 19, pp. 76–84, 2015.
- [18] M.-E. Han, S.-H. Kim, H. D. Kim, *et al.*, “Extracellular matrix-based cryogels for cartilage tissue engineering,” *Int. J. Biol. Macromol.*, vol. 93, pp. 1410–1419, 2016.
- [19] T. R. Cox and C. D. Madsen, “Relative stiffness measurements of cell-embedded hydrogels by shear rheology in vitro,” *Bio-protocol*, vol. 7, no. 1, pp. e2101–e2101, 2017.
- [20] Z. Ji, L. Yu, Q. Duan, *et al.*, “Morphology and rheology of a cool-gel (protein) blended with a thermo-gel (hydroxypropyl methylcellulose),” *Foods*, vol. 11, no. 1, p. 128, 2022.
- [21] Y. Liu and T. M. Reineke, “Hydroxyl stereochemistry and amine number within poly(glycoamidoamine)s affect intracellular DNA delivery,” *J. Am. Chem. Soc.*, vol. 127, no. 9, pp. 3004–3015, 2005.
- [22] M. Torres-Lugo, M. García, R. Record, *et al.*, “Physicochemical behavior and cytotoxic effects of p (methacrylic acid–g-ethylene glycol) nanospheres for oral delivery of proteins,” *J. Control. Release*, vol. 80, no. 1–3, pp. 197–205, 2002.
- [23] E. W. Merrill, K. A. Dennison, and C. Sung, “Partitioning and diffusion of solutes in hydrogels of poly(ethylene oxide),” *Biomaterials*, vol. 14, no. 15, pp. 1117–1126, 1993.

## CHAPTER 5: Tunable drug eluting hydrogel wound dressings for prolonged field care

### 5.1 Introduction

Extremity injuries remain the most commonly sustained combat wounds, and the predominant cause of long-term disability [1]. One of the major demands in battlefield trauma care is minimizing the time between critical injury and definitive care. This has been partly addressed by the “golden hour policy” where transport time for treatment was halved. However, the evacuation of significantly injured military personnel to a treatment facility within 60 minutes is often not possible for those who are deployed to remote & austere locations for prolonged periods [2].

These instances, in which there is no immediate access to first-world medical infrastructure for days, is driving interest in prolonged field care (PFC) [3]. PFC is field medical care applied for a longer duration in order to decrease mortality and morbidity until the patient receives appropriate care. Limited resources and harsh operational environments, which inherently contribute to infection, pose significant challenges to PFC [4]. Extremity wounds in the battlefield are at great risk of infection, which is life threatening and can lead to impaired healing or delayed amputation. For instance, open tibia fractures sustained on the battlefield have an infection rate of 20-30%. Bacterial species, primarily *Staphylococcus aureus*, *Escherichia coli*, *Pseudomonas spp.*, are known to colonize battlefield wounds either on-site, enroute to treatment facilities, or from the patient’s own micro-flora [5], [6]. Furthermore, these microbes can coexist and display synergistic interactions which enhance colonization and persistence, increasing risk of mortality [7], [8].

While current PFC treatment involves sealing and passively protecting the wound, there is an unmet need to actively stop the bleeding without limb ischemia, provide pain relief, and stop

the proliferation of bacteria [4], [9]. To address the potential for robust polymicrobial infections, dual-antibiotic therapy using a combination of tobramycin and vancomycin, which work synergistically, can be employed [10]. When used together, these antibiotics have also demonstrated increased bone defect re-ossification, particularly relevant for blast injuries associated with fracture [11]. Following combat injury, tranexamic acid can be employed to reduce blood loss. Tranexamic acid, an antifibrinolytic agent, helps keep blood clots in place and significantly reduces mortality in trauma patients with bleeding [12], [13]. Finally, lidocaine can be introduced into PFC treatment to provide local pain relief. Due to the nature of combat injuries sustained in austere environments, transport to a fully equipped medical facility may not be feasible for several days. As such, there is an unmet need for a PFC wound dressing system that is able to rapidly deliver tranexamic acid and lidocaine to immediately address bleeding and pain, while providing sustained delivery of vancomycin and tobramycin to stave off infection.

Hydrogels have the potential to simultaneously serve as drug delivery vehicles and PFC wound dressings. Hydrogels are crosslinked 3D networks of hydrophilic polymer chains which are able to swell in water while retaining their shape. They have been increasingly used as wound dressings because of their high water content, biocompatibility, and tunable modulus similar to that of soft tissue [14], [15]. Polymeric dressings were initially viewed as passive dressings that did not play an active role in wound healing. However, use of hydrogel wound dressings introduces the potential to load the network with different therapeutic or biologic agents. In particular, synthetic poly(ethylene glycol) hydrogels are good candidates for active wound healing because they mimic chemical and physical properties of the native extracellular matrix [16], [17], [18]. Further, diffusion of physically entrapped therapeutics can be tailored by changing the mesh size

of the hydrogel (via polymer molecular weight, polymer concentration used, or the mechanism of hydrogel crosslinking) or by introducing affinity interactions to slow drug release [19].

The goal of this work was to design a field-polymerizable hydrogel wound sealant and dressing that can be applied in far-forward, remote environments that provides sustained release of gram-positive and gram-negative antibiotics over a 3-day period, along with burst release of a hemostatic agent and analgesic (within 3 hours) (**Figure 5.1**) [12].

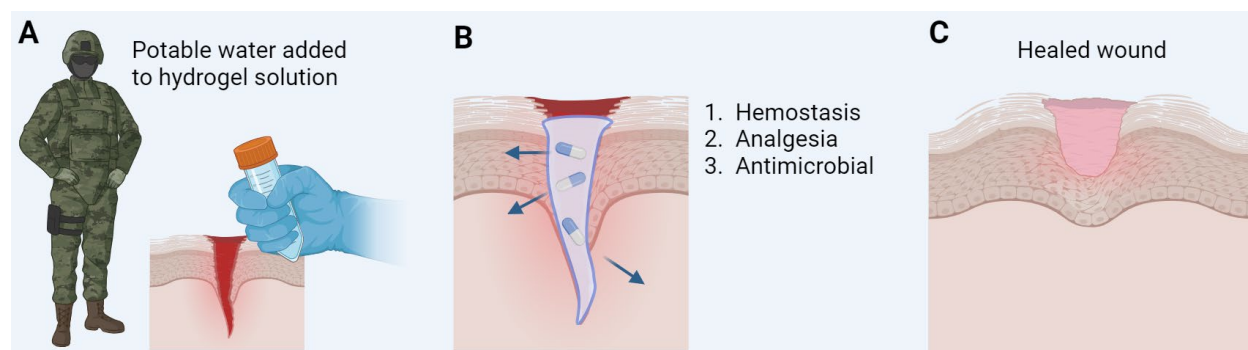


**Figure 5.1.** Graphical depiction of the hydrogel wound dressing used in far-forward combat setting.

(A) After sustaining a combat injury, potable water is added to a tube containing powdered reagents and (B) is applied to the site of the injury, releasing therapeutic agents to prevent infection and provide hemostasis and analgesia, (C) healing the wound and preventing loss of life or limb.

To achieve this goal, we relied on computational modeling performed by Kaitlyn Cook to predict drug diffusion out of various poly(ethylene glycol)-diacrylate (PEGDA) hydrogel systems to narrow down candidates [20]. We then experimentally investigated and optimized the *in vitro* release profile of tranexamic acid, lidocaine, tobramycin, and vancomycin from the PEGDA hydrogels. The mechanical properties and stability of the optimized system were evaluated. Finally, to ensure that the released therapeutic agents retained their activity, we performed a broth microdilution assay (to determine the minimum inhibitory concentration of released antibiotics against gram-positive and gram-negative bacteria) and our collaborators evaluated blood clotting time after exposure to tranexamic acid released from the hydrogels.

The optimized PEGDA 3350 hydrogels underwent *in vivo* evaluation in a small and large animal models (completed by our collaborators in Dr. Nick Bernthal's and Dr. Josh Wenke's groups). An open fracture murine model was used to evaluate the *in vivo* release kinetics, antibiotic efficacy against polymicrobial infections, immune response, and toxicity. Large animal *in vivo* studies in Merino sheep were used to investigate field readiness and efficacy treating wound infections.

This approach provide an easy to use wound care method for PFC that is lightweight and does not need heavy equipment, requiring only a tube filled with powdered reagents (**Fig. 5.1A**), making it highly mobile for combat settings. Our system enables extremely fast formation of the PEGDA hydrogel wound dressing ( $\leq 2$  min) via redox polymerization, following the addition of potable water from a canteen. Water is simply added to the tube containing powdered reagents, the initiators are added, and the contents are shaken and poured into the site of injury (**Fig. 5.1B**). The rapid redox crosslinking enables the wound dressing to gel *in situ*, fitting into the contours of the wound bed. Our hydrogel platform is also modular and tunable. The hydrogel mesh size and loaded therapeutic agents can be tailored to either i) adjust to the unique endemic flora of a region or ii) accommodate the specific requirements of diverse dermal injuries. For instance, colloidal silver or iron oxide nanoparticles can be incorporated to address chronic ulcers or common dermatophilosis infections that affect humans and animals, or have the potential to be multiplexed by adsorbing antifungals to the gel treat fungal lesions, while still enabling the release of additional entrapped therapeutic agents [21], [22], [23], [24], [25]. This versatility highlights the adaptability of our hydrogel platform, allowing for precise customization to meet varying clinical needs. Moreover, this system is expected to be fully compatible with the initiator systems developed in **Chapter 4**,

paving the way for future research fabricating this drug-releasing wound dressing using non-toxic initiators.

## 5.2 Results and Discussion

**Hydrogel fabrication.** PEGDA 2000, 3350, and 4600 were prepared with high purity and yield as described in **Chapter 4** (*Synthesis of poly(ethylene glycol)-diacrylate 3350*). Commercially available PEGDA 700 was used as received (**Figures S5.1-S5.3**). Unless otherwise specified, all hydrogels had the following reagent concentrations: 24.14 wt% PEGDA, 30 mM APS, and 30 mM TEMED.

Hydrogel sample discs were prepared by casting the pre-gel solution onto a glass slide with 2 mm spacers, with a glass slide placed on top, where they solidified within approximately 3 minutes. After gelation, a 6 mm biopsy punch was used to isolate uniform sample discs, which were used for mechanical characterization and to quantify in vitro release kinetics.

**Mechanical properties of hydrogels.** Building off of K. Cook's work, mechanical characterization was performed on hydrogels fabricated using PEGDA of molecular weights: 700, 2000, 3350, and 4600. Triplicate hydrogel sample discs for elastic modulus and mass swelling characterization were prepared for each molecular weight of PEGDA. The hydrogels were placed in DI H<sub>2</sub>O until they reached equilibrium swelling, after which they were subjected to mechanical characterization. Dynamic mechanical analysis (DMA) was used to generate a stress-strain curve to evaluate the elastic moduli of the gels. The mass of the swollen hydrogel was then compared to the mass of a lyophilized hydrogel to determine mass swelling ratio,  $Q_m$ . There are clear inverse trends between elastic modulus and mass swelling, with the latter increasing as a function of PEGDA molecular weight. (**Figure 5.2**). As the molecular weight of PEGDA increases, the hydrogel mesh becomes looser, with crosslinks spaced out further along the polymer chains.

Because of this, elastic modulus—essentially resistance to elastic deformation—decreases as PEGDA molecular weight increases. The opposite holds true for mass swelling ratios.  $Q_m$  increases as a function of molecular weight, because the more spaced out mesh of the hydrogels allows them to uptake more water. These properties have important implications for hydrogel wound dressings, as the elastic modulus should be similar that of skin, while a higher  $Q_m$  would indicate a greater ability to absorb wound exudate.

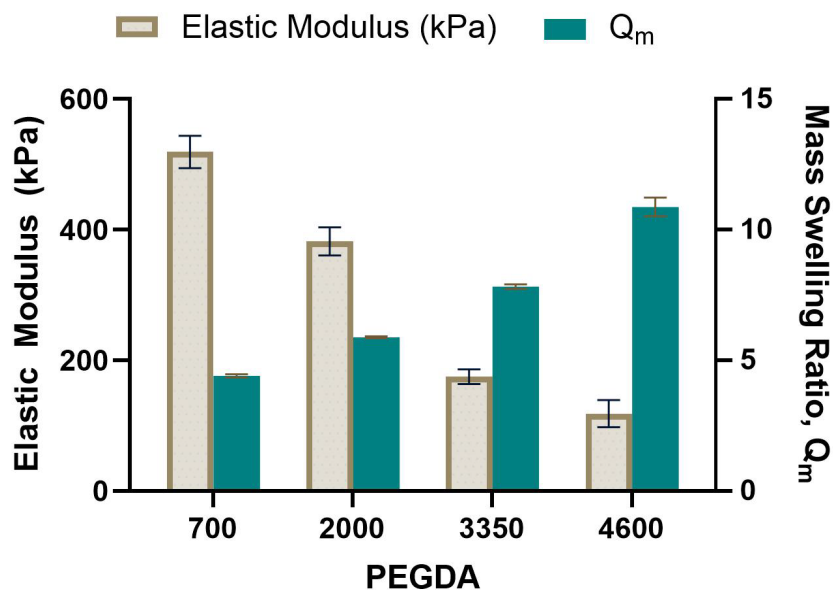


**Figure 5.2.** Elastic moduli and mass swelling ratios of hydrogels fabricated with varied molecular weights of PEGDA.

The elastic moduli and mass swelling ratios were used to determine volumetric swelling ratio and mesh size by applying the equations outlined in **Chapter 4**, Appendix C, “*Calculating volumetric swelling ratio, degree of crosslinking, and mesh size*”. These values are listed along with the estimated hydrodynamic radii of the therapeutic agents used in this work (**Table 5.1**). As anticipated, mesh size increases as a function of PEGDA molecular weight. This has a direct

impact on the release rates of therapeutic agents from the hydrogels, as drugs will diffuse out of a larger mesh more rapidly.

**Table 5.1.** Experimental and derived mechanical properties of hydrogels.

PEGDA	Elastic Modulus (kPa)	$Q_m$	$Q_v$	Mesh size (nm)	Therapeutic Agent	$r_s$ (nm)
700	519 ± 24.9	4.41 ± 0.06	4.88 ± 0.07	18.8 ± 0.09	Tranexamic acid	0.49
2000	382 ± 21.6	5.88 ± 0.04	6.95 ± 0.05	35.2 ± 0.09	Lidocaine	0.55
3350	175 ± 11.4	7.82 ± 0.09	9.25 ± 0.11	50.6 ± 0.20	Tobramycin	0.69
4600	118 ± 20.8	10.9 ± 0.35	12.9 ± 0.43	68.4 ± 0.76	Vancomycin	1.00

Electrostatic and physical interactions were explored to modulate the release rates of therapeutic agents through the introduction of polyacrylic acid or sodium polyacrylate (SPA). The mechanical properties of hydrogels incorporating these additional polymers were quantified prior to advancing them to kinetic release studies.

To evaluate the effect of polyacrylic acid on mechanical properties, it was added to PEGDA 2000 hydrogels at 0,  $1.34 \times 10^{-5}$ ,  $2.69 \times 10^{-5}$ ,  $4.03 \times 10^{-5}$ ,  $5.38 \times 10^{-5}$ , or  $6.72 \times 10^{-5}$  mol. It was immediately apparent that polyacrylic acid interfered with gelation, as the highest concentrations required an overnight incubation to solidify. All concentrations (other than the lowest) required  $\geq 20$  min to gel. This gelation time renders them ineffective for our wound dressing platform, which requires rapid gelation since the hydrogel forms *in situ*.

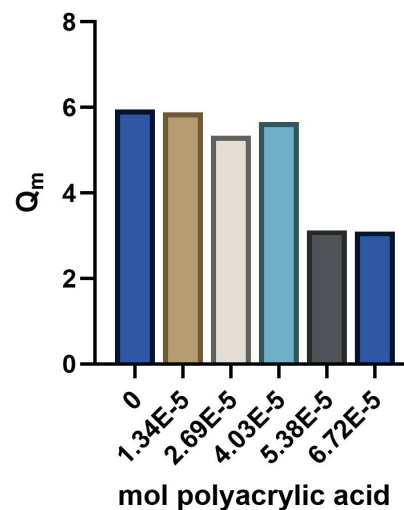


**Figure 5.3.** Mass swelling ratios of PEGDA 2000 hydrogels with varied concentration of polyacrylic acid.



The hydrogels that had been fabricated were used in mass swelling ratios, but further investigation into their mechanical and release properties was terminated because it was unsuitable for this platform. After swelling the polyacrylic acid hydrogels to equilibrium, the swollen mass was recorded and compared to the dry mass after lyophilization. The mass swelling ratios,  $Q_m$ , supported the inhibitory effect of polyacrylic acid on gelation, with  $Q_m$  decreasing as the amount of acrylic acid increased (Fig. 5.3).

SPA was introduced into the PEGDA 3350 hydrogels to evaluate its effect on mechanical properties and release kinetics of the therapeutic agents. Hydrogels were prepared as usual, adding 0-40 mg/mL SPA (0-4 wt%, respectively). After reaching equilibrium swelling, the hydrogels underwent mechanical characterization, evaluating elastic moduli and mass swelling ratios (Figure 5.4). There is a clear downward trend in elastic modulus as a function of SPA concentration, decreasing from 189.3 kPa for 0 mg/mL to 8.1 kPa for 40 mg/mL SPA. Aligned with our previous findings, mass swelling exhibits the opposite trend, increasing from 7.4 to 9.6. It is worth nothing that the addition of SPA made the hydrogels inhomogeneous, with visible lumps. This heterogeneity is reflected in the high standard deviations of the elastic moduli.

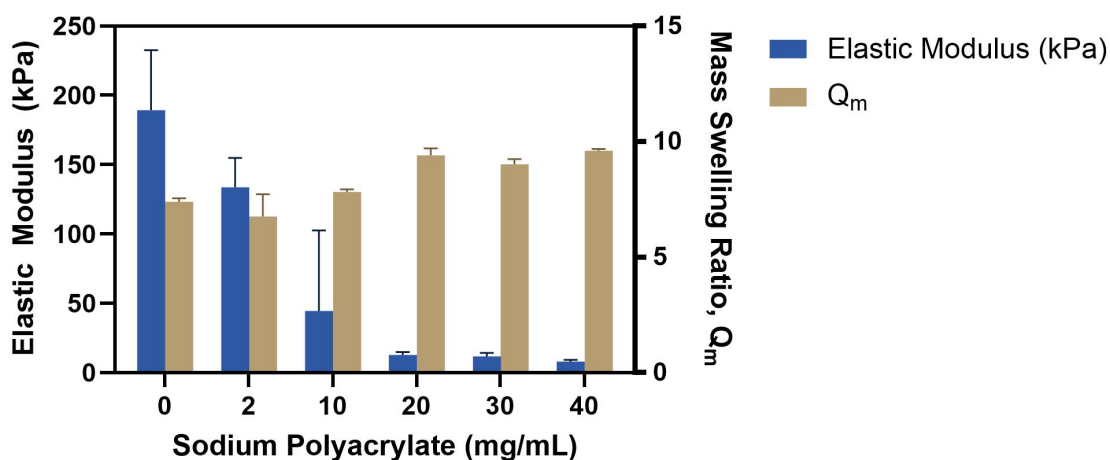


**Figure 5.4.** Mechanical properties of PEGDA 3350 hydrogels incorporating varied amounts of sodium polyacrylate.

**Stability studies.** Stability studies were designed to evaluate macromer solubility, chemical stability, and hydrogel gelation after storage for 1 day, 1 week, and 3 months at elevated temperatures. At each time point, <sup>1</sup>H NMR spectra of PEGDA 3350 and TEMED were recorded to evaluate degradation and autopolymerization. The percent acrylation of PEGDA at Day 0 was 75% and remained unchanged at Month 3, indicating it had not autopolymerized (**Figure S5.4**). While both PEGDA and APS remained stable for the duration of this experiment, TEMED rapidly evaporated from the Eppendorf tube and was unable to be characterized. This indicates the need for improved packaging or a less volatile amine-based initiator for the system. Using the PEGDA and APS after each incubation period, and freshly prepared TEMED, the reagents solubilized easily and hydrogel gelation proceeded normally, indicating high stability of this system.

**Therapeutic Release Kinetics.** To evaluate the rate of drug diffusion out of the hydrogels, calibration curves were first made to relate concentration to UV absorbance (**Figure S5.5**). This was done without issue for bupivacaine, lidocaine, and vancomycin. However, tobramycin and tranexamic acid lack UV absorbing chromophores, necessitating alternative detection approaches. A ferric chloride assay was used to detect tobramycin and tranexamic acid, and an additional copper sulfate assay was developed to quantify tobramycin at high concentrations (**Fig. S5.6**). While this ferric chloride assay has previously been reported to detect tranexamic acid, to our knowledge, this is its first reported use for the detection of tobramycin [26].

Kinetic release profiles were generated for hydrogels containing each of the individual therapeutic agents (**Figure 5.5**). The amount of drug to be loaded into the hydrogels was determined using the calibration curves, such that the eluted drug—particularly at the earlier time points—would be detectable by UV-Vis spectroscopy. Hydrogel sample discs were fabricated as previously described using a 6 mm biopsy punch, preparing three drug-loaded replicates and one

blank (unloaded sample disc) for each time point. The discs were placed in 1 mL DI H<sub>2</sub>O in a 48-well plate. At each time point (e.g. 30 min, 1 h, 2 h, etc.) the absorbance of the water from the drug-loaded hydrogels was quantified with a UV-Vis spectrometer, using water from the blank hydrogel at the absorbance blank. This control ensures that if any components, such as initiators or polymer impurities, leach from the hydrogels, it is

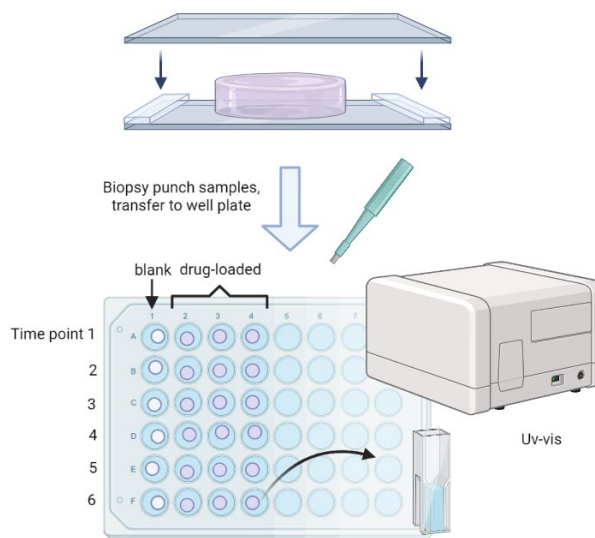


**Figure 5.5.** *In vitro* therapeutic release characterization workflow.

corrected for. Using the calibration curves that had been created for each therapeutic agent, the absorbance is converted into concentration. Through this, we can determine the concentration of released drug at each time point, creating a kinetic release curve.

Kinetic release profiles of each therapeutic agent from PEGDA 3350 hydrogels are shown in **Figure 5.6**. For each, the concentration of drug eluted into the water “sink” increases over time until it eventually plateaus, indicating that release of the drug has stopped. Vancomycin slowly eluted from the hydrogels over a 4-day period, while tobramycin released faster, with concentration plateauing after approximately 24 h. Lidocaine diffuses out of the hydrogel over a 2.5 day period, with 80% released within 8 h. Finally, tranexamic acid exhibits burst release, diffusing out of the hydrogel within 8 h.

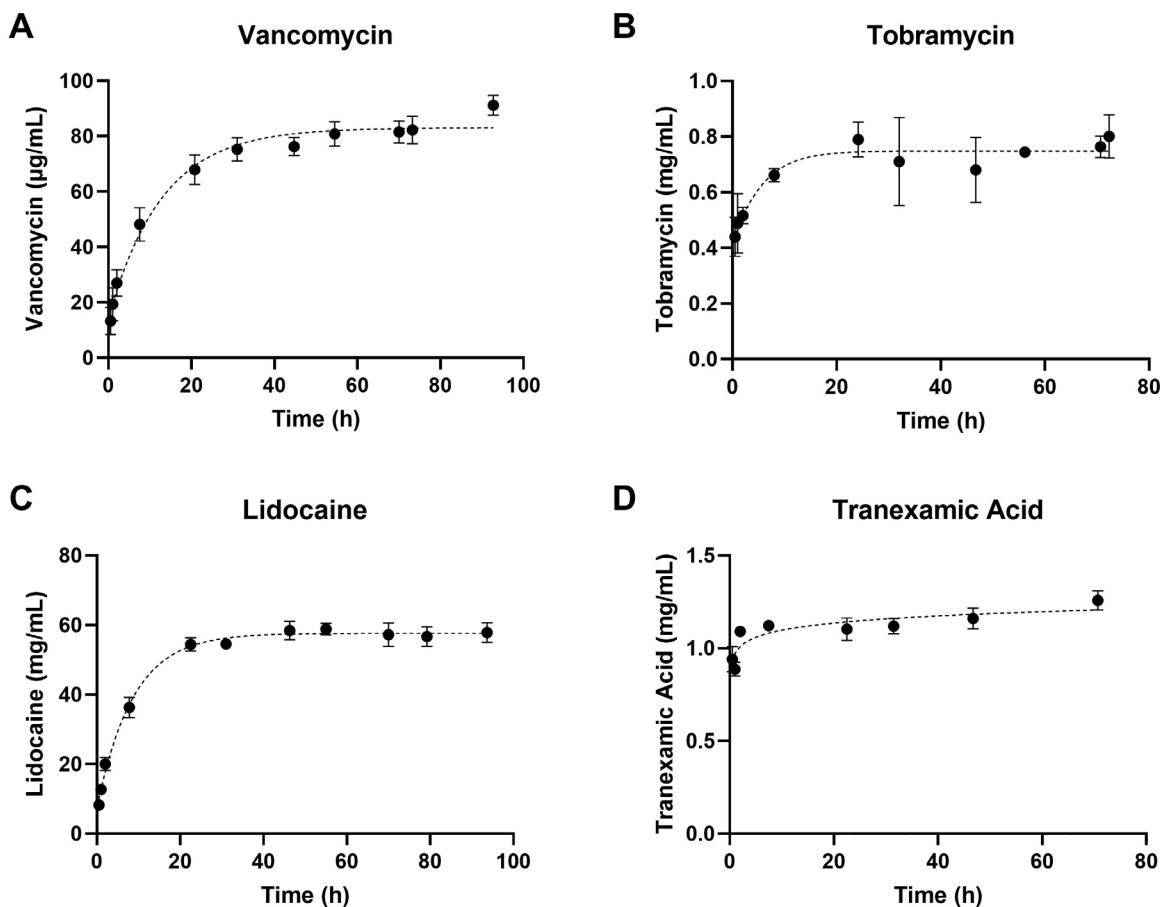


**Figure 5.6.** Therapeutic release curves of (a) vancomycin, (b) tobramycin, (c) lidocaine, and (d) tranexamic acid from PEGDA 3350 hydrogels.

**Adjusting Release Kinetics.** Polyacrylic acid introduces negative charges throughout the hydrogel network. This was expected to electrostatically interact with the loaded therapeutics and slow their release from the system. Incorporating  $6.72 \times 10^{-5}$  mol acrylic acid (a 5:1 molar ratio of acrylic acid to drug) into a PEGDA 2000 hydrogel showed a marked slowing of lidocaine release (**Figure S5.7**). Lidocaine release from the acrylic acid-containing hydrogel was sustained for at least 60 hours, while release from the control hydrogel, free of acrylic acid, plateaued after approximately 32 h. Vancomycin release from PEGDA 3350 and PEGDA 4600 hydrogels, with and without the same concentration of acrylic acid, was then evaluated (**Figure 5.7**). There was a marginal decrease in the release rate of vancomycin from acrylic acid-containing hydrogels of both

molecular weights. The overall amount of drug released from the PEGDA 4600-based hydrogels was lower, which is unexpected, as the larger mesh size of these hydrogels is expected to permit more rapid diffusion and release of the large antibiotics.

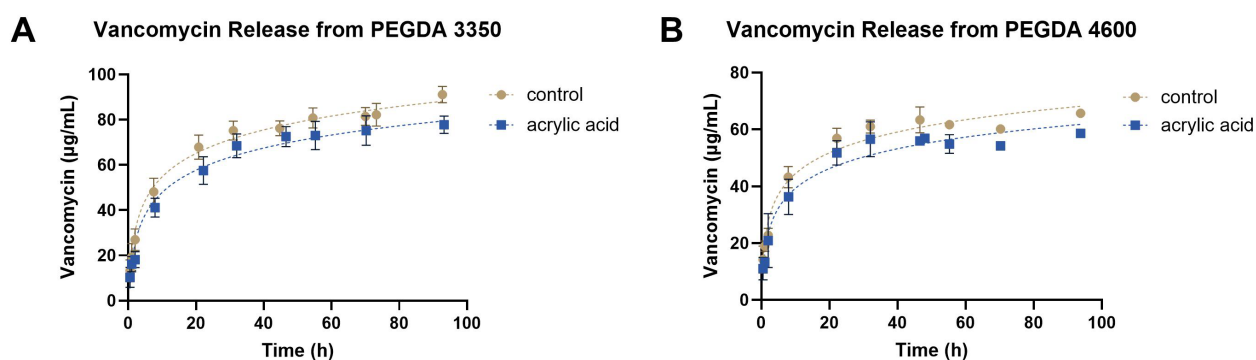


**Figure 5.7.** Vancomycin release from (A) PEGDA 3350 and (B) PEGDA 4600 hydrogels with and without acrylic acid.

Alternatively, SPA forms a network within the crosslinked PEGDA mesh that should physically entrap therapeutic agents within the network, slowing their release. To evaluate its effect on the release rate of therapeutic agents, a 0.0020 g SPA (or 2 wt%) was added to the PEGDA 3350 hydrogel solutions. The release of vancomycin and lidocaine from these hydrogels were evaluated relative to control hydrogels with no SPA (**Figure 5.8**). The release of vancomycin in hydrogels containing SPA appeared to plateau after approximately 30 h. Lidocaine exhibited burst release in hydrogels with and without SPA, but in the latter released an additional 0.02 mg after the first 30 h.

However, these approaches to modifying release rates were not further pursued, due to their marked impact on mechanical properties and incomplete homogenization, leading to unpredictable hydrogels.

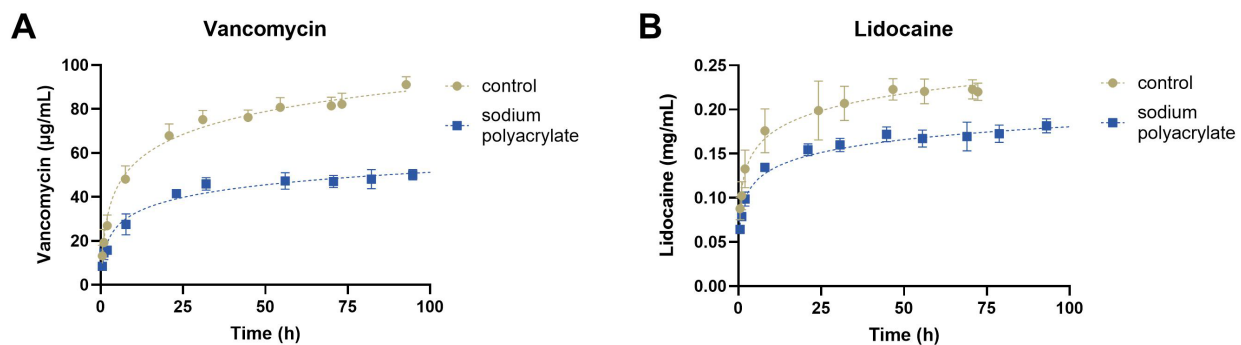


**Figure 5.8.** Therapeutic release curves of (A) vancomycin and (B) lidocaine from PEGDA 3350 hydrogels with and without sodium polyacrylate.

The mechanical characterization and therapeutic release profiles were used to guide the selection of the final hydrogel system. Because of the significant adverse effects on mechanical properties, we chose to proceed using hydrogels without polyacrylic acid or sodium polyacrylate. Additionally, the ideal polymer would be powder based to eliminate the weight and storage concerns of liquid reagents. Lower molecular weight poly(ethylene glycol) is a liquid at room temperature, directing us toward poly(ethylene glycol) of molecular weight 2000 (which is a waxy solid) and greater. For the optimized system, we selected PEGDA 3350. Hydrogels fabricated using this polymer had a good swelling ratio and elastic modulus close to that of the human (40 kPa) [27]. Further, poly(ethylene glycol) 3350, used to synthesize PEGDA 3350, is FDA approved for laxatives (MiraLax®). This will streamline the regulatory approval process for our novel wound dressing.

**Efficacy of released antibiotics.** This work was done in direct collaboration with Amaka Enueme. This study aimed to validate that antibiotics released from the hydrogels over 5 days retained their antimicrobial activity against *S. aureus* and *E. coli*. The standard hydrogel sample discs—either drug-free (“blank”), or loaded with vancomycin, tobramycin, or both antibiotics—were fabricated and incubated in PBS for 5 days. An additional set of calibration curves for

vancomycin and tobramycin were prepared in PBS (**Figure S5.8**) to evaluate the amount of antibiotics released after a 5-day incubation. We determined that approximately 177.5  $\mu\text{g}$  vancomycin (23.6%) and 239.3  $\mu\text{g}$  tobramycin (27.8%) had been released from hydrogel discs.

The minimum inhibitory concentration (MIC) for these released antibiotics was determined using a broth microdilution assay with the hydrogel eluent. Briefly, the eluent underwent serial dilutions in LB broth and was added to media cultures of *E. coli* and *S. aureus*. After an overnight incubation, the dilution at which bacterial growth is inhibited (where the wells appear clear instead of turbid) is considered the MIC. Plate maps showing the eluent dilutions of each well are shown in **Figure S5.9**. The tobramycin- and vancomycin-loaded hydrogels were first evaluated individually against *E. coli* and *S. aureus*, respectively (**Figure 5.9A**). Tobramycin released from the hydrogels exhibited a MIC of  $7.48 \pm 1.70 \mu\text{g/mL}$ , and vancomycin demonstrated a MIC of  $4.60 \pm 1.50 \mu\text{g/mL}$ . While both of these values are marginally higher than the literature MICs for these antibiotics, they remain on the same order of magnitude. Antimicrobial activity of the eluent from

the dual antibiotic-loaded hydrogels was then tested against both *E. coli* and *S. aureus* (**Figure 5.9B**).

Interestingly, hydrogels containing both antibiotics demonstrated improved efficacy against the two bacterial species, despite one being gram-positive

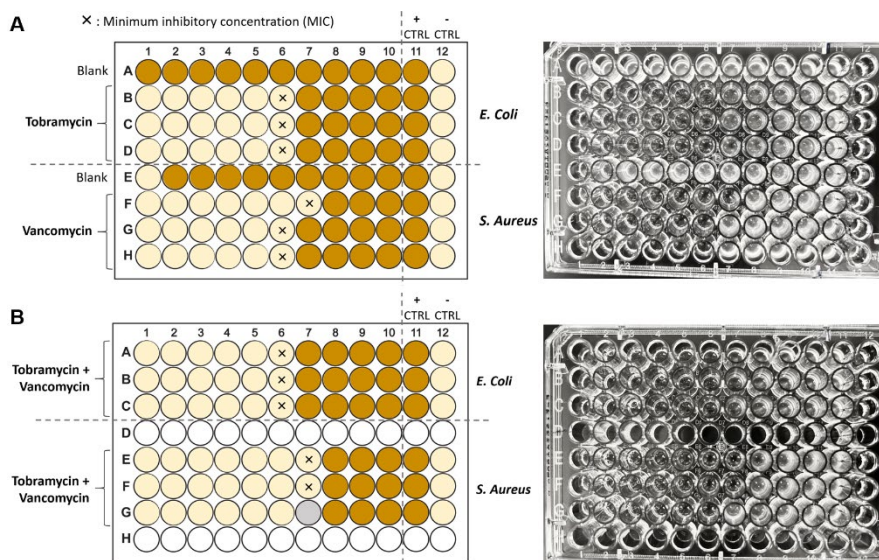


**Figure 5.9.** Broth microdilution assay for PEGDA 3350 hydrogels (A) loaded with either tobramycin or vancomycin and (B) loaded with both tobramycin and vancomycin. MIC results are graphically depicted (*left*) and the original scanned plates are shown (*right*).

and the other being gram-negative. Vancomycin released from the dual-antibiotic hydrogel resulted in a MICs of  $3.60 \pm 0.30 \mu\text{g/mL}$  for *S. aureus*, and the released vancomycin had a MIC of  $5.37 \pm 0.50 \mu\text{g/mL}$  for *E. coli*. These results, alongside CLSI and literature standards, are listed in **Table 5.2**.

**Table 5.2.** MIC of antibiotics released from hydrogels against *S. aureus* and *E. coli*.

	<b>MIC (CLSI/Lit.)</b>	<b>Tobramycin Hydrogel</b>	<b>Vancomycin Hydrogel</b>	<b>Tobramycin + Vancomycin Hydrogel</b>
<i>S. Aureus</i>	$\leq 2 \mu\text{g/mL}$	–	$4.60 \pm 1.50 \mu\text{g/mL}$	$3.60 \pm 0.30 \mu\text{g/mL}$
<i>E. Coli</i>	$\leq 1 \mu\text{g/mL}$	$7.48 \pm 1.70 \mu\text{g/mL}$	–	$5.37 \pm 0.50 \mu\text{g/mL}$

***In vivo* testing.** *In vivo* testing of this hydrogel system was performed by our collaborators at UCLA’s David Geffen School of Medicine (Dr. Bernthal’s group, who performed small animal studies) and University of Texas Medical Branch (Dr. Wenke’s group, who performed large animal studies). These results are briefly overviewed here to highlight the *in vivo* efficacy of our hydrogel wound dressing. Our collaborators with Dr. Bernthal’s group first performed *ex vivo* thromboelastography analysis to verify that tranexamic acid released from the hydrogels was able to form stable clots. This was tested on hydrogels that only contained tranexamic acid as well as those that contained all four therapeutic agents. They found that multidrug-loading did not affect tranexamic acid release, and in both groups, it was able to prevent fibrinolysis and form stable clots. They also tested the wound dressing in an open fracture murine model was inoculated with  $1 \times 10^5$  CFUs of *S. aureus*,  $1 \times 10^2$  CFUs of *P. aeruginosa*, and  $1 \times 10^3$  CFUs of *E. coli* (all strains bioluminescent). A 300  $\mu\text{L}$  hydrogel solution, with drug concentrations outlined in 5.3 “*Drug Stock Solutions*”, was prepared and pipetted into the wound bed. After gelation, the incision was



sutured closed (Fig. S5.10).

Bioluminescence, reflective of bacterial burden, was tracked in real-time. The bioluminescence of the drug-loaded hydrogel group gradually decreased over three days until it reached the sterile control line (Fig. 5.10). This indicates that antibiotics

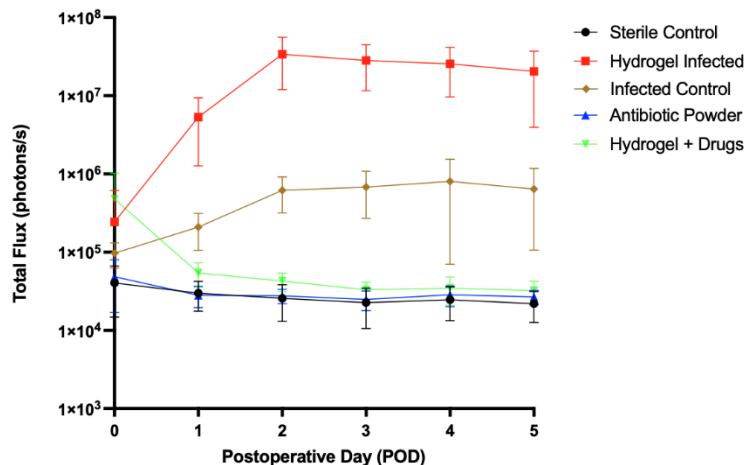


**Figure 5.10.** Longitudinal bioluminescence, reflecting bacterial burden, of murine open fracture model treated with hydrogel wound dressing.

consistently elute from the hydrogel over three days, which aligns with our *in vitro* kinetic release profiles. The drug-loaded hydrogel was able to eradicate an aggressive polymicrobial infection in murine models.

Finally, our collaborators in the Wenke group advanced *in vivo* studies into large animals. An open fracture and complex wound was created in the proximal tibia of ten adult Merino female sheep ( $39.5 \pm 1.3$ kg) under deep anesthesia [28]. After removing a 35 cm<sup>2</sup> rectangular section of skin and fascia, the periosteum was stripped and a 10 mm unicortical defect was created in the proximal tibia. Thirteen grams of muscle was removed, followed by a freeze injury and a thermal burn injury (Fig. S5.11). Finally, the wound was contaminated with  $1 \times 10^8$  CFUs of bioluminescent *S. aureus*. Six hours after inoculation, the wound was imaged using a photon-counting camera, thoroughly debrided, and imaged again. The wound was either bandaged (control group) or a 35 mL pre-cast hydrogel containing all four therapeutic agents was applied to the injury (hydrogel group). After 48 h, the bioluminescent bacterial burden of the wound was imaged again.

After a 48 h incubation following debridement, the control group (*grey*) exhibited an *S. aureus* burden of  $632.1 \pm 602.6\%$  relative to pre-debridement levels (**Fig. 5.11**). The hydrogel-treated group had a significantly lower burden of  $8.1 \pm 11.9\%$  (*blue*). The large standard deviation of the hydrogel group is due one of the animal participants, in which the hydrogel had slipped out of place. Even in this instance, the bacterial burden was 25.8% relative to pre-debridement levels. Were this animal participant excluded from analysis, the hydrogel-treated group exhibits a burden of  $2.3 \pm 2.0\%$ . Even factoring in the potential for error, the PEGDA wound dressing appears highly effective in eliminating infections in large animal models as well as small animal.

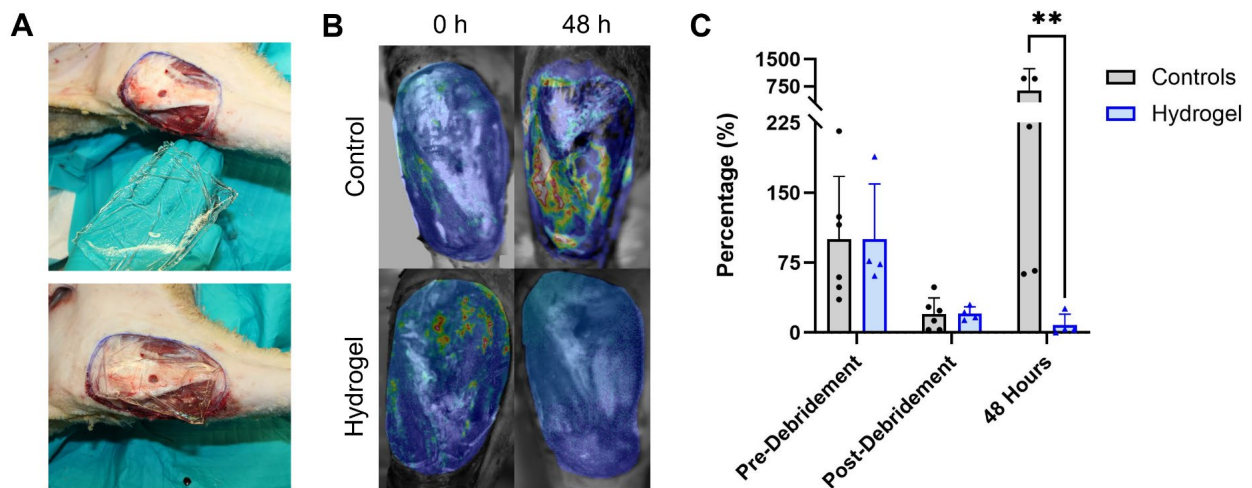


**Figure 5.11.** Hydrogel wound dressing eradicated a robust *S. aureus* infection in Merino sheep wound model.

(A) A 35 mL hydrogel containing all therapeutic agents was cast, placed into the wound bed, and secured with a compression bandage. (B) Images of bioluminescent bacteria after debridement (*left*) and after 48 h (*right*) in the control and hydrogel-treated groups. (C) *S. aureus* burden, normalized to pre-debridement values, in the control and hydrogel-treated groups.

### 5.3 Conclusions

Military operations in remote environments require innovations to PFC to better care for wounded soldiers. This work aimed to develop a easy to use field-polymerizable hydrogel wound dressing that can provide controlled delivery of antimicrobial, analgesic, and hemostatic agents.

Preliminary mechanical characterization and therapeutic release profiles were used to guide our selection of PEGDA 3350 for the hydrogel wound dressing. Poly(ethylene glycol) 3350 is FDA approved for laxatives, and we anticipate that this will streamline regulatory approval process for the described wound dressing system. Unlike lower molecular weight PEGDA, it is a powder at room temperature, satisfying the PFC criteria for lightweight interventions.

Using commercially available poly(ethylene glycol) 3350 as the starting material, we synthesized PEGDA 3350 with high yield and purity. This polymer remained stable at an elevated temperature (46°C) for at least 3 months, which is particularly important due to the inhospitable conditions of some remote combat environments. These hydrogels rapidly form in less than 2 min after adding redox initiators, with high reproducibility. The PEGDA 3350 hydrogel was tailored to provide controlled release of antibiotic agents over 4 days, while allowing for the burst release of smaller analgesic and hemostatic agents into the local wound environment. This addresses the acute need for hemostasis and pain relief, while aiming to prevent bacteria from colonizing the wound in the days following injury.

*In vivo* studies confirmed that these wound dressings are both safe and effective. In a murine open fracture model, the hydrogels eradicated a robust polymicrobial infection. Even after scaling hydrogel volume by 35× when advancing to large animal models, the wound dressing proved effective. It successfully eliminated an aggressive *S. aureus* infection in a complex musculoskeletal wound in Merino sheep,

The next phase of this work will be i) optimizing release kinetics using hydrogels crosslinked with the nontoxic initiators from Chapter 4 (simultaneously overcoming the issues associated with the volatility of TEMED) and ii) transitioning to clinical trials. Under Public Law 115-92, the FDA is able to expedite review of products to treat life-threatening conditions that impact military personnel. Once the current hydrogel platform begins this transition, we can begin exploring the plethora of other applications for this tunable wound dressing. The system developed in this work may have a significant impact not only on PFC, but on a wide range of humans and animals suffering from dermal injuries.

## 5.4 Experimental

**Synthesis of poly(ethylene glycol)-diacrylate.** Poly(ethylene glycol)-diacrylate (PEGDA) was synthesized as described in **Chapter 4**. In addition to poly(ethylene glycol) 3350 (INTEGRA – Kent, WA, USA), we also acrylated poly(ethylene glycol) 2000 (Alfa Aesar – Ward Hill, MA, USA) and 4600 (Sigma Aldrich – St. Louis, MO, USA) using the same procedure to isolate PEGDA 2000, 3350, and 4600 as white powders (**Figures S5.1-S5.3**).

*PEGDA 2000.* Yield: 1.2 g, 62.5%, Conversion: 82.3%.  $^1\text{H NMR}$  ( $\text{CDCl}_3$ , ppm):  $\delta=6.50$  (d, 2H), 6.20 (m, 2H), 5.82 (d, 2H), 4.25 (t, 4H), 3.73 (t, 4H) 3.64 (m, 172H).

*PEGDA 3350.* Yield: 6.9 g, 80.1%; Conversion: 90.5%.  $^1\text{H NMR}$  ( $\text{CDCl}_3$ , ppm):  $\delta=6.50$  (d, 2H), 6.20 (m, 2H), 5.82 (d, 2H), 4.25 (t, 4H), 3.73 (t, 4H) 3.64 (m, 292H).

*PEGDA 4600.* Yield: 3.0 g, 65.2%; Conversion: 87.2%.  $^1\text{H NMR}$  ( $\text{CDCl}_3$ , ppm):  $\delta=6.50$  (d, 2H), 6.20 (m, 2H), 5.82 (d, 2H), 4.25 (t, 4H), 3.73 (t, 4H) 3.64 (m, 408H).

**Drug Stock Solutions.** Each therapeutic agent was used to create fresh aqueous stock solutions. The drugs were weighed and diluted using DI H<sub>2</sub>O to the desired concentrations. For *in vitro* experiments, concentrations of 10.5 mg/mL for bupivacaine (Alfa Aesar – Ward Hill, MA, USA) or lidocaine HCl (MP Biomedicals – Santa Ana, CA, USA), 191.6 mg/mL for tranexamic acid (Acros Organics – Geel, Belgium), 5.2 mg/mL for vancomycin (ThermoScientific Chemicals – Waltham, MA, USA), and 92.9 mg/mL for tobramycin (TCI – Tokyo, Japan) were used. For *in vivo* murine experiments, each hydrogel contained 4 mg vancomycin, 4.57 mg tobramycin, 5.56 mg tranexamic acid, and 1.38 mg lidocaine. The mass of each therapeutic agent added was kept constant, regardless of final hydrogel volume. *In vivo* Merino sheep experiments used concentrations of 0.5375 g vancomycin, 0.6390 g tobramycin, 0.7790 g tranexamic acid, and 0.1925 g lidocaine in each 35 mL hydrogel.

**Table 5.3.** Final reagent concentrations in pre-gel solution.

Reagent	Concentration
PEGDA	24.14 wt%
APS	30 mM
TEMED	30 mM

**PEGDA Hydrogels.** Final concentrations of PEGDA, APS, and TEMED were kept consistent for *in vitro* and *in vivo* experiments (**Table 5.3**). PEGDA was diluted to 35.5 wt% in DI H<sub>2</sub>O and vortexed until dissolved. TEMED (Amresco – Solon, OH, USA) and APS (VWR – Radnor, PA, USA) were diluted to 1 M, prepared fresh prior to each use.

To prepare 1 mL hydrogels, 680 μL 35.5 wt% PEGDA and 260 μL DI H<sub>2</sub>O or drug stock solution were combined in an Eppendorf tube. To initiate crosslinking, 30 μL 1 M TEMED and 30 μL 1 M APS were added, pipette mixed, and immediately used. For murine experiments, hydrogel volume was reduced to 300 μL, with each reagent scaled by 0.3. For ovine experiments, hydrogel volume was increased to 35 mL, scaling each reagent by 35.

**Mechanical characterization.** Mechanical characterization was performed on hydrogels fabricated using a range of PEGDA molecular weights to evaluate elastic moduli and swelling ratios. Mass swelling ratios were calculated by taking the ratio of swollen hydrogel mass to the dry hydrogel mass following lyophilization. A dynamic mechanical analyzer (Q-800, TA Instruments – New Castle, DE, USA) was used to measure the elastic modulus of hydrogels. The diameter of each hydrogel was measured at three locations using trace calipers, and the average was recorded. The height was measured prior to the run using the “Measure” feature of the Q-800 program. Using a uniaxial compression test, the initial preload force was set to 0.001 N and the initial strain was set to 0.5%, and the system ramped the strain 2.5%/min to a maximum strain of -20%. The resultant stress-strain curve was analyzed using the TA Instruments Universal Analysis 200 program to take the product of the linear region of the graph and the maximum strain of the run to calculate elastic modulus. Both of these characterization techniques were performed on separate triplicate samples.

**Stability studies.** PEGDA 3350, TEMED, and APS samples stored in capped Eppendorf tubes were placed on a pre-heated heat block at 46°C. At each time point, <sup>1</sup>H NMR spectra of PEGDA and TEMED were recorded to evaluate degradation. PEGDA was diluted to the standard 35.5 wt%, and the solubility was observed to ensure that it had not prematurely polymerized. Finally, the samples were used to fabricate hydrogels to verify the gelation time had not significantly changed.

**Calibration curves.** *In vitro* calibration curves of each therapeutic agent in water within relevant concentration ranges were obtained, to relate UV-Vis absorbance to drug concentration. During *in vitro* kinetic release experiments, these calibration curves were used to plot concentration as a function of time, producing drug release profiles.

Because tobramycin and tranexamic acid lack UV absorbing chromophores, they required additional reagents to make them detectable via UV-Vis spectroscopy. A final concentration of 0.2% FeCl<sub>3</sub> (99+%, Acros Organics – Geel, Belgium) was added to drug dilutions and absorbance was measured at 370 nm to produce calibration curves for tobramycin and vancomycin (**Fig. S5.5B** and **D**).

A copper sulfate assay was also developed to quantify tobramycin at high concentrations (**Fig. S5.6**). Biuret reagent was prepared by combining 0.4500 g sodium potassium tartrate (99+%, Alfa Aesar – Ward Hill, MA, USA), 0.1500 g copper(II) sulfate pentahydrate (99+%, Acros Organics – Geel, Belgium), and 8 mL 0.1 M NaOH (ACS grade, Fisher Chemical – Waltham, Massachusetts, USA ) and bringing the volume to 50 mL with DI H<sub>2</sub>O. The sample was combined with the reagent in a 1:2 ratio, and absorbance was recorded at 330 nm and 540 nm at each time point.

**Therapeutic Release Kinetics.** For *in vitro* experiments, the experimental work-flow is depicted in **Figure 5.5**. The pre-gel solution was pipetted onto a glass slide with 2 mm spacers, and a glass slide was placed on top. After gelation, a 6 mm biopsy punch was used to make uniform hydrogel sample discs, which were then transferred into individual wells in a 48 well plate. Each time point included one blank PEGDA hydrogel disc and three drug-loaded hydrogel discs in separate wells. One mL DI H<sub>2</sub>O was added to each well, and samples were taken at the following time points: 30 min, 1 h, 2 h, 4 h, 8 h, and every 12 h thereafter for 5 days or until release plateaued.

At each time point, 750 μL of the eluent from the drug-loaded hydrogels was transferred to a cuvette and the absorbance was measured using a UV-Vis spectrometer (Biomate 3S, Thermo Scientific – Waltham, MA, USA), with the unloaded hydrogels serving as the blank. Bupivacaine, lidocaine, and vancomycin were recorded at wavelengths of 262 nm, 263 nm, and 281 nm,

respectively. For tobramycin and tranexamic acid hydrogels, the supernatant was transferred from the wells into individual Eppendorf tubes at each time point, and stored at  $-20^{\circ}\text{C}$  until the last time point had been collected. After thawing,  $400\ \mu\text{L}$  of each sample was transferred into a 48 well plate and  $54.55\ \mu\text{L}$  of a 1.67% solution of  $\text{FeCl}_3$  was added. The absorbance was recorded within 1 h using a plate reader (BioTek Synergy H1 Microplate Reader, Agilent – Santa Clara, CA, USA) at 370 nm, though absorbance remained stable for at least 24 h. The absorbance was converted into concentration, using the calibration curves of each therapeutic agent, allowing the amount of drug released at each time point to be determined.

**Adjusting Release Kinetics.** For gels incorporating polyacrylic acid, stock solutions containing known concentrations of acrylic acid were prepared in DI  $\text{H}_2\text{O}$ , either with or without therapeutic agents. These stock solutions were added to hydrogels in various molar amounts for preliminary testing ( $0\ \text{mol}$ ,  $1.34 \times 10^{-5}$ ,  $2.69 \times 10^{-5}$ ,  $4.03 \times 10^{-5}$ ,  $5.38 \times 10^{-5}$ , and  $6.72 \times 10^{-5}\ \text{mol}$  acrylic acid). Hydrogels incorporating  $6.72 \times 10^{-5}\ \text{mol}$  polyacrylic acid were used to determine the effect of polyacrylic acid incorporation on the release kinetics of lidocaine from PEGDA 2000 hydrogels, and of vancomycin and lidocaine from both PEGDA 3350 and PEGDA 3600 hydrogels.

For hydrogels with SPA, amounts of 0, 2, 10, 20, 40, or 40 mg of SPA (0, 0.2, 1, 2, 3, 4 wt%, respectively) were added to the standard pre-gel solutions before APS and TEMED. For therapeutic release studies, a standard concentration of 2 wt% SPA was used.

**Efficacy of Released Antibiotics.** This work was done in direct collaboration with Amaka Enueme. A broth microdilution assay was performed to validate that antibiotics released from the hydrogel system retained their antimicrobial activity. Drug-free, vancomycin-loaded (V), tobramycin-loaded (T), and vancomycin+tobramycin-loaded (V+T) PEGDA 3350 hydrogels were



prepared as previously described. Antibiotic concentrations were scaled to remain consistent with those used in the murine studies.

The sample discs were incubated at room temperature in 500  $\mu$ L PBS (pH 7.4) for 5 days. UV-Vis spectrometry was used to determine the concentration of vancomycin and tobramycin released from each hydrogel disc. The eluent was then used in an LB broth microdilution assay with *E. coli* and *S. aureus* at burdens of  $5 \times 10^5$  CFU/mL, with sterile media controls and growth controls (**Fig. S5.9**) [29]. If any of the sterile media controls appeared turbid, or any of the growth controls appeared clear, the results are deemed invalid. After incubating at 37°C for 18 h, the plates were examined to determine the minimum inhibitory concentration. The MICs of tobramycin and vancomycin released from hydrogels containing each antibiotic alone was quantified for *E. coli* and *S. aureus*, respectively. These were then compared to the MICs of antibiotics released from the dual-antibiotic-loaded hydrogels.

## 5.5 Appendix D

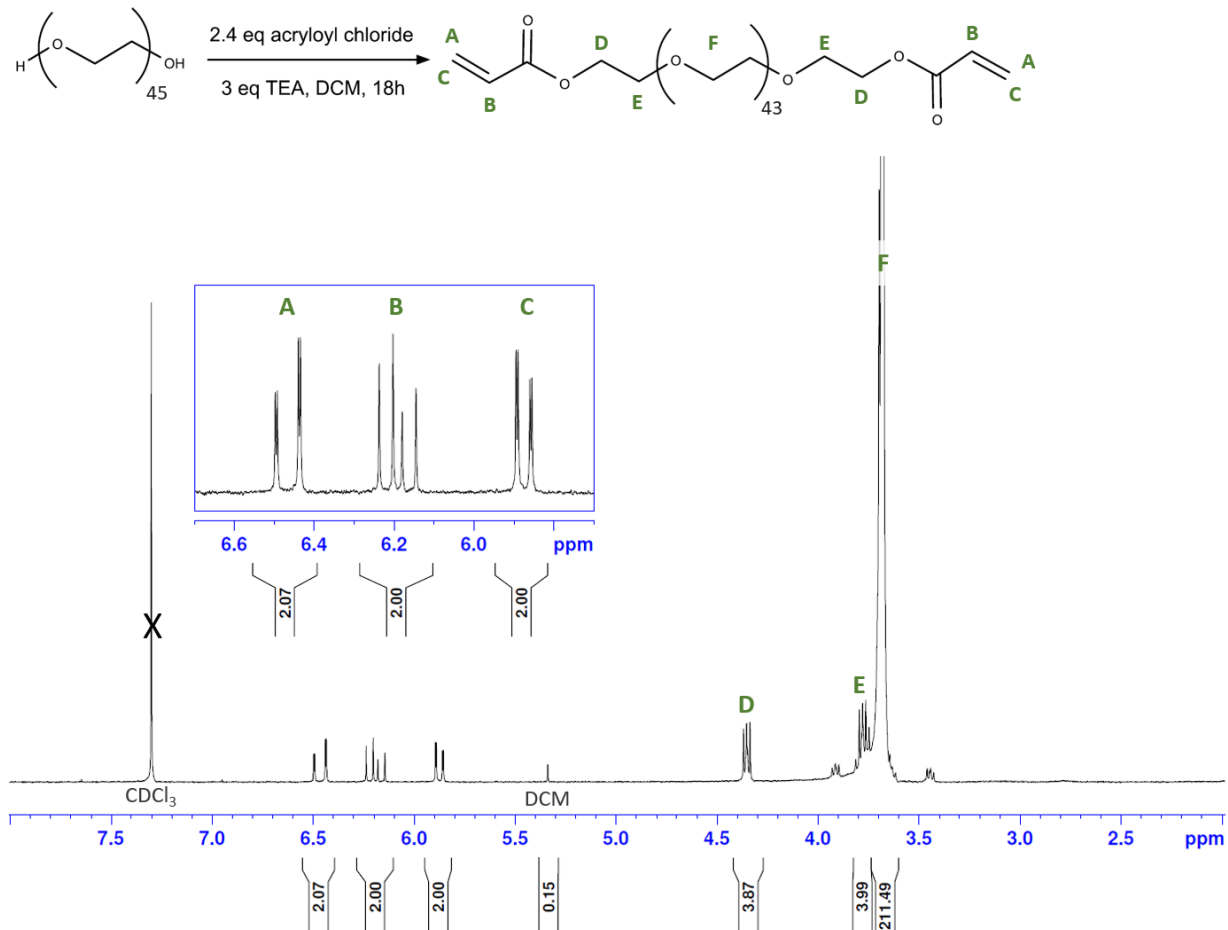


Figure S5.1.  $^1\text{H}$  NMR of PEGDA 2000, in  $\text{CDCl}_3$ .

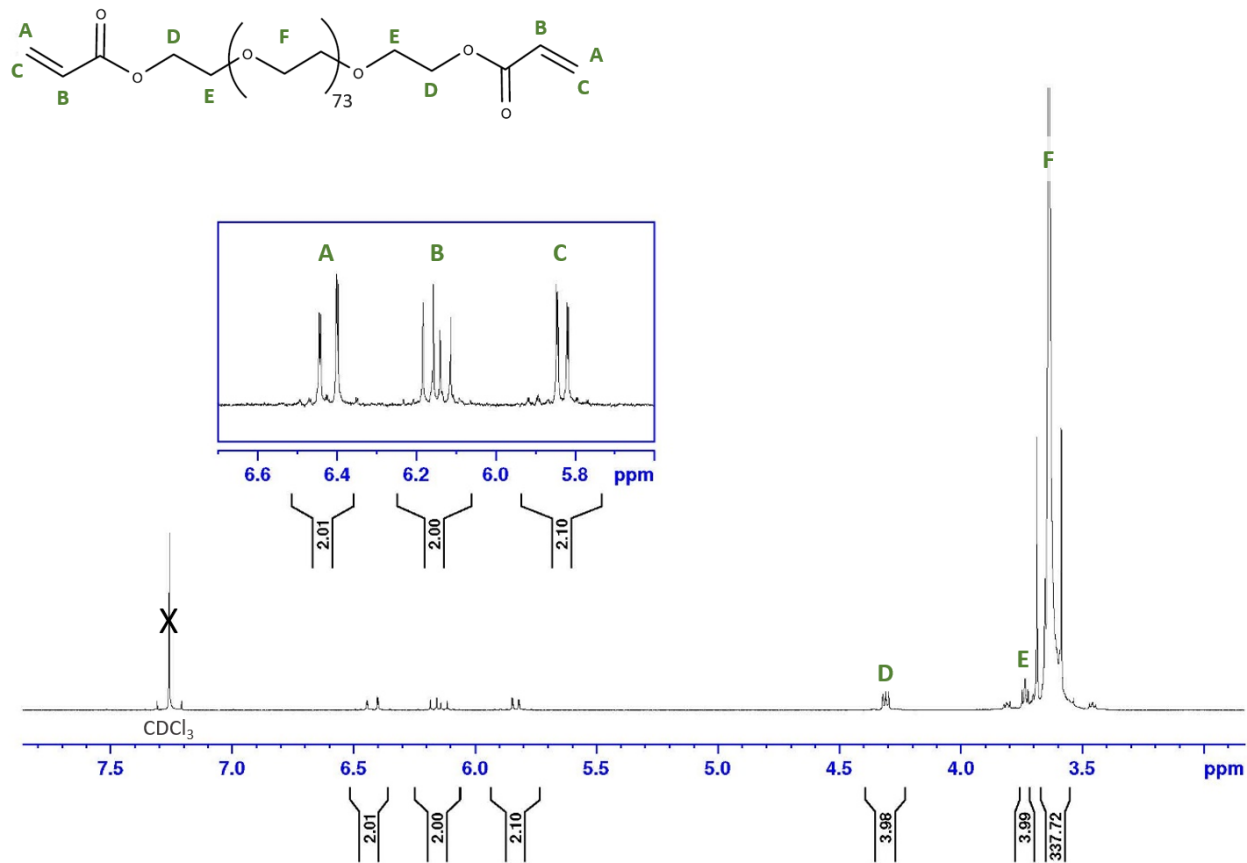
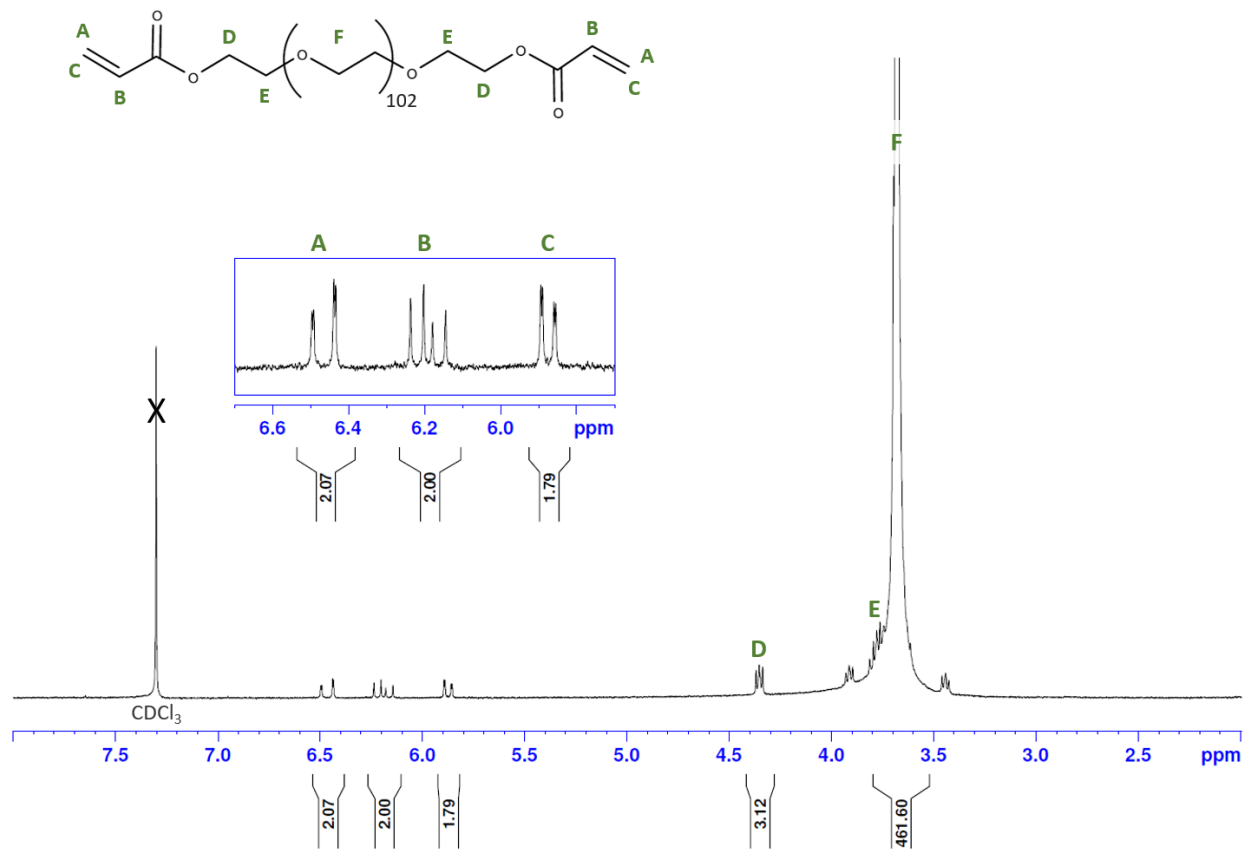
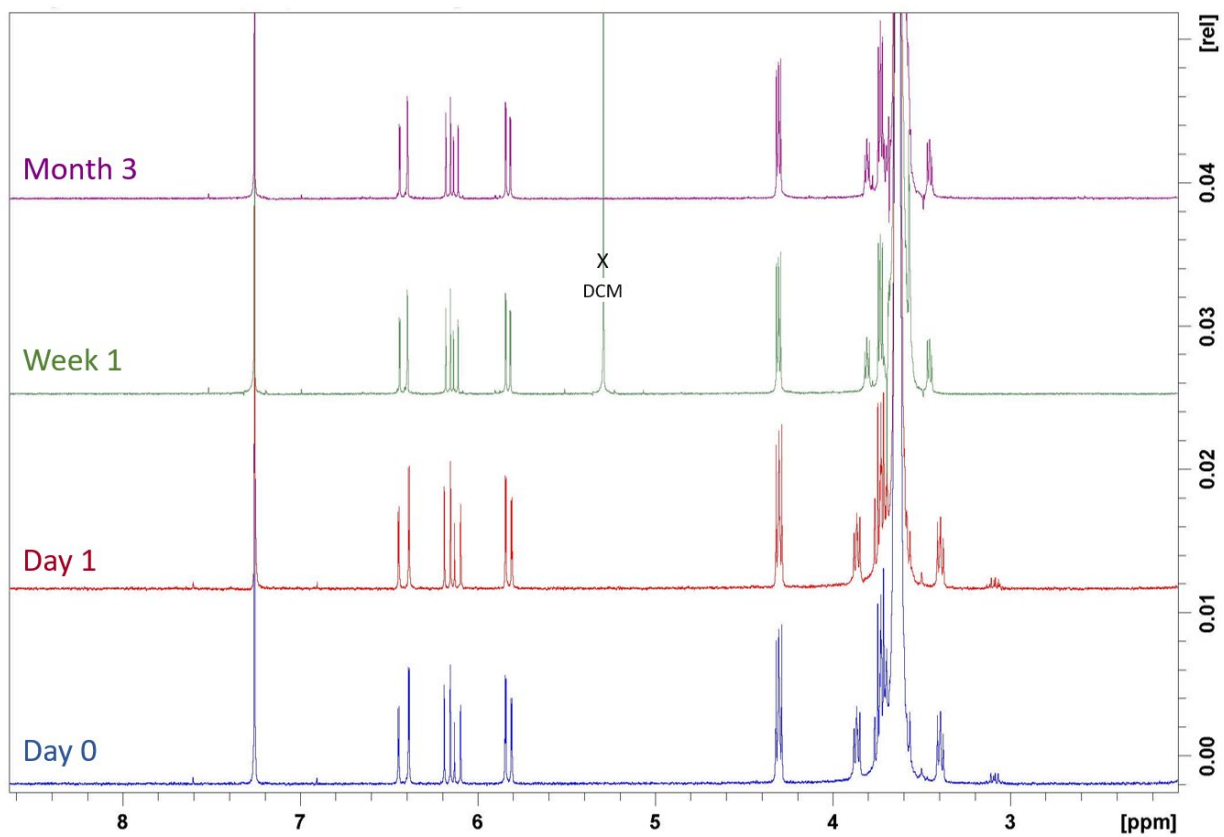


Figure S5.2. <sup>1</sup>H NMR of PEGDA 3350, in CDCl<sub>3</sub>.



**Figure S5.3.**  $^1\text{H}$  NMR of PEGDA 4600, in  $\text{CDCl}_3$ .



**Figure S5.4.**  $^1\text{H}$  NMR of PEGDA 3350 at 0 days (*blue*), 1 day (*red*), 1 week (*green*), and 3 months (*purple*), in  $\text{CDCl}_3$ .

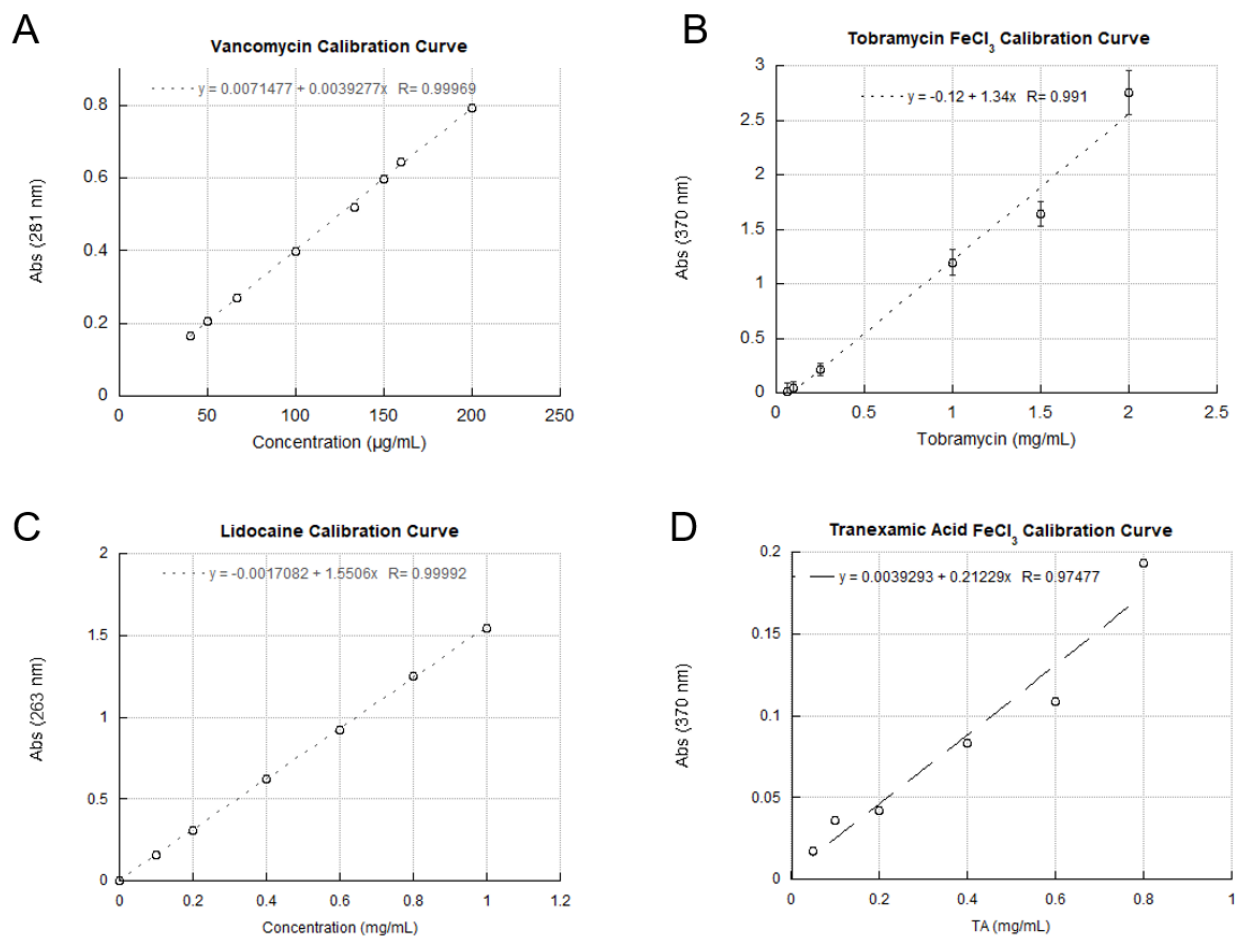


**Figure S5.5.** Calibration curves relating concentration to absorbance of (A) vancomycin at 281 nm, (B) tobramycin with 0.2% Fe(III)Cl at 370 nm, (C) lidocaine at 283 nm, and (D) tranexamic acid with 0.2% Fe(III)Cl at 370 nm.

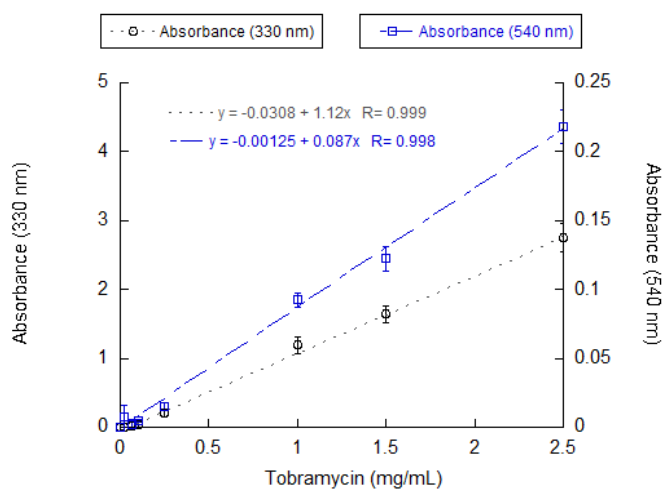


**Figure S5.6.** Calibration curve for tobramycin at high concentrations, with copper sulfate detection at either 330 nm (grey) or 540 nm (blue).

### Lidocaine Release from PEGDA 2000 +/- Acrylic Acid

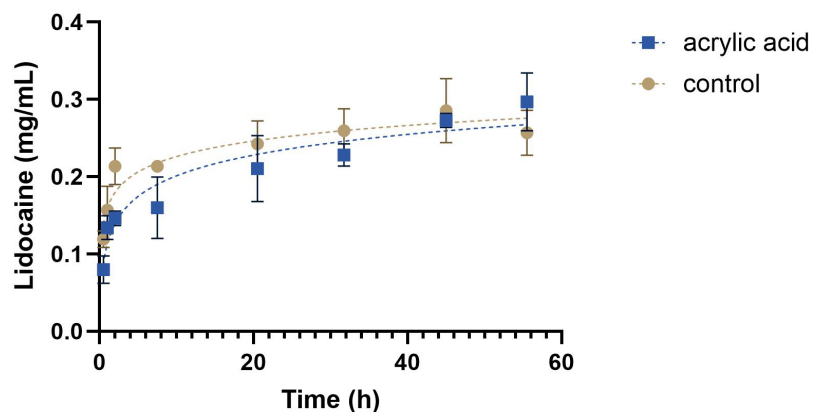


Figure S5.7. Lidocaine release from PEGDA 2000 with and without acrylic acid.

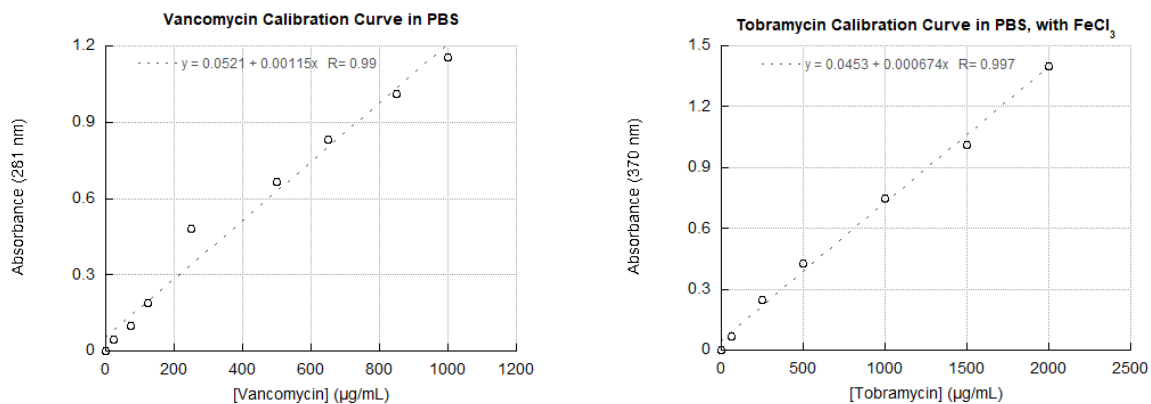
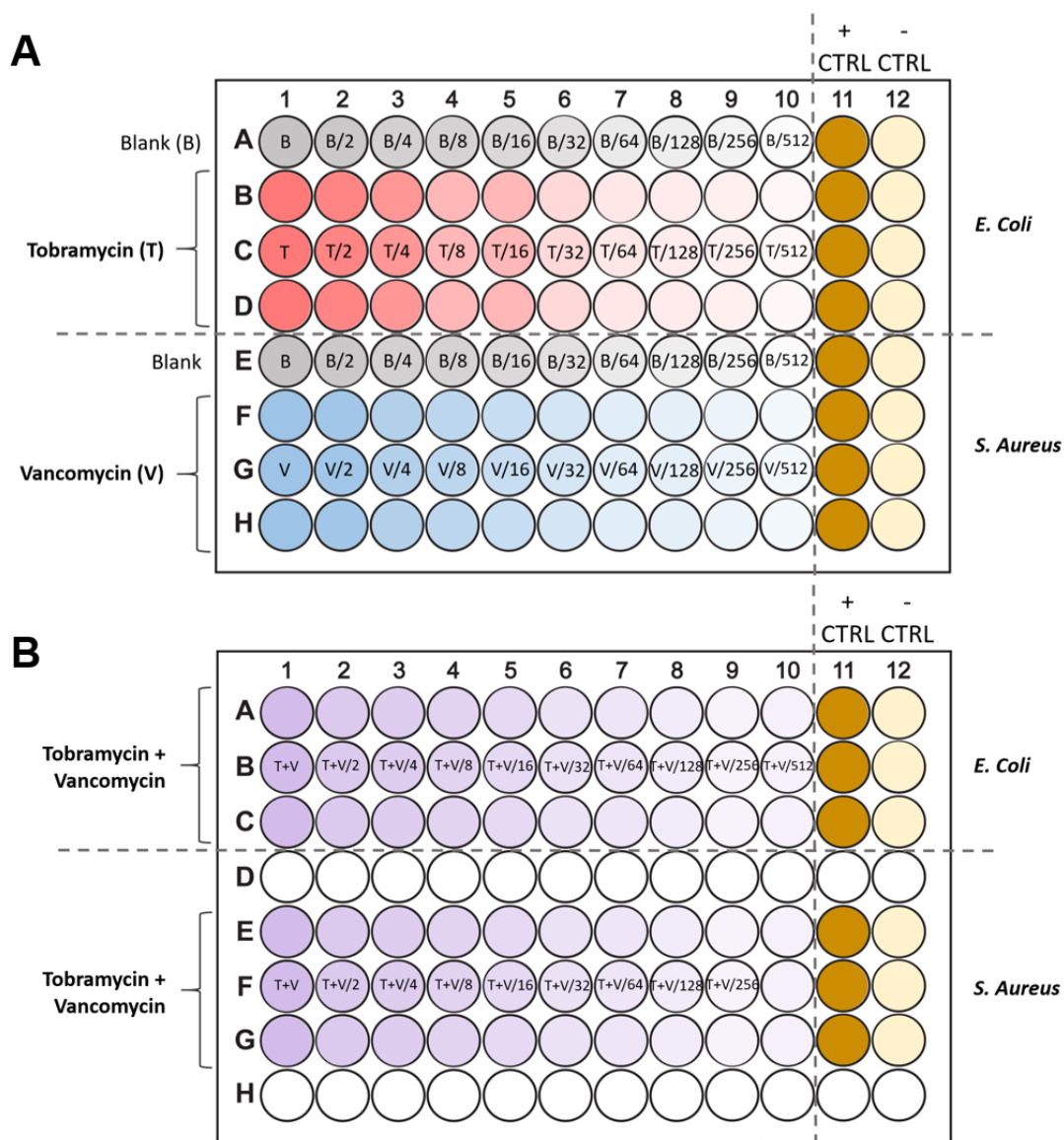
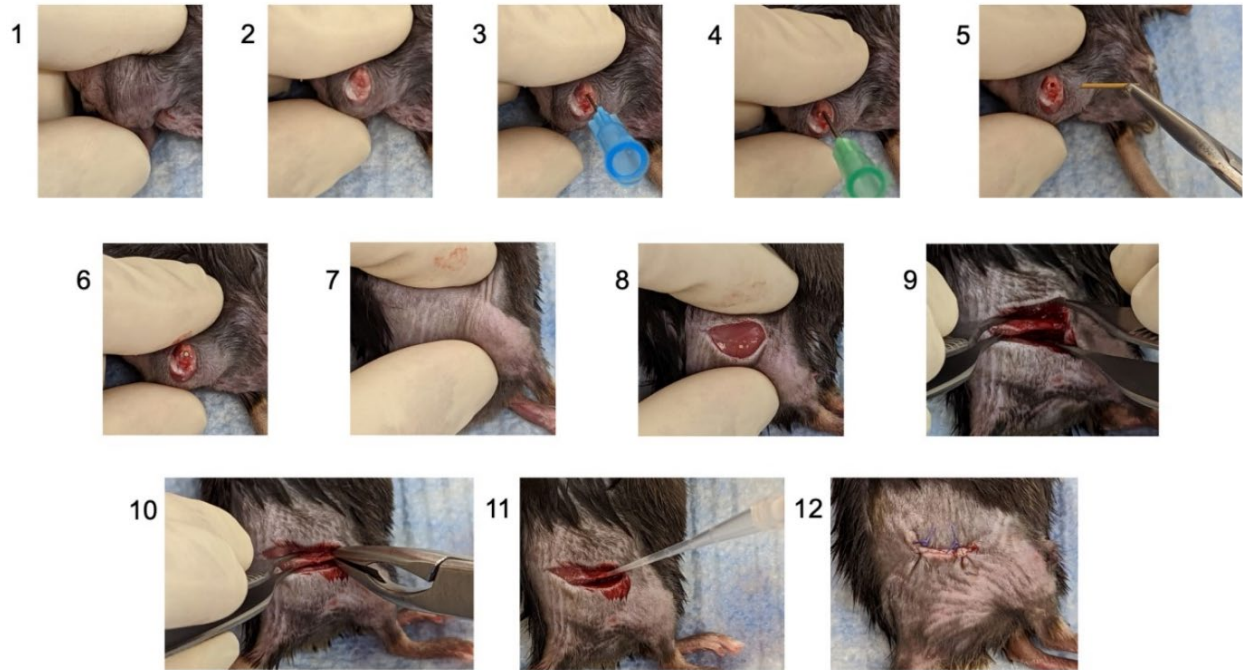


Figure S5.8. Additional calibration curves of vancomycin and tobramycin in PBS.



**Figure S5.9.** Plate maps for broth microdilution assay using tobramycin and vancomycin released from hydrogel. Positive growth controls (11) contain log-phase bacterial culture in media, and negative sterile controls (12) contain media alone.





**Figure S5.10.** Murine open fracture model. After exposing the knee joint (2), the femur is reamed (3,4) and a titanium implant is inserted inside the bone (5,6). The femur is exposed (9) and a cortical defect is created along the distal femur (10). The cortical defect is inoculated with the bacterial suspension (11) and the wound is sutured closed (12).

\*Images provided by Chris Hamad, MD

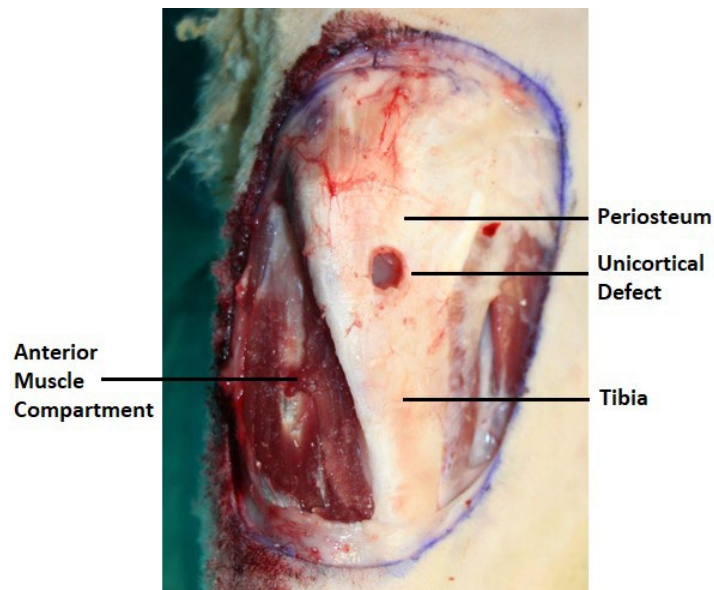


**Figure S5.11.** Ovine complex musculoskeletal wound with injuries to the anterior tibia, muscle, fascia, and periosteum.

\*Image provided by Josh Wenke, PhD and Jared Wainwright, MD

## 5.6 References

- [1] J. D. Cross, J. R. Ficke, J. R. Hsu, *et al.*, “Battlefield orthopaedic injuries cause the majority of long-term disabilities,” *J. Am. Acad. Orthop. Surgens*, vol. 19, pp. S1–S7, 2011.
- [2] R. S. Kotwal, J. T. Howard, J. A. Orman, *et al.*, “The effect of a golden hour policy on the morbidity and mortality of combat casualties,” *JAMA*, vol. 151, no. 1, pp. 15–24, 2016.
- [3] S. Keenan and J. C. Riesberg, “Prolonged field care: Beyond the ‘golden hour,’” *Wilderness Environ. Med.*, vol. 28, no. 2, pp. S135–S139, 2017.
- [4] C. P. Dolan, M. S. Valerio, W. L. Childers, *et al.*, “Prolonged field care for traumatic extremity injuries: defining a role for biologically focused technologies,” *NPJ Regen. Med.*, vol. 6, no. 1, p. 6, 2021.
- [5] X. Wei, J. Cai, C. Wang, *et al.*, “Quaternized chitosan/cellulose composites as enhanced hemostatic and antibacterial sponges for wound healing,” *Int. J. Biol. Macromol.*, vol. 210, pp. 271–281, 2022.
- [6] K. P. Valentine and K. M. Viacheslav, “Bacterial flora of combat wounds from eastern Ukraine and time-specified changes of bacterial recovery during treatment in Ukrainian military hospital,” *BMC Res. Notes*, vol. 10, pp. 1–7, 2017.
- [7] C. B. Ibberson, J. P. Barraza, A. L. Holmes, *et al.*, “Precise spatial structure impacts antimicrobial susceptibility of *S. aureus* in polymicrobial wound infections,” *PNAS*, vol. 119, no. 51, p. e2212340119, 2022.
- [8] S. DeLeon, A. Clinton, H. Fowler, *et al.*, “Synergistic interactions of *Pseudomonas*

- aeruginosa and *Staphylococcus aureus* in an in vitro wound model,” *Infect. Immun.*, vol. 82, no. 11, pp. 4718–4728, 2014.
- [9] S. A. Shackelford, D. J. Del Junco, J. C. Riesberg, *et al.*, “Case-control analysis of prehospital death and prolonged field care survival during recent US military combat operations,” *J. Trauma Acute Care Surg.*, vol. 1, no. 91, p. (2S Suppl 2):S186-S193, 2021.
- [10] C. Watanakunakorn and J. C. Tisone, “Synergism between vancomycin and gentamicin or tobramycin for methicillin-susceptible and methicillin-resistant *Staphylococcus aureus* strains,” *Antimicrob. Agents Chemother.*, vol. 22, no. 5, pp. 903–905, 1982.
- [11] W. Han, L. Zhang, L. Yu, *et al.*, “Effect of local delivery of vancomycin and tobramycin on bone regeneration,” *Orthop. Surg.*, vol. 13, no. 5, pp. 1654–1661, 2021.
- [12] J. J. Morrison, J. J. Dubose, T. E. Rasmussen, *et al.*, “Military application of tranexamic acid in trauma emergency resuscitation (MATTERs) study,” *Arch. Surg.*, vol. 147, no. 2, pp. 113–119, 2012.
- [13] O. behalf of C.-2 trial Collaborators, “Effects of tranexamic acid on death, vascular occlusive events, and blood transfusion in trauma patients with significant haemorrhage (CRASH-2): a randomised, placebo-controlled trial,” *Indian J. Neurotrauma*, vol. 9, no. 1, pp. 3–14, 2012.
- [14] Y. Liang, J. He, and B. Guo, “Functional hydrogels as wound dressing to enhance wound healing,” *ACS Nano*, vol. 15, no. 8, pp. 12687–12722, 2021.
- [15] E. A. Kamoun, E.-R. S. Kenawy, and X. Chen, “A review on polymeric hydrogel membranes for wound dressing applications: PVA-based hydrogel dressings,” *J. Adv.*

- Res.*, vol. 8, no. 3, pp. 217–233, 2017.
- [16] M. J. Kratochvil, A. J. Seymour, T. L. Li, *et al.*, “Engineered materials for organoid systems,” *Nat. Rev. Mater.*, vol. 4, pp. 606–622, 2019.
- [17] U. Blache and M. Ehrbar, “Inspired by nature: Hydrogels as versatile tools for vascular engineering,” *Adv. Wound Care*, vol. 7, no. 7, pp. 232–246, 2018.
- [18] J. Smith, A. Johnson, and M. Garcia, “Biomimetic hydrogels: Inspired by the extracellular matrix for biomedical applications,” *J. Biomed. Mater. Res. Part A*, vol. 101, no. 8, pp. 2201–2215, 2023.
- [19] E. W. Merrill, K. A. Dennison, and C. Sung, “Partitioning and diffusion of solutes in hydrogels of poly(ethylene oxide),” *Biomaterials*, vol. 14, no. 15, pp. 1117–1126, 1993.
- [20] K. A. Cook, “Drug release kinetics from poly(ethylene glycol) hydrogels for wound dressings,” 2020.
- [21] B. S. Palmeiro and H. Roberts, “Clinical approach to dermatologic disease in exotic animals,” *Vet. Clin. North Am. Exot. Anim. Pract.*, vol. 16, no. 3, pp. 523–577, 2013.
- [22] A. C. Parker, C. Rhodes, J. A. Jennings, *et al.*, “Preliminary evaluation of local drug delivery of amphotericin B and in vivo degradation of chitosan and polyethylene glycol blended sponges,” *J. Biomed. Mater. Res. Part B Appl. Biomater.*, vol. 104, no. 1, pp. 78–87, 2016.
- [23] T. P. Popova and I. Ignatov, “In vitro antimicrobial activity of colloidal nano silver,” *Bulg. J. Vet. Med.*, vol. 26, no. 2, pp. 168–181, 2023.
- [24] A. A. Hassan, N. H. Oraby, E. M. E. El-Dahshan, *et al.*, “Antimicrobial potential of iron

- oxide nanoparticles in control of some causes of microbial skin affection in cattle,” *Eur. J. Acad. Essays*, vol. 2, no. 6, pp. 20–31, 2015.
- [25] L. T. Zaria, “Dermatophilus congolensis infection (dermatophilosis) in animals and man! An update,” *Comp. Immunol. Microbiol. Infect. Dis.*, vol. 16, no. 3, pp. 179–222, 1993.
- [26] M. S. Arayne, N. Sultana, F. A. Siddiqui, *et al.*, “Spectrophotometric techniques to determine tranexamic acid: Kinetic studies using ninhydrin and direct measuring using ferric chloride,” *J. Mol. Struct.*, vol. 891, no. 1–3, pp. 475–480, 2008.
- [27] X. Feng, G.-Y. Li, A. Ramier, *et al.*, “In vivo stiffness measurement of epidermis, dermis, and hypodermis using broadband Rayleigh-wave optical coherence elastography,” *Acta Biomater.*, vol. 146, pp. 295–305, 2022.
- [28] S. J. Lalliss, D. J. Stinner, S. M. Waterman, *et al.*, “Negative pressure wound therapy reduces pseudomonas wound contamination more than Staphylococcus aureus,” *J. Orthop. Trauma*, vol. 24, no. 9, pp. 598–602, 2010.
- [29] I. Wiegand, K. Hilpert, and R. E. Hancock, “Agar and broth dilution methods to determine the minimal inhibitory concentration (MIC) of antimicrobial substances,” *Nat. Protoc.*, vol. 3, no. 2, pp. 163–175, 2008.

## CHAPTER 6: Conclusions and Broader Impact

### 6.1 Conclusions and Summary

This work was largely motivated by nature and the principles of the Circular Economy [1], [2]. The first half of this dissertation sought to develop sustainable polymers using bio-based starting materials. The latter half focused on bioinspired hydrogels (as an extracellular matrix analogue) for wound dressing applications. Chapter 4 in particular bridges the gap between these projects, testing the potential of a variety of bio-inspired polymers as hydrogel crosslinkers.

**6.1.1. Lignin-Derived Polymers.** Chapters 2 and 3 used lignin precursors for polymer synthesis. In the former, poly(ether-amide)s synthesized by a previous Kasko lab member [3] were successfully modified through a thiol-ene reaction. While thiol-ene reactions in literature were performed almost exclusively on terminal alkenes, we were able to optimize this reaction to proceed on 1,2-disubstituted alkenes, even post-polymerization. Through thiol functionalization, polymer flexibility increased as the double bond was reduced, resulting in improved solubility and thermal properties. The hydroxycinnamate dimers from Chapter 2 were then used in condensation polymerizations with diol linkers. These linkers were synthesized via ring-opening polymerizations of lactones sourced from nature (i.e. lactide, glycolide,  $\epsilon$ -caprolactone) [4]. We also demonstrated that the symmetrical diols could be synthesized using enzyme catalysis in ionic liquids, further advancing the sustainability of the polymers [5]. Condensation polymerization between the diol linkers and hydroxycinnamates proceeded efficiently, and the series of polyesters displayed desirable molecular weights and thermal properties—with a surprisingly low  $T_g$ . Moreover, they all featured repeating ester bonds, and are expected to be hydrolytically degradable and compostable, breaking down into hydroxycinnamates and lactic/glycolic acid.

**6.1.2. Hydrogels.** *In situ* hydrogel crosslinking often relies on redox initiators—most commonly TEMED and APS. However, TEMED is cytotoxic, which is especially relevant in the context of hydrogels for wound dressing applications. In Chapter 4, Dr. Brooke Jackson Hoffman and I screened six bioinspired amine-containing compounds to test their ability to serve as a drop-in replacement for TEMED. We determined that Glycofect™ [6] and polyethyleneimine can be used with APS to generate radicals and successfully crosslink poly(ethylene glycol)-diacrylate (PEGDA) hydrogels. Beyond exhibiting comparable mechanical properties to the TEMED “gold standard”, these hydrogels were significantly more biocompatible, as determined by incubating in direct contact with fibroblasts.

Chapter 5 was the more translational branch of PEGDA hydrogel research conducted in this work. In a collaboration with the Department of Defense, the David Geffen School of Medicine, and University of Texas Medical Branch, we successfully designed and implemented a *in situ* forming, drug-loaded hydrogel wound dressing for prolonged field care. After significant *in vitro* optimization, the hydrogel was tailored to provide burst release of an analgesic and hemostatic agent and sustained release of two antibiotics—one for gram-positive and one for gram-negative species. Our collaborators confirmed in small animals its ability to eradicate polymicrobial infections and its safety through histological analysis. Our hydrogel platform was then advanced to complex contaminated open fracture Merino sheep wound models, where it again proved highly effective against significant *S. aureus* infections. Most importantly, the wound dressing prevented sepsis in all cases. Through these studies, the feasibility, scalability, safety, and efficacy of this hydrogel wound dressing have been demonstrated

## 6.2 Future Development

The next phase of work for the lignin-derived polymers is two-fold. First, both the thiol-modified poly(ether-amide)s and the condensation polymers will undergo compostability studies. Compostability testing comprises disintegration—examining polymer breakdown in a stable environment, biodegradation in soil—recording the amount of CO<sub>2</sub> released by microorganisms as the material decomposes, and ecotoxicity—testing plant seed germination in the composted packaging. Secondly, after scaling up the synthesis of these polymers, they will be used to attempt extrusion, heating the material to its T<sub>g</sub> or T<sub>m</sub> as pressure is applied to shape filaments through a die. Successful extrusion will pave the way for transitioning to scalable 3D printing of the polymers from biomass.

Finally, we hope to implement our non-toxic hydrogel initiator system in the drug-loaded wound dressing. This will require adjusting the polymer:initiator ratios to re-optimize mechanical properties and therapeutic release profiles of each of the therapeutic agents. Using the Glycofect™ initiation system for the wound dressing platform has a number of distinct advantages. Hydrogels initiated with Glycofect™ have a tendency to degrade over time, which would reduce risk of large polymer chunks becoming entrapped in the wound bed, causing an inflammatory response. Additionally, these hydrogels are non-toxic and would not kill the cells at the site of injury, expected to promote faster healing and reduced susceptibility to infection.

## 6.3 Broader Impact

The thiol-ene modifications in this paper can be applied to the vast majority of biopolymers using lignin building blocks, as they should all incorporate the repeating  $\alpha,\beta$ -unsaturated bonds. This has great potential to help overcome the solubility limitations that plague biomass-derived



polymers. Additionally, the modular and largely green condensation polymers in this work have great room for expansion, as the hydrolytically degradable diol linkers can be customized in both length and lactone.

The most significant impact of this work, however, will most likely be the hydrogel wound dressings. The amine polymer crosslinking system that Dr. Jackson Hoffman and I developed marks a drastic improvement in cytocompatibility, which is particularly important in this cell-interfacing application. Additionally, the drug eluting hydrogel wound dressing for prolonged field care has shown immense success *in vitro*, in small animals and in large animals. Given that the Department of Defense is able to obtain expedited FDA review for medical products to treat life-threatening conditions that military personnel are faced with, it is possible that this product will make it to the market. If this happens, it will open the door to expanding the wound dressing platform to an expansive number of applications, with a more facile FDA review process. Because it is modular, the therapeutic agents can be exchanged and the hydrogel's mechanical properties can be adjusted to optimize release kinetics for the new therapeutics. This had broad-reaching implications for dermal injuries ranging from diabetic ulcers to dermatophilosis in animals.

## 6.4 References

- [1] N. Suchek, C. I. Fernandes, S. Kraus, *et al.*, “Innovation and the circular economy: A systematic literature review,” *Bus. Strateg. Environ.*, vol. 30, no. 8, pp. 3686–3702, 2021.
- [2] J.-G. Rosenboom, R. Langer, and G. Traverso, “Bioplastics for a circular economy,” *Springer Nat.*, vol. 7, no. 2, pp. 117–137, 2022.
- [3] B. M. Upton and A. M. Kasko, “Biomass-derived poly(ether-amide)s incorporating hydroxycinnamates,” *Biomacromolecules*, vol. 20, no. 2, pp. 758–766, 2019.
- [4] H. R. Kricheldorf and S. M. Weidner, “About the influence of salicylic acid on tin(II)octanoate-catalyzed ring-opening polymerization of l-lactide,” *Eur. Polym. J.*, vol. 119, pp. 37–44, 2019.
- [5] C. Ortiz, M. L. Ferreira, O. Barbosa, *et al.*, “Novozym 435: the ‘perfect’ lipase immobilized biocatalyst?,” *Catal. Sci. Technol.*, vol. 9, no. 10, pp. 2380–2420, 2019.
- [6] Y. Liu and T. M. Reineke, “Hydroxyl stereochemistry and amine number within poly(glycoamidoamine)s affect intracellular DNA delivery,” *J. Am. Chem. Soc.*, vol. 127, no. 9, pp. 3004–3015, 2005.